Pili: the Microbes' Swiss Army Knifes

Inauguraldissertation

zur

Erlangung der Würde eines Doktors der Philosophie

vorgelegt der

Philosophisch-Naturwissenschaftlichen Fakultät

der Universität Basel

von

Matteo Sangermani

aus Italien

Basel 2018

Genehmigt von der Philosophisch-Naturwissenschaftlichen Fakultät auf Antrag von:

Prof. Dr. Urs Jenal

Prof. Dr. Rikke Louise Meyer

Basel, 27 März 2018

Prof. Dr. Martin Spiess

Dekanat

AUTHOR:
Matteo Sangermani

PHD THESIS
to achieve academic degree in:
BIOPHYSICS

PILI: THE MICROBES' SWISS ARMY KNIFES

FACULTY REPRESENTATIVE AND THESIS ADVISOR:
Urs Jenal

CO-REFEREE:
Rikke Louise Meyer

CO-EXAMINER:
Pfohl Thomas, Marek Basler

COMPLETED AT:
Biozentrum, University of Basel
Klingelbergstrasse 70, 4056 Basel, Switzerland

TIME FRAME OF THE PROJECT:
November 2013 – April 2018

Science is much more than a body of knowledge.

It is a way of thinking.

Carl Sagan (1934 -1996)

Table of Contents

LIST OF ABBREVIATIONS:

T4P: type 4 pili

CU pili: chaperone assembled pili

SMS pili: single membrane spanning pili

SA pili: sortase-assembled pili

T2SS: type 2 secretion system

T3SS: type 3 secretion system

T4SS: type 4 secretion system

T6SS: type 6 secretion system

IM: inner membrane

OM: outer membrane

NTD: N-terminal domain

CTD: C-terminal domain

EPS: extracellular polysaccharides

UPEC: uropathogenic *E. coli*

EPEC: enteropathogenic *E. coli*

EPS: extracellular polysaccharides

Cryo-EM: cryo-electron microscopy

PDMS: Polydimethylsiloxane

ABSTRACT:

Surface attachment is the crucial first step for a single cell transitions from a planktonic to a surface associated state, which can lead to the development of multicellular communities called biofilms. Microbes extensively use pili for initial surface attachment. Pili are filamentous appendages that extend into the extracellular environment and can attach to a wide range of surfaces. This Thesis contributes to the understanding of how pili work and how bacteria transition from a planktonic to a surface bound life style. This will aid future development in creating new ways to prevent bacterial attachment and biofilm formation and thereby avoid the necessity for the removal of fully developed biofilms which often requires harsh physical and chemical treatments which can be impractical in a biomedical context.

We used single cell studies, microfluidic methods and quantitative computational analysis to study in detail the mechanism of pili-mediated attachment in *Caulobacter crescentus* and *Pseudomonas aeruginosa*. In *C. crescentus* we confirm the recently described ability of pili to retract, which was previously considered not possible for this type of pili. We characterized this functionality in greater detail and our results highlight the importance of pili in reorienting cells and bringing the cell body closer to surfaces, whereby cells can promote long term attachment by secreting a glue-like substance called holdfast. We also investigated the role of the second messenger c-di-GMP during pili-mediated cell attachment and biofilm formation. We show a novel role for c-di-GMP in directly regulating elongation and retraction of pili in *C. crescentus* and *P. aeruginosa*. In *P aeruginosa* a novel c-di-GMP effector, FimW, regulates surface attachment and walking behaviour, and how its asymmetric distribution drives surface colonization. In *C. crescentus* we show that c-di-GMP positively regulates attachment. We manipulated a key component of the secretion machinery, HfsK, and show that c-di-GMP not only regulates the timing of holdfast synthesis, but also its cohesion and adhesion properties. Lastly, we report a novel protein, PdeL, which is both a phosphodiesterase and a transcriptional factor that regulates the expression of biofilm related genes in *Escherichia coli*.

In the appendixes we describe in detail the process for creating microfluidic devices, extensively used in the studies described in this thesis. Moreover, we include a manual for the use of WHISIT, a custom-made software program for the analysis of bacterial fluorescent signals in an automated and quantitative approach.

CHAPTER 1 - INTRODUCTION

0.   Preface

Using a microscope of his own design and construction, around the year 1670, Antonie van Leeuwenhoek was the first scientist to observe and describe the presence of *animalcules* inside a drop of lake water. Upon reading his work, many members of the Royal Society reacted with scepticism to what he reported:

"Examining this water next day, I found floating therein divers earthy particles, and some green streaks, spirally wound serpent-wise…. I judge that some of these little creatures were above a thousand times smaller than the smallest ones I have ever yet seen, upon the rind of cheese, in wheaten flour, mould, and the like."
(Letter to Henry Oldenburg, 7 September 1674)

Their very existence, small size and abundance surprised the scientific community of the time. Today we know that he was looking at microbial life: prokaryotes, unicellular eukaryotes and algae. However, van Leeuwenhoek observed that those *animalcules* where not found living only in water environments. He indeed found *animalcules* on surfaces of materials like cheese mould and tooth plaque:

"In the morning I used to rub my teeth with salt and rinse my mouth with water and after eating to clean my molars with a toothpick…. I then most always saw, with great wonder, that in the said matter there were many very little living animalcules, very prettily a-moving. The biggest sort had a very strong and swift motion, and shot through the water like a pike does through the water; mostly these were of small numbers."

Microbes have been traditionally associated with a planktonic life style: solitary unicellular organisms living in liquid environments. Therefore, their ability to create multicellular communities, named biofilms, was overlooked. Today is accepted that the ability of prokaryotes to colonize objects and form biofilms on surfaces is very common and widespread in many diverse environments.

In an aquatic environment, any zooplankton and floating object, dead or alive, provides a surface that can be colonized. Microbes colonize virtually any surface on the planet. For prokaryotes colonizing a surface is an important opportunity to survive and proliferate because surfaces can provide protection from physical damage and can anchor a biofilm in a favourable environment. Surfaces can also provide a source of nutrients. Biofilm formation has both positive and negative aspects for human society. From the negative point of view, biofilms are often what makes bacteria more resilience to the immune system and antibiotics and the virulence of some pathogens has been linked to the ability to form biofilms. But multicellular communities of prokaryotes do play fundamental beneficial roles as well, like supporting the habitable state of our planet and constituting the microflora of many organisms.

The development of a biofilm can be divided in the several steps. In this Thesis we will focus to the first step, when a free-floating bacteria land and attach on a surface. Microbes can employ different strategies and appendages to achieve this. However, pili are widely used by prokaryotes to promote initial surface interaction as well as a variety of secondary phenotypes. Pili are extracellular appendages, each made of a thin protein filament that possesses adhesive properties and can be a few micrometers long. In the following introduction we will review the current knowledge on pili with particular focus on type 4 pili (T4P) which are the most studied and of greater relevance in the context of the studies reported in Chapter 2 and 3. The ability of these pili to attach and retract make T4P an incredibly versatile tool for bacteria, such that they earned the title of "prokaryotic Swiss army knife" (Berry, J.-L., and Pelicic, V., 2015). In the second part we will explore the plethora of uses and phenotypes related to pili. In the last part of the Introduction we will have a general overview of other types of pili and compare them with the T4P.

1. Pili in Gram-negative bacteria

Non-flagellar appendages were first observed in 1949 using an electron microscope (Brinton, C.C., 1959). Over time, various nomenclatures arose to describe the many filaments protruding from the cell body of bacteria, which has led to redundant naming. Non-flagellar appendages can be organized according to the presence or absence of a cavity within the filament. The filaments formed by chaperone-usher pili, curli, type 4 pili (T4P), type 5 pili (T5P) and sortase-assembled pili (SA pili), do not have a cavity and are called "pili" (or "fimbria"). The filaments created by type 3 secretion (T3SS), type 4 secretion (T4SS) and type 6 secretion (T6SS) systems are called "needles", because those appendages are hollow and are used for injection or secretion of macromolecules (see Box 2) (Hospenthal, M.K. et al., 2017a; Pelicic, V., 2008). Within the pili appendages there is a great diversity in types of pili machineries. In the following sections, we will describe three main types of pili that can be found in Gram-negative bacteria: type 4 pili (T4P), chaperone-usher pili (CU) and type 5 pili.

1.1. Type 4 Pili

Type 4 pili (T4P) constitute machineries embedded in both the OM (outer membrane) and IM (inner membrane) and are capable to elongate and retract a filament in the surrounding environment. From attachment to twitching, contributing to biofilm adhesion and uptake of extracellular DNA, the ability to dynamically elongate and retract makes this type of pili a versatile tool used for many biological functions. They are widespread among Gram-negative bacteria, Gram-positive bacteria and archaea (Berry, J.-L., and Pelicic, V., 2015). T4P in Gram-negative bacteria have been by far the most studied and are understood in greater detail than pili of archaea and Gram-positive bacteria. This is because a majority of Gram-negative pathogens express T4P that function as crucial virulence factors (Craig, L., and Li, J., 2008; Pelicic, V., 2008).

ORGANIZATION OF THE T4P MACHINERY

1.1.1. THE FILAMENT

The extracellular filament protruding from the cell envelope is the visually striking feature of pili. The pilus filament is about 4 to 8 nm wide and several micrometers in length (Craig, L. et al., 2003; Wang, F. et al., 2017). The filament is made of many repeating protein subunits, called pilins, assembled in a helix (see Figure 1A and 1B). The major pilin is the main component of the filament. The first 5 to 30 amino acids at its N-terminus constitute the leader peptide, a signal sequence that directs pilins to be incorporated into the IM (Giltner, C.L. et al., 2012). This sequence is subsequently removed by prepilin peptidases, concluding the maturation process of pilins. Mature pilins are then ready to be assembled into a filament. During disassembly of a filament, pilins are brought back into the IM where they can be recycled in multiple rounds of elongation/retraction (Skerker, J.M., and Berg, H.C., 2001). The last subunits at the base of the filament are embedded in the IM, strongly contributing to hold the filament anchored to the cell envelope. All type 4 pilin subunits have a similar architecture composed of two domains (Giltner, C.L. et al., 2012, Wang, F. et al., 2017). The N-terminal domain, around 50 amino acids long (leader peptide excluded), is a conserved sequence forming an alpha helix. The α1-N part of the alpha helix is hydrophobic and protrudes out of the globular head while the α1-C part is amphipatic and has the hydrophilic face covered by the C-terminal domain (see Figure 1A). The two halves of the alpha helix are often divided by a flexible region or kink. The C-terminal domain constitutes the globular head. The conserved structural core is made of a beta sheet that wraps around the α1-C region. Two additional regions complete the C-terminal globular head. The $\alpha\beta$ loop region connects the N- to the C- terminal domain. The D region is a highly variable stretch of the protein, close to C-terminus and bordered by two conserved cysteines that form an important disulphide bridge. $\alpha\beta$ loop can harbour glycosylation sites ($\alpha\beta$ loop) (Craig, L. et al., 2006). In some species, both $\alpha\beta$ loop and D region constitute a hypervariable region, as a measure to escape the immune system (Criss, A.K. et al., 2005). The $\alpha\beta$ loop and the D region from different species vary markedly in length, bulge out of the globular head domain and form the main interaction interfaces with the environment (Craig, L., and Li, J., 2008).
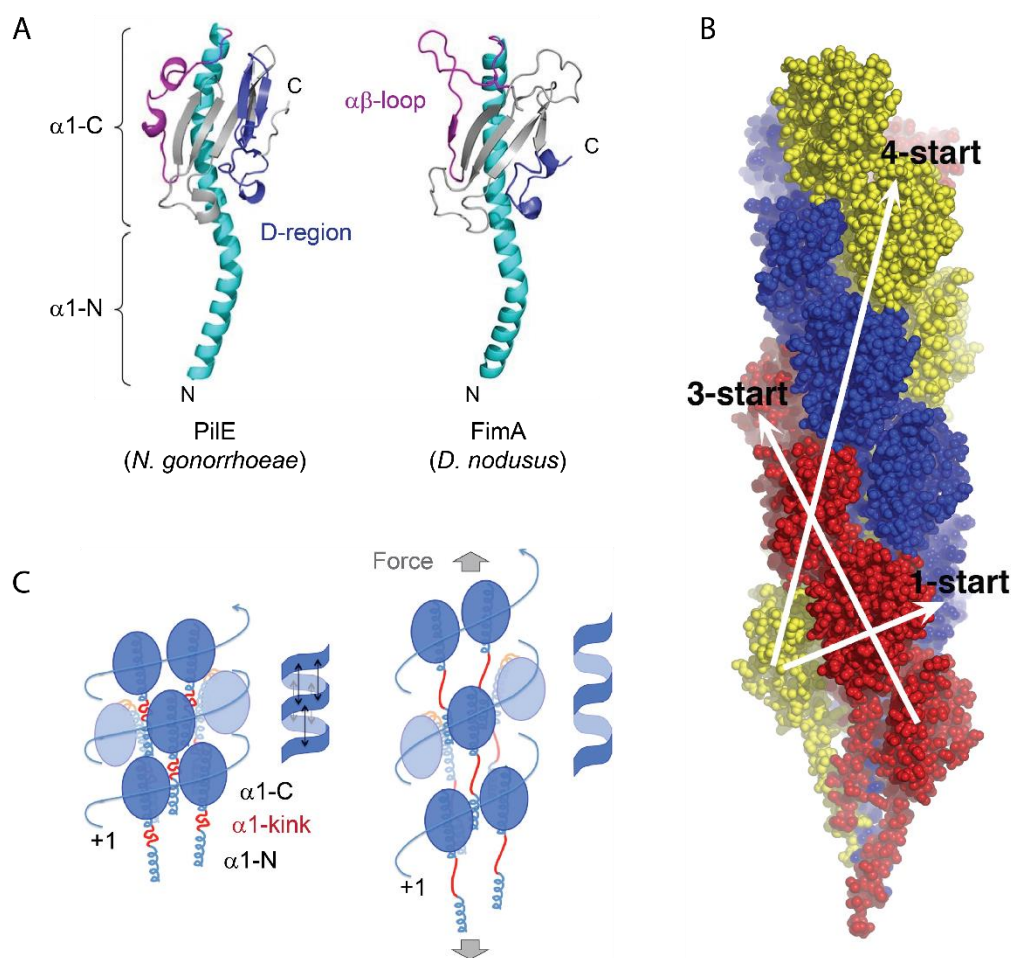
(A) Type 4a pilin crystal structures of *Neisseria gonorrhoeae* (PBD: 1AY2) and *Dichelobacter nodusus* (PDB: 3SOK). The α1 helix is coloured in cyan. The globular head core structure is in grey, while in blue and magenta are represented the D-region and $\alpha\beta$-loop, respectively. **(B)** The filament of *N. gonorrhoeae* possesses a 1-start helical architecture as well as a 3-start and 4-start symmetry. The 3 colours depict the 3-start architecture of the filament. **(C)** When a filament is not subject to tension, the heads of different coils of the helical architecture are closely packed. However, upon tension the weak interaction between the heads of the coils break up, allowing the small stretch of amino acids between α1-N and α1-C to unfold, granting a degree of elasticity to the filament. [The figures shown are reproduced from the following sources: **A** – Giltner, C.L. et al., 2012; **B** - Craig, L. et al., 2004 ; **C** – Kolappan, S. et al., 2016]

Electron cryotomography (Cryo-EM) studies have revealed that pili filaments are formed by arranging major pilins in a helical array. The subunits stacking creates a right-handed 1-start helix, with rise of abut 10Å and rotation of 85-100° per subunit, amounting to 3.6 to 4 subunits per turn (Craig, L. et al., 2006; Kolappan, S. et al., 2016; Wang, F. et al., 2017). However, pilin subunits also form a left-handed 3-start and 4-start helical architecture in the filament, alongside the 1-start helix (see Figure 1B). The 1-start helix appears to be the way pilin subunits are added into the filament of a growing pilus (see section 1.1.3).

The core of the filament is formed by tightly packed α1 helixes lying almost parallel to the axis of the filament. Each pilin α1 helix interacts with a total of 4-6 neighbouring partners (Craig, L. et al., 2006).

One extremely conserved polar residue, Glu5, is present in the α1 region of mature pilins (Craig, L. et al., 2004; Wang, F. et al., 2017). The filament core is overall charge neutral and α1 helices form extensive hydrophobic interactions. These are the major contributions to the intermolecular forces holding the filament together and are responsible for the stability and tensile properties of the filament (Craig, L. et al., 2006; Kolappan, S. et al., 2016; Wang, F. et al., 2017).

The C-terminal globular domain of pilins does not contribute to the filament cohesion in *Neisseria gonorrhoeae* (Kolappan, S. et al., 2016). There are limited polar interactions between the globular heads of neighbouring subunits. The globular heads protrude from the hydrophobic core of the filament and completely shields it from the environment. Globular heads are lining the filament surface, presenting a highly corrugated surface, with grooves and cavities created by the interlocking neighbours and protruding $\alpha\beta$ loop and D region (see Figure 1B). Grooves and cavities are responsible for the ability to bind to specific molecules. There are indications that pili in *P. aeruginosa* can bind DNA in a sequence-independent manner (Schaik, E.J. Van et al., 2005) (see section 1.1.11). In *N. gonorrhoea* a positively charged groove along the filament surface is wide enough to possibly bind double stranded DNA (Craig, L. et al., 2006), which could explain the role of T4P in promoting natural competence for DNA uptake.

The pili filaments have considerable tensile properties and yet are flexible at the same time, with a persistence length, measure of the stiffness of a polymer, of only a few nanometers in *P. aeruginosa* (Lu, S. et al., 2015). Pili can withstand up to 250 pN before rupture (Touhami, A. et al., 2006). Pili in *Neisseria meningitidis* display spring-like properties, whereby upon tension interactions between globular heads of each coil of the helical structure of the filament unfold (see Figure 1C). Moreover, the kink between the α1-N and α1-C can be stretched, allowing a spring-like motion of the coils of the filament and granting elastic properties to the pilus (Kolappan, S. et al., 2016). In *N. gonorrhoeae* conformational changes during tensional stresses can stretch pili to become 2-3 times longer and it was shown that the elongated pilus exposes new epitopes that were previously hidden in the tight coils of the filament (Biais, N. et al., 2010).

1.1.2. THE ASSEMBLY MACHINERY

The genes that comprise the pilus machinery have been divided in core and non-core components. The core components are always present and genetically conserved, comprising: (1) one or several pilins, (2) one or two type II/type IV secretion motor NTPase, (3) an IM platform protein (homologues of PilC) and (4) an OM secretin pore protein (homologues of PilQ) (Pelicic, V., 2008). In addition, each pilus machinery has several non-core components that usually are specific to each species. In the following section we will describe how the core components are organized in the assembly machinery.
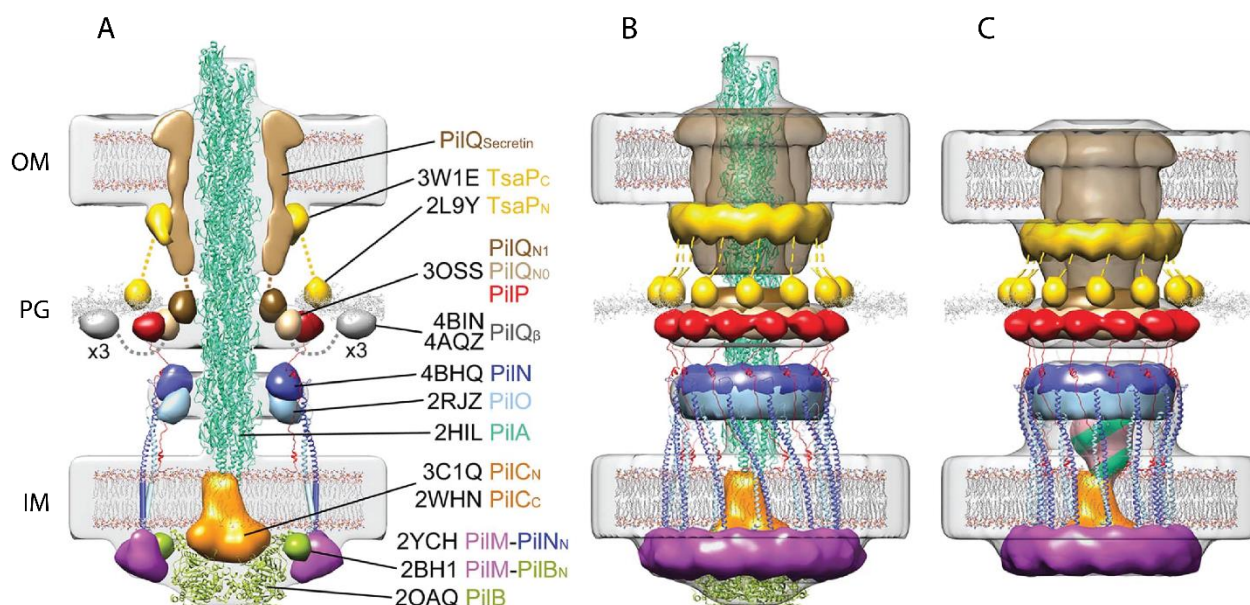
The images show the cryo-EM density maps of the T4P machinery. Panel **A** shows a longitudinal cross section of the machinery, while **B** and **C** show the whole machinery with and without the filament, respectively. Every component of the machinery assembles into ring structures around the cavity that host the filament. The only exceptions are PilC and the motor PilB. When the filament is disassembled, a small step filament is present at the base of the machinery, composed of major and minor pilins. Density clusters are coloured to highlight different components of the machinery and were fitted with crystal structures when available. [The figures shown are reproduced from: of Y.W. Chang et al., (2016)]

Until recently the organization of the assembly machinery was unknown. However, breakthroughs using Cryo-EM made possible to appreciate the 3-dimentional *in situ* structure of the whole machinery and the organization of the components within it (Chang, Y.W. et al., 2017; Chang, Y.W.Y.-W. et al., 2016; Gold, V.A.M. et al., 2015). In *Myxococcus xanthus*, the assembly machinery is constituted by 10 proteins, spanning from the inner to the outer membrane and is where the filament is assembled, disassembled and hold attached to the cell (Chang, Y.W.Y.-W. et al., 2016) (see Figure 2). The assembly machinery can be divided into three functional parts: an OM pore complex, and IM complex and a motor complex located in the cytoplasm.

Most components of the machinery assemble into ring-like structures around a cavity that can hosts the pilus filament (Chang, Y.W.Y.-W. et al., 2016). PilQ, a member of the secretin family proteins, assembles at the OM to form a secretin pore. This barrel-like structure has a gate that is closed when the pilus filament is absent and extends into the periplasm, where it interacts with the peptidoglycan layer. Associated with the secretin pore on the inner side of the OM is the protein TsaP, which may help to stabilize PilQ and/or connect the OM complex to the peptidoglycan. The IM complex is composed of PilC, PilM, PilN and PilO. PilC constitutes the inner membrane platform that recruits pilins from the membrane. PilC directly interacts with the motor ATPases (Takhar, H.K. et al., 2013) and its position in the machinery strongly suggests that it binds to pilin subunits and guides their assembly (Chang, Y.W.Y.-W. et al., 2016) (see section 1.1.3). PilN and PilO are homologues and form

heterodimers (Sampaleanu, L.M. et al., 2009), which create a ring structure in the lower part of the periplasm. PilM forms a ring structure on the inner side of the IM. It has been suggested that homologues of PilM are localization factors for the other components of the machinery and also help in recruiting the motor components. PilP is a crucial component, interacting with both PilQ, PilN/O and the IM. PilP helps to connect and align the IM complex with the OM pore complex. In the work of Y.W. Chang et al., (2016) each ring structure and the OM pore complex could be fitted with 12 copies of each corresponding component. This results in a 1:1 stoichiometry between the different components (Chang, Y.W.Y.-W. et al., 2016).

The last component is the motor complex, formed in *M. xanthus* by PilB, for assembly, or PilT, for disassembly. Both PilB and PilT have similar structures and they belong to the large family of type II/type IV secretion NTPases. In this family of motor proteins six monomers assemble into a hexameric ring to form an active complex. The main functional difference is thought to be that they work in inverse directions (see section 1.1.3) (McCallum, M. et al., 2017). On the cytoplamatic side of the machinery there is place for only one of the two motor complexes and no motor complex was associated with an assembly machinery lacking the pilus filament (Chang, Y.W.Y.-W. et al., 2016). In *Aquifex aeolicus* and *Geobacter metallireducens*, the structure of the monomeric ATPases showed two globular domains divided by a cleft that hosts the ATP binding site (McCallum, M. et al., 2017; Misic, A.M. et al., 2010). Binding of ATP and release of ADP drives considerable conformational changes between the two domains of a subunit, which in turn leads to large reorganizations of the hexameric complex, with motions between different subunits of 10 Å or more (Misic, A.M. et al., 2010; Satyshur, K.A. et al., 2007). This is very close to the 11 Å measured for elongation of the filament at each pilin added (see section 1.1.3). Those large conformational changes could, directly or indirectly, provide the mechanical force to drive major pilins out of the membrane and into the growing filament.

Minor pilins are often necessary components of the pilus machinery, though their role is not always clear. Structurally, minor pilins are similar to major pilins. They possess an N-terminal α1 helix and a globular head at the C-terminus. This allows minor pilins to be included into the filament. However, the globular domain is much less conserved and can be bigger (Craig, L. et al., 2004; Giltner, C.L. et al., 2012). Minor pilins are difficult to detect in intact pili because they are present only in fractional amounts, sometime one copy per filament. Some minor pilins are essential for assembly of filaments while others are not. Some minor pilins can functionalize the tip of the pilus fiber or are sparsely incorporated in the fiber, where interact in specific binding or promote pilus-to-pilus adhesion (Hélaine, S. et al., 2005, 2007). Other minor pilins can be the components that initiate pilus assembly. In *Vibrio cholerae*, the minor pilin TcpB plays a pivotal role as both an initiator as well as a terminator of pilus assembly in toxin coregulated pili (TCP) (Ng, D. et al., 2016). In the absence of a pilus filament, the gate of the OM secretin pore is closed. Interestingly, the machinery retains a short stem fiber at the base of the machinery (Chang, Y.W. et al., 2017; Chang, Y.W.Y.-W. et al., 2016). This is composed of both, minor and major, pilins, and it has been proposed to be the initiator complex. However, it could have a structural function, possibly as a placeholder: in fact mutants in

minor and major pilins often cannot assemble pili and have defects in the structure of the lower periplasmic part of the machinery (Chang, Y.W.Y.-W. et al., 2016).
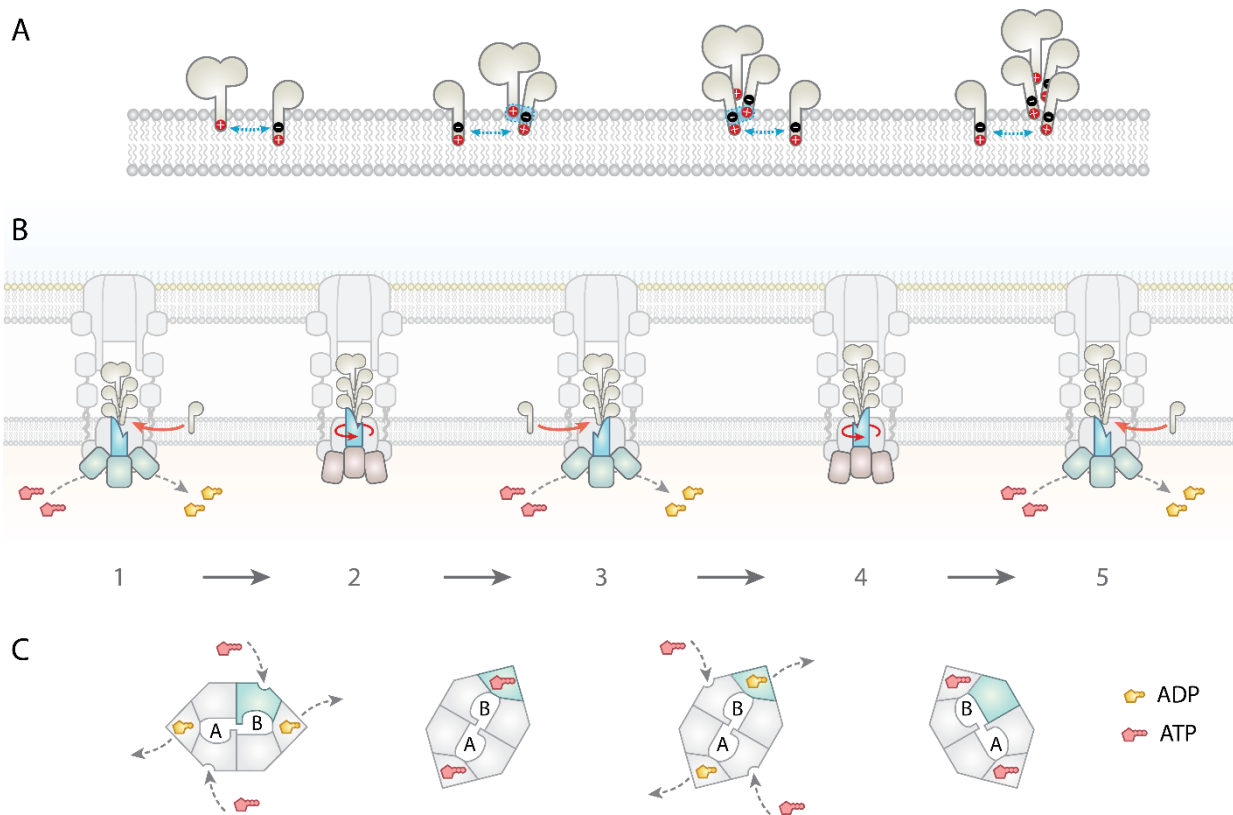

FIGURE 3 – A MODEL OF THE WORKING MECHANISM OF PILI MACHINERY

(A) The schematic depiction shows how the Glu5 at N-terminus of pilins mediate a salt bridge and recruit the next subunits to add in the filament. **(B, C)** The IM platform PilC, in cyan, is embedded in the membrane when the motor complex PilB is bound to ADP and it may create a binding pocket for recruiting free pilins. Each of the dimer of PilC is thought to sit in one of the two pores created within the structure of the hexameric motor. Upon binding of ATP to available subunits, they undergo extensive conformational changes that affect the entire hexameric motor. ADP is released from two subunits during the rearrangement. Ultimately the rearrangement lead to the reorientation of the pores in the center of the complex, with a rotation of about 60°. In the process, PilC is thrust upward in the periplasm and rotates of 60°, after which PilC is aligned with the new position of the pores and will fall back into the membrane. [The schematic draw is based on the studies and supplementary movies found in the work of Y.W. Chang et al., (2016) and M. McCallum et al., (2017)].

1.1.3.   THE WORKING MECHANISM

There is limited data on the working mechanism of the pili machinery. However, theoretical models have been proposed, based on our understanding of the structure of the machinery explained above. Pili are grown bottom-to-top, adding , or removing, one subunit at a time from the proximal end of the filament (McCallum, M. et al., 2017; Misic, A.M. et al., 2010). As mentioned above, each pilin contains a conserved Glu5 amino acid at N-terminus. Each Glu5 of a free pilin interacts with the, usually positive, first or second amino acid of the last subunit in the filament, thereby neutralizing these charges in the otherwise hydrophobic core of the filament (Wang, F. et al., 2017). This

interaction is crucial and it is thought to be responsible to help recruiting new subunits into the assembling pilus.
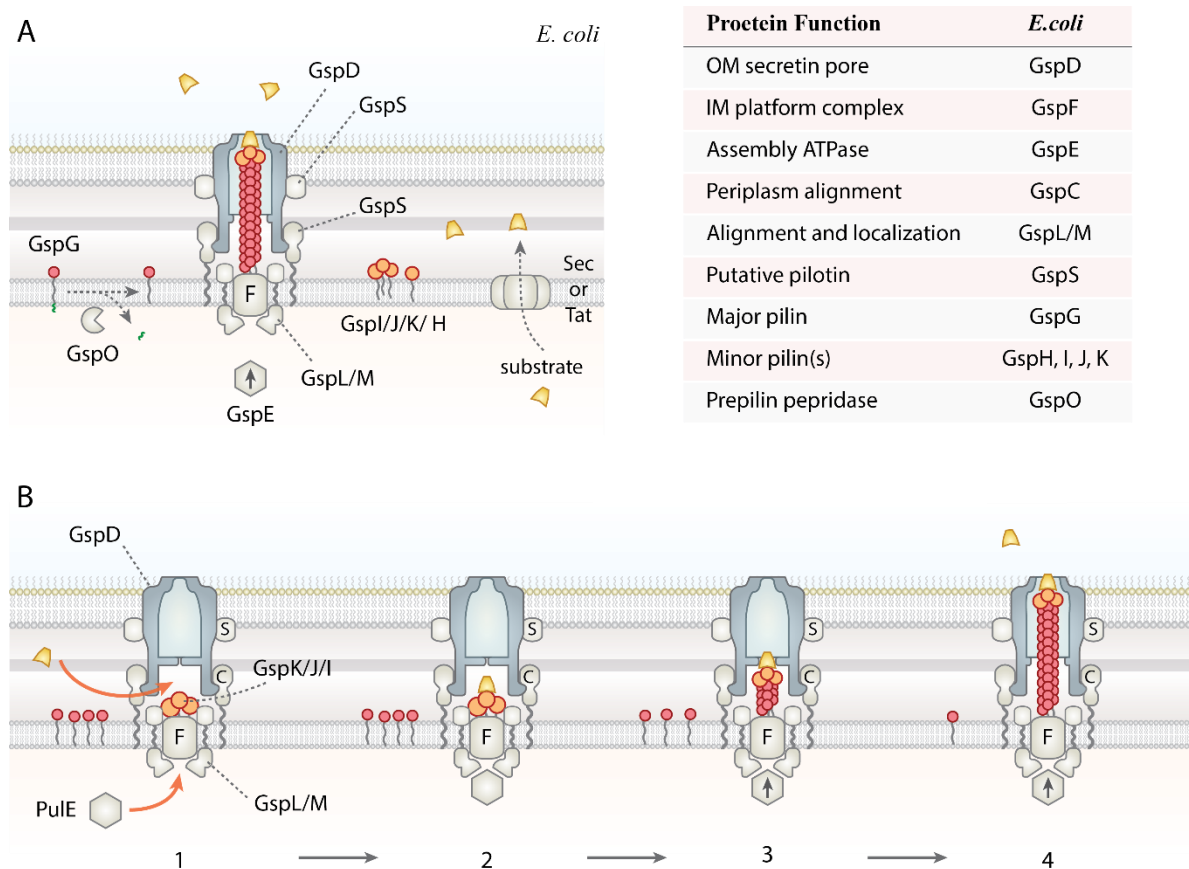
Two mechanisms have been proposed to be at work during pilus extension and retraction (Maier, B., and Wong, G.C.L., 2015). One is the piston model. As shown above, the hexameric form of the ATPase undergo considerable conformational changes upon ATP binding and hydrolysis (Misic, A.M. et al., 2010). In the piston model, those conformational changes are transmitted to the IM protein PilC. In turn, the IM platform PilC transmits the molecular movements to propel one pilin subunit out of the membrane and into the filament. The second mechanism, rotation, was proposed due to the helical structure of the filament. The assembly of a 1-start helical filament requires that either the filament or some components of the machinery rotate during assembly. In the closely related machinery of the T2SS (see Box 2), it has been suggested that the pseudopilus rotates as it elongates (Nivaskumar, M. et al., 2014). T4P and the archaellum, the swimming organelle of archaea (see Box 3), also have homologies between several components, and the latter machinery can indeed rotate its filament (Poweleit, N. et al., 2016). However, a rotation of the T4P filament or of cells during the elongation/retraction of surface-anchored pili has never been observed. Thus, it is likely that some components of the machinery rotate during filament elongation rather than the filament.

The two mechanisms, piston and rotation, are not mutually exclusive and a recent model suggests that both mechanisms might be at work at the same time (see Figure 2B and 2C). The following model is drawn from the structural insight taken from the assembly ATPase PilB in *G. metallireducens* and the pilus machinery of *M. xanthus* (Chang, Y.W.Y.-W. et al., 2016; McCallum, M. et al., 2017). The IM platform PilC dimer is the only component that can rotate within the machinery (Chang, Y.W.Y.-W. et al., 2016). The motor complex formed by PilB is held in place by interactions with the PilM ring structure (Chang, Y.W.Y.-W. et al., 2016). The hexameric form of PilB presents two small pores, which are potential binding sites for the PilC dimer (McCallum, M. et al., 2017). In this model PilC dimer also interacts with the proximal end of the filament in the IM, where it creates a favourable hydrophobic binding pocket to recruit one free pilin subunit. Extensive rearrangement of the motor complex (see Figure 2C) thrust PilC dimer upward into the periplasm, helping to push pilin subunits out of the IM and into the filament. During this piston mechanism, PilC dimer rotates by ~60° and by the end of the rotation it interacts with different subunits of the motor complex. This new position coincides with the new location of the two small pores in PilB hexamer, whereby the PilC dimer falls back from the IM, ready for a new cycle (Chang, Y.W.Y.-W. et al., 2016; McCallum, M. et al., 2017). In this way PilC could sequentially interact with different pairs of subunits of the hexameric motor, thereby rotating for each pilin subunit added (McCallum, M. et al., 2017). Sequential activation of single subunits in the hexameric structure could also grant the high processivity observed in pili assembly and retraction (Misic, A.M. et al., 2010).

BOX 1 – TYPE 2 SECRETION SYSTEM (T2SS)

Type 2 secretion system (T2SS) is found in many Gram-negative bacteria, but to date, not in Gram-positive or archaea. This nanomachinery is used to secrete folded exoproteins into the extracellular environment. A single T2SS can secrete from one to 20 different types of substrates (Korotkov, K. V. et al., 2012). Substrate range from be enzymes, toxins. A special secretion motif created upon folding in the periplasm allows exoproteins to be recruited by the T2SS.

The general structure and organization of the machinery is similar to the T4P (see Box 2). They possess an IM platform, an OM secretin pore and a motor complex. As in T4P and archaellum, the machinery assembles helical fibers using a pool of subunits, called major and minor pseudopilins, lying in the IM when the pseudofilament is not assembled (McLaughlin, L.S. et al., 2012). Pseudopilins are structural homologues of T4P pilins, with a striking conservation in the N-terminal α1 sequence (Giltner, C.L. et al., 2012). In fact, some species use a common prepilin peptidase for both systems. Minor pseudopilins are known to be at the tip of the pseudopilus and their assembly initiates elongation of the filament. The assembly motor is closely related to T4P ATPases, together they are part of the large family of type II/type IV secretion NTPases.

Proctein Function	E.coli
OM secretin pore	GspD
IM platform complex	GspF
Assembly ATPase	GspE
Periplasm alignment	GspC
Alignment and localization	GspL/M
Putative pilotin	GspS
Major pilin	GspG
Minor pilin(s)	GspH, I, J, K
Prepilin pepridase	GspO

Interestingly, the working mechanism of T2SS closely resembles the one for T4P (Nivaskumar, M. et al., 2014), outlining a possible ancient share origin for the two organelles. The pseudopilus does not extend into the extracellular environment. Due to the size of minor pseduopilin, the pseudopilus cannot pass through the secretin pore, limiting its elongation to the periplasm. However, this does not prevents its normal function. An exoprotein gets recruited by the secretin pore and/or minor pseudopilins, which trigger filament assembly. The growing pilus acts like a piston that pushes the exoprotein through the secretin pore and release it in the extracellular medium. Since there is no retraction ATPase, pseudopili are proposed to self-disassemble, freeing the machinery for the next secretion and allowing for recycling of pseudopilins (Campos, M. et al., 2013; Korotkov, K. V. et al., 2012).

T2SS is an ancient and widespread machinery present in many Gram-negative bacteria and share a common ancestor with T4P, T4SS and the archaellum. Indeed, some mutants point to the ability of T2SS to act as primitive pili. Reducing the size of the pseudopilus tip by deleting a minor pseudopilin, allow *P.aeruginosa* cells to secrete long extracellular filaments (Campos, M. et al., 2013). Interestingly, those primitive pili have adhesion properties and increase attachment rates of cells (Durand, É. et al., 2003; Vignon, G. et al., 2003).

Disassembly ATPase PilT is structurally similar to PilB, except PilT hexamer forms only one small pore instead of the two (McCallum, M. et al., 2017). Therefore, disassembly of pili is perhaps just the inverse mechanism of assembly. PilT could act by rotating PilC in the opposite direction than PilB does and pull PilC back from the periplasm, which in turn drag a pilin subunit back into the IM (Chang, Y.W.Y.-W. et al., 2016). However, another interesting model proposed self-disassembly driven by free energy minimization as mechanism for pili retraction. In this model, the energy for disassembly is stored in the filament during assembly, assuming pilin subunits are in a more favourable state embedded in the IM rather than in the filament. Therefore, a PilT motor would use ATP to constantly move PilC dimers away from the most proximal subunit of the filament, and allow pilins to move back into the IM due to free energy minimization. Interestingly, some types of pili (see section 1.1.4), lack a dedicated retraction ATPase, but in some organisms they are still capable of retraction (Ellison, C.K. et al., 2017; Ng, D. et al., 2016). In *V. cholerae* the minor pilin TcpB can block elongation of a growing pilus, possibly displacing the assembly ATPase, and initiates retraction event driven by self-disassembly (Ng, D. et al., 2016). Similarly, tad-like pili in *C. crescentus* are capable of retraction, although the mechanism is not yet known. Also, it cannot be excluded that the same motor complex could work in reverse and that the direction is modulated by a yet unknown interaction partner. Regardless of the mechanism, absence of retraction ATPases does not always preclude retraction of pili. On the other hand, dedicated retraction ATPases are present in all bacteria performing twitching, a pili-mediated surface motility (see section 1.1.6). We could speculate that having both assembly and retraction ATPases would help to better coordinate the action of different pili within a cell and achieve directed motion (see section 1.1.8). A detailed representation of the working mechanism of the pilus machinery can be appreciated in the supplementary movies provided in the work of work Y.W. Chang et al., (2016) and M. McCallum et al., (2017).

There are some gaps in our knowledge that remain to be addressed. How PilC dimer contributes to create an active site for pilin subunits and promote assembly is still unknown. Also, pilins at the base of the filament are embedded in the IM, which would provide a substantial anchor for the filament, but more support may be required to explain the high tensile strength observed. PilN/O form a periplasmic ring that is also thought to interact with the filament and may provide additional interactions to counteract tensile stresses. Lastly, it cannot be excluded that other components, such as the motor, are also rotating during the assembly/retraction of pili.

1.1.4.   CLASSES OF TYPE 4 PILI

From the sequence and structural similarities of major pilin subunits, T4P have been divided into two major classes: type 4a and type 4b pili (see Figure 4) (Craig, L. et al., 2004). Type 4a pilins have shorter leader peptides and an average length of 150 amino acids. Type 4b pilins have longer leader peptides, but their full length can be either very long (180-200 amino acids) or very short (40-60 amino acids). The shorter form has been proposed to be a class of its own, named tad-like pili or type
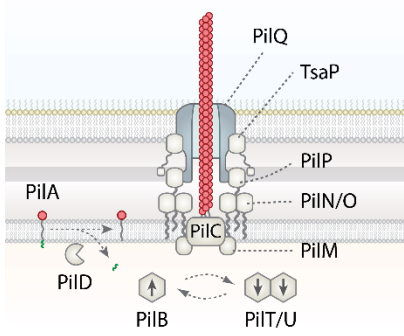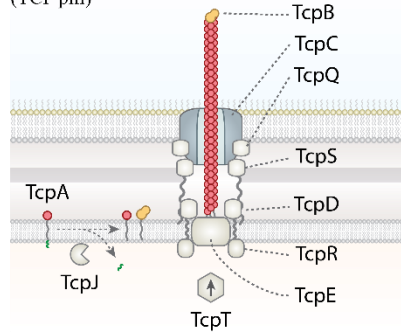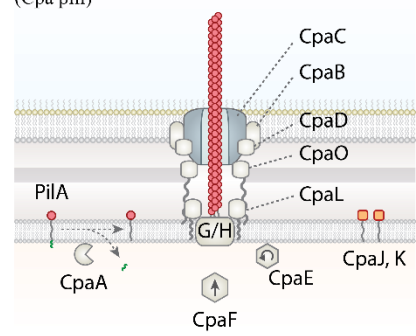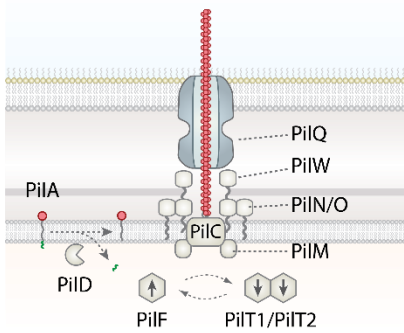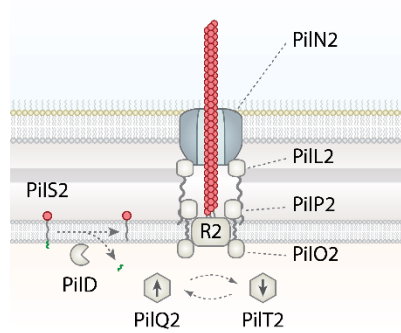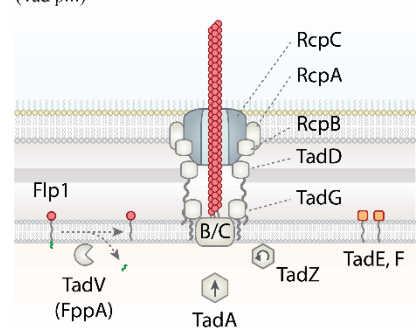
Proetein Function	Type 4a		Type 4b		Tad-like	
	M. xanthus *P. aeruginosa* *Xanthomonas* sp.	*N. meningitidis* *N. gonorrhoeae*	*V. cholera*	*E. coli*	*A. actinomyce-temcomitans*	*C. crescentus*
OM secretin pore	PilQ	PilQ	TcpC	BfpB	RcpA	CpaC
IM platform complex	PilC	PilG	TcpE	BfpE	TadB/G	CpaG/H
Assembly ATPase	PilB	PilF	TcpT	BfpD	TadA	CpaF
Retraction ATPase	PilT/PilU	PilT	-	BfpF	-	CpaE
Periplasm alignment	PilN, O, P	PilN, O	TcpD, S	-	TadG	CpaL
Localization	PilM	PilM	TcpR	-	-	-
Putative pilotin	TsaP (PilF)	-	TcpQ	-	RcpB, C, D	CpaB, D, O
Major pilin	PilA	PilE	TcpA	BfpA	Flp	PilA
Minor pilin(s)	PilV, W, X , FimU	PilV, X	TcpB	BfpI, J, K	TadE, F	CpaJ, K
Prepilin pepridase	PilD	PilD	TcpJ	BfpP	TadV	PilD
References	*(a)*	*(b)*	*(c)*	*(d)*	*(e)*	*(d)*

FIGURE 4 – DIFFERENT CLASSES OF TYPE 4 PILI

(A) Schematic representation of different classes of T4P. Some schematics are based on resolved structural studies, indicated next to the organism name. Notice that type 4a always have both elongation and retraction motors. Tad-like pili do not possess retraction ATPases, while type 4b can have them. CpaE and TadZ are depicted as possible "switch", although their role is still unclear. Most of the components depicted are the conserved core proteins of the type 4 pili machinery. For most minor pilins, their role is unclear.

(B) The table lists different organisms and compares the components of pili, grouping them by function. Note: for type 4a and 4b pili the function of most components has been experimentally determined. For tad-like pili the function of each component is assigned based on homology studies.

(a) - Burrows, L.L., 2012; Chang, Y.W.Y.-W. et al., 2016; Dunger, G. et al., 2014; Zhang, Y. et al., 2012
(b) - Karuppiah, V., and Derrick, J.P., 2014
(c) - Chang, Y.W. et al., 2017; Seitz, P., and Blokesch, M., 2013
(d) - Ramboarina, S. et al., 2005; Roux, N. et al., 2012
(e) - Kachlany, S.C. et al., 2001a; Planet, P.J. et al., 2003; Tomich, M. et al., 2007
(f) - Christen, M. et al., 2016; Mignolet, J. et al., 2018; Skerker, J.M., and Shapiro, L., 2000

4c pili (Planet, P.J. et al., 2003; Tomich, M. et al., 2007). From the structural point of view, pilins of both types, 4a and 4b, are similar. The N-terminal α1 helix is conserved among all pilins and differences are concentrated in the globular head domain, especially the length and arrangement of the $\alpha\beta$ loop and D region (Giltner, C.L. et al., 2012).

The genetic organizations of type 4a and type 4b pili presents clear differences. Type 4a pili are encoded by 10-12 genes. Type 4a are a relatively homogenous group with differences mainly concerning the non-core genes. Type 4a pili are found widespread among many unrelated bacterial families, for example in *P. aeruginosa*, *N. gonorrhoeae, M. xanthus* and *Xanthomonas* species (Craig, L. et al., 2004). Moreover, the genes are clustered in small groups and distributed across the entire genome, although each cluster is flanked by the same housekeeping neighbouring genes. This strongly suggests that type 4a pili are very ancient in origin (Giltner, C.L. et al., 2012; Pelicic, V., 2008). Type 4b pili have 10 to 18 components and they almost always cluster together at a single genetic locus. However, the order of the genes within the locus is not conserved. The clustered genetic organization of type 4b pili has been suggested to be a pathogenicity island that could have hopped from species to species by horizontal gene transfer (Giltner, C.L. et al., 2012; Pelicic, V., 2008). Type 4b pili are a far less homogenous group than type 4a pili. The non-core proteins within this class are far less conserved, compared to type 4a pili. The two classes of pili share a common ancestry, but were separated in ancient times and evolved in parallel ever since. In fact, almost none of the non-core components are shared between the two classes.

There are also functional differences between type 4a and type 4b pili. Type 4a machineries always possess both an assembly and a retraction ATPase. They are the pili responsible for twitching behaviour displayed by some bacteria (see section 1.1.6). Type 4b pili do not always possess a retraction ATPase: in some cases they are are still capable of retraction, like TCP pili of *V. cholerae*, while in other the machinery cannot retract the filaments once assembled. A peculiar ability of some type 4b pili is to form bundles, as it is the case for bundle forming pili (Bfp) pili of *E. coli* (Ramboarina, S. et al., 2005), TCP pili of *V. cholerae* (Kirn, T.J. et al., 2000), and tad pili of *Aggregatibacter actinomycetemcomitans* (Kachlany, S.C. et al., 2000). Bundles, sometime called fibrils, are made of parallel pili adhering to one another and this arrangement create thicker fibers displaying increased tensile properties.

The shorter pilins in type 4b form a monophyletic group and are sometime placed in a family of their own, the tad-like pili (Planet, P.J. et al., 2003). The major pilins of this family are small (50-60 amino acids), predicted to have only the α1 domain and lacking a globular head (Tomich, M. et al., 2007).

Some bacteria express pili as single filaments, like *C. crescentus*, (Skerker, J.M., and Shapiro, L., 2000), others as bundles, like *A. actinomycetemcomitans* (Kachlany, S.C. et al., 2000). Retraction has not been observed for this family of pili because tad pili often possess only one motor ATPase. However, the first case of tad-like pili capable of retraction was recently reported in Cpa pili of *C. cresentus* (Ellison, C.K. et al., 2017). As discussed above (see section 1.1.3), a model have been proposed to explain how a single motor could allow both assembly and retraction of pili. With only about 12 components, the tad genes are all clustered together at a single genetic locus, like the type 4b pili. However, unlike type 4b pili, the position of genes within the cluster is conserved among different bacteria (Tomich, M. et al., 2007). Indeed, order conservation allowed to reconstruct a complex history of multiple horizontal gene transfers across bacterial species (Planet, P.J. et al., 2003). The tad locus has also been found widespread among archaea (Peabody, C.R., 2003) and, interestingly, some tad components and archaellum proteins have important homologies, specifically the motor TadA (CpaF) and the IM platform TadB/C being homologues to FlaI and FlaJ, respectively (Kachlany, S.C. et al., 2001a, 2001b) (see Box 3). To date there are very few structures of tad components and in many cases they have little sequence homology with either type 4a or 4b pili, making it difficult to understand the role and the organization of this type of machinery (see Figure 4).

WHAT ARE TYPE 4 PILI USED FOR?

1.1.5.   SURFACE ATTACHMENT AND BIOFILM

Pili function like "sticky ropes" that establish first contact with a surface. Pili can transition a cell from planktonic to a surface associated state, even against propelling of the rotating flagellum and considerable fluid flow. The main attribute of T4P is in fact the ability to attach and retract, upon which all other T4P related phenotypes can be explained, as it will be shown in the next sections. Some pili are thought to attach on the target only by the tip, but in some organisms, like *P. aeruginosa*, the pilus attach can along the entire length of the filament. Moreover, the highly corrugated surface of the filament makes attachment on both hydrophobic and hydrophilic surfaces possible, by non-specific reversible interactions (Lu, S. et al., 2015). In some pathogens, T4P promote attachment to specific cell tissues of the host (Comolli, J.C. et al., 1999a; Saiman, L., and Prince, A., 1993; Zahavi, E.E. et al., 2011).

Observations in many species show that single cells in planktonic phase can use T4P to quickly attach on a surface. For example, in *C. crescentus* tad-like pili promote quick and fast attachment under flow (Hug, I. et al., 2017; Li, G. et al., 2012). In *N. gonorrhoeae* and *P. aeruginosa*, landing on surfaces is immediately followed by twitching (Holz, C. et al., 2010; Klausen, M. et al., 2003a; Nudleman, E., and Kaiser, D., 2004; Skerker, J.M., and Shapiro, L., 2000). Single bacteria swimming near a surface can exploit a hydrodynamics phenomenon that keeps them swimming parallel to the surface thereby remaining close to it and having time to choose a location (Berke, A.P. et al., 2008). The ability to choose have been studied in details in *V. cholerae*, which uses mannose-sensitive hemagglutinin

(MSHA) type 4a pili to attach to surfaces and organisms like zooplankton (Chiavelli, D.A. et al., 2001). In mono-flagellated crescent-shaped bacteria, flagellar rotation causes the cell body to rotate in the direction opposite of flagellar rotation (Liu, B. et al., 2014). This allows MSHA pili in *V. cholerae* to have continues transient mechanical contacts with the surface, enabling them to scan the surface and attach proportionally to the strength of pili-surface interaction, thereby biasing the organism to find the spot with highest affinity (Utada, A.S. et al., 2014). This is also possible because the attachment that T4P promote is reversible and unspecific, allowing cells to detach (Kachlany, S.C. et al., 2000; Maier, B., and Wong, G.C.L., 2015).

The presence of a filament is not always sufficient to promote T4P mediated attachment. For example, in *V. cholerae* deletion of PilT and inability to perform retraction compromises attachment and biofilm formation, despite the presence of extended pili on the surface of cells (Jones, C.J. et al., 2015). This highlights the importance in some species of having dynamic pili, capable of performing elongation as well as retraction, in order to promote attachment.

While first surface contact can be mediated by T4P, long-term attachment of biofilms relies heavily on EPS (Flemming, H.-C., 2011). EPS are the main components of the biofilm matrix, which strongly attaches the community to a surface, shields it from physico-chemical damages, limits diffusion of harmful agents like antibiotics and phages (Lewis, K., 2007). However, some T4P play an important role in later stages of biofilm development as well. T4P support the optimal development of a biofilm in *P. aeruginosa*, where they are required for the cell migration within a biofilm and rearrangement of cells to form 3D mushroom-like structures (Klausen, M. et al., 2003b). Those structures permit better nutrient diffusion and therefore promote growth of more biomass (Hall-Stoodley, L. et al.,
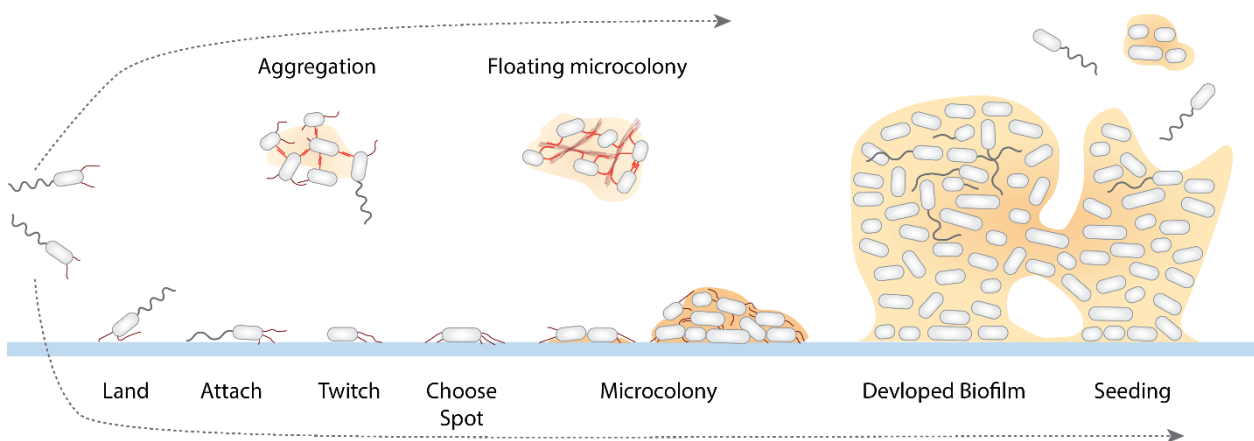
FIGURE 5 – FROM A SINGLE CELL TO A COLONY
The picture depicts the archetypal development of a biofilm from a single cell. A swimmer has a flagellum (in black) and often pili (in red) are displayed in planktonic phase as well. Upon landing in some specie cells employ T4P to explore the surface and find a favourable spot. The cell can then start duplicating and secrete the matrix (orange), which will embed, protect and attach the colony to the surface. A developed biofilm can have a complex structure devoted to the dispersion of cells for founding new colonies, either releasing single cells or via flow shedding. Using pili, cells in planktonic phase can aggregate to form small floating microcolonies in some bacterial species.

2004). Similarly, in the plant pathogen *Xanthomonas citri*, T4P are pivotal in the formation of mushroom-like structures after surface adhesion (Dunger, G. et al., 2014).

Some species of bacteria use T4P to increase biofilm cohesion. For example, *A. actinomycetemcomitans* secretes tad pili that allow to tenaciously attach on the surface of teeth. The enhanced biofilm cohesion in this species is due to the ability of tad pili to bundle together into thick fibrils (see section 1.1.4) (Kachlany, S.C. et al., 2000). In biofilms, *A. actinomycetemcomitans* secretes high levels of tad pili, where they aggregate into a dense network of thick fibrils interlocked with one another by sharing individual pili. This bundle also tightly adheres on the surface (Kachlany, S.C. et al., 2001b). T4P are also important in promoting aggregation of cells in the planktonic phase. Aggregation of cells in liquid and growth in small floating biofilms has an important role in protecting cells from stresses, nutrient deprivation, and predation by unicellular eukaryotes and phages (Teschler, J.K. et al., 2015). Bfp pili encoded in EPEC strains (Enteropathogenic *E. coli*) are necessary to promote autoaggregation (Bieber, D. et al., 1998, 2010). In *N. gonorrhoeae* pili need to be able to retract in order to promote aggregation (Park, H.S.M. et al., 2001). In *V. cholerae* a second type of pili, TCP pili promote aggregation (Kirn, T.J. et al., 2000). TCP pili can also create pilus-to-pilus contacts that establish a network of interactions between bacteria in a microcolony. Lastly, it is also important to mention that in some species, like *P. aeruginosa* and *V. cholerae*, the flagellum as well contributes to surface attachment (Conrad, J.C. et al., 2011; Utada, A.S. et al., 2014).

1.1.6.   TWITCHING – EXPLORING SURFACES

Bacteria can use T4P to move on surfaces, a process called twitching. To date, twitching has been described only for bacteria possessing type 4a pili (Burrows, L.L., 2012), *e.g. M. xanthus* (Sun, H. et al., 2000; Zusman, D.R. et al., 2007), *P. aeruginosa* (Conrad, J.C. et al., 2011), *N. gonorrhoeae* (Merz, A.J. et al., 2000), and *Xanthomonas* species (Dunger, G. et al., 2014). In *V. cholerae*, however, twitching behaviour was not observed despite the presence MSHA pili, which are type 4a pili. Usually during twitching pili are employed at a single pole to promote motion and each pilus undergoes a dynamic cycle involving four steps: elongation, attachment to surface, retraction, and detachment (Burrows, L.L., 2012). Twitching allows single cells to crawl on surfaces at speeds ranging from 0.5 to 1.6 μm/s (Holz, C. et al., 2010; Maier, B., and Wong, G.C.L., 2015; Skerker, J.M., and Berg, H.C., 2001). The location of pili on the cell and coordination of their activity can influence the types of movement the cell experiences (Maier, B., and Wong, G.C.L., 2015). For instance, two types of movements have been described for *P. aeruginosa* (Conrad, J.C. et al., 2011; Jin, F. et al., 2011). One is walking orthogonally to the surface, with low directional persistence (2 μm) although its speed is faster than during twitching (see Figure 6A and 6B). This type of movement allows cells to quickly explore a small area and perhaps to orient and employ the T3SS, an organelle capable to inject macromolecules into eukaryotic cells via a needle structure. The second type of movement is horizontal twitching. This type of motility has a higher directional persistence (6 μm) and cells can cover greater distances. In

horizontal twitching cells can move upstream against the flow despite considerable drag forces (Shen, Y. et al., 2012). This allows cells to colonize environments that may not be accessible to species relaying only on swimming via a flagellum. *M. xanthus* employ pili at a single pole (Zhang, Y. et al., 2012), whereas *P. aeruginosa* can distribute pili at one or at both poles at the same time, regulated by the availability of nutrients (Ni, L. et al., 2016). Pili are distributed asymmetrically in nutrient scarcity, in order to favour surface exploration. On the other hand, expressing pili at both poles arrests cell movement. This makes single cells of *P. aeruginosa* able to search and to select favourable conditions on a surface with high precision, and to adhere tightly on a spot favourable for biofilm formation (Ni, L. et al., 2016).

Asymmetry in pili distribution at the poles allows directional motion in single cells of *P. aeruginosa* and *M. xanthus*. However, *N. gonorrhoeae*, a spherically shaped bacterium with pili positioned randomly around the cell, remains capable of twitching with a high directional persistence. This is possible due to a mechanism named tug-of-war (Marathe, R. et al., 2014). No biochemical coordination control is required, unlike in *M. xanthus* for instance. Pili are coordinated by mechanical forces alone: the dynamic properties of each pilus is influenced by the forces generated by the other pili (see Figure 6C). An important prerequisite is that *N. gonorrhoeae* pili have an unbinding force of 10-20 pN, far lower than the >100 pN a single pilus can generate during retraction (Holz, C. et al., 2010). Stochastic activity of pili at one side of the cell and pulling in same direction can increase the detachment rate of pili on the opposite side of the cell, leading to even stronger pulling forces from the winning side. This in turn lead one side to constantly pull at higher forces and a kind of directional memory determines a leading side for a cell, which allow *N. gonorrhoeae* to twitch with high directional persistence (Holz, C. et al., 2010; Marathe, R. et al., 2014).

Chemotaxis in bacteria has typically been associated with swimming, but recent studies show that it is also used to guide twitching motility (Oliveira, N.M. et al., 2016). The small size of bacteria makes sensing chemical gradients over such short distances theoretically difficult (Rusconi, R., and Stocker, R., 2015). For example, *M. xanthus* is unable to direct its surface motility according to a chemical gradient (Taylor, R.G., and Welch, R.D., 2008). However, in *P. aeruginosa* chemotaxis pathway regulates and guides the twitching of single cells with high precision (Oliveira, N.M. et al., 2016). Using the Chp chemosensory system, single cells are able to rapidly revert the direction of twitching movements upon changes in a chemical gradient and are capable of seeking favourable conditions with sub-micrometer precision.
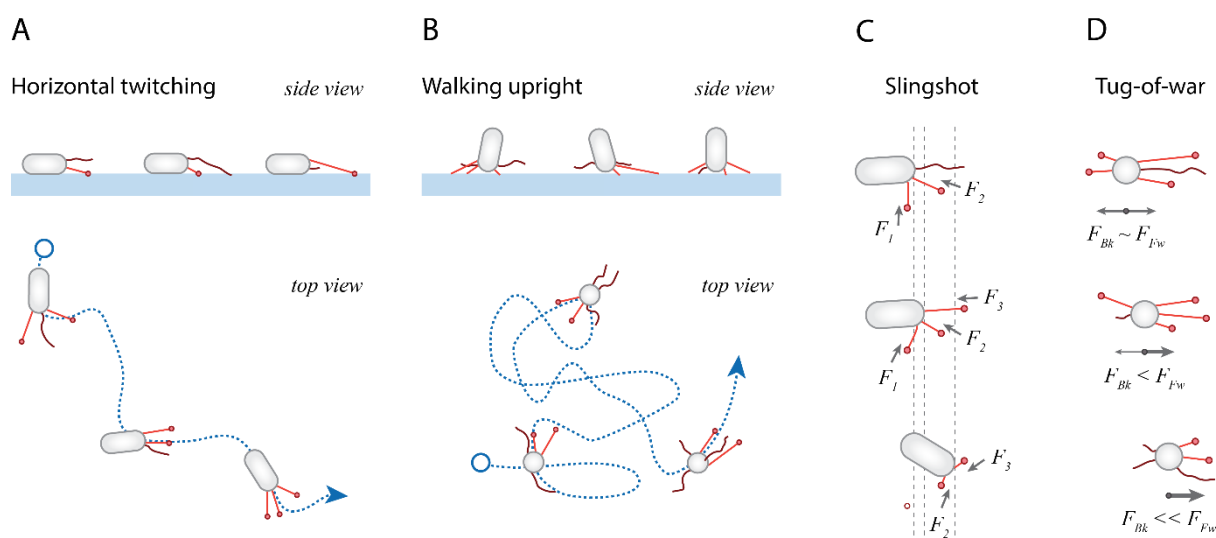
A Horizontal twitching *side view*

B Walking upright *side view*

C Slingshot

D Tug-of-war

top view

top view

F_2

F_1

F_3

F_2

F_1

F_3

F_2

$F_{Bk} \sim F_{Fw}$

$F_{Bk} < F_{Fw}$

$F_{Bk} << F_{Fw}$

FIGURE 6 – T4P-BASED MOTILITY TYPES

(A) The picture schematically represents horizontal twitching, used for example by *P. aeruginosa* and *M. xanthus*. This allows for a high directional persistence, and therefore is more efficient to cover long distances and efficiently follow a gradient. **(B)** However, *P. aeruginosa* is also able to walk upright, with low directional persistence, the arrangement of pili is such to drive the cell in a random walk allowing for a quick exploration of the local area. Panel **C** and **D** depict the mechanism for slingshot and the tug-of-war, drawn based on the studies from F. Jin et al., (2011) and C. Holz et al., (2010), respectively.

A detailed study in *P. aeruginosa* revealed that during horizontal twitching cells experience two motility regimes: a slow twitch and a peculiar slingshot motion (Jin, F. et al., 2011). Most of the time cells twitch slowly (<0.3 µm/s) and with high directional persistence. Occasionally a single pilus at the leading pole can pull in a direction contrary to the motion of the leading pole (see Figure 6D). As pili pull in different direction they accumulate tension. Upon release of the opposing pilus, the accumulated tension "slingshots" the cell forward at high speed (0.5 to 5 µm/s.). Interestingly, despite slingshot event being very short, slow twitching and slingshots contribute equally to the distance covered by single cell trajectories. This rapid movement mechanism of slingshot has been proposed to promote (1) random and rapid reorientation of the cell direction and (2) to locally reduce the viscous drag of the media, thereby allowing easier movement within viscous material, like biofilm matrix or the mucus of a host (Jin, F. et al., 2011).

In *M. xanthus* pili are used to power a collective motility, rather than single cells. This peculiar motility is called S motility ("S" for social), which occur when cells in a tightly packed colony are starving or have found new source of nutrients (Zhang, Y. et al., 2012; Zusman, D.R. et al., 2007). This behaviour has been subject of considerable scrutiny due to its relevance in understanding cooperative behaviour in strictly unicellular organisms. Tightly packed cells are interlocked with one another and use T4P to coordinate meovements and to aggregate into 3D mound, which will then develop into the fruiting body that will disperse Myxospores in the surrounding environment (Zhang, Y. et al., 2012). Moreover, the secretion of EPS in *M. xanthus* biofilms is required to strongly stimulate piliation as well as retraction, via yet an unclear mechanism (Li, Y. et al., 2003).

While T4P play an important role in surface motility of single cells, it is worth mentioning that bacteria have evolved different ways to power motility on surfaces. For example, *M. xanthus* is also capable of single cell motility, called adventurous (A) motility, which use a "gliding" motility for powering the individual cell movement (Shi, W., and Zusman, D.R., 1993; Sun, H. et al., 2000). The gliding motility involves first the creation of focal adhesions that anchor a cell to EPS-covered surfaces. Motors can then power motion of the focal adhesions along protein-based tracks within the cell. However, since the adhesins are anchored to the surface the result is that the motors slowly push the cell body forwardly relative to the focal adhesions (Islam, S.T., and Mignot, T., 2015). Gliding motility is present in different bacterial phyla and, interestingly, different gliding mechanism appear to have evolved in different bacteria (Jarrell, K.F., and McBride, M.J., 2008; McBride, M.J., 2001).

1.1.7. MECHANOSENSING VIA PILI

Upon landing on a surface, cells must be able to sense its presence and efficiently attach to it if conditions are favorable. Once a single cell is on a surface and the right conditions for growth are met, cells switch to a sessile lifestyle in order to consolidate their new niche and survive in the new environment (Lewis, K., 2007). The flagellum or T4P are possible sensors of surface contact and there are examples supporting both models (Belas, R., 2014). There is a long history of studies pointing to flagella acting as sensor by reading stresses in the flagellum machinery, like in *V. cholerae* and *C. crescentus* (Hug, I. et al., 2017; McCarter, L. et al., 1988). T4P as well can act as sensors in some organisms, although the mechanism is still unclear. One model proposes that pili could perceive surface via conformational changes occurring in the filament itself when subjected to tension (see section 1.1.1) (Touhami, A. et al., 2006). Those conformational changes could be read from the proximal end of the pilus by some component in the machinery, which then initiates a signal cascade (O'Toole, G.A. et al., 2016). A possible candidate in *P. aeruginosa* is a repurposed chemoreceptor-like protein called PilJ. A component of the Pil-Chp system, PilJ is an IM protein shown to interact with the pili machinery. It is unclear if PilJ can directly interact with the filament at all, since cryo-EM study of *M. xanthus* shows that the pilus filament is completely surrounded by other components of the machinery (Chang, Y.W.Y.-W. et al., 2016). PilN/O may act as intermediary that directly interact with the filament and conveys its state to PilJ (McCallum, M. et al., 2016). Nevertheless, PilJ initiates a signal cascade when the filament of pili is subjected to tension during retraction that leads to changes in gene expression (Persat, A. et al., 2015) (see Figure 7). PilJ induces production of cAMP (cyclic AMP) through enzyme CyaB. Higher levels of cAMP in turn activate Vfr, a master transcription factor of virulence that regulates more than 100 genes. (Luo, Y. et al., 2015). Among those genes are the ones of minor pilins and PilY1. The latter, upon interaction with the T4P, is capable to increase production of c-di-GMP (cyclic diguanylate) in a surface dependent manner and down regulate cAMP production by suppressing PilJ signaling (Luo, Y. et al., 2015). Both cAMP and c-di-GMP are used to signal surface contact, making the process partially redundant. The authors

argued that the response of each signal molecule is related to the time spent on a surface, and therefore coordinates two different behaviours. cAMP regulates a rapid response to surface attachment that favours single cell adaptation to the surface, for example, increasing piliation and twitching as well as retaining the flagellum, phenotypes related to surface exploration. High concentrations of c-di-GMP build up over time and activate genes responsible for growth in a biofilm, such as for EPS secretion, changes in metabolism and loss of the flagellum.

In the case of *C. crescentus*, there are studies supporting both flagellum and T4P as possible surface sensors (Ellison, C.K. et al., 2017; Hug, I. et al., 2017). *C. crescentus* has a cell cycle divided in two phases: (1) a swarmer phase, a newborn cell expressing a single flagellum and pili at the new pole, and (2) a sessile phase, when cells can be permanently attached to surfaces via secretion of a strong glue-like substance, called holdfast. In *C. crescentus* swarmer cells are not capable of reproduction. Swarmer cells, upon finding a favourable location on a surface, can readily attach by secreting the holdfast and switch to a sessile life style. Despite expressing only about 2-3 tad-like pili per cell, they play a pivotal role in promoting surface contact and aid in the efficient secretion of the holdfast (Hug, I. et al., 2017). A recent study showed that blocking the retraction of pili elicited the secretion of holdfast material and initiated the switch to the sessile lifestyle (Ellison, C.K. et al., 2017). In another study, it was found that pili are not the sensors in *C. crescentus*, nor was the flagellar filament, but rather the flagellar motor. The study suggests that upon landing, surface-induced obstruction of the motor activity initiates a signal cascade that results in a fast rise in the levels of c-di-GMP (Hug, I. et al., 2017). This then initiates holdfast secretion and the transition to sessile lifestyle. It was proposed that the flagellar motor acts like a mechanosensitive channel, capable of changing the flow of ions according to the deformation experienced by the surrounding membrane. The role of pili in this model would then be to orient and pull the flagellar motor nearer to the surface. Retraction could contribute to deform the membrane at the flagellated pole, thereby initiating a response (Hug, I. et al., 2017).

1.1.8. REGULATION OF PILI ACTIVITY

In this section, we will primarily explore how type 4 pili control elongation and retraction in order to coordinate pili activities. Like in mechanosensation, c-di-GMP plays an important role in regulating the dynamic activity of pili. To date, this is still a topic of active investigations and only for few organisms we have a comprehensive understanding of the regulation of pili.

c-di-GMP in *V. cholerae* controls several aspects of motility and the switch to a sessile lifestyle (Conner, J.G. et al., 2017). High concentration of c-di-GMP inhibits swimming motility and induces production of VPS (Vibrio polysaccharide) (Srivastava, D. et al., 2013). Four DGCs (diguanylate cyclase) and two PDEs (phosphodiesterase) were found to directly affect motility of *V. cholerae* and strains lacking CdgJ, a PDE, have limited motility, increased secretion of VPS and biofilm formation (Liu, X. et al., 2010). In *V. cholerae* c-di-GMP can also alter the activity of MSHA pili and in a recent
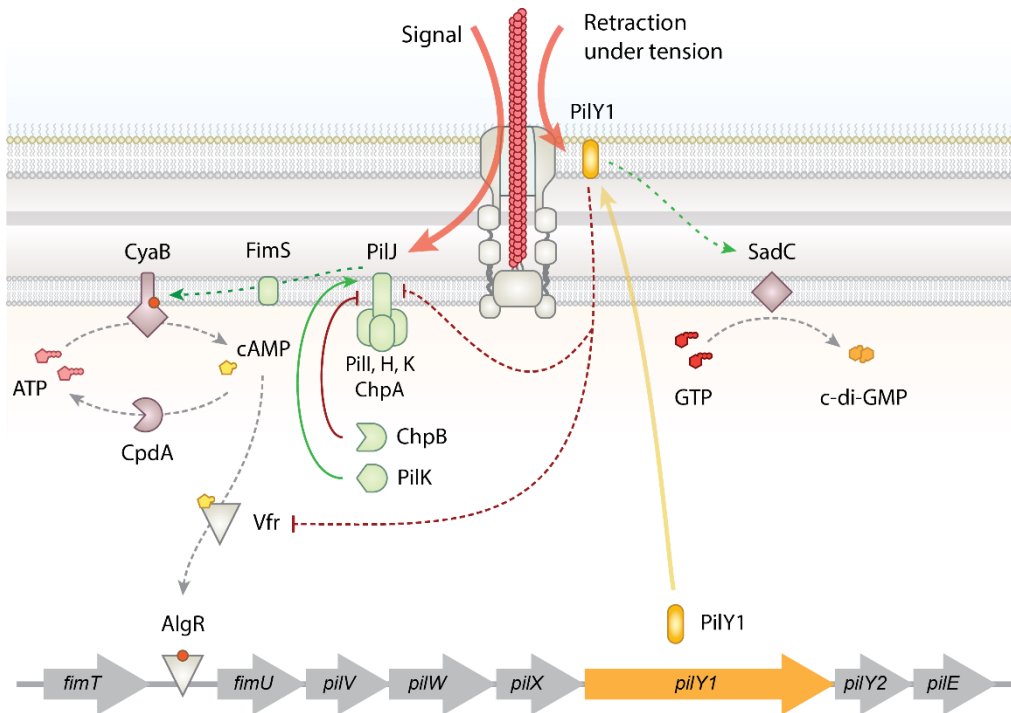
The components involved in mechanosensing in *P. aeruginosa* control the production of two signal molecules. The chemotaxis-like receptor PilJ can read tensional state of the pili filament and initiates a signal cascade. Via FimS, PilJ promotes the phosphorylation of CyaB, which synthesises cAMP. The transcriptional regulator Vfr can bind cAMP and in turn phosphorylates AlgR. The latter will start the expression of PilY1, amongst the expression of other genes. PilY1 may be located to the OM and upon further retraction of pili repress the signalling from PilJ and Vfr. Without the action of CyaB, CpdA will decrease the levels of cAMP. PilJ is also able to activate SadC, which in turn synthetizes c-di-GMP. As levels of c-di-GMP increase, the cell will transition to a sessile lifestyle. It is yet unclear how the PilJ and PilY1 are able to read the tensional state of the pilus filament. Moreover, it is unclear how PilY1 interact with components in the IM or if there are intermediary proteins involved. [The pathway depicted is based on the work of Y. Luo et al., (2015)].

study, the altered phenotypes of $\Delta cdgJ$ could be restored by suppression mutations in *mshA*, *mshE* and *pilT*, respectively the major pilin, the assembly and the retraction ATPases of MSHA pili (Jones, C.J. et al., 2015). MSHA pili allow cells swimming near a surface to transiently interact with surfaces and without them cells cannot attach on abiotic surfaces (Utada, A.S. et al., 2014). On the other hand, $\Delta cdgJ$ strains have higher levels of c-di-GMP inside cells, which lead cells to a strong and rapid attachment to surfaces, with almost all cells attached within 3 minutes of surface exposure, a rate faster than for wild type. It was concluded that increased levels of c-di-GMP induce elongation of pili due to the assembly ATPase MshE directly binding c-di-GMP (with affinity of ≈0.1 μM). It was demonstrated that c-di-GMP binding to MshE promotes polymerization of pili in a c-di-GMP dose-dependent manner, without affecting the levels of MshA proteins in the cell (Jones, C.J. et al., 2015).

P. aeruginosa presents another example where pili are regulated directly by c-di-GMP via a protein called FimX. FimX is a protein possessing both a GGDEF domain, an EAL domain and a REC domain. The first domain is defective in DGC activity, while the second can bind c-di-GMP with high affinity (≈90 nM), but possess only a residual PDE activity (Kazmierczak, B.I. et al., 2006). The

REC domain is necessary for correct localization. Deletion of either GGDEF or EAL domains, or compromising binding of c-di-GMP, results in lower levels of twitching motility. The localization of FimX within cells determines motility: during twitching FimX localizes at a single pole, while immobile cells have it at both poles (Jain, R. et al., 2017). Localization of FimX is dependent on the expression of the assembly ATPase: deletion of PilB results in FimX being mostly dispersed in the cytosol, while Δ*pilT* strains have a bipolar distribution of FimX. In order to determine the direction of motion in *P. aeruginosa*, the current studies suggest that c-di-GMP-bound FimX localizes at the leading pole and promotes PilB-dependent assembly of pili (Jain, R. et al., 2017; Kazmierczak, B.I. et al., 2006). Although a Δ*fimX* Δ*pilT* strain can still secrete pili, this is achieved at a 3-4 times slower rate. Therefore, FimX promotes pili assembly via PilB by either increasing the rate of activity of PilB or binding time/affinity of PilB to the assembly machinery (Jain, R. et al., 2017). Assembly machineries are likely present at both poles of cells. FimX does not inhibit PilT activity, which is present and active at both poles, but by limiting assembly activity at one pole it determines the leading pole, and in turn ensures directional motion (Jain, R. et al., 2017). Spatial separation of PilB and PilT is not necessary, though it cannot be excluded. Indeed, in *M. xanthus* the spatial separation of the motors is the mechanism by which cells govern the direction of movement (Mercier, R., and Mignot, T., 2016).

M. xanthus possess a chemotaxis-like Frz system, which coordinates the periodical reversal of movement direction every 7-8 min and plays a central role in coordinating pili action at the two poles. The Frz signaling also possess other functions, which have been covered in several reviews on the subject (Mercier, R., and Mignot, T., 2016; Zhang, Y. et al., 2012; Zusman, D.R. et al., 2007). In *M. xanthus* PilQ, PilC and PilM are bipolarly localized, indicating that the machinery is assembled and ready at each pole. However, the distribution of PilB and PilT is spatially separated (Bulyha, I. et al., 2009). The model suggested is that Frz system recruits PilB proteins to the leading pole where they monopolize the assembly machinery. PilT instead concentrates at the lagging pole where free binding to the assembly machinery is available, although PilT remains free to move in the cell and can occasionally interact with the pili machinery at the leading pole, initiating a retraction event. Upon signal for reversal, the Frz system reset the PilB asymmetry. PilB progressively leaves the leading pole and move the lagging pole, while PilT in turn quickly accumulates to the leading pole (Bulyha, I. et al., 2009). There are still several gaps in this model, like what guides and triggers localization, and the organization and interaction between the different components remain elusive.

In *Xanthomonas campestris*, FimX interacts with PilB indirectly, via an intermediary protein called PilZ. PilZ homologue domains were among the first proteins found capable to bind c-di-GMP. PilZ orthologues are linked in the control of pili activity, and deletions lead to decreased motility in different bacteria (Carbonnelle, E. et al., 2004; Pratt, J.T. et al., 2007). However, not all PilZ homologue domains are capable to bind c-di-GMP, and in fact the original PilZ protein in *P. aeruginosa* is among those (Alm, R.A. et al., 1996). Another example is PilZ$_{XAC}$ in *X. campestris* (Guzzo, C.R. et al., 2009). PilZ$_{XAC}$ is capable to interact with the EAL domain of FimX, without compromising the ability of

FimX to bind c-di-GMP. Moreover, PilZ$_{XAC}$ directly interacts with PilB via its C- terminal domain. PilZ$_{XAC}$ is the intermediary protein of a ternary complex formed by FimX-PilZ-PilB that promote pili assembly (Guzzo, C.R. et al., 2009). FimX binding of c-di-GMP could indirectly regulate PilB via PilZ, and promote pili elongation by either control the ATPase activity or by influencing the probability of interaction of PilB with the assembly machinery.

1.1.9. FORCES GENERATED BY T4P

As an example of a complex biological nanomachinery, T4P attracts the curiosity and research efforts of biophysicists because of its dynamic nature and its capability to generate forces in the range of a few tens of pN. In *N. gonorrhoeae*, using optical tweezers, measurements of single pili retraction events recorded forces of 80 to 100 pN, with retraction speeds of about 1 μm/s (Maier, B. et al., 2002, 2004; Merz, A.J. et al., 2000). Considering a 10 Å step for every subunit added or removed from the filament (Craig, L. et al., 2006; Kolappan, S. et al., 2016), this amounts to around 1000 subunits per second, a considerable speed that highlight the processive working mechanism of motor ATPases during assembly and disassembly (Maier, B., and Wong, G.C.L., 2015). In fact, a study of *N. gonorrhoeae* shows that once started the retraction of T4P is irreversible, meaning it will stop only if the filament is fully retracted or it breaks (Maier, B. et al., 2004). Only in a strain expressing low amounts of PilT it was possible to interrupt retraction and force-induced elongation when applying forces >50 pN, possibly by disrupting the interaction of PilT with the machinery and allowing the recruitment of PilB (Maier, B. et al., 2004).

T4P of *P. aeruginosa* generate lower forces during retraction compared to *N. gonorrhoeae*. Retraction of fluorescently labelled pili generated a force of 10 pN, and speeds of 0.5 μm/s (Skerker, J.M., and Berg, H.C., 2001). Using direct measurements via optical tweezers, a recent study found a maximum stall force generated during retraction of about 30 pN and retraction speeds of about 1 μm/s (Ribbe, J. et al., 2017). By binding cells on AFM tips, it was possible to determine the maximal tensile force before rupture in pili of *P. aeruginosa*. The rupture force was about 95 pN, 3 times the maximal force their motors can generate (Touhami, A. et al., 2006).

Pili of *C. crescentus* can generate forces during pili retraction of around 15 pN (Ellison, C.K. et al., 2017). As mentioned before, pili mediate only a temporary attachment. However, cells quickly deploy holdfast to permanently attach on surfaces (Li, G. et al., 2012), and the detachment forces necessary to remove a single cell attached via the holdfast are around 0.6 μN, 2-3 orders of magnitude higher than the forces that pili can generate (Tsang, P.H. et al., 2006).

1.1.10. VIRULENCE

We saw above that pili can activate the expression virulence factors (Luo, Y. et al., 2015; Persat, A. et al., 2015; Shen, Y. et al., 2012), but pili can have a more direct role during infections. A study on *P.*

aeruginosa lung infections in mouse models highlighted the importance of pili and their dynamic retraction for adherence during infection (Comolli, J.C. et al., 1999b). The study also demonstrated that cytotoxicity required both the assembly as well as the retraction motor. It could be that walking motility by pili (Conrad, J.C. et al., 2011) is necessary to bring cells close to the surface and facilitate the use of the T3SS, whose needle length is around 200 nm. Alternatively, the ability to use pili could aid cells in moving through the mucus layer in animal hosts and reach the underlying cells.

As mentioned above (see section 1.1.5), pili play a role in biofilm cohesion, which in turn increases virulence. A *V. cholerae* strain deficient in TCP pili is unable to colonize the human intestine. The role of TCP pili in initial surface attachment is not clear, since *V. cholerae* also express two other T4P and a flagellum that promote attachment (Utada, A.S. et al., 2014). However, TCP pili are crucial for biofilm development. They form pilus-to-pilus contacts within a microcolony, increasing its cohesion, thus increasing resistance to host defences and antibiotics (Faruque, S.M. et al., 2006; Kirn, T.J. et al., 2000). Pilus-to-pilus contacts have been studied in details in *N. gonorrhoeae* (Hélaine, S. et al., 2007). The minor pilin PilX is expressed and integrated at low level into the pilus filament. When two pili are put in an antiparallel orientation, a special conformation in the D region of PilX of one filament can perform an intermolecular interaction with a PilX on another filament, blocking retraction. PilX does not influence attachment on surfaces, however it is necessary for microcolonies aggregation and cohesion, which promote virulence in a host (Hélaine, S. et al., 2005). Moreover, as above mentioned (see section 1.1.1), *N. gonorrhoeae* has a high recombination level of the globular head of the major pili (Criss, A.K. et al., 2005), allowing a route to escape the adaptive immune response and making development of vaccine harder.

E. coli displays many appendages and has a high variety of chaperone-usher pili, which play an important role in pathogens like uropathogenic *E. coli* (UPEC) (see section 1.2.1). However, in *enteropathogenic E. coli* (EPEC) Bfp plays a dominant role in attachment to the brush border of intestinal epithelial cells (Cleary, J. et al., 2004). Bfp promotes direct attachment to intestinal epithelial cells, ensuring colonization of the appropriate tissue where the bacteria can prosper (Tobe, T., and Sasakawa, C., 2002). As shown above, having dynamic pili capable of retraction increases virulence of a pathogen (see section 1.1.5). Mutations in the retraction motor BfpF resulted in EPEC strains capable to elongate pili and attachment onto epithelial cells, but the strains were avirulent, (Bieber, D. et al., 1998). In another study, having retractable Bfp contributed to disrupt tight junctions in the host tissue, which in turn allow tissue penetration (Zahavi, E.E. et al., 2011). As shown above for *P. aeruginosa*, retraction has also been suggested to close the gap between bacteria and host tissue and aid efficient use of T3SS.

V. cholerae has two types of pili and uses them for different purposes. MSHA pili are used for attachment on phytoplankton and zooplankton and do not appear to be relevant during infections (Attridge, S.R. et al., 1996; Chiavelli, D.A. et al., 2001). *V. cholerae* uses TCP pili to promote aggregation and biofilm formation during infections (Kirn, T.J. et al., 2000), as well as aggregation in

aquatic environments to protect bacteria against predation and stresses (Teschler, J.K. et al., 2015). During infection, aggregation could help to overcome the defences posed by the stomach and allow cells to reach the intestine alive (Faruque, S.M. et al., 2006). In fact, simple filtrations of contaminated water that remove aggregates above 20 μm in size can reduce *V. cholerae* infections of about 50% (Colwell, R.R. et al., 2003). On the other hand, a recent study showed that cells in *V. cholerae* biofilm are in a particular hyperinfectious state (Tamayo, R. et al., 2010). Dispersed-biofilm cells were as efficient in colonizing the intestinal tract as intact biofilms in mouse infection models, suggesting some phenotypical changes in the biofilm-associated cells that made them capable to overcome the stomach defences as single cells.

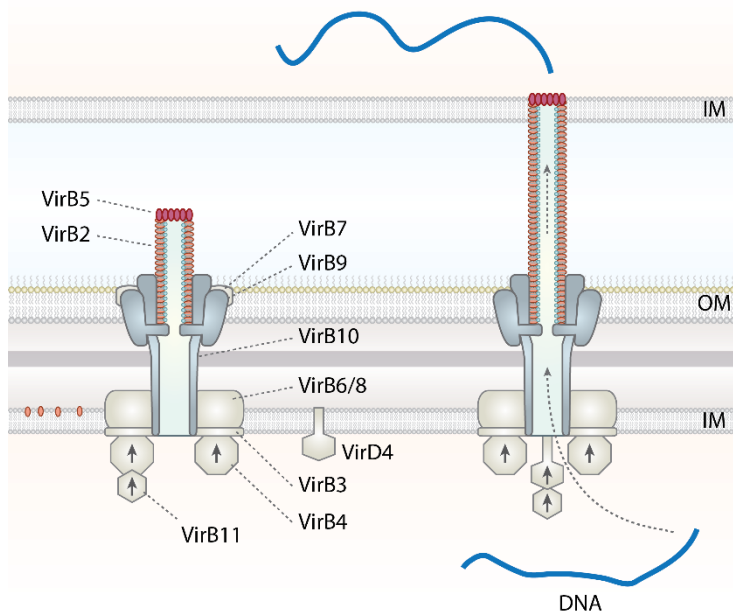It is also worth mentioning that T4P are the binding site and entry point for bacterial phages. Indeed, phages of diverse species have been shown to directly bind to pili. Moreover, the retraction of pili is sometime necessary for infection of phages, possibly bringing a bound phage closer to the cell envelope for the injection of foreign genetic material (Dunger, G. et al., 2014; Guerrero-Ferreira, R.C. et al., 2011).

BOX 2 – TYPE 4 SECRETION SYSTEM (T4SS)

The T4SS is a very versatile system found in both Gram-negative and Gram-positive bacteria, which can assemble a hollow needle filament. T4SS can be classified according to what is secreted (Fronzes, R. et al., 2009). The first and most curious one is the ability to deliver single stranded DNA directly into the cytoplasm of a target cell. DNA exchange between bacteria (even different species) is a process called conjugation (Trieu-Cuot, P. et al., 1985). This is a major asset for bacteria, since DNA exchange grants greater adaptability to environmental conditions. This type of DNA exchange is considered a major cause for the fast rise in antibiotic resistance in pathogenic bacteria. Interestingly, DNA can also be delivered to plants, yeast and mammalian cells (Bundock, P. et al., 1995; Heinemann, J.A., and Sprague, G.F., 1989). This unidirectional horizontal gene transfer, from bacteria to eukaryotes, could potentially have yet unknown repercussion in the evolution of higher eukaryotes (Soucy, S.M. et al., 2015). Second type of secretion is still DNA, but it is secreted in the extracellular environment. This is used, for example, by *N. gonorrhoeae,* where genetic material secreted by T4SS can then be recovered by other bacteria via T4P and the Com uptake system (Hamilton, H.L., and Dillard, J.P., 2006). Third secretion substrate of T4SS are proteins and toxins that *H. pylori* and *L. pneumophila* use to deliver toxins into eukaryotic cells during infections (Backert, S., and Meyer, T.F., 2006).

The F pilus is one of the best-described types of T4SS delivering DNA between bacteria. The 12 proteins that makes the conjugative pilus are encoded by the F plasmid. The structure of T4SS has mostly been resolved and has substantial differences from T4SS (Low, H.H. et al., 2014). The nanomachinery can be divided in an OM pore complex (made of VirB9/10), an IM complexes (made of VirB3/6/8), and motor ATPases (VirB4/11 and VirD4), creating hexameric barrel-like structures in the cytoplasmic side of the IM. OM and IM complex are linked by a thin stalk and a hollow cavity run through the entire length of the machinery, about 30 Å in width, mostly created by VirB10, witch span both membranes. At the OM there is at least a gate to controlling the opening of the pore.

Most of the fundamental mechanisms that lead to the formation of the needle and secretion of substrates are still unclear. Only VirB11 and VirB4 are necessary for assembling the needle filament. Upon elongation the needle can be 2-20 µm long and about 80 Å wide, with a lumen of around 30 Å. The base of the filament is not near the IM, but embedded in the OM complex. A striking feature of the needle is that it is composed in equal parts by VirB2 subunits (also called TraA) and phospholids, with the latter having their polar head lining the filament lumen (Costa, T.R.D. et al., 2015, 2016). The presence of phospholipids could create a hydrophilic environment and facilitate transport of DNA. VirD4, also referred to as a coupling protein, is necessary to recruit the substrate for secretion. How VirB4, Virb11 and VirD4 are assembled and cooperate is not yet fully understood (Chandran Darbari, V., and Waksman, G., 2015).

Schematic inspired by M.K. Hospenthal et al. (2017a)

1.1.11. DNA EXCHANGE

Bacteria possess dedicated organelles called T4SS (see Box 2), which are capable of conjugation, DNA exchange between the cytosol of two cells. However, bacteria evolved another method to scavenge and uptake DNA from the extracellular environment, often derived from lysed cells (Chen, I., and Dubnau, D., 2004). Pili in *P. aeruginosa* can bind DNA in a sequence-independent manner (Schaik, E.J. Van et al., 2005). However, *N. gonorrhoeae* pili are capable to bind DNA in a sequence dependent manner, which makes cells statistically more likely to uptake species specific DNA sequences (Cehovin, A. et al., 2013). This can increase the chance of selective horizontal gene transfer, since transformation efficiency is increased if the source DNA is from the same species. This could represent a novel way for bacteria to transfer drug resistance, by simply scavenging DNA material in the surrounding environment.

In *V. cholerae* DNA uptake proceeds in two distinct steps. First, DNA binds to the pilus filament which brings part of the DNA into the periplasm. A second pilus-independent step uses a dedicated set of proteins (called Com) for powering the uptake of the DNA into the cytoplasm and is necessary for efficient transformation (Seitz, P., and Blokesch, M., 2013). T4P mutants were still able to perform transformations, albeit at 3-4 orders of magnitude lower frequencies. The mechanism powering DNA translocation was shown in *N. gonorrhoeae*. ComE proteins bind free DNA as it become available in the periplasm and using a ratchet mechanism they bias the diffusion direction of the filament in favour of the periplasm (Hepp, C., and Maier, B., 2016). This mechanism does not depend on ATP, which is not available in the periplasm, and is not powered by retraction of the T4P

1.1.12. PREDATION

Prokaryotes are often preyed on by unicellular eukaryotes. But there exist bacteria that prey upon other bacteria as well. *Bdellovibrio bacteriovorus* is such an example. It is a small, highly motile bacterium swimming at an astonishing speed of 160 μm/s and it is able to outrun and feed on other bacteria such as *E .coli*. *B. bacteriovorus* is found ubiquitously in soil and fresh water environments. Upon contact with another bacterium, *B. bacteriovorus* embeds itself inside the host and grows as a parasite by consuming the host macromolecules. *B. bacteriovorus* duplicates until it consumes all resource in the host and then burst out releasing the next generation of cells into the environment (Negus, D. et al., 2017). Interestingly, T4P are necessary for successful predation, possibly by anchoring to the prey and/or providing the force to penetrate the host membrane (Evans, K.J. et al., 2007).

Another use of pili in the context of predation and scavenging is observed for *M. xanthus*. With 8% of the genome dedicate to the production of antibiotics, twice the number of Streptomyces spp., this bacteria is quite effective in killing competing bacteria through chemical warfare. The striking feature of social motility described above (see section1.1.6) can be used to create a rippling effect. Powered by pili and connected to one another by EPS and yet unknown adhesin, group of cells

undergo coordinated rhythmic changes in the direction of movement. This creates the rippling effect, appearing as travelling waves of cells moving back and forth in coordinated fashion (Berleman, J.E. et al., 2006). It is used when cells come in contact with preys or when encountering large source of nutrients released by lysed cells. This behaviour is thought to allow a thorough mechanical scraping of a surface, so that the colony exploit any resource available. Moreover, the social motility is used by *M. xanthus* to follow gradients of molecules using a complex chemotaxis system (Shi, W. et al., 1993).

1.1.13. NANOWIRES

Another interesting function of T4P is the ability of *Geobacter sulfurreducens* to exchange electrons between cells and the environment. *G. sulfurreducens* produces a network of T4P in the presence of Fe(III), that connects cells within a biofilm (Reguera, G. et al., 2005). These pili act as microbial nanowires, and *G. sulfurreducens* biofilm build a complex network of nanowires connecting cells. The network promote long range electron transport (up to a few cm) between microorganisms and ferric iron (Fe(III)), which *G. sulfurreducens* use as ultimate acceptor of electrons. Rather than using extracellular cytochromes as electron shuttles, pili themselves have a metallic-like conductivity, contrary to the fact that protein are electrical insulators (Malvankar, N.S. et al., 2011; Malvankar, N.S., and Lovley, D.R., 2012). However, a recent structural study highlighted the possible arrangement of aromatic amino acids into a continuous chain on the pili filament surface. The aromatic rings are close enough to one another to potentially have overlapping orbitals, which would allow metallic-like conductivity (Xiao, K. et al., 2016). The physiological relevance is still being investigated, but this phenomenon has interesting potential applications in the field of biotechnology, such as biofuel cells.

1.2. Single-membrane-spanning pili

The chaperone-usher (CU) pili, Type 5 pili (T5P) and curli are additional types of pili expressed in Gram-negative bacteria. CU pili are especially widespread and have been studied in details. The function of those pili is adhesion, mostly targeting specific protein expressed at the surface of eukaryotes cells (Hospenthal, M.K. et al., 2017a). The most striking difference compared to T4P are: (1) single-membrane-spanning pili are anchored to the OM and (2) they cannot be retracted. The CU pili have been shown to be crucially important for some pathogens.

1.2.1. CHAPERONE-USHER PILI.

Two well studies CU pili machineries are called type 1 pili (Fim) and P pili (PaP) (see Figure 8A). Both are found in uropathogenic *E. coli* (UPEC). We will introduce the structure and assembly of Fim pili as example of an archetypal CU pili. There are three key differences that distinguish Fim pili from T4P: (1) elongation of the filament is top-to-bottom, (2) since assembly occurs at the OM, no ATP is available to power the process and (3) CU pili are non-retractable. The filament is divided in two parts: a thin tip fibrillum on top of a helical rod fiber (Choudhury, D. et al., 1999). The tip fibrillium is a short section, up to 20 subunits, arranged with a bead-on-a-string architecture. At the very tip is present a receptor-binding adhesin (FimH or PapG). This special subunit can bind specific molecular targets present in eukaryotic cells. The rod comprises the main part of the filament and, unlike the tip fibrillum, is made of a single type of subunit, FimA, arranged in a helical manner. The rod is a right-handed helix with 3.1 subunits per turn, 8 Å axial rise per subunit, 6-8 Å wide and can be 1-2 μm long (Busch, A. et al., 2015, Hospenthal, M.K. et al., 2017b). Those dimensions are comparable to T4P, which could explain the historical confusion in the identification and classification of pili.

The first step of assembly involves SecYEG-mediated transport of subunit precursors into the periplasm (see Figure 8B). Since the filament is assembled top-to-bottom, the first subunit is always the tip adhesion FimH. In the periplasm a chaperone, FimC, binds and stabilizes any subunit by protecting their hydrophobic groove. The chaperone-adhesin complex can then shuttle to an OM pore called usher. The complex first interacts with the NTD of the usher and then is transferred to the CTD, thus placing the adhesin half through the channel. The now free NTD of the usher recruit the next chaperone-subunit complex and is oriented so that the N-terminal extension (Nte) of the last subunits can extend and interacts with the hydrophobic groove of the previous subunit. The polymerization process is called donor-strand exchange: the chaperone progressively uncovers the hydrophobic groove as it gets associated with the Nte (Phan, G. et al., 2011). The CTD chaperone is no longer needed and is released from the adhesion subunit which can conclude folding. The complex sitting at NTD of the usher is moved to the now free CTD site, pushing the adhesion subunits through the channel in the process. All subunits are added in an ordered sequence, following this mechanism. Some systems, like P pili, have a special terminator subunit, whose lack of a hydrophobic grove stop polymerization. Other systems lack a terminator subunits and the
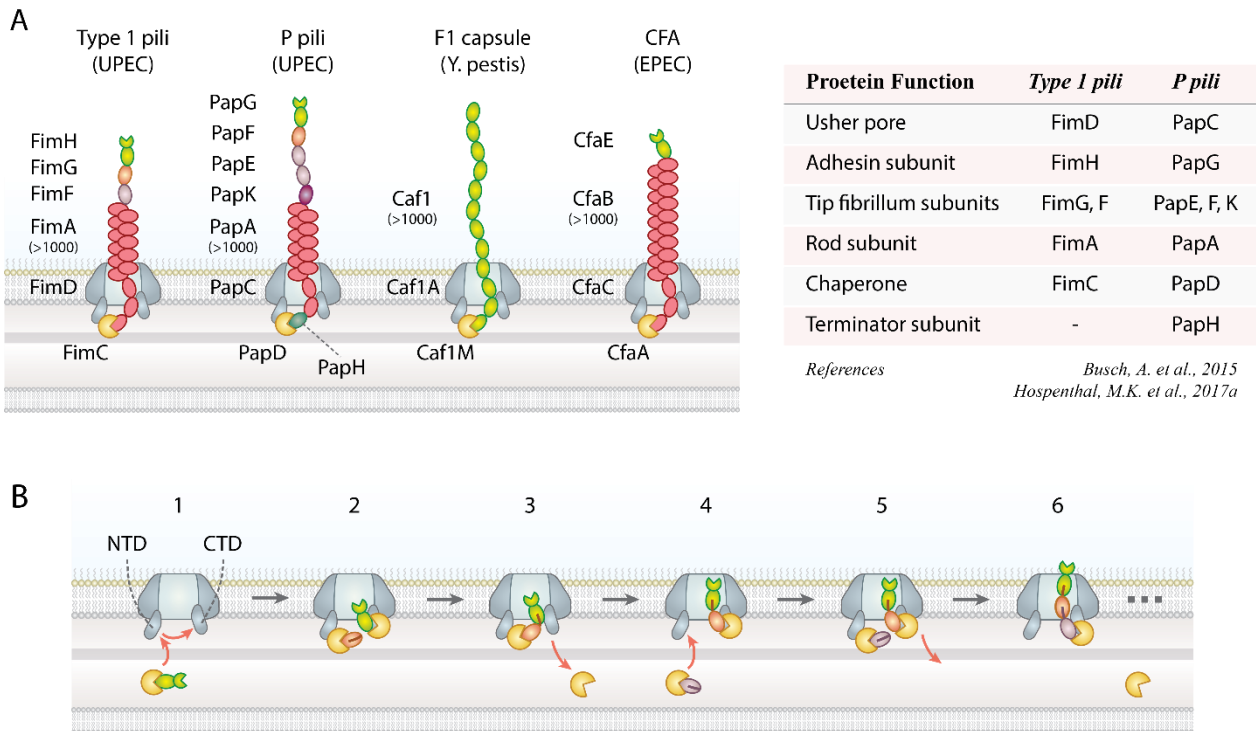
FIGURE 8 – CHAPERONE-USHER PILI: DIFFERENCES IN FORM AND ASSEMBLY

(A) CU pili from different organisms are represented. The rod has a length of 1-2 μm on average. Some types of CU pili have a longer tip fibrillum than others, while in some the tip fibrilum is only the adhesion subunit itself. The F1 capsule in *Y. pestis* is basically a very long fibrillum where each subunit is also an adhesion site.

(B) During the assembly process, a chaperone binds a subunit, shielding the hydrophobic groove in the process. The first chaperone-subunit complex interacts with the CTD of the usher pore (**1**). The NTD is available for a second chaperone-subunit complex. Then two chaperones complexes are positioned in such a way that the Nte (N-terminal extension) of the NTD bound subunits can extend into the hydrophobic groove of the CTD bound subunit (**2**). This stabilizes the first subunit and the CTD bound chaperone is not required anymore (**3**), allowing the NTD bound chaperon to transfer to the CTD position. In this way the growing filament is pushing through the channel (**4**). A new subunit can bind to the NTD and the step for elongation of one subunit is repeated hundreds of times (**5,6**).

termination mechanism is unclear. Since ATP is absent in the periplasm, assembly is powered by hydrophobic effect and folding energy stored by chaperone interacting with the partially folded subunit (Geibel, S. et al., 2013), which can explain why CU pili cannot be retracted once assembled (Busch, A. et al., 2015).

Hydrophobic interactions held the fiber together. However, subunits in the rod filament form many hydrophilic interactions between one another. Those can be gradually broken if the filament is extended allowing it to extend without compromising its integrity, since the process is reversible. This gradual uncoiling give spring like characteristics to T5P when subjected to tension (Hospenthal, M.K. et al., 2016).

1.2.2. USES OF CU PILI

CU pili have been extensively studied in *E. coli*. Above we saw that Bfp (type 4b) are critical to promote virulence in EPEC strains. However, in uropathogenic *E. coli* (UPEC) strains CU pili are the determining factor for establishing surface attachment. A recent study has identified a total of 38 different CU pili expressed in *E. coli*, with each strain examined having an average of 10-15 different types in the genome (Wurpel, D.J. et al., 2013). It is possible that CU pili have coevolved with a host, to specifically bind the targeted tissue. Each CU pili has specific tip adhesion that can bind one particular target. Groups of CU pili are associated together for different pathogens and determine the specific tissue that the pathogenic *E. coli* can target (Busch, A. et al., 2015). A nice representative example is UPEC. The expression of type 1 pili tipped with FimH adhesin, specifically target binding to mannosylated surface exposed proteins, which are expressed by epithelial cells lining the interior of the bladder (Busch, A. et al., 2015). After adhesion, bacteria form microcolonies damaging the tissue to extract essential nutrients. If the infection persists, the cells have a chance to reach the kidney. In the kidney FimH is useless, but UPEC possess also P pili, whose tip adhesin is PapG, capable of binding receptors present in the epithelial cells of the kidney cells (Teschler, J.K. et al., 2015). Similarly, different CU pili encoded by *Proteous mirabilis* are used for attachment at different stages of the infection: the NAF pili for the colonization of uroepithelial tissue and the PMF pili for the bladder and finally MPR pili for the kidney (Armbruster, C.E., and Mobley, H.L.T., 2012). To promote colonization efficiently, CU-mediated attachment must be able to held the cell against the shear flow present in the urinary system. Interestingly, FimH evolved to have an increased affinity binding when subjected to tension generated by shear flow (Sauer, M.M. et al., 2016; Thomas, W.E. et al., 2002).

The Gram-negative *Y. pestis* has a tad locus, but T4P have never been reported. In fact a deletion event removed the major pilin and a frameshift mutation affects several genes in the tad operon, making expression of T4P impossible (Thomson, N.R. et al., 2006). However, both the less pathogenic *Y. enterocolitica* and *Y. pseudotuberculosis* possess type 4b tad operon, and in *Y. enterocolitica* T4P are secreted and used to promote microcolony formation (Schilling, J. et al., 2010). Interestingly, *Y. pestis* emerged as a species from *Y. pseudotuberculosis* 2000 to 20000 years ago (Achtman, M. et al., 1999), with the loss of T4P not affecting pathogenicity, which is much higher than the original strain. Instead of T4P, *Y. pestis* can produces two CU pili: the pH 6 antigen (Psa) and the cluster fraction 1 antigen (Caf). Both contribute to tissue adhesion, biofilm formation and evasion of the immune system (Du, Y. et al., 2002; Felek, S. et al., 2011; Galván, E.M. et al., 2007). One strategy for immune evasion is the secretion of many Caf pili on the cell envelope in order to create a thick capsule that impairs phagocytosis by macrophages (Du, Y. et al., 2002). A suggested role of Psa pili is to bind the Fc receptor of the antibody, therefore hindering detection from the immune system. Caf and Psa pili have two important differences compared to type 1 pili. First, the Caf and Psa pili do not have a rod filament, but are essentially very long and thin fibrillum, at about 2 nm in diameter (see Figure 8A). Second, Caf and Psa pili are an example of polyadhesines, whereby each subunit in the filament have

an available binding site, greatly increasing the number of potential adhesive interactions per pilus (Zavyalov, V. et al., 2010).

1.2.3. TYPE 5 PILI

The general architecture of the filament Type 5 pili (T5P) resembles F1 capsule pili, with a thin, non-retractable filament of about 4.5 nm in diameter, held at the OM. This type of pili is relatively new and while the structure of the filament has been resolved in one case, the overall assembly process is unknown. So far the use of T5P have been described mostly in *Porphyromonas gingivalis*, an oral pathogen responsible for periodontitis (Xu, Q. et al., 2016).

The filament is probably assembled in a tip to bottom manner (see Figure 9). Precursor subunits are all lipoproteins and subunits are lipated at the first N-terminal stand in the periplasm. Like in CU pili subunits have a hydrophobic cleft, but is longer and run through the whole length of the protein. Before assembly the hydrophobic cleft is probably covered by one C-terminal and the first N-terminal strands (Xu, Q. et al., 2016). Through an unknown mechanism precursor subunits are shuttled from the IM to the OM. Here the N-terminal strand hosting the anchoring lipid is cleaved, removing the lipid. An unknown temporary anchor protein likely keeps the growing pilus associated to the OM. The elongation mechanism is unknown, except that a strand exchange keeps the filament together: each subunit extends the last two C-terminal strands, which are amphipathic, into the hydrophobic groove of the last subunit added to the filament (Kloppsteck, P. et al., 2016). The anchoring subunit does not undergo the cleavage of the N-terminal strand, keeping the whole filament anchored to the OM, and do not possess a hydrophobic groove. The tip subunit does not have the two C-terminal strands and possess adhesion properties. Specific role and uses of this type of pili are still under investigations (Hospenthal, M.K. et al., 2017a).

Box 3 – The Archaellum

The archaellum is the organelle that allows archaea to swim. Except for the function of swimming, there are no structural or genetic similarities with the bacterial flagellum. In fact, the archaellum architecture and components are related to T4P and T2SS, and the rotation is powered by ATP hydrolysis (Ghosh, A., and Albers, S.-V., 2011).

Recent cryo-EM studies revealed the general organization of the archaellum (Daum, B. et al., 2017). The machinery is embedded in the IM, since archaea normally lack a cell wall and the OM. The IM platform is made by FlaJ, which is similar to PilC: it probably binds the filament and transfers the rotational motion generated by the motor. FlaF may be a periplasmic protein creating a protective ring around the filament. The motor complex is made by FlaI, a homologue to ATPases present in T2SS and T4P, and FlaH, and incomplete ATPase. Both FlaH and FlaJ proteins are likely assembled in two hexameric ring structures with a FlaI ring sandwiched in between. FlaC and FlaD/E form a complex that surrounds the motor, with the possible role of modulating the direction of rotation.

In *Pirococcus furiosus* cells, a single pole could have up to 50 archaellum machineries. At the same pole at 15 nm from the IM, a continue proteins surface overlapped the area occupied by the archaellum machineries. This is called the polar cap and it probably anchors archaellum machineries, providing a rigid structure to support the considerable torsional stress generated (Daum, B. et al., 2017).

Archaellin subunits are the building blocks of the archaellum filament. Structurally similar to pilins, they are embedded in the IM and processed by a preflagellin before being assembled in a filament. The archaellum machinery assembles archaellins with the same architecture used in T4P: a right handed helix with a hydrophobic core composed by the N-terminal α-helixes of archaellins, and the C-terminal globular heads lining the surface of the filament. A helical rise of 5.4 Å and about 100° rotation per subunit. The diameter of the filament is 11 nm, only half as wide as a bacterial flagellum (Poweleit, N. et al., 2016).

Pyrococcus furiosus   *Daum, B. et al., 2017*
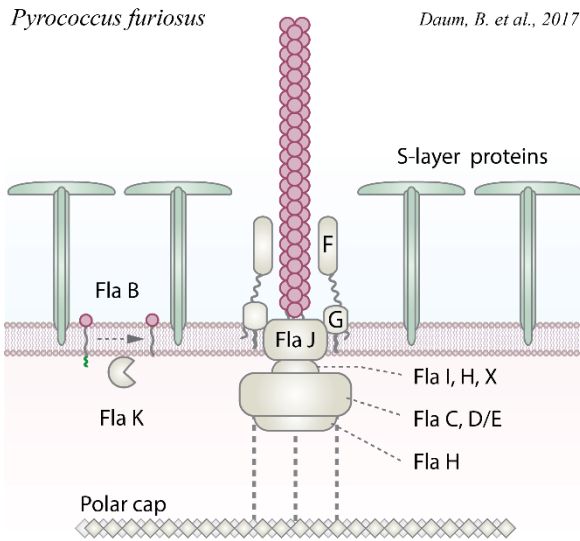
Proetein Function	P. furiosus
Motor complex	FlaI, H, X
IM platform complex	FlaJ
S-layer "channel"	FlaF, G
Main flagellin	$FlaB_0$
Minor flagellin	$FlaB_1, B_2$
Preflagellin peptidase	FlaK
Chemotaxis (?)	FlaC, FlaD/E

References   *Daum, B. et al., 2017*
          Albers S.V. & Jarrel K.F., 2015

2. Pili in Gram-positive Bacteria and Archaea

To date, pili in archaea and Gram-positive bacteria have remained mostly uncharacterized both structurally and functionally. Most of what we know is drawn from metagenomics studies. However, metagenomics can only give us hypotheses about structure and function, and very little information on what they may be used for. Nonetheless, metagenomics have allowed us to explore the diversity of pili in the prokaryotic kingdom. Many of the Gram-positive bacteria analysed had T4P-like operons, with several species having multiple operons (Imam, S. et al., 2011). The N-terminal motif is well conserved in the major pilins of Gram-positive bacteria analysed, containing both a Glu5 and the peptidase cutting site, as well as a stretch of hydrophobic amino acids. Some operons did not encode any pilin, nor were pilin-like genes found in other parts of the genome in some species. This raises the possibility that the ability to secrete T4P has been lost, as mentioned above for *Y. pestis* (see section 1.2.2). Direct observation of T4P in Gram-positive bacteria was only reported in a few cases. T4P have been observed in *Ruminococcus albus*, a bacterium able to digest plant cellulose. A study showed that T4P are necessary in *R. albus* to perform degradation of plant fibers, with indications that pili attach on cellulose (Rakotoarivonina, H. et al., 2002). Another study showed that *Clostridium perfringens* can express T4P and displayed an unusual gliding motility that depends on expression of retraction ATPase (Varga, J.J. et al., 2006).

In archaea, tad-like operons have been found, especially in thermophile species which live in turbulent environments and may require pili to hold onto the mineral rich surfaces of geothermal vents (Makarova, K.S. et al., 2016). However, indications of pili in archaea are still restricted primarily to *in silico* analysis. In archaea, outside the archaellum (see Box 3), very few other appendages have been visualized and studied extensively. Interestingly, archaeal T4P appear to be hybrids between T4SS and T4P/T2SS (Makarova, K.S. et al., 2016). On the one hand, the ATPases and membrane platform are more closely related to T4SS (Tomich, M. et al., 2007), while on the other hand, pilins, prepilin peptidases and filament are more closely related to T4P and T2SS (Pohlschroder, M. et al., 2011). One example of pili in archaea is the hyperthermophilic *Sulfolobus solfataricus*, where UV light triggers piliation and autoaggregation in a dose dependent manner (Fröls, S. et al., 2008).

Gram-positive bacteria have only the IM and a thick cell wall, while archaea lack a cell wall. To date there is no structure of T4P machinery for single membrane organism. Since the key working mechanism of pili occur in the IM, it is possible that the architecture of pili machineries is similar to that of Gram negative bacteria, minus the OM complex. Whereas in Gram-negative bacteria T4P and the flagellum are most likely derived from two distinct ancestral machineries, the archaellum has no similarity, genetically or structurally, with the bacterial flagellum (see Box 3). In fact, archaellum and T4P show homology between several components and in the working mechanism of the machineries (Makarova, K.S. et al., 2016). The archaellum has some unique features, but retains remarkable similarities with T4P in the structure of archaellin subunits and architecture of the filament (Daum,

B. et al., 2017; Poweleit, N. et al., 2016). Moreover, the rotational mechanism of the archaellum is powered by ATP hydrolysis and the motor subunit belong to the large family of type II/type IV secretion NTPases (Kinosita, Y. et al., 2016). This suggests that archaellum and T4P may derive from a common ancestral machinery, and then diverged to perform separate functions.

SORTASE-ASSEMBLED (SA) PILI

Using the sortase enzymes, Gram-positive bacteria synthesize so-called sortase-assembled (SA) pili which are covalently bound to the cell wall. However, the study of SA pili has started only recently. While the structure of some SA pili have been explored in detail, the assembly mechanics and how the SA pili promote virulence remain to be uncovered.

 The sortases are a family of transpeptidase enzymes capable of creating a covalent bond between a protein and a target molecule (see Figure 10). Sortases are capable of cleaving a lipoprotein encoding a specific sorting signal and linking it to the cell wall. (Hendrickx, A.P.A. et al., 2011a; Mazmanian, S.K. et al., 1999). Soon after their discovery, a sub-class of sortases was discovered in *Corynebacterium diphtheria*, capable to assemble linear filaments. Those were recognized as a new type of pili and named sortase-assembled (SA) pili (Ton-That, H., and Schneewind, O., 2003, 2004). Cryo-EM pictures of *Streptococcus pneumonia* revealed hundreds of SA pili displayed on the cell envelope. The flexible filaments have a diameter of around 6 nm and a length of up to 1 μm with a beads-on-a-string arrangement of subunits, repeating every ~10 nm (Hilleringmann, M. et al., 2009). Peculiarly, all subunits of the filament are covalently joined, due to assembly by sortases, creating a polymeric fibers that possesses high tensile strength (Kang, H.J. et al., 2009). A detailed structural study on the
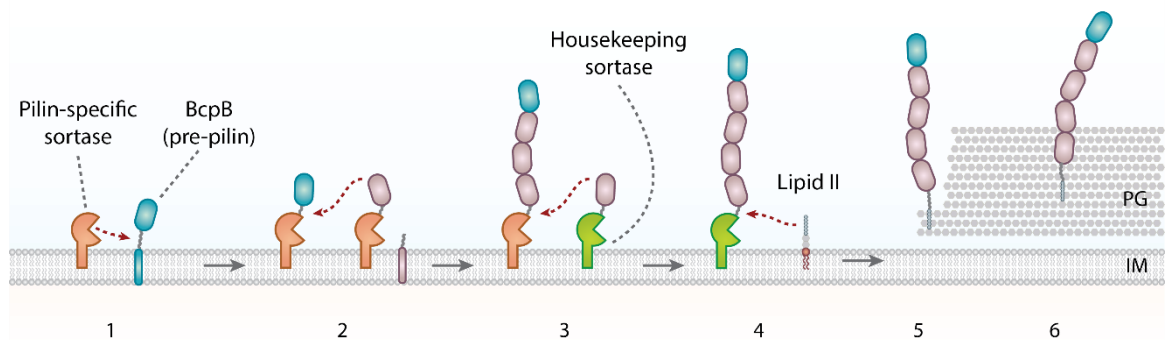

FIGURE 9 – SORTASE-ASSEMBLED PILI IN GRAM-POSITIVE BACTERIA

The assembly of a SA pili involves at least two types of sortases. The pili-specific sortases cleave the precursor pilins and covalently bind them at a specific amino acid (**1**). Two sortases interact such that one sortase can transfer its attached pilin subunit (and any other pilin linked to it) to the subunit of another sortase (**2**). Repetition of this step results in bottom-up elongation of a filament of subunits, covalently linked with one another. The housekeeping sortase performs the last elongation step (**3**) by covalently linking its subunit to the sugar moiety of a lipid II building block for peptidoglycan synthesis (**4, 5**). Therefore, SA pili are ultimately integrated in the cell wall (**6**).

major pilin of *C. diphtheria* revealed a head to tail arrangements of the pilins and highlighted the presence of an internal isopeptide bond joining the subunits together.

Several sortase enzymes work sequentially to assemble the different pilins in a filament in an orderly manner (Hendrickx, A.P.A. et al., 2011b). A basal pilin subunit and tip adhesin pilins have been identified in SA pili. Basal pilins allow the linkage to the cell wall, via a covalent bond (Linke, C. et al., 2010). Tip adhesins are present in several SA pili and in both *S. pneumoniae* and *S. pyogenes* the structures of the tip adhesin have been resolved, further confirming that they work as monoadhesin filaments. In *S. pyogenes* the adhesin binding site possesses a thioester motif. This thioester bond is present in so-called complement-like proteins serves to mediate a covalent bond upon interaction with a target (Izoré, T. et al., 2010). This rises the interesting possibility that some SA pili could covalently bind to their target during an infection, promoting an even stronger adherence compared to other types of pili.

3. Analogies between different types of pili

The filaments of single-membrane-spanning pili (SMS pili) and T4P look similar, with comparable diameters and length, and only closer studies of the structures revealed clear differences in the architectures and the assembly machineries. Their unique ability to retract may lead to conclude that T4P are superior. While indeed retraction is an advantage, SMS pili are probably cheaper to produce. In SMS pili each subunit contributes about 40-50 Å to the length of the filament. Instead, due to the helical arrangement in T4P each subunit contributes only about 10 Å to the elongation of: T4P need more material per unit length to build a filament. Moreover, SMS pili assembly do not need additional energy for assembly as they use folding energy. On the other hand, T4P require hydrolysis of ATPs for assembly of the filament as well as disassembly. Therefore, while dynamic pili may be more versatile, they are more expensive to build as well as maintain for the multiple cycles of elongation and retraction.

The cost for producing pili may be reflected in the number of pili expressed. There are few estimates on the numbers of T4P per cell. Bacteria like *P. aeruginosa*, *N. gonorrhoeae* and *V. cholerae* express at most up to ten T4P per cell (Jones, C.J. et al., 2015; Skerker, J.M., and Berg, H.C., 2001; Utada, A.S. et al., 2014). *C. crescentus* expresses 2-3 pili per cell on average, with a maximum of five to six pili (Skerker, J.M., and Shapiro, L., 2000). While the number of assembly machineries per cell may be higher in some species, the amount of pilin subunits as well as localized assembly limits the number of filaments assembled at any time. In electron microscope images SMS pili appear in some cases to be assembled as dense brushes at the cell envelope, while in other cases they are sparser. In the former case, single cells may have several hundreds of SMS pili on their surface. However, estimates on the number of SMS pili are hard to find and the paucity of data does not allow a conclusive evaluation.

Why are there all this different types of pili? While in general all pili promote some sort of attachment, different types lead to different phenotypes. CU pili are static filaments with a sticky tip targeting specific ligands and cells using them must rely on random dispersion to reach their target. This is a reliable and efficient method for dispersion, as shown above in the example of UPEC and *Y. pestis*, where the sequential expression of different CU pili allows bacteria to propagate their infection from tissue to tissue (see section 1.2.2). T4P promote unspecific binding, making them capable to potentially target a diverse range of surfaces. Although T4P are capable to power twitching and directional motion, it is unlikely that single cells use them to move all the way to a desired tissue: dimensions and speed involved hinder this approach. It is likely that bacteria with T4P use random dispersion, and if possible swimming, to reach their target. Nevertheless, at their scale the surrounding environment can be is extremely heterogeneous. Therefore, the ability to twitch, even a few tens of microns, allows bacteria to explore the microenvironment and settle in the best available spot. Moreover, having functional T4P capable of retraction increases the cohesion in

biofilms and aggregation, which in turn promotes survival within a host as well as in the environment.

As mentioned above (see section 1.1.4), all T4P pili share a common ancestry and there are important homologies with the T2SS, the archaellum and to a smaller degree with T4SS (see Box 1, 2 and 3). Most of these homologies are in core protein components, like pilin subunits and ATPases. Structural studies show that T2SS has an architecture similar to T4P and the operating mechanism of T2SS is very similar to the piston mechanism of T4P (see Box 1). Some components of T2SS and T4P are interchangeable, for example in some species the prepilin peptidase is shared for both systems. Furthermore, the structures of filaments in different systems are remarkably similar. All those indications point to the possibility that T2SS, T4P and archaellum derive from one ancestral machinery that was widespread among prokaryotes. This ancestral machinery then may have evolved to perform quite different functions: protein secretion (T2SS), attachment appendages (T4P) and swimming (archaellum). However, the underlying common feature in all these organelles is the assembly of a protein-based filament and we can speculate that it was present in the ancestral machinery as well. Also, the rotational mechanism during assembly is a central feature of all organelles, perhaps necessary and dictated by the helical structure of the filaments. In archaea, the evolution of the ancestral machinery somehow uncoupled rotation from assembly, repurposing the organelle to power swimming. As mentioned above, no structural similarity exists between the archaellum and the flagellum and in fact the flagellum likely originates from a different ancient organelle, shared with the T3SS. This indicates that swimming organelles in prokaryotes could have evolved independently at least twice.

4. Aims of the Thesis

In **Chapter 2** we show how pili-mediated surface attachment in *C. crescentus* relays on pili being retracted and how they reorient cells on a surface and bring them closer to surfaces. This contradicts previous knowledge that described this family of pili (tad-like pili) as unable to retract. We found that medium flow influences pili-mediated attachment and the forces generated by the pili motor during retraction. Lastly, our results suggest that pili activity is directly regulated by the second messenger molecule c-di-GMP. On the same line of research, but for a different organism, *P. aeruginosa*, **Chapter 3** explores the role of a receptor protein, FimW that is activated by c-di-GMP. FimW controls the dynamics of pili, promoting attachment and walking behaviour. This protein is also asymmetrically inherited in each generation, and this work highlights a new aspect of surface colonization in *P. aeruginosa*.

Chapter 4 investigates a novel c-di-GMP effector, HfsK. This is a protein involved in holdfast biogenesis, which is a powerful glue-like substance that *C. crescentus* secretes upon surface contact in order to attach permanently. Mutations in HfsK can lead to decreased holdfast cohesion, which served as an interesting tool used in Chapter 1. Moreover, this study shows how localization of HfsK is regulated by c-di-GMP binding and concentration. **Chapter 5**, elaborates the role of c-di-GMP in the transition to biofilm formation in *E. coli*. This study shows a novel mechanism where a protein, PdeL, can act as both a phosphodiesterase and a transcriptional factor. Two interconnected positive feedback loops regulate both functions of the protein, and their regulation governs the transition to a biofilm lifestyle. Lastly, **Chapter 6** summarizes the main findings of the studies presented in this Thesis and discuss some concluding remarks for the field of research they encompass.

The appendixes describe crucial methods, machines and programs developed for the studies presented in this Thesis. **Appendix 1** introduces the process of photolithography, crucial for the fabrication of microfluidic devices. As example we will show the protocol for creating a "mother machine" device, currently used in our lab. The protocol can be adapted to create any other microfluidic device. **Appendix 2** presents an example for so-called thin chamber device (Deshpande, S., and Pfohl, T., 2012, 2015). In **Appendix 3** we review how to create microfluidics valves using photolithography, which in turn allow to programmable devices. This microfluidic technology allows to create complex designs for a device and greater control and parallelization of experiments. The appendix also describes also how to build, program and use the "automated valve controller" (AVC), a machine that allows to control and coordinate the action of such complex devices. The **Appendix 4** is a detailed manual on the custom made Matlab based program called WHISIT, capable to perform quantitative analysis of the fluorescent signal distributions inside bacterial cells.

CHAPTER 2

_____

SANGERMANI M. ET AL., 2018

Dynamic role of Tad pili in Caulobacter crescentus surface colonization.

Matteo Sangermani[1,2], Isabelle Hug[1], Nora Sauter[2,3], Thomas Pfohl[2,3,4], and Urs Jenal[1]*

Affiliations:

[1] Biozentrum, University of Basel, Klingelbergstrasse 50/70, 4056 Basel, Switzerland.

[2] Department of Chemistry, University of Basel, Klingelbergstrasse 80, 4056 Basel, Switzerland.

[3] Swiss Nanoscience Institute, 4056 Basel, Switzerland.

[4] Current addresses:

Institute of Physics, University of Freiburg, Hermann-Herder-Str 3, 79104 Freiburg, Germany.

Abstract

Prokaryotes are capable of forming multicellular communities adhering and growing on surfaces. Many prokaryotes as single cells express filamentous appendages called pili and use them to attach on surfaces. In this work, we investigate how Tad pili promote surface attachment in *Caulobacter crescentus*. We show that Tad pili in *C. crescentus* are dynamic and are able to retract, contrary to the behaviour of other T4c pili. Using microfluidic controlled flow conditions to mimic natural environments, we found a non-linear attachment and detachment behaviour. We measured the surface attachment in flow conditions and found that flow speed of 0.75 mm/s promotes the highest attachment level, while lower or higher flow speeds affect surface colonization negatively. Using optical tweezers we measured forces generated by pili retraction and found the maximum force at about 8 pN. After surface contact cells used pili to reposition their body in a horizontal position, in respect to the attached surface, for secretion and adhesion of the holdfast, a glue-like substance that promote long-term attachment. We found that pili are active before cell division and are used for around 20 minutes after cell separation. Our results suggest that dynamic pili are necessary to promote surface attachment. We also found that second messenger c-di-GMP can regulate pili activity and increase pili-mediated attachment at low concentrations. On the other hand, higher concentrations can abolish surface adhesion. Lastly, we show that a single mutation causing lower cohesion of the holdfast caused the bacteria to walk upright for small distances, a novel phenotype specific to this strain.

Introduction

Bacteria have evolved effective mechanisms to colonize abiotic and biotic surfaces in order to scavenge nutrients or assemble into refractory communities called biofilms. A pivotal role in this process is played by adhesive pili, also called fimbriae, protein-based filaments exposed on the surface of bacteria that have adopted a variety of functions including adherence, motility, electron transfer, acquisition of DNA and protein secretion [1, 2]. Accordingly, pili are crucial virulence factors during infection processes [3]. They mediate direct contact between pathogens and specific host tissues, promote pathogen spreading and cellular invasion [4–8]. The most sophisticated class of these filaments, the Type IV pili, are dynamic machineries that can undergo cycles of extension and retraction through the rapid assembly and disassembly of pilin subunits at the proximal end of the structure [6, 9]. Extension and retraction are powered by specific cytoplasmic ATPases, which power rotational movements of the assembly platform in the inner membrane that incorporate pilin subunits into or extract them from the helical filaments [4, 10]. Single retracting pili are able to generate forces ranging from 50 to 150 pN [5, 11–13]. Through the coordinated extension and retraction of multiple polar pili, single cells are able to twitch and walk on surfaces and explore their environments [1, 14, 15].

Type IV pili are widespread in bacteria and archaea [10, 14]. Distinctive features divide these structures into two classes, called Type IVa and Type IVb. Type IVa represent a uniform class that is found in important human pathogens like *Pseudomonas aeruginosa*, *Vibrio cholerae* or *Neisseria* spp. and in environmental bacteria like *Myxococcus xanthus*, *Shewanella putrefaciens* or *Bdellovibrio bacteriovorus*. The Type IVb subclass is less homogenous and best-characterized for enteropathogenic *Escherichia coli* or *V. cholerae* [11]. A subclass of Type IVb are the tight adherence pili (Tad) (Figure 1A) that are widely distributed among Gram negative and positive bacteria [12, 16]. Tad pili, also called Flp (fimbrial low-molecular-weight protein) pili, have pilin subunits with characteristically shorter sequence as compared to other Type IV pili systems, but show similar hydrophobic intermolecular interactions providing the main force holding the fibers together [11, 15, 16]. Tad pili promote surfaces colonization, cell-to-cell aggregation, biofilm cohesion and are required for virulence in different bacterial pathogens [11, 15–19]. In contrast to other Type IVa and Type IVb pili systems, Tad clusters lack a gene coding for a retraction ATPase, raising the question if these systems show a similar dynamic behaviour as other Type IV pili fibers. However, a study found that in *Vibrio cholerae* toxin-coregulated pili (TCP) are retractable, despite the lack of a retraction ATPase [20]. When the minor pilin TcpB is incorporated in a growing pilus, it blocks assembly and initiates retraction, which is proposed to be a spontaneous disassembly event, rather than an enzymatic activity.

In *C. crescentus* polar Tad pili facilitate the attachment of motile planktonic cells to surfaces [21, 22]. During *C. crescentus* division, a polarized sessile stalked cell (ST) produces a motile offspring, the swarmer cell (SW). A single flagellum and multiple pili are assembled in the predivisional cell at the

pole opposite the stalk (Figure 1B) [12, 23]. The newborn SW cell remains in a motile, non-replicating state for a defined period called G1. After this period, chromosome replication resumes coincident with cell differentiation, during which the flagellum and pili are shed and are replaced by an adhesive exopolysaccharide, the holdfast, and the stalk. While the developmental program defines the time window during which planktonic SW cells retain their motility, SW cells challenged with surface are able to transit to the sessile state within seconds [21, 24, 25]. This process is executed by a surface recognition program that involves the rotary flagellum and the polar pili. It was recently proposed that SW cells encountering surface are able to sense mechanical cues through an interference with motor components in the cytoplasmic membrane. Motor interference stimulates a motor-associated diguanylate cyclase to produce a burst of c-di-GMP, a second messenger that allosterically activates a preassembled holdfast synthesis machinery located at the same cell pole [21]. Thus, by rapidly activating holdfast secretion, cells irreversibly anchor to surfaces via their piliated and flagellated cell pole. Polar Tad pili are critical components of surface sensing and surface colonization in *C. crescentus*. It was postulated that initial surface adherence is mediated by pili and that pili retraction positions the flagellar pole in close contact with the surface to allow mechanosensation to occur [22]. A recent study demonstrate that pili in *C. crescentus* are also capable of retraction [21]. The alternative model proposed a more direct role for the Tad pili as mechanosensitive devices that are able to sense surfaces by using the resistance experienced when pili retract [21].

To more closely define the role of Tad pili in *C. crescentus* surface recognition and colonization, we analysed their regulation and dynamic behaviour. Our results show that pili-mediated attachment on surfaces is flow depend. Flow speed above 5 mm/s were capable to abolish surface attachment, while a speed of 0.75 mm/s resulted in maximum colonization levels. Interestingly, lower flow velocity had a negative effect on surface attachment. We confirm that pili in *C. cresentus* are capable of retraction. Pili activity was found to constantly position surface attached cells in upright position. Surface attachment and upright positioning were found to be influenced by intracellular levels of c-di-GMP. Low concentrations positively affect cell adhesion, but higher concentrations have the opposite effect and can abolish pili-mediated attachment. A strain secreting a lower cohesion holdfast was found to display the ability to walk in the flow conditions tested, an peculiar phenotype never described for *C. crescentus* and any bacteria possessing type IVc pili. Lastly we determined the maximum force generated by pili retraction by optical tweezers measurements, at about 8 pN.

Results

PILI MEDIATE TEMPORARY SURFACE ATTACHMENT UNDER MEDIA FLOW

Surface adhesion of *C. crescentus* via their polar pili is transient and weaker as compared to the strong and long-lasting attachment via the adhesive holdfast [26]. To investigate the overall contribution of pili to surface attachment without interference of the holdfast, we analysed the behaviour of the *C. crescentus* "wild type" control strain (NA1000 *hfsA-*), which carries an inactivating mutation in the *hfsA* gene, rendering this strain unable to produce holdfast [27]. Simple flow channels were used with a single inlet supplying a culture with a constant flow of medium [21]. To evaluate pili-mediated attachment, time lapse images were recorded microscopically to determine the rate of colonization. Importantly, mutants lacking pili were unable to attach in such an assay (Figure 1C).

As shown in Figure 1C, different medium flow velocities resulted in different attachment rates. A plateau of attached cells per unit surface area was reached when the rate of attachment of incoming bacteria equalled the rate of detachment of cells from the substratum (Supplemental Movie 1). The average residence time of swarmer cells on the surface was about 2 min (Supplemental Figure 1A). A fraction of cells remained attached for several minutes and their proportion increased at higher flow rates (Supplemental Figure 1A). However, the probability of newly attaching cells rapidly decreased when flow rates were increased (Figure 1D). Short-lived surface attachment of swarmer cells can be described by a Langmuir-like adsorption model, taking into account the adsorption from solution with attachment and detachment rates depending on the surface density of the cells. The evolution of the colonization density $\theta(t)$ can be fitted by a function of the form $\phi(t) \sim \phi_{eq}\left(1 - e^{\left(\frac{-t}{\tau}\right)}\right)$, where ϕ_{eq} is the plateau density and τ, characteristic time. The equilibrium constant can be determined by $k_{eq} = \frac{k_{on}}{k_{off}} = \frac{\phi_{eq}}{(1-\phi_{eq}) \cdot c_{bulk}}$, with the attachment rate k_{on}, the detachment rate k_{off}, and the cell concentration in the solution c_{bulk}. The detachment rate can be obtained from $k_{off} = \frac{\phi_{eq}}{\tau \cdot (2 - \frac{1}{\phi_{eq}})}$.

The plateau values of the colonization density ϕ_{eq} (Figure 1D) as well as the obtained k_{eq} and k_{off} (Supplemental Figure 1B) show a strong dependency on the flow velocity. At lower flow velocities, an increase of ϕ_{eq} with increasing flow can be observed with a maximal plateau ϕ_{eq} and k_{off} at a flow velocity of 0.75 mm/s. At higher medium flow rates, ϕ_{eq} decreased and the k_{off} increased (Supplemental Figure 1B). This suggested that pili-mediated surface attachment depends on the flow rate with optimal adherence values observed at intermediate flow velocities. We found that flow velocities above 5 mm/s completely abolished cell attachment. To estimate the strength of pili adherence, we calculated the drag force experienced by cells close to a surface in a microchannel (Supplemental Figure 1C). A flow rate of 5 mm/s corresponds to a drag force of 40-60 pN. At optimal attachment, 0.75 mm/s, the theoretical drag force corresponds to around 7-15 pN.
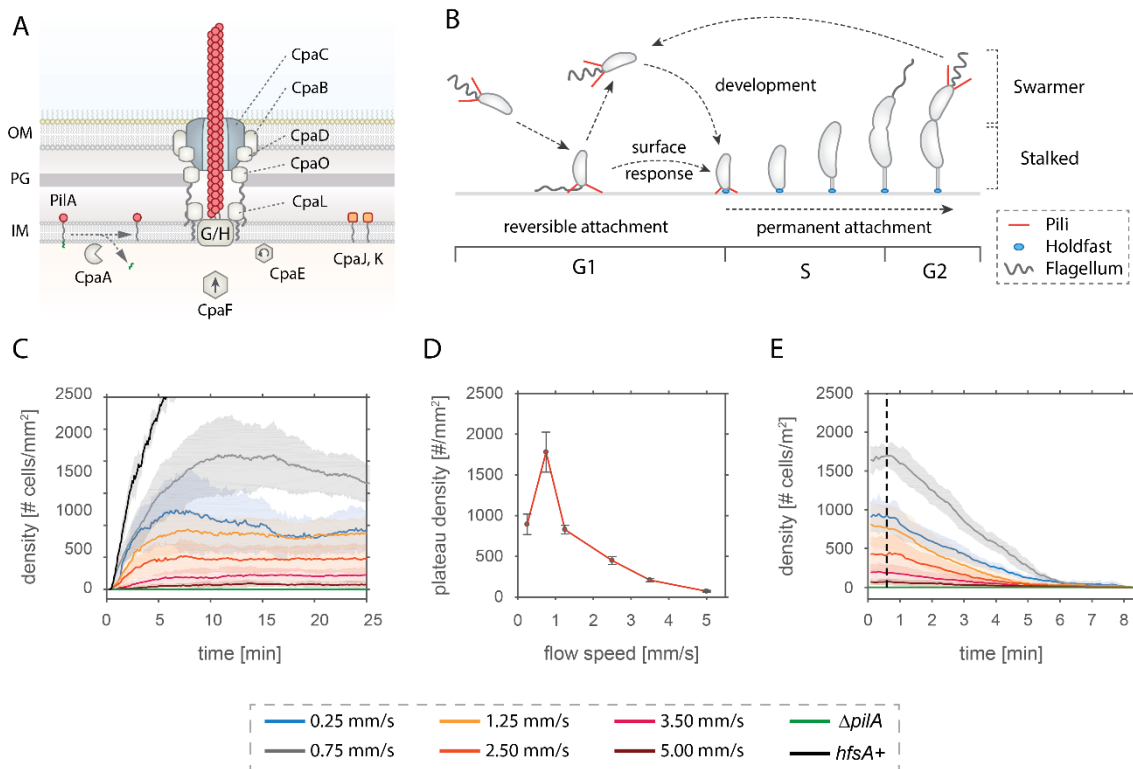
FIGURE 1 – Pili-mediated surface attachment of C. crescentus cells in flow conditions

A – Schematic model of pili machinery in *C. crescentus*. The function of most components is drawn according to comparative analysis of the *cpa* locus with other Tad pili [11, 28]. CpaC is the secretin OM pore, which could be stabilized by CpaD and CpaB. CpaG and CpaH form the inner membrane platform that is located at the base of the filament. CpaO and CpaL aid in aligning the OM complex with the IM platform. CpaF is the functional motor protein, while the role of CpaE is unclear, although it is required to recruit several Cpa components to the cell pole. PilA is the major pilin subunit that matures upon removal of the signal peptide by the prepilin peptidase CpaA. Mature PilA can then be assembled into a filament by the machinery [11, 28].

B – Schematic of the *C. crescentus* cell cycle. Swarmer cells are born with assembled pili (red) and flagellum (grey). Upon surface encounter, pili promote temporary attachment and position the flagellated cell pole close to the surface. This triggers the secretion of an adhesive exopolysaccharide, the holdfast (blue) and results in permanent attachment of the cell. Attached cells differentiate into stalked cells and, concomitantly initiate replication and an asymmetric cell division to generate another motile swarmer cell.

C – Pili-mediated surface attachment at different flow rates. The chart shows the rate of colonization of a microfluidic channel by *C. crescentus* strain NA1000 (*hfsA⁻*) at different flow velocities as indicated.

D – Optimal attachment rates depend on medium flow. The plateau level of surface colonization reached at different flow velocities are plotted. Values are averages of the rates of colonization shown in C between 10 and 25 minutes after the start of the experiment.

E – Detachment of adherent cells at high flow rates. The detachment behaviour of NA1000 (*hfsA⁻*) from different levels of colonization as indicated in (C) is shown. The vertical dashed green line at 30 seconds marks the time point when the flow was increased to 25 mm/s. Opaque areas in panels C and E represent standard deviations. (n>3).

To determine the detachment rates of surface attached *C. crescentus* swarmer cells, the medium flow rate was increased from a steady-state situation with constant plateau density (Figure 1C) to a very high flow rate of 25 mm/s. Under these conditions, cells were unable to attach (Figure 1C) and the surface bound cells detached following an almost exponential decay, with a decay time of roughly

$\tau_d = x$ min/s (Figure 1E). Together, these observations demonstrated that pili mediate transient surface attachment of *C. crescentus* swarmer cells in devices with media flow. We conclude that pili-mediated immobilization negotiates a time window during which motile swarmer cells are able to recognize surface exposure and initiate holdfast production to undergo the transition from temporary to permanent attachment.

C. CRESCENTUS PILI ARE DYNAMIC AND CAN FORCE ATTACHED SWARMER CELLS INTO AN UPRIGHT POSITION

Surface attached *C. crescentus* swarmer cells were most often found standing upright perpendicular to the surface, irrespective of their ability to synthesize an adhesive holdfast (Figure 2A, Supplemental Movies 1, 2) [21]. This is an unfavourable position considering the constant drag force from the media flow. Moreover, we observed that after landing, cells occasionally moved a few microns mostly upstream against the medium flow, as if walking upright for small distances. Since only an active force could move cells against the flow or position them in an upright orientation, we speculated that the *C. crescentus* Tad pili may be able to actively retract [13]. To investigate pili dynamics we first analysed strains capable of secreting an adhesive holdfast in flow channels mimicking conditions that *C. crescentus* encounters in its natural aquatic environment [25]. Under such conditions, offspring of attached stalked mothers are exposed to surface as a consequence of medium flow over the crescentoid dividing cells. This positions the flagellated and piliated pole in close proximity to the substratum, allowing cells to sense surface and triggering immediate holdfast production (Figure 2A) [21].

To quantify the movements of newborn swarmer cells into an upright position, we measured the 2D projections of individual cells in the xz plane and used this information to infer the cells' 3D orientation (Figure 2A). The resulting tilt angle (θ) was compared five minutes before and five minutes after cell division (Figure 2B). Swarmer cells in wild type control strain (NA1000 *hfsA*+) were unable to change their position as long as they were physically connected to their stalked mothers. However, upon separation, swarmer cells rapidly changed their tilt, moving into an upright position of about 80° degrees (Figure 2B). In contrast, stalked cells retained their low θ value after cell division. A strain lacking the major pilus subunit (*ΔpilA*) showed extremely low attachment, making it impossible to collect statistically relevant data on the fate of newborn swarmer cells in this strain. However, we have shown earlier that cells lacking the outer components of the polar flagellum show a hypersensitive surface response with rapid deployment of the adhesive holdfast that partially alleviates the strict requirement for pili [21]. In agreement with this observation, cells of a strain that lacked both external flagellar structures and the major pilin subunit (*flgDE ΔpilA*), occasionally attach to surfaces, but in all such instances cells were unable to stand up (Supplemental Movie 3). In contrast, a strain lacking only the flagellar structures (*ΔflgDE*) showed wild type-like behaviour (Figure 2B). A strain lacking the crescentin cytoskeleton (*ΔcreS*), has a rod-like cell shape instead of
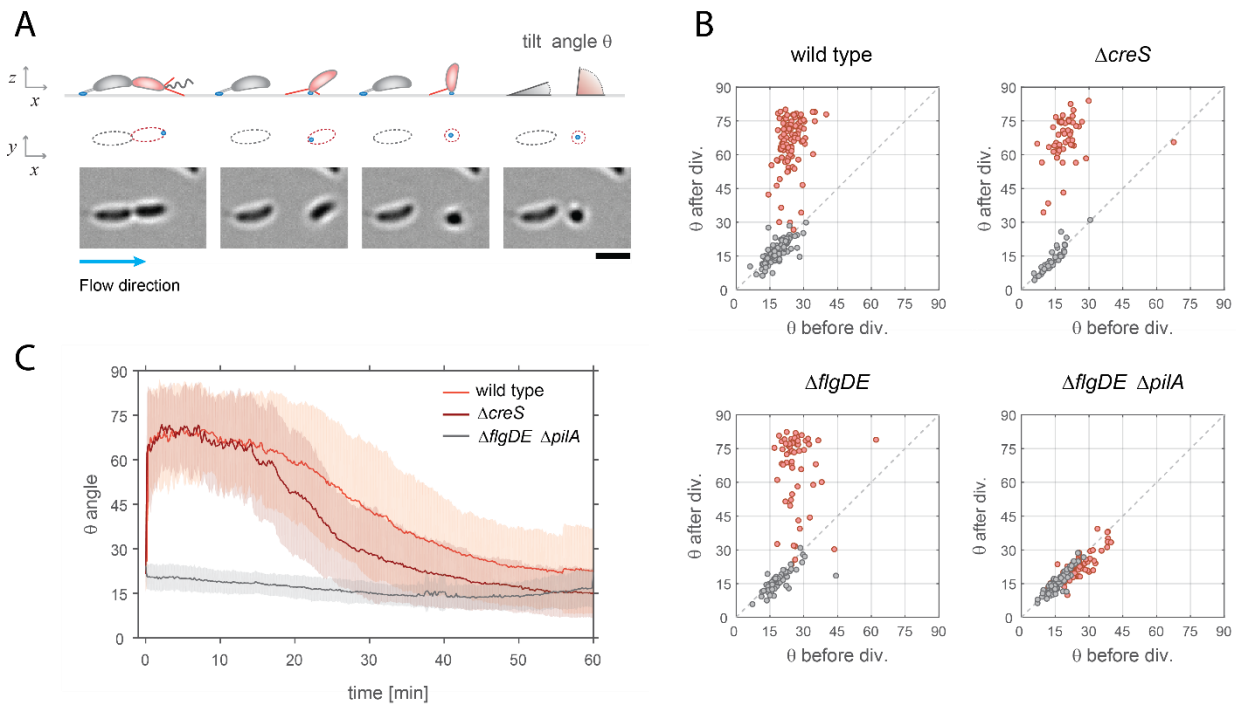
FIGURE 2 – PILI RETRACTION CAUSES C. CRESCENTUS CELLS TO STAND UP.

A – *C. crescentus* cell division under flow. A schematic view (top) and respective light micrographs (bottom) are shown. The sequence of images illustrates a stalked mother cell, which is attached to the surface via its holdfast (blue), producing a swarmer offspring. A schematic representation of the cell outline in the xy plane is shown as identified by the program. Polar pili are highlighted (red). Upon surface sensing [21] the newborn SW cell produces a holdfast for surface anchoring. Newborn SW cells, but not ST mothers are able to move into a vertical position after separation. The tilt angles θ (angle between the cell main body axis and the glass surface) of mother (grey) and daughter (red) were calculated from the cell contour shape (xy plane) with cells lying parallel to the glass surface and being in an upright position scoring $\theta=0°$ and $\theta=90°$, respectively. An arrow indicates the direction of the medium flow. Scale bar: 2 µm.

B – Pili are required for newborn swarmer cells to stand up. Scatter plots comparing the average angle θ of the same cells recorded 5 minutes before and 5 minutes after cell division, respectively. The results shown were obtained with the strains indicated. Coloring of swarmer cells are in red, stalked cells are in grey).

C – Dynamics of pili-mediated standing up of swarmer cells. The chart shows the time evolution of the angle θ in daughter cells of *C. crescentus* wild type (*wt*), the *ΔcreS* and the *ΔflgDE ΔpilA* mutant strains. Time zero corresponds to the time when mother and daughter cells separate. Solid lines represent average values; the standard deviation is shown as an opaque area. *n* = 98 (wt); *n* = 56 (*ΔcreS*); *n* = 57 (*ΔflgDE*); *n* = 75 (*ΔflgDE ΔpilA*).

the typical curvature of *C. crescentus*. The strain *ΔcreS* provides a control to demonstrate that curvature does not influence the ability of attached cells to stand up (Figure C). Together, this strongly argued that the ability of newborn swarmer cells to move into a vertical, upright position requires the presence of dynamic, force-generating pili. The process of standing up is initiated immediately after division with piliated cells changing their tilt angle within a few seconds after cell separation (Figure 2C; Supplemental Movie 2). Despite the relatively strong medium flow, daugther cells were able to keep their upright position for about 10-15 minutes before the angle θ gradually decreased. This coincides well with the timing of cell differentiation and the disappearance of pili during the SW-to-ST cell transition (Figure 1B).

PILI ARE ACTIVE BEFORE DIVISION AND CAN DRIVE PREDIVISIONAL CELL STRETCHING

The above results demonstrated that pili are dynamic and that they are active after swarmer cells have separated from their mothers. However, pili are assembled at the flagellated pole in the predivisional cell and during division facilitate surface interaction and mechanosensation [21, 22]. To investigate if pili are actively retracting already before cells divide, movements of surface attached dividing cells were carefully analysed. We observed that the piliated pole of late predivisional cells was pulled away from the stalked pole, stretching the typical crescentoid shape into a straight line (Figure 3A, Supplemental Movie 4). To quantify this behaviour, we determined the angle (α) between the two cell bodies five minutes and one minute before cell separation. *C. crescentus* wild type cells (NA1000 *hfsA-*) showed discrete peaks of angle α at 180° and at 150° (Figure 3B). The $\Delta creS$ mutant showed only a single peak at 180° indicating that the peak at 150° represents the natural, unstrained angle of crescentin-mediated curvature in the late predivisional stage (Figure 3B). A strain unable to assemble pili lacked the peak at 180°, but retained peaks at 150° (Figure 3B), arguing that cell stretching before division is mediated by the action of polar pili. Consistent with this, cells lacking a polar flagellum retained their stretching ability. Moreover, cell stretching became more prominent at very late stages of division, with the peak at 180° increasing at the expense of the peak at 150° (Figure 3B). Finally, we observed a striking difference between the behaviour of predivisional cells that gave birth to offspring able to attach after separation (Figure 3B, attach) and predivisional cells producing swarmer cells that were washed out after cell division (Figure 3B, wash out). While the former showed a prominent peak at 180°, this peak was missing in dividing cells destined to produce offspring unable to attach. Instead, the latter showed a distribution of angle α resembling the pilus-deficient strain (Figure 3B). This suggested that predivisional cells unable to attach after division either lacked pili activity or were simply not successful in deploying pili for surface adherence under media flow.

Together, these experiments indicated that pili are active before cell division and that pili dynamics increases as dividing cells approach the stage where mother and daughter separate from each other. This also suggest that pili activity is instrumental for surface attachment, given it is absent in wt (wash out). We had proposed earlier that pili retraction at this stage of cell division is critical to position the flagellar mechanosensor in close proximity to the surface in order to successfully initiate biogenesis of the adhesive holdfast and therefore preventing cells from being washed out [21]. Of note, the orientation of the concavity of attached predivisional cells showed a strong bias to one side with respect to the flow direction (Figure 3B, Supplemental Figure 3). While the concavity distribution is expected to be random for cells with a straight *C*-shape, we found that cells were more likely to orient to the left with respect to the flow direction, irrespective of their position within the channel or the nature of the surface. Cells attached to the channel's ceiling showed the opposite orientation, displaying a leftward orientation with respect to the direction of the flow. Based on this, we propose that *C. crescentus* cells have a *C*-shape with a small helical twist (Supplemental Figure 3).
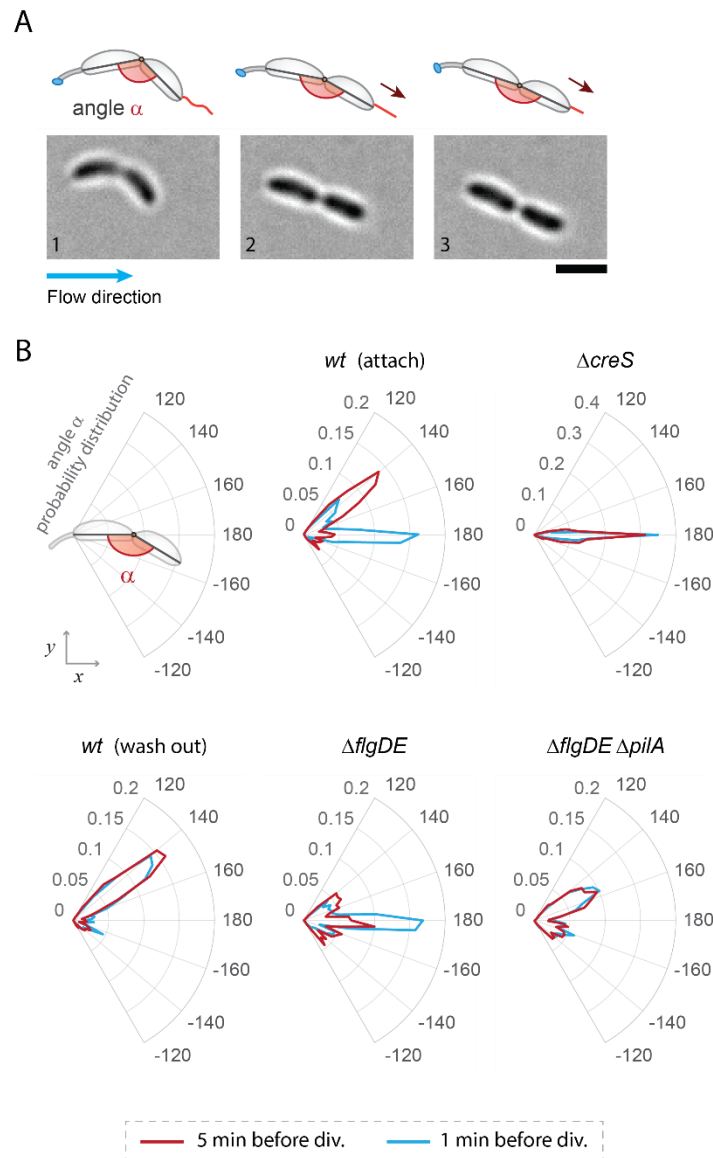
FIGURE 3 – Pili are active before cell division.

A – Image sequence of a crescentoid predivisional cell stretching due to activity of the pili. A schematic representation of the cell is shown above the micrographs illustrating how the angle alpha was determined in each experiment (scale bar: 2 μm).

B – Angle distribution along the long axis of predivisional cells. A schematic of a dividing cell with the angle between stalked and swarmer progeny is shown on the top left as reading aid for the polar charts. Each plot shows the distribution of angle α in different strains recorded five minutes (dark red) and one minute (blue) before cell division. The wild type strain NA1000 *hfsA+* has a peak at about 150° resulting from the crescentoid shape of predivisional cells at rest. A second peak is observed at 180° resulting from pili retraction at the pole opposite the surface attached stalked pole and stretch of the predivisional cell into a straight line. A lack of pili results in the absence of a peak at 180°.

$n = 130$ (wt - attach); $n = 119$ (wt - swim); $n = 56$ ($\Delta creS$); $n = 57$ ($\Delta flgDE$); $n = 75$ ($\Delta flgDE \, \Delta pilA$)

PILI DYNAMICS MEDIATES SWARMER CELL WALKING AGAINST MEDIA FLOW

The swarmer cells analysed under flow generally moved to an upright position only once, right after cell division (Figure 2C). In contrast, the stretching behaviour of predivisional cells (Figure 3A) was observed multiple times for a single cell, arguing that pili can go through repeated cycles of extension and retraction (Supplemental Movie 5). We reasoned that consecutive activity of pili could be

masked in attached swarmer cells by the rapid synthesis of the holdfast adhesin, which immobilizes cells in an upright position. To address if *C. crescentus* pili are capable of undergoing multiple cycles of extension and retraction, we used a *C. crescentus hfsK* mutant, which produces holdfast material with reduced cohesive force. We had shown earlier that this mutant secretes adherent holdfast material that was strong enough to glue cells to the surface in flow chambers, but failed to firmly anchor cells at the place of initial attachment [29].

In flow chambers, this strain left trails of holdfast material, confirming the reduced cohesive properties of the adhesin material [30]. Intriguingly, we observed that newborn swarmer cells, after standing up, were able to move upstream against the medium flow leaving stretched trails of holdfast material behind (Figure 4A,B). This behaviour was fully dependent on the presence of pili as a *ΔhfsK ΔpilA* mutant was unable to move against the medium flow. These results indicated that active pili were able to dislodge cells that are surface attached by a weakened holdfast. Tracking the trajectories of individual cells identified the time period, step size, and speed of pili-driven movements (Figure 4B and Supplemental Movie 5). On average, each step event covered distances of up to 500 nm with an average upstream crawling speed of about 300 nm/sec (Figure 4C and Supplemental Figure 4A). Cells covered distances of several micrometers in repetitive small steps with a frequency of about 2-3 step events per minute. While the step frequency remained high for the first 10-15 minutes after division, it gradually decreased over time and discontinued about 20 min after the daughter had separated from its mother, at which point cells had either settled or were washed away by flow (Figure 4C, Supplemental Movie 5). During their movements, swarmer cells, although unable to remain standing for longer periods of time, repeatedly moved back into an upright position (Figure 4D). This behaviour was particularly pronounced at the end of each step event (Supplemental Figure 4B), arguing that standing up against the media flow directly results from shortening of polar pili towards the end of a retraction period thereby inflicting spatial constraints that move cells into an upright position (Figure 4D). Together, these results confirmed that *C. cresc*entus pili are dynamic in nature and indicated that these structures can be repeatedly employed engaging in consecutive cycles of extension and retraction.
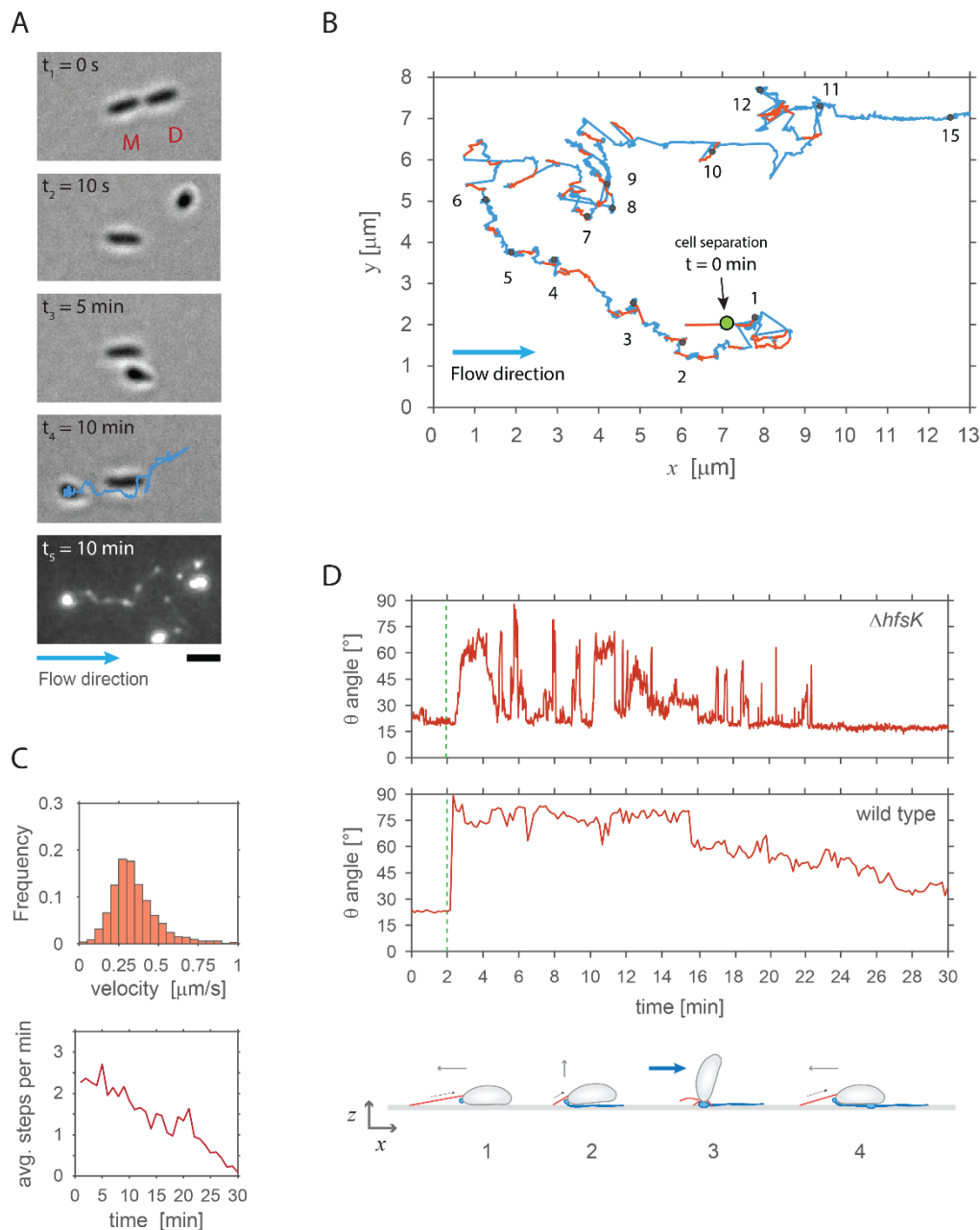
FIGURE 4 – DYNAMIC PILI ASSIST WALKING-LIKE MOVEMENTS AGAINST THE MEDIUM FLOW.

A – Example of a newborn swarmer cell of strain *ΔhfsK* moving against the medium flow. The time after cell division is indicated. Mother (M) and daughter (D) are individually labelled. Time point 1 and 2 show the swarmer cell immediately before and after separation from its mother. After 5 min (t3), the cell has moved upstream and after 10 min (t4) the swarmer cell has moved passed its mother. The blue track indicates the trajectory of the cell recorded during its 10 min walk (t4). The cell track matches the trails of holdfast material left behind by the walking cell as shown by fluorescence imaging using the Oregon green labelled lectin wheat germ agglutinin (t5).

B – Representative trajectory of a swarmer cell after birth from its mother (cell separation). The trajectory (blue) was assembled from sequential images of an *ΔhfsK* mutant strain in the microchannel. Step events were identified as fast movements against the flow and are highlighted in red. Black points in the track indicated the time passed from cell separation, in minutes.

C – Distribution of retraction velocities of pili-mediated walking movements on surfaces under flow conditions. The plots show velocity (top) and the average number of step events per minute recorded over time (bottom) in swarmer cells of the *ΔhfsK* mutant strain (n = 56).

D – *C. crescentus* swarmer cells are standing up during movements against medium flow. The tilt angle θ was recorded over time in two representative examples of moving cells as shown in (B). A swarmer cell of the *ΔhfsK*

mutant (upper panel) and of *C. crescentus* wild type (lower panel, NA1000 *hfsA+*) are shown respectively. Movies were recorded at 1 and 0.1 frames per second for wild type and *ΔhfsK* mutant, respectively. Below the charts is shown a schematic of the possible steps in the walking behaviour displayed by *ΔhfsK* mutant. From a horizontal position (1) retraction of an extended pilus pull a cell forward. At the end of pili retraction a cell pull its body aright (2), against the drag force of flowing media (3). When retraction of a pilus is concluded the cell is pushed down by the flow (4) and the cycle can start again

DETERMINING FORCE AND ENERGY OF PILI RETRACTION

To measure the forces generated by pili retraction we made use of optical tweezers. Because *C. crescentus* cells are highly susceptible to phototoxicity elicited by the strong light source used in optical traps, it was not practical to directly immobilize cells with this method. To avoid this problem we exploited the ability of *C. crescentus* predivisional cells to permanently adhere to surfaces via their adhesive holdfast positioned at the pole opposite of the piliated pole. By coupling bacteria to polystyrene beads and immobilizing the beads in the optical trap phototoxicity could be drastically reduced as cells could be kept in the optical trap for at least 1 hour without losing viability and the ability to grow and divide (Figure 5A). By exposing beads carrying predivisional cells to glass surface, pili were able to attach and, upon retraction, displace the beads from the trap (Figure 5A, Supplemental Movie 6). To avoid potential interference from the flagellum, we used a strain lacking the external parts of the rotary motor (*ΔflgDE*).

Figure 5B shows a representative example of an optical trap measurement. Initially, the bead is resting in the optical trap center, with some noise due to Brownian motion. Upon pilus attachment to the surface, Brownian motion decreases followed by bead displacement of up to 1 μm from the center for about 20 seconds before rapidly moving back into its original position (Figure 5B). Occasionally the system backtracked to an intermediate level followed by a renewed movement out of the trap that restored the original displacement. Repeated displacements may represent detachment events of the pilus engaged, followed by the retraction of a second pilus. The varying displacement distance likely reflects the length of the pilus at the onset of the retraction event. The average speed of pili retraction was 100 nm/s (Figure 5C). From the displacement of the beads and the trap stiffness K_{trap} we calculated the maximum force applied ($F = K_{trap} \cdot \Delta x$) at around 8 pN. The force determined by these experiments is proportional to the distance of bead displacement. Since electron microscopy studies showed that pili can reach a maximal length of 5 μm (mean 1.14 ± 0.92 μm; n = 270) (Supplemental Figure 5), most displacement events measured in the optical trap likely underestimate the dynamic range of these structures and, as a consequence, underestimate the maximal force generated by pili retraction.

Cryo-EM reconstruction of the gonococcal Type IVb pilus filament revealed 3.6 subunits per single turn of a 37Å helix [31]. This amounts to a length change for the fiber of 1.05 nm per subunit added or removed. Based on this we calculated that average pili with lengths of 1.14 μm can generate a force of ~8 pN and have a potential energy of $4.5 \cdot 10^{-18}$ J (or 1089 k_BT) during retraction. Assuming a

100% efficiency in energy conversion, we estimate that the pilus machinery would disassemble 20 nm of the filament per ATP hydrolyzed. However, a figure of about 1.0 nm/ATP is more realistic in line with previous structural studies [6], and it results in the pilus machinery having an energy conversion efficiency of around 5%. Thus, one pilus subunit can be assembled/disassembled for each ATP hydrolyzed, which is consistent with the proposed piston model of the pili machinery [32]. Stronger forces measured in our experiments could be achieved if the machinery was more efficient or, alternatively, if multiple pili were employed at the same time.
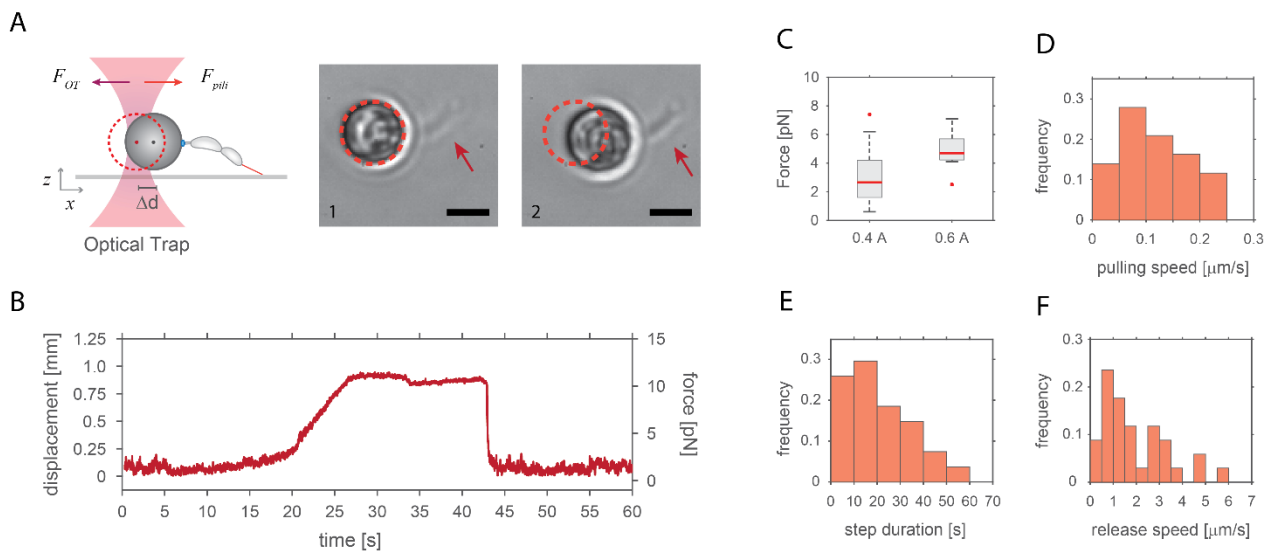

FIGURE 5 – Measurements of pili retraction force and speed using optical tweezers

A – Schematic representation of the experimental setup used for optical trap measurements of pili retraction forces. Beads carrying late predivisional cells attached via their holdfast adhesin were trapped by optical tweezers. Pili extending from the new pole (red) can attach to the glass surface and upon retraction, displace the bead from the trap. The two images show a representative example of a bead with one attached predivisional cell (arrow) of the mutant *ΔflgDE* before (1) and after (2) retraction. The trapped bead is displaced by the retraction of pili by about 1 μm (scale bar: 2 μm).

B – Pili mediated displacement of trapped beads over time. The plot is a representative example of an optical tweezers measurement, showing the displacement and the respective force generated by pili retraction.

C, D– Force and pulling velocity measurements of pili retraction at the optical tweezers. The box plots (C) show the median (red line), 25th and 75th percentiles (bottom and top edges of the box), and most extreme data points (whiskers). Outliers are plotted as red points. The measurements were conducted with the laser power of the optical trap at either 0.4 A (n = 100) or at 0.6 A (n = 11). (for D, laser power at 0.4A).

E - The step duration for pili retraction is defined as the time passed from the start of bead displacement to the moment the bead is released and moves back into the center of the optical trap (n = 28).

F – The chart shows the speed at which the bead moves back into the trap, at the end of a step event (n = 34).

C-DI-GMP INFLUENCES PILI ACTIVITY

In the *C. crescentus* surface sensing activate the diguanylate cyclase DgcB, which boost levels of the second messenger c-di-GMP and trigger rapid surface attachment [21]. We assayed how components of surface sensing can influence pili-mediated colonization to test if c-di-GMP controls pili-mediated attachment. The setup employed is similar to the one described above (see Figure 1), using a flow speed of 0.75 mm/s and different strains, all unable to secrete a holdfast (*hfsA-*). The protein DgcB is a diguanylate cyclase that plays an important role in surface sensing. In the flow channel, the *ΔdgcB* deletion mutant reached the same colonization level as wild type control strain (NA1000 *hfsA-*) (see Figure 6A). However, the attachment rate of *ΔdgcB* was markedly slower. Wild type reached the colonization level of 1500 cells/mm² in about 5 minutes, compared to the 20 min needed for *ΔdgcB*. One possible explanation for the lower rate of attachment is that *ΔdgcB* mutant are less sensitive to surface and pili activity is lower. However, later in the experiment cells entering the microfluidic channel have been exposed to surface for long time, waiting in the upstream tubing (500 μm in width) that connect the microdevice with the reservoir. Inside the tubing cells have time and available surface to activate secondary ways to sense surface and generate a holdfast, and then when reaching the microchannel attach seemingly just like wildtype, which instead senses and attaches on the spot. Deletion of *ΔflgDE* or *ΔmotB* resulted in almost complete abolishment of surface attachment. This suggests that non-motile bacteria in our flow conditions were unable to reach the surface. However, cells of strain *ΔflgDE* occasionally attached which resulted in a slightly higher colonization level compared to *ΔmotB* (see Supplemental Figure 6A). CheY-like Cle proteins can bind c-di-GMP and interact with the motor of the flagellum. Their deletion lowered the colonization levels compared to the control strain (see Figure 6A). We also created strain with mutations in minor pilins, *cc_0832*[E5V] and *cc_2951*[E5V], modifying the critical Glu5 amino acid. A similar mutation in the minor pilin TcpB in *V. cholerae* resulted in decreased retraction of pili [20]. In strain *cc_0832*[E5V] the mutation had no effect on colonization levels, while in *cc_2951*[E5V] it decreased the colonization levels to half that of wild type (see Supplemental Figure 6B).

We also directly manipulated the levels of c-di-GMP inside the cells by regulating the expression of an exogenous diguanylate cyclase (*dgcZ*) in the strain NA1000 *hfsA-* rcdG⁰ *dgcZ* [33]. Without induction intracellular c-di-GMP concentrations were similar to wild type due to leaky expression. However, colonization efficiencies under flow were lower than wild type. Small levels of induction of *dgcZ* increased attachment efficiency, with 0.5 μM of IPTG reaching closest to wild type. Further increase of the intracellular c-di-GMP concentration diminished the density of attached cells in the flow. Induction at 100 μM IPTG, the highest level tested, completely abolished cell attachment. The results suggest that low c-di-GMP concentrations promote pili-mediated surface attachment until a tipping point is reached, after which a further c-di-GMP increase negatively interferes with attachment.
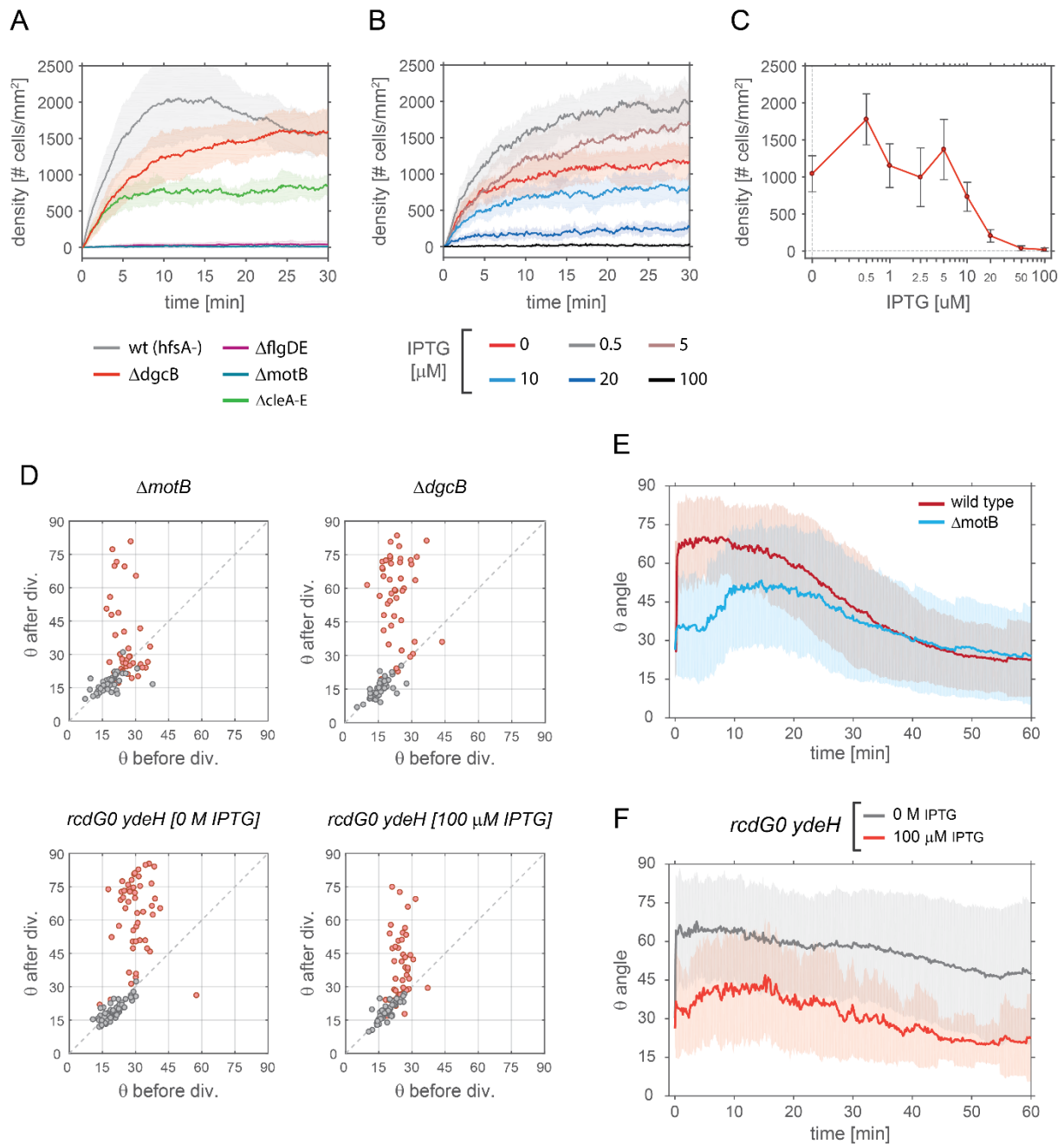
FIGURE 6 – EFFECT OF C-DI-GMP ON ATTACHMENT BEHAVIOUR.

A, B - Pili mediated attachment efficiency in *C. crescentus* is measured as colonization levels at a constant flow of 0.75 mm/s. We tested several deletion mutants (A) and for the strain NA1000 *hfsA-* rcdG⁰ *dgcZ* different levels of c-di-GMP concentrations (B), indicated as different induction levels. Shadow areas correspond to respective standard deviations.

C –Plateau levels of surface colonization with respect to c-di-GMP concentration for the strain NA1000 *hfsA-* rcdG⁰ *dgcZ*. Each point is the average value of colonization levels between minute 10 and 25. Error bars are relative standard deviations.

D –Scatter plots show the average angle *θ* of cells recorded 5 minutes before and 5 minutes after cell division. The results shown were obtained with the strains indicated. (Colouring of swarmer cells are in red, stalked cells are in grey) [*n* = 41 (*ΔmotB*); *n* = 45 (*ΔdgcB*), *n* = 50 (*rcdG0 dgcZ* [0 M]); *n* = 46 (*rcdG0 dgcZ* [1 μM])].

E, F – Dynamics of pili-mediated standing up of swarmer cells. The chart shows the time evolution of the angle *θ* in daughter cells of *C. crescentus* wild type (wt) and *ΔmotB* (E) and rcdG⁰ *dgcZ* with IPTG concentrations of 0 and 100 μM (F). Time zero corresponds to moment of separation of mother and daughter cells. [E: *n* = 98 (wt); *n* = 41 (*ΔmotB*); F: *n* = 50 (*rcdG0 dgcZ* [0 M]); *n* = 46 (*rcdG0 dgcZ* [1 μM])].

We also quantified the movements of newborn swarmer cells into an upright position, as described above (Figure 6D). The $\Delta dgcB$ mutant strain behaved similar to wild type, but a higher proportion of cells had intermediate θ after division, between 30° to 60° degrees. The measured tilt angles of cells in from this strain were generally slightly lower compared to wild type but followed the same trend (Supplemental Figure 6C). In contrast, $\Delta motB$ swarmer cells had low θ value after cell division and only a few cells stood up above 60° degrees. Interestingly, this initial low θ value increased 5-10 minutes after cell division and then followed similar values as wild type (Figure 6E). This suggests that pili activation may be delayed.

The effect of c-di-GMP on the standing up behaviour was tested with the strain NA1000 $hfsA$- rcdG^0 $dgcZ$. Without induction (0 M IPTG), the tilt angle in the 5 minutes after division was similar to wild type. Inducing $dgcZ$ with 100 μM IPTG resulted in intermediate θ values, rarely above 60° (Figure 6D). Different expression levels of $dgcZ$ also influenced the time evolution of the tilt angle (Figure 6F). No induction (0 M IPTG), resulted in cells standing up for longer than 10-15 minutes. After 1 hour the average tilt angle in the population was still about 45° degrees, compared to an average θ value of 20° degrees for wild type. Induction levels of with 100 μM IPTG resulted in almost the opposite phenotype. Swarmer cells were able to stand up, but only at low θ values between 20° and 45° degrees.

Discussion

At the late predivisional stage compartmentalization between stalked and swarmer cells has already occurred and all components of the pili machinery are expressed [12, 30]. Our results show that pili machineries are already assembled and operating before cell separation. Pili retraction can pull the new pole away from the stalked pole, supporting surface sensing (Fig 3). The short surface residence time of swarmer cells (Fig 1) suggests that pili mediate transient surface contact, offering a short time window for holdfast to be formed in order to irreversibly glue cells to the surface. Swarmer cells obtain upright position when, probably, multiple surface attached pili are pulling in different direction at the same time. The cell pole is forced down on the surface and may acts like a hinge, thereby rotating the cell body into an upright position. Despite the drag forces inflicted by the flow, the constant force of retracting pili maintains cells in such position, regardless of the presence of holdfast (see Fig 2C and Supplemental Movie 1). Pili-mediated attachment and retraction optimally positions the pole on the surface for tactile sensing and rapid anchoring of the holdfast for permanent attachment [21].

Our results show that cells able to attach at higher flow rates were able to remain attached longer (Supplemental Figure 1A,B). In response to the drag force experienced by flow pili fibers may undergo conformational changes that strengthen the interaction with the surface. In line with this hypothesis in *N. gonorrhoeae* tensional stresses bring conformational changes that expose new epitopes in the filament [34, 35]. Moreover, a bimodal behaviour has been reported to occur for the adhesion of FimH Type 1 pili of *Escherichia coli* [36].

We were able to observe walking-like behaviour in the *C. crescentus* mutant *ΔhfsK*, by weakening the holdfast and applying flow to force cells to orient the leading/piliated pole upstream. The ability of *C. crescentus* to walk after only a single mutation in the holdfast machinery was surprising, considering that twitching and walking have only been observed in bacteria expressing Type IVa pili. The upstream direction of walking when subjected to laminar flow has been reported in studies where *P. aeruginosa* exhibits an upstream zig-zag motion [37]. The reorientation induced by the flow, coupled with the polar localization of pili explains the directed walk. Our results suggest that for simple walking upright to evolve, bacteria need only to localize pili at one pole. Stochastic cycles of elongation and retraction may then be sufficient for a random walk on a surface. Cells must coordinate pili to ensure one pilus remain attached to the surface at any time, in order to prevent removal by flow. *C. crescentus* cannot do that, which is demonstrated by the small residence time and lack of walking behaviour in *hfsA-* strain (see Supplemental Movie 1). However, the *ΔhfsK* mutant can use the lower cohesion holdfast function as an weak anchor, avoiding the need of coordinating pili activity.

Using the *ΔhfsK* mutant with its weakly coherent holdfast we could demonstrate that pili remain active after holdfast production and our results suggest they are capable of multiple cycles of elongation/retraction within a window of 10-20 minutes after cell separation and attachment. These

results suggest that holdfast secretion does not lead to pili removal. Instead, the removal of the pili machinery may simply be a consequence of cell cycle progression and the motile-sessile switch [12].

Lastly, our results suggest that pili retraction may be directed by the intracellular levels of c-di-GMP. Interestingly, deletion of *motB* has major effects. Pili-mediated standing up is not abolished, but instead delayed (Figure 6E). Swarmer cells might fail to stand up after division due to an inability to rise intracellular levels of c-di-GMP upon surface contact [21]. However, c-di-GMP levels increase over time due to cell cycle progression, activating pili at later point. The *ΔdgcB* mutant which fails to raise c-di-GMP in response to surface contact [21] displays only marginally lower pili activity than wild type (Figure 6D and F). This suggests that some other downstream effectors may regulate pili activity. Our results also show that low levels of c-di-GMP improve pili mediated attachment (Figue 6B) and retraction (Figure 6F). On the other hand, higher c-di-GMP levels have the opposite effect (Figure 6B and 6F). Taken together those results may suggest that a newborn swarmer cell having low intracellular levels of c-di-GMP can express and extend pili but upon surface contact the c-di-GMP levels rise to some intermediate levels or locally at the flagellated pole which could promote surface attachment and pili retraction. As the cell cycle progresses, intracellular c-di-GMP rises up to levels that may signal cells to disassemble the pili machineries.

Methods

Bacterial Strains and growth conditions

The wild type (*wt*) strain of reference was *NA1000 hfsA+*, which have functional pili and holdfast. *NA1000* is a lab adapted strain with a point mutation in gene *hfsA*, which makes it unable to secrete the holdfast, therefore the functional gene was reintroduced (*hfsA+*). Strain *NA1000 hfsA+ ΔcreS* produce rod-shaped cells, due to deletion of crescentin gene. Deletion of the major pilin subunit, *NA1000 hfsA+ ΔpilA,* make cells unable to secrete pili fibers. However, in the flow channel setting the attachment efficiency was extremely low. Therefore, the strain *NA1000 hfsA+ ΔflgDE ΔpilA* was used for testing the absence of pili. The train *NA1000 hfsA+ ΔflgDE*, resulting in cells without flagellar filaments, due to deletion of flagellar hook genes, was used as control.

NA1000 hfsA+ rcdG0 dgcZ ΔhfsK is a mutant which secrete a holdfast having lower cohesion, resulting in weaker surface attachment. To tune the amount of holdfast generated, the *hfsK* deletion was engineered in a strain that allowed to modulate intracellular levels of c-di-GMP, the primary allosteric regulator of the holdfast secretion machinery [29, 33]. The lack of cdGMP cyclases (*rcG0*) is compensated by the presence of exogenous *dgcZ*, which was regulated by a *lac*-promoter.

Cultures of *C. crescentus* were grown overnight at 30°C in PYE media, under agitation. They were then diluted and regrown to exponential phase, at OD_{660} = 0.2-0.3. The culture was then used for experiments in microfluidic devices, which were all conducted at room temperature.

Microfluidic devices

Masters were fabricated via standard photolithography protocols [38]. PDMS (polymethyldisiloxane) device were created via replica molding, and then aged via heat treatment, placing them on hotplate at 150°C for 30 min [39]. This treatment increases the hydrophilicity of microchannel walls during experiments. Holes were drilled at inlet(s) and outlet(s), devices were treated in oxygen plasma and covalently bound onto borosilicate cover glass. To supply the fluids inside microfluidic devices one end of a PTFE microtube (0.56 x 1.07 mm, Fisher Scientific) was connected to an inlet/outlet. The other end was connected to a 1 mL plastic syringe (Soft-ject, Henke-Sass, Wolf), via a needle (23G, 0.6 x 30 mm, BraunMelsungen AG). All microflow experiments were conducted in single microchannel device having a height of 20 μm and a width of 100 μm.

Microfluidics and microscopy setup

Microfluidic devices were placed on the stage of an inverted microscope (IX81, Olympus GMBH). For the colonization experiments (see Fig 1), cultures were grown at precisely OD_{660} = 0.15 and loaded in a syringe. The latter was connected to the device and mounted on a syringe pump (neMESYS low pressure module V2, 14:1 gear; Cetoni GMBH). The flow was initially set at 25 mm/s for 5 min to

ensure that the microchannel surface was devoid of cells. Then time lapse recording was started and the flow was set to the desired target flow for a duration of 30-45 minutes. The flow was then switched back at 25 mm/s to test the detachment behaviour for 15 min. During the whole procedure images were recorded at 0.1 fps, using 40x oil immersion objective. In order to ensure that the concentration of supplied cell did not vary, always new batch of culture at OD660 of 0.15 was used to conduct each single experiment.

For experiments of single cell division events, the cells were loaded in the device and left to colonize the surface to a level where the average distance between cells was ≥15 µm. This colonization required 2-10 min, depending on the attachment efficiency of the strain being used. This ensured that single cell division events would not be influenced by neighbouring cells. A syringe supplied fresh media from the inlet at a steady flow of 1 mm/s. Cells were left to growth for 1-2 h before starting recording image sequences at 1 or 5 fps, using a 100x oil immersion objective. The experiments were conducted for no more than 10-12 h. This procedure ensured steady growth conditions and no overgrowth/clogging in the inlet (see Supplementary Figure 5).

Optical Tweezers setup and force measurements

The optical tweezers experiments were performed on a custom built bright field microscope, complemented with a laser diode setup (LD830-MA1W, $\lambda = 830$ nm, Thorlabs). A water immersion, high aperture objective (UPlanSApo 60x water, Olympus) was used to focus the laserbeam, trap the beads with attached bacteria, and image the fluctuations of the bead in the trap and the attached bacteria. The experiments were carried out in position clamp mode at a constant laser power. The images of the bead and the attached cell were recorded with 50 Hz and 75 Hz using a fast camera (Phantom Miro EX4, Vision Research Inc.). The images were used to determine the position change of the bead during the experiment and observe the active cell.

Calibration of the optical tweezers was carried out via fluctuation calibration. For each laser power used, an image sequence of a bead in the trap was recorded at 1000 Hz. From the fluctuation of the bead in the trap the variance σ was determined. The trap stiffness K_{trap} was calculated as: $K_{trap} = k_B T / \sigma^2$, with k_B the Boltzmann constant and T the room temperature.

An exponential culture of *NA1000 hfsA+ ΔflgDE* at OD660 of 0.2 was mixed with polystyrene beads (Fluoresbrite YG Carboxylate Microspheres 3.00 um, Polysciences) to a final concentration of $1.7 \cdot 10^8$ beads per mL cell suspension. The mix was let stand for 2 min, allowing the time for cells to attach to the beads. Then a 1:1 dilution with fresh PYE was injected into the device, end experiments conducted in condition of no flow inside the device. Devices used for optical tweezers measurements had chambers at the side of a main channel [38, 40] connected by an opening of less than 10 µm. Single bead-carrying predivisional cells were chosen and placed inside the chambers where the optical tweezers measurements could be performed undisturbed by other cells.

Image analysis

Cell outline detection was carried out using Matlab-based program microbeTracker [41]. Further tracking, analysis and statistics were carried out with in-house developed Matlab scripts. Cell outline was fitted to an ellipse and we extracted the value ε, which is the eccentricity of the ellipse, the ratio between its the major and minor axes. We used the eccentricity to get the inclination of cells in respect of the surface, angle θ. We place an ε value of 1 for to be an angle θ of 90° and an ε value of 0.1 to be a tilt of 0°. Eccentricity value below 0.1 can be excluded as they represent very elongated ellipse, with a ratio length-to-width ratio that do not occur for single *C. crescentus* cells.

To track the trajectories of cell we choose to follow the position of the holdfast. This position would lie in a point between a vertex and a focus of the ellipse which fit the 2D projection of the cell. The position was dependent on ε, such that as the cell is upright, it coincides with the focus, and the cell lies flat, it is the close to the vertex (see Fig 4 A).
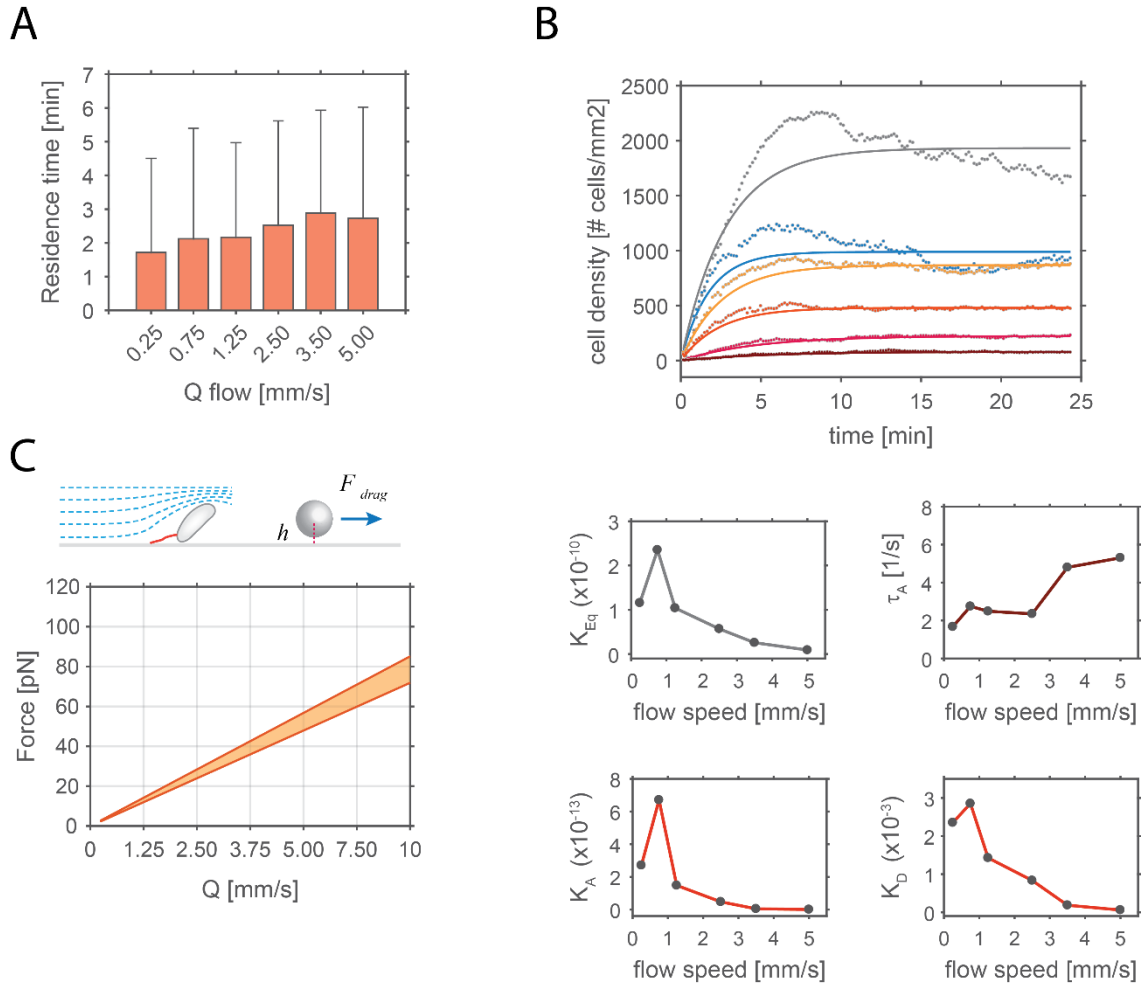
Step events in the trajectories of *ΔhfsK* strain (see Fig 4 B and C) were determined as the time windows when fast upstream advancements (in the x-axis direction) occurred.

Acknowledgements

Supplemental Figures

A

B

C

A – *Average time of residence of single cell on a surface via pili* - Pili mediate transient attachment to glass surface. Bar chart showing the average residence time on surface for swarmer cells having pili, but no holdfast (strain NA1000 *hfsA-*), under different flow rates. There is no statistically relevant difference between different flow velocities.

B – *Modelling after a Langmuir adsorption process* - The upper chart shows the colonization behaviour at different flow rates (dots) with the respective fitting after Langmuir adsorption isotherm process. The 4 lower charts show the extrapolated reaction constants (K_{eq}, K_A and K_D) and time constant (τ_A).

C – *Theoretical drag force near a surface* - The graph shows the theoretical drag force experienced by a typical swarmer cell and stalked cell attached to a surface at different flow rates. The drag force is calculated using the equation shown below. The equation the drag force experienced by a sphere near a surface, with a volume equal to the average swarmer (orange) or stalked cell (red). The two areas show the range for the sphere having a distance from the surface (h) ranging from 0 to 0.5 um.

$$F_{Drag} = \frac{3\pi \, a \, \mu \, u_z}{2 \, (- \frac{0.0625 \, a^5}{h^5} - \frac{0.1758 \, a^4}{h^4} + \frac{0.125 \, a^3}{h^3} - \frac{0.5625 \, a}{h} + 1)}$$

(a = radius of the sphere with equivalent volume ≈ 0.62 μm³ for swarmers and ≈ 0.71 μm³ for stalked cells, h = height from the surface, μ = viscosity, u_z = flow velocity at height h from the surface). Equation eq 7-4.37 from [42].

SUPPLEMENTAL FIG 2
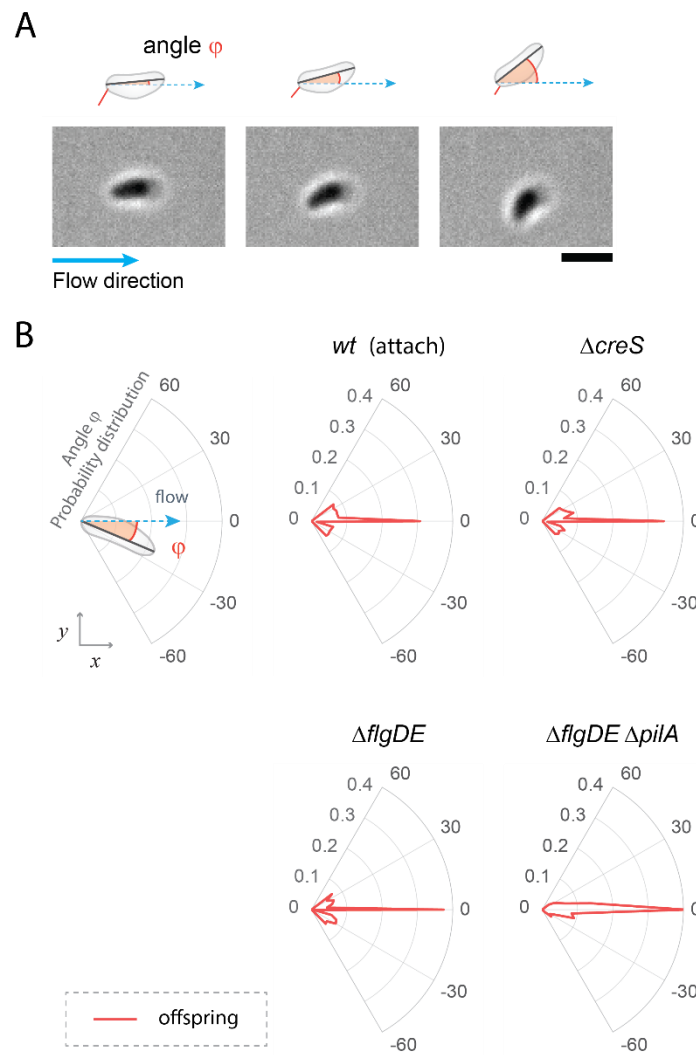
A – Image sequence interval of a swarmer cell reorienting its body away from flow lines due to the activity of polar pili. A schematic representation of the cell positioning and the angle ϕ is shown above the images.

B – Polar plots showing the distribution of angle ϕ in swarmer cells during a five-minute window after cell division. The angle ϕ describes the angle between the cell body axis and the flow line and changes in ϕ indicate the deviation from the flow. *C. crescentus* wild type cells (attach) show a prominent peak at 0°, since cells spend most of the time in a position parallel to flow lines. However, cells are able to deviate from this position and reorient their body with an angle of up to ±40°. The same trend can be observed for *ΔcreS* and *ΔflgDE* strains. In contrast, a *ΔflgDE ΔpilA* strain shows a much narrower distribution around 0°, indicating that cells lacking pili are unable to actively reorient.

[wt (attach), *n* = 130; wt (swim), *n* = 119; *ΔcreS*, *n* = 56; *ΔflgDE*, *n* = 57; *ΔflgDE ΔpilA*, *n* = 75] (scale bar in A and C is 2 μm)

SUPPLEMENTAL FIG 3
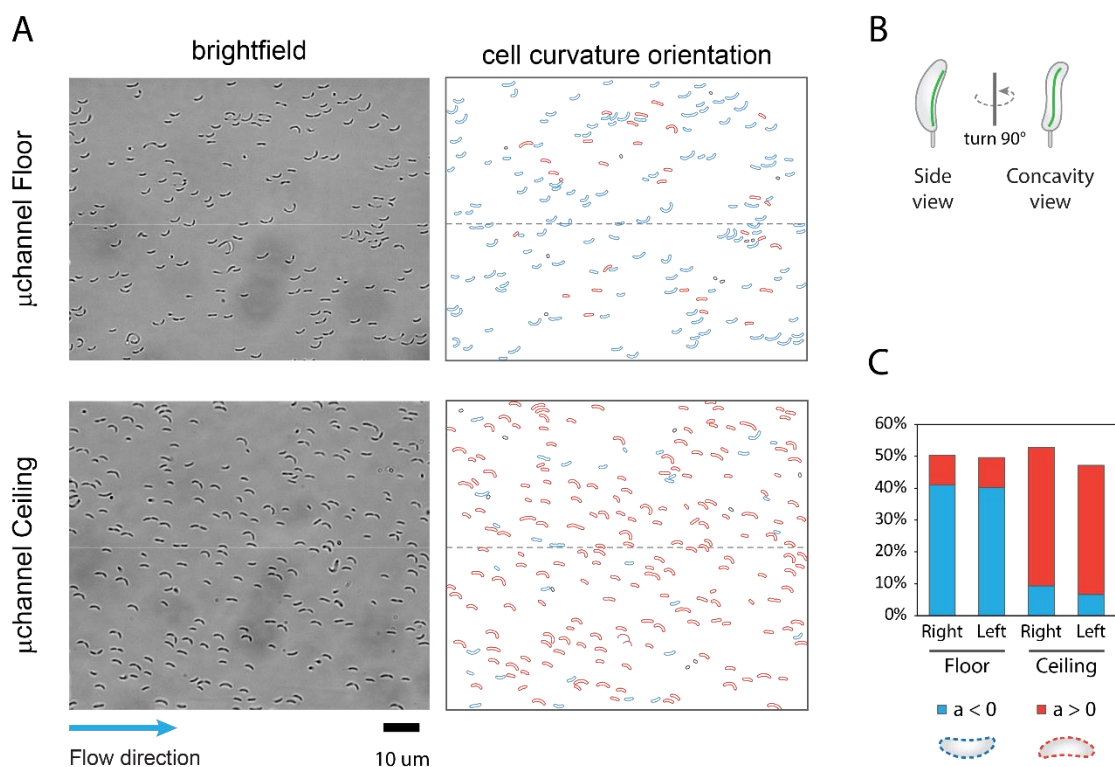
A – Bright field images of *C. crescentus* cells attached to the floor and ceiling of a microfluidic channel. Cells with the concavity oriented to the right in the direction of the flow are shown in red, while cells oriented to the left are shown in blue.

B – Schematic drawing show the proposed cell shape of crescentoid *C. crescentus* with a small left-handed twist.

C – The chart shows the result of the analysis of three independent experiments with cells scored on ≥ 0.3 mm², for both ceiling and floor surfaces of a device. Concavity distribution is also scored also in respect of cells position: the right half or left half of the channel, have the same concavity distribution.

A

B — Tilt angle before, during and after a step

before   *during*   *after*
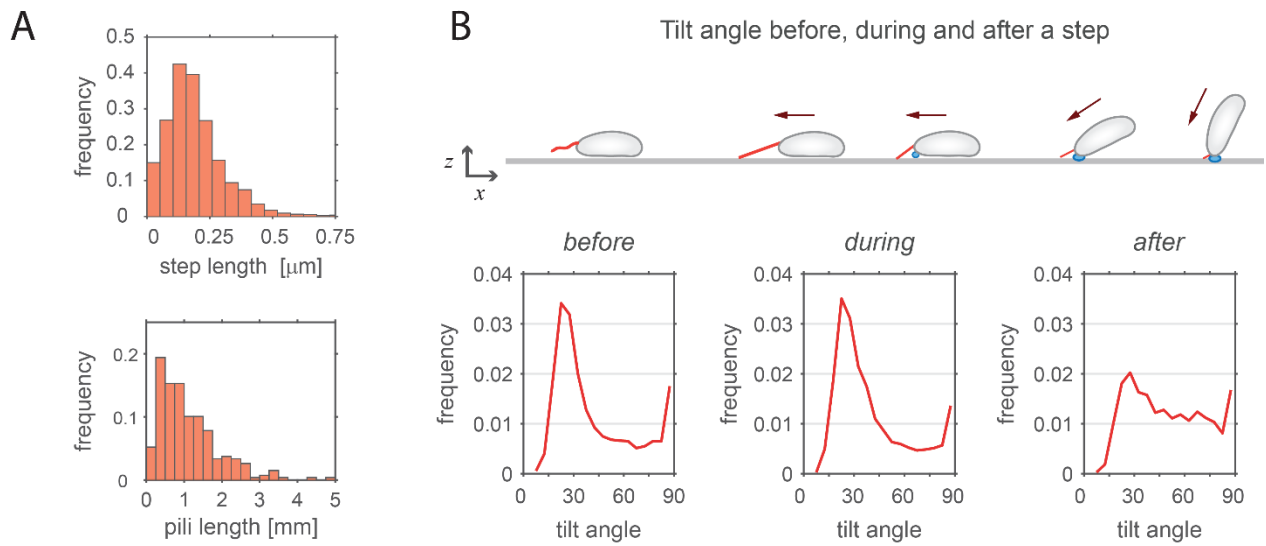
A – Upper plot show the step length distribution for NA1000 ΔhfsK mutant strain (n = 56). The lower plot shows the distribution of pili length in wild type strain observed at TEM (n = 271). Cells in a planktonic culture where fixed with 0.1% glutaraldehyde and then spotted on a grid for electron microscope. Samples were then washed with water and negatively-stained with 0.5% uranyl acetate. Images taken at the TEM were visually inspected to locate cell-attached pili and measure their length.

B – Schematic drawing of a *C. crescentus* swarmer cell moving against the medium flow and the standing upright at the end of each dislocation step. Pili (red), holdfast (blue) and cell movement (red arrow) are indicated. The charts below the graph show the distributions of tilt angle values five seconds before (left), during (middle) and five seconds after (left) a step event. Three different flow velocities were analysed. Before and during a step event cells lie flat on the surface, while standing up upon completion of an upstream movement.

SUPPLEMENTAL FIG 5
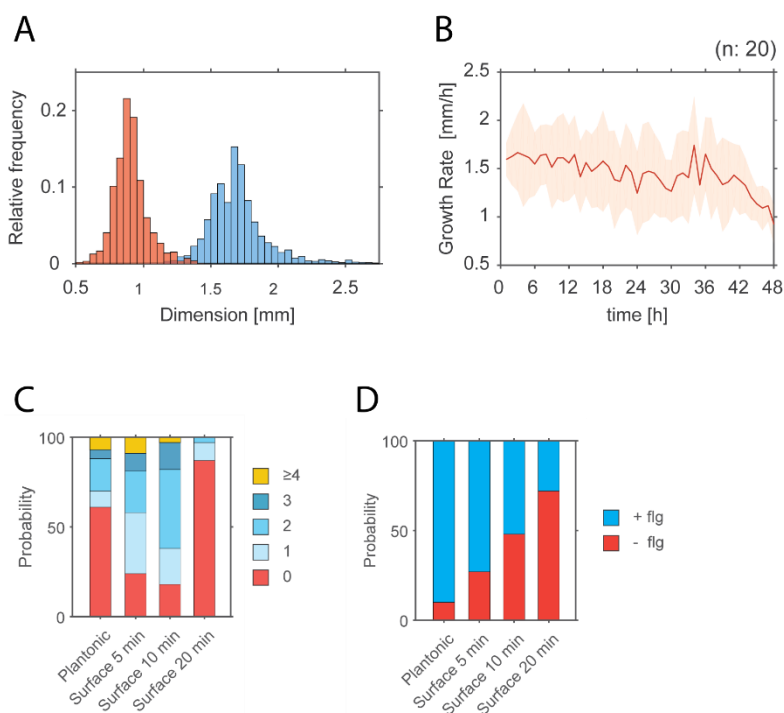
A – Distribution of the cell diameter (red) and cell length (blue) of swarmer cells at the time of separation from their stalked mothers ($n = 130$).

B – Growth rate of individual cells in a microfluidic device for 3 days (n = 20). Cells of *C. crescentus* strain NA1000 *hfsA*[+] *ΔpilA* attached the surface of a microfluidic channel were grown for three consecutive days under constant imaging conditions and imaged at 0.5 fpm. The red line is the average and the opaque area is the standard deviation. The results show no significant decrease in growth rate in the first 24 hours.

C and D – Number of pili (C) and the presence of flagellum (D) observed at the pole of individual *C. crescentus* swarmer cells. A cell culture was fixed with 0.1% glutaraldehyde while still in a planktonic culture, or after being spotted on the TEM grid for 5, 10 and 20 min, in order to allow them to make surface contact. Samples were then washed with water and negatively-stained with 0.5% uranyl acetate. Images taken at the TEM were visually inspected to locate swarmer cells, defined as cells with length <2.4 μm. Cells were categorized in five different classes according to the number of pili (C) and the presence of attached flagellum flagellum was recorded (D).
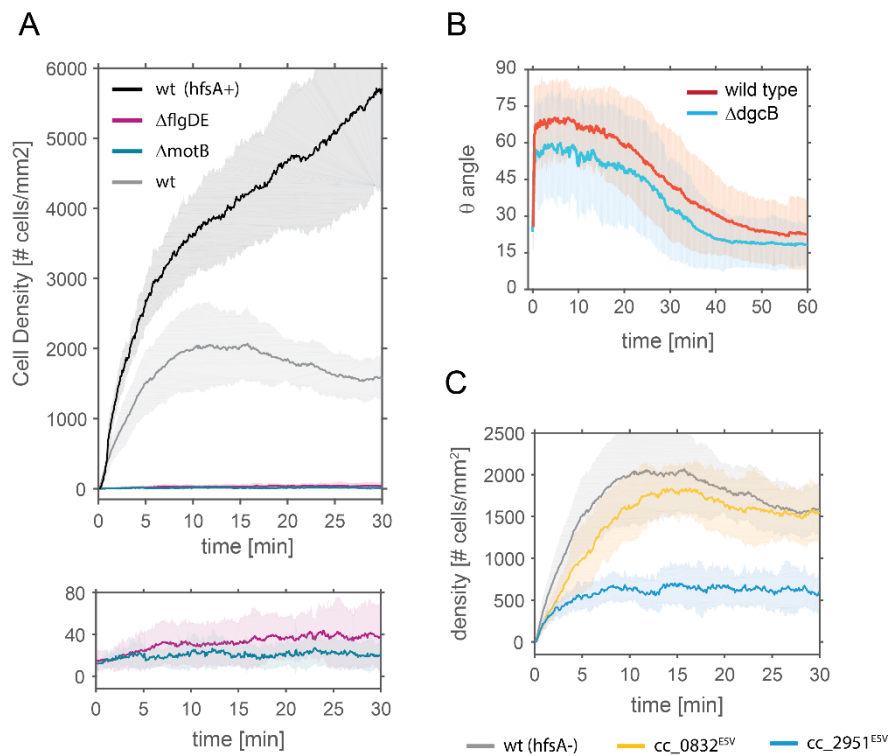
A – The chart is the same shown in Figure 6A. Wider y-axis range allow to appreciate differences in attachment levels between strains without a holdfast (NA1000 *hfsA-*) and strains capable with a holdfast (NA1000 *hfsA+*). In the lower part is shown an enlarged view of *ΔmotB* and *ΔflgDE* strain.

B - Dynamics of pili-mediated standing up of swarmer cells. The chart shows the time evolution of the angle *θ* in daughter cells of *C. crescentus* wild type (NA1000 *hfsA-*), and *ΔdgcB* mutant strain. Time zero corresponds to the time when mother and daughter cells separate. (n = 98 (wt); n = 45 (*ΔdgcB*)).

C – The chart show the colonization levels in strain *cc_0832* [E5V] and *cc_2951* [E5V]. Both have single amino acid substitution for the highly conserved Glu5 at N-terminal. Wild type (NA1000 *hfsA-*) is reported as control.

References

1. Giltner CL, Nguyen Y, Burrows LL. 2012. Type IV Pilin Proteins: Versatile Molecular Modules. *Microbiol. Mol. Biol. Rev.* 76(4):740–72

2. Hospenthal MK, Costa TRD, Waksman G. 2017. A comprehensive guide to pilus biogenesis in Gram-negative bacteria. *Nat. Rev. Microbiol.* 15(6):365–79

3. Craig L, Pique ME, Tainer JA. 2004. Type IV pilus structure and bacterial pathogenicity. *Nat. Rev. Microbiol.* 2(5):363–78

4. Merz AJ, So M, Sheetz MP. 2000. Pilus retraction powers bacterial twitching motility. *Nature.* 407(6800):98–102

5. Skerker JM, Berg HC. 2001. Direct observation of extension and retraction of type IV pili. *Proc. Natl. Acad. Sci.* 98(12):6901–4

6. Chang YWY-W, Rettberg LA, Treuner-Lange A, Iwasa J, Sogaard-Andersen L, et al. 2016. Architecture of the type IVa pilus machine. *Science (80-.).* 351(6278):aad2001-aad2001

7. Chang YW, Kjær A, Ortega DR, Kovacikova G, Sutherland JA, et al. 2017. Architecture of the Vibrio cholerae toxin-coregulated pilus machine revealed by electron cryotomography. *Nat. Microbiol.* 2(February):

8. Gold VAM, Salzer R, Averhoff B, Kühlbrandt W. 2015. Structure of a type IV pilus machinery in the open and closed state. *Elife.* 4(MAY):1–12

9. McCallum M, Tammam S, Khan A, Burrows LL, Lynne Howell P. 2017. The molecular mechanism of the type IVa pilus motors. *Nat. Commun.* 8(May):1–10

10. Pelicic V. 2008. Type IV pili: e pluribus unum? *Mol. Microbiol.* 68(4):827–37

11. Tomich M, Planet PJ, Figurski DH. 2007. The tad locus: postcards from the widespread colonization island. *Nat. Rev. Microbiol.* 5(5):363–75

12. Skerker JM, Shapiro L. 2000. Identification and cell cycle control of a novel pilus system in Caulobacter crescentus. *EMBO J.* 19(13):3223–34

13. Conrad JC, Gibiansky ML, Jin F, Gordon VD, Motto DA, et al. 2011. Flagella and pili-mediated near-surface single-cell motility mechanisms in P. aeruginosa. *Biophys. J.* 100(7):1608–16

14. Berry J-LL, Pelicic V. 2015. Exceptionally widespread nanomachines composed of type IV pilins: The prokaryotic Swiss Army knives. *FEMS Microbiol. Rev.* 39(1):134–54

15. Schilling J, Wagner K, Seekircher S, Greune L, Humberg V, et al. 2010. Transcriptional activation of the tad type IVb pilus operon by PypB in Yersinia enterocolitica. *J. Bacteriol.* 192(14):3809–21

16. Kachlany SC, Planet PJ, DeSalle R, Fine DH, Figurski DH, Kaplan JB. 2001. flp-1, the first representative of a new pilin gene subfamily, is required for non-specific adherence of Actinobacillus actinomycetemcomitans. *Mol. Microbiol.* 40(3):542–54

17. Wang Y, Haitjema CH, Fuqua C. 2014. The Ctp type IVb pilus locus of Agrobacterium tumefaciens directs formation of the common pili and contributes to reversible surface attachment. *J. Bacteriol.* 196(16):2979–88

18. Nykyri J, Mattinen L, Niemi O, Adhikari S, Kõiv V, et al. 2013. Role and Regulation of the Flp/Tad Pilus in the Virulence of Pectobacterium atrosepticum SCRI1043 and Pectobacterium wasabiae SCC3193. *PLoS One.* 8(9):e73718

19. Bernier SP, Hum C, Li X, O'Toole GA, Magarvey NA, Surette MG. 2017. Pseudomonas aeruginosa-derived rhamnolipids and other detergents modulate colony morphotype and motility in the Burkholderia cepacia complex. *J. Bacteriol.* 199(13):1–15

20. Ng D, Harn T, Altindal T, Kolappan S, Marles JM, et al. 2016. *The Vibrio cholerae Minor Pilin TcpB Initiates Assembly and Retraction of the Toxin-Coregulated Pilus*, Vol. 12. 1-31 pp.

21. Hug I, Deshpande S, Sprecher KS, Pfohl T, Jenal U. 2017. Second messenger–mediated tactile response by a bacterial rotary motor. *Science (80-.).* 358(6362):531–34

22. Ellison CK, Kan J, Dillard RS, Kysela DT, Ducret A, et al. 2017. Obstruction of pilus retraction stimulates bacterial surface sensing. *Science (80-.).* 358(6362):535–38

23. Viollier PH, Sternheim N, Shapiro L. 2002. Identification of a localization factor for the polar positioning of bacterial structural and regulatory proteins. *Proc. Natl. Acad. Sci.* 99(21):13831–36

24. Li G, Brown PJB, Tang JX, Xu J, Quardokus EM, et al. 2012. Surface contact stimulates the just-in-time deployment of bacterial adhesins. *Mol. Microbiol.* 83(1):41–51

25. Persat A, Stone H a, Gitai Z. 2014. The curved shape of Caulobacter crescentus enhances surface colonization in flow. *Nat. Commun.* 5(May):3824

26. Berne C, Ma X, Licata NA, Neves BRA, Setayeshgar S, et al. 2013. Physiochemical

Properties of Caulobacter crescentus Holdfast: A Localized Bacterial Adhesive. *J. Phys. Chem. B.* 117(36):10492–503

27. Marks ME, Castro-Rojas CM, Teiling C, Du L, Kapatral V, et al. 2010. The genetic basis of laboratory adaptation in Caulobacter crescentus. *J. Bacteriol.* 192(14):3678–88

28. Mignolet J, Panis GL, Viollier PH. 2018. More than a Tad: spatiotemporal control of Caulobacter pili This review comes from a themed issue on Cell regulation. *Curr. Opin. Microbiol.* 42:79–86

29. Sprecher KS, Hug I, Nesper J, Potthoff E, Mahi M-A, et al. 2017. Cohesive Properties of theCaulobacter crescentusHoldfast Adhesin Are Regulated by a Novel c-di-GMP Effector Protein. *MBio*. 8(2):1–15

30. Judd EM, Ryan KR, Moerner WE, Shapiro L, McAdams HH. 2003. Fluorescence bleaching reveals asymmetric compartment formation prior to cell division in Caulobacter. *Proc. Natl. Acad. Sci. U. S. A.* 100(14):8235–40

31. Craig L, Volkmann N, Arvai AS, Pique ME, Yeager M, et al. 2006. Type IV Pilus Structure by Cryo-Electron Microscopy and Crystallography: Implications for Pilus Assembly and Functions. *Mol. Cell*. 23(5):651–62

32. Maier B, Wong GCL. 2015. How Bacteria Use Type IV Pili Machinery on Surfaces. *Trends Microbiol.* 23(12):775–88

33. Abel S, Bucher T, Nicollier M, Hug I, Kaever V, et al. 2013. Bi-modal distribution of the second messenger c-di-GMP controls cell fate and asymmetry during the caulobacter cell cycle. *PLoS Genet.* 9(9):e1003744

34. Kolappan S, Coureuil M, Yu X, Nassif X, Egelman EH, Craig L. 2016. Structure of the neisseria meningitidis type IV pilus. *Nat. Commun.* 7:1–12

35. Biais N, Higashi DL, Brujic J, So M, Sheetz MP. 2010. Force-dependent polymorphism in type IV pili reveals hidden epitopes. *Proc. Natl. Acad. Sci.* 107(25):11358–63

36. Sauer MM, Jakob RP, Eras J, Baday S, Eriş D, et al. 2016. Catch-bond mechanism of the bacterial adhesin FimH. *Nat. Commun.* 7:

37. Shen Y, Siryaporn A, Lecuyer S, Gitai Z, Stone HA. 2012. Flow directs surface-attached bacteria to twitch upstream. *Biophys. J.* 103(1):146–51

38. Deshpande S, Pfohl T. 2012. Hierarchical self-assembly of actin in micro-confinements using microfluidics. *Biomicrofluidics*. 6(3):1–13

39. Göllner M, Toma AC, Strelnikova N, Deshpande S, Pfohl T. 2016. A self-filling microfluidic device for noninvasive and time-resolved single red blood cell experiments. *Biomicrofluidics*. 10(5):1–11

40. Deshpande S, Pfohl T. 2015. Real-time dynamics of emerging actin networks in cell-mimicking compartments. *PLoS One*. 10(3):1–19

41. Sliusarenko O, Heinritz J, Emonet T, Jacobs-Wagner C. 2011. High-throughput, subpixel precision analysis of bacterial morphogenesis and intracellular spatio-temporal dynamics. *Mol. Microbiol.* 80(3):612–27

42. Happel J, Brenner H. 1981. *Low Reynolds number hydrodynamics*, Vol. 1. Dordrecht: Springer Netherlands

CHAPTER 3

_____

LAVENTIE B.J. ET AL., 2018

Touch-Seed-and-Go: Surface-induced asymmetric colonization program of Pseudomonas aeruginosa

Benoît-Joseph Laventie [1], Matteo Sangermani [1], Etienne Meunier [10] , Pablo Manfredi [1], Isabelle Hug [1], Tina Jaeger [1], Isabella Santi [1], Petr Broz[1], Urs Jenal [1]*

[1] Focal Area Infection Biology, Biozentrum, University of Basel, Basel, Switzerland

[0] Present address: IPBS - UMR 5089, Toulouse, France

* Corresponding author: Urs Jenal, urs.jenal@unibas.ch

Abstract

The human pathogen *Pseudomonas aeruginosa* activates its virulence program upon interaction with surfaces. Recent findings suggested that Type IV pili transduce surface-mediated mechanical stimuli to induce virulence gene expression. Here we investigate how *P. aeruginosa* adapts when it switches from a free swimming to the surface associated state. We find that within seconds after surface encounter *P. aeruginosa* increases the level of the second messenger cyclic-di-GMP (c-di-GMP). C-di-GMP activates the newly discovered receptor FimW (PA4958, K_d = 50 nM) that dimerizes and re-localizes to the cell poles. Polar localization of FimW depends on a functional flagellum and Type IV pili. At the cell poles, FimW controls T4P dynamics to promote surface adherence and the vertical standing up of cells. This allows *Pseudomonas aeruginosa* to "walk" upright and rapidly explore the surface. Upon division of surface grown cells, FimW asymmetrically positions to the poles of only one daughter cell, while it becomes cytoplasmically distributed in the other progeny. Asymmetric positioning of FimW after cell division is driven by the c-di-GMP degrading enzyme Pch which is asymmetrically inherited by the flagellated daughter, triggering its detachment from the surface. Lastly, our cell infection data suggest a role for FimW in surface induced-virulence via T4P regulation. Together, our data support a model where *P. aeruginosa* surface contact rapidly activates FimW that asymmetrically positions to the cell poles during cell division to regulate T4P for virulence induction.

Introduction

Bacteria have evolved strategies to optimize survival by securing access to nutrients and energy supplies and by protecting themselves from assaults by predators or environmental strain. While goods can be available in solution, nutrients are often associated with surfaces on marine particles, plants or mammalian tissue. Likewise, surfaces offer the ability to form structured consortia, so-called biofilms, that protect individual cells from damage by chemical or physical impact or from phagocytosis. While it is clear that bacteria thrive on surfaces, our knowledge on how they colonize surfaces and how and how quickly they are able to respond to surface encounter is still fragmentary. To reach and explore surfaces bacteria utilize nanomachines like the rotary flagellum or dynamic pili, which in combination with chemosensory systems direct cells towards favourable conditions. Surface attached bacteria exploit flagella to swarm on moist surfaces or use Type IV pili (T4P) to spread on the solid substratum. T4P dynamics is driven by the sequential extension and retraction of individual pili, a process that is catalyzed by specific ATPases. The opportunistic human pathogen *Pseudomonas aeruginosa* uses T4P for at least two distinct types of surface motility: twitching and walking. Twitching cells crawl over the surface with strict directionality that warrants them to explore larger surface areas (Burrows, 2012). In contrast, walking bacteria move laterally in an upright position and with high instantaneous velocity, allowing them to quickly explore a more local surface area (Conrad et al., 2011). In addition to their important role in surface-based motility, T4P act as primary surface adhesins to overcome repulsive van der Waals, electrostatic and hydrophobic forces and to help anchoring cells on a very wide variety of abiotic and biotic surfaces (Bruzaud et al., 2015; Burrows, 2012; Toutain et al., 2007).

Surface attachment not only changes the motility behavior of pathogenic bacteria but also seems to activate their virulence program. Recent studies demonstrated that *P. aeruginosa* responds to non-specific mechanical cues to turn on virulence gene expression (Persat et al., 2015; Siryaporn et al., 2014). These studies also proposed a model where mechanical activation of virulence requires T4P. In this model, attachment and retraction leads to a change in the T4P filament, which is signaled through the Pil-Chp chemosensory-like pathway to increase the second messenger cAMP during the first hours on surfaces (Luo et al., 2015; Persat et al., 2015). cAMP binds to and activates the transcription factor Vfr, which in turn triggers the expression of numerous virulence factors (Fulcher et al., 2010; Wolfgang et al., 2003). While these and other studies propose a role for T4P in sensing mechanical stimuli upon surface encounter (Ellison et al., 2017; Jones et al., 2015), other studies implicated the rotary flagellum as a major sensor of surface impact (Hug et al., 2017; McCarter et al., 1988).

T4P are quickly deployed to anchor the cell on a very wide variety of surfaces (glass, plastic polymers, steel, mammalian cells, ...) (Burrows, 2012). While a lot of knowledge has been gained regarding the surface adaptation program hours or even days after landing, little is known about how bacteria sense the surface and make the decision to switch from planktonic to the surface life. The flagellar machinery is described to be involved in surface sensing in some bacterial species such as *E. coli*, *Vibrio cholerae* and *Bacillus subtilis* (Belas, 2014; Lele et al., 2013). An emerging model is that the flagellar motor transduces the "surface" information by altering the membrane potential, while but the flagellar filament seems to be dispensable (Van Dellen et al., 2008). A concurrent model argues that surface is sensed by the increased drag force on the filament subsequently altering the motor rotation (Lele et al., 2013). The flagellum has not been described as a mechanosensor in *P. aeruginosa* to date. Mutation of the *motAB* stators render *P. aeruginosa* defective for biofilm formation, indirectly arguing in favour of flagellar mechanosensing (Toutain et al., 2007). T4P have been proposed to serve as mechanosensors in *P. aeruginosa* (Persat et al., 2015). In this model, retraction of surface-tethered T4P "stretches" the T4P filament. The conformation change of PilA would signal through the Pil-Chp chemosensory-like system, to translate into a surface signal by a mechanism that remains to elucidate.

For the human opportunistic pathogen *P. aeruginosa*, infection starts with making contact with the host tissues. A countdown starts, as it will very soon face the response of the immune system. It has to rapidly create a niche, release food from host cells, and protect itself. *P. aeruginosa* developed a strategy based on surface recognition to initiate the virulence program (Siryaporn et al., 2014). This is a non-host specific signal, allowing very broad host spectra. Mechanosensing by T4P signals through the Pil-Chp pathway to induce the surface-virulence program by increasing levels of the second messenger cAMP during the first hours on surfaces (Persat et al., 2015). cAMP binds to and activates the transcription factor Vfr, triggering the expression of numerous virulence factors.

The other key second messenger of surface adaptation is c-di-GMP. It promotes T4P dynamics and T4P-based twitching motility by activating the c-di-GMP effector FimX (Jain et al., 2012; Russell et al., 2013). T4P activation on surfaces is not only important for motility, but also for virulence. An emerging concept is that T4P may mechanically help T3SS effectors injection and allow high local exotoxins concentration by ensuring a close contact between *P. aeruginosa* and its target cells (Basso et al., 2017; Shikata et al., 2016). c-di-GMP drives the transition from planktonic to sessile by inhibiting flagellar rotation, then at higher levels by inhibiting flagellar machinery synthesis, and increasing the production of exopolysaccharides to form the biofilm matrix (Baraquet et al., 2012; Jenal et al., 2017). At high concentration, c-di-GMP inhibits cAMP synthesis, and *P. aeruginosa*

undergoes an acute-to-chronic transition (Almblad et al., 2015). Although it is clearly established that c-di-GMP levels increase on surfaces, the timing is only known with a low precision in the hour range, due to lack of sensitivity and speed of c-di-GMP reporters. Surface-induction of c-di-GMP in *P. aeruginosa* is thought to be slow, and was reported no earlier than 30 min after surface contact (Rodesney et al., 2017).

Results

PA4958 is a novel high affinity binding protein of c-di-GMP. We used capture compound technology coupled to LC-MS/MS mass spectrometry (Laventie et al., 2015; Nesper et al., 2012) to screen for novel c-di-GMP effector proteins in *Pseudomonas aeruginosa* (Suppl. Fig. S1). One of the top hits, PA4958, was further analysed biochemically. Isothermal titration calorimetry (ITC) revealed that this protein binds c-di-GMP with high affinity (K_d of 50 ± 3 nM, n = 5) and with a stoichiometry of two molecules of c-di-GMP per molecule of PA4958 (N = 1.93 ± 0.06) (Fig. 1A). Differential Scanning Fluorimetry (DSF), a qualitative method for protein-ligand interactions (Niesen et al., 2007), showed that PA4958 binds c-di-GMP specifically with related nucleotides (GMP, GDP, GTP and ATP) being unable to bind (Fig. 1B). Because the gene encoding PA4958 is positioned on the *P.*
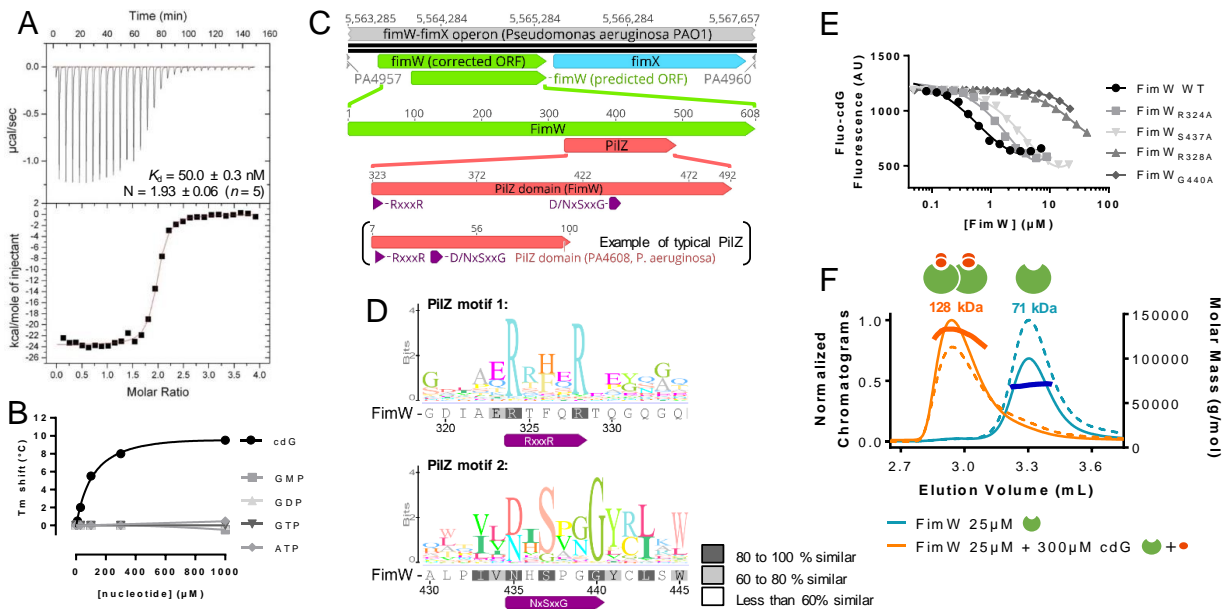

FIG. 1: FimW IS A NOVEL C-DI-GMP BINDING PROTEIN IN *P. AERUGINOSA*. (A) Binding affinity and stoichiometry of the c-di-GMP/FimW interaction was measured by Isothermal Titration Calorimetry (ITC). The upper panel represents the energy necessary to maintain a constant temperature (µcal/s) over time, indicating the heat released upon ligand binding. The lower panel represents the binding isotherm of the integrated heat peaks against the molar ratio c-di-GMP:protein. Affinity, molar ratio and statistical parameters are indicated. **(B)** FimW nucleotide binding specificity as measured by Differential Scanning Fluorimetry. Concentration-dependent stabilization of FimW is shown for different ligands as indicated. Stability of FimW is measured as the increase of thermal stability (Tm shift). **(C)** Schematic of the *P. aeruginosa* chromosomal *fimW-fimX* locus and of the FimW protein architecture. The *fimW* gene is annotated with both the predicted ORF, as it appears on the NCBI database, and the corrected and experimentally validated ORF (see Suppl. Fig. S2). The atypical PilZ domain of FimW is superimposed for comparison on a typical PilZ domain (from PA4608, *Pseudomonas aeruginosa*). **(D)** Conservation of PilZ motifs 1 and 2 in FimW and its orthologues. The reference sequence is from *P. aeruginosa* FimW. Logos were generated with Geneious from the 517 closest non-redundant sequences after 3 PSI BLAST iterations. **(E)** Relative c-di-GMP affinity of wild-type and mutant versions of FimW as measured by Microscale thermophoresis. The decrease in fluorescently labelled c-di-GMP signal for increasing concentrations of FimW reflects the binding of c-di-GMP to the protein. The labeling of amino acids corresponds to the numbering in (D). **(F)** Apo- and Holo-FimW oligomeric states. Size exclusion chromatographs representing absorbance at 280 nm of FimW (25 µM) in absence (blue) or presence (orange) of 300 µM c-di-GMP as measured by SEC-MALS (left y-axis). The Rayleigh Ratios (light scattering) are represented by the thin solid curves, while the Differential Refractive Index (concentration) is represented by the thin dashed curves. The segments in the peaks correspond to the measured molar mass of the complex (right y-axis). Signals are normalized to show the relative magnitude of each signal type for each sample.

aeruginosa chromosome immediately upstream of the *fimX* gene encoding the c-di-GMP binding protein FimX (Fig. 1C) (Kazmierczak 2006), we renamed this protein FimW.

Protein homology prediction by HHpred revealed a PilZ-like fold at the C terminus of FimW (Fig. 1C). PilZ domains are characterized by two conserved c-di-GMP binding motifs, RxxxR and D/NxSxxG (Benach 2007, Chou 2016). In *Pseudomonas aeruginosa*, eight PilZ proteins were identified originally using bioinformatics (Amikam and Galperin, 2006). While all of these, but one, bind c-di-GMP, functional information is available for only four members of this family (Baker et al., 2016; Merighi et al., 2007; Pultz et al., 2012; Xu et al., 2016a; Xu et al., 2016b). Although FimW was not classified previously as a PilZ domain protein, a position-specific iterated BLAST search revealed that FimW and its orthologues contain both conserved PilZ motifs (Fig. 1D). However, the linker between the two conserved c-di-GMP binding motifs, which is generally between 21-30 amino acids long, is largely extended in FimW (106 amino acids) (Fig. 1C). Mutational analysis of the RxxxR and D/NxSxxG motifs of FimW revealed that replacing R324 and S437 with Ala residues decreased c-di-GMP affinity by 5.6- and 9.3-fold, respectively (Fig. 1E), while replacing R238 and G440 reduced c-di-GMP binding to a level below detection limit.

Upon c-di-GMP binding, PilZ proteins generally undergo small conformational changes (Benach et al., 2007; Habazettl et al., 2011) that can have large effects on the overall protein structure by creating interaction surfaces or changing the oligomeric state. Multi angle light scattering (MALS) analysis of FimW showed a monomeric state in the absence of c-di-GMP (measured: 70 kDa at half-peak-height, predicted for monomer: 70 kDa). The protein shifted to a concentration dependent monomer-oligomer equilibrium in the presence of c-di-GMP, with a molar mass close to the mass of a FimW dimer (measured: 128 kDa at half-peak-height, 133 kDa at peak top, predicted for dimer: 140 kDa) (Fig. 1F). Thus, FimW is the first example of a PilZ domain protein undergoing a monomer-to-oligomer transition upon c-di-GMP binding. Altogether, these experiments identified FimW as a novel but atypical PilZ domain-containing protein that binds c-di-GMP with high affinity and, in response, undergoes dimerization.

FimW localizes to the cells poles in a c-di-GMP dependent manner. Bacteria immobilized on an agar patch clearly displayed a polar localization of the fluorescent fusion protein Venus-FimW (Fig. 2A). Nevertheless, a small percentage of the population had a cytoplasmic distribution of FimW. About 70% of exponentially growing wild type cells had a polar localization (Fig. 2B, C). When the phosphodiesterase PA5295 was introduced in *trans* to decrease the c-di-GMP concentration Venus-FimW was never visualized at the poles. At the opposite, the overexpression of the diguanylate cyclase SadC, to increase the intracellular c-di-GMP concentration, led to a polar localization in nearly all the bacteria (85%, Fig. 2C). In addition, the c-di-GMP blind mutant Venus-FimW[R328A] was never observed at the pole. To show that the polar localization is reversible and dynamic, we
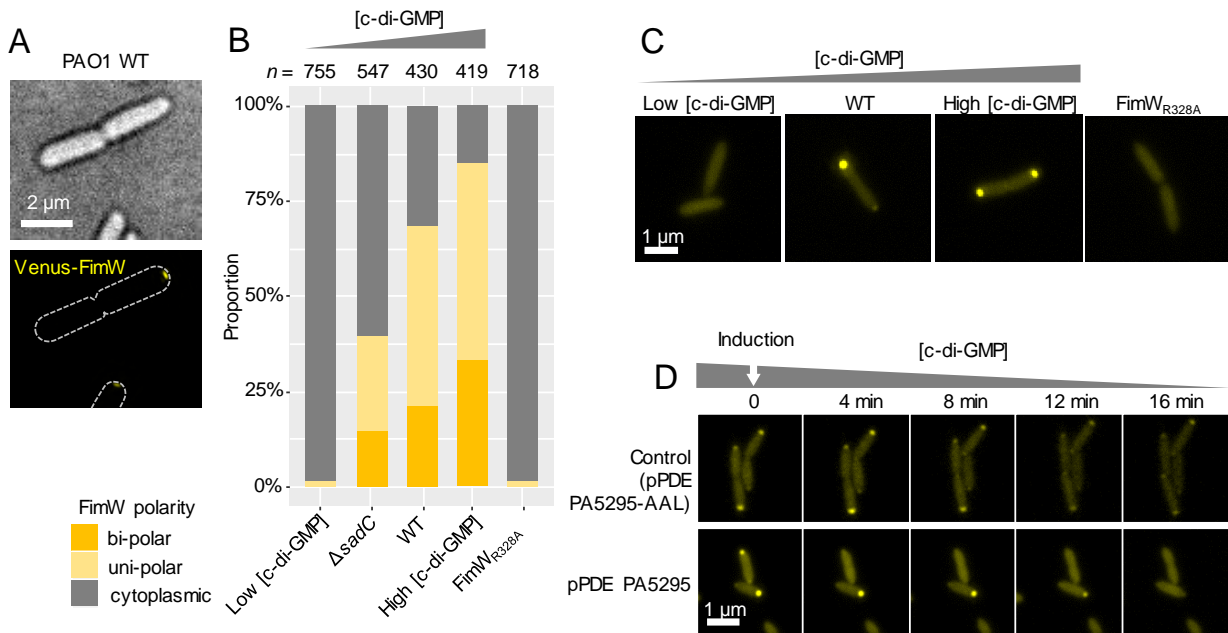
FIG. 2. C-DI-GMP DEPENDENT POLAR LOCALIZATION OF FIMW

(A) Venus-FimW localization observed by Super Resolution Microscopy. Venus is a brighter YFP derivative. The white dashed line represents the bacteria outline. (B, C) Venus-FimW localization over a large range of c-di-GMP concentration, and for the c-di-GMP blind FimWR328A mutant. The y-axis indicates the percentage of cells displaying a cytoplasmic, uni- or bi-polar localization of Venus-FimW. (C) Representative fluorescence microscopy pictures are shown. Bacteria were grown in LB medium to an optical density of c.a. 0.5. The fluorescent proteins were expressed in trans from a pME6032 vector induced with 100μM IPTG. Low c-di-GMP condition: PDE PA5295 induced with 1 mM vanillate from a pBV-PA5295 vector. High c-di-GMP condition: chromosomally integrated DGC SadC (PA4332) induced with 1% (w/v) arabinose. (D) FimW dynamically de-localizes from the pole to the cytoplasm when c-di-GMP concentration decreases. The PDE PA5295 was induced at time 0 with 1 mM vanillate, from a pBV::PA5295 vector. Negative control: catalytically inactive PA5295E328A mutant.

observed the localization of Venus-FimW immediately after inducing the phosphodiesterase PA5295. Within few minutes (5-20min), required for the phosphodiesterase expression, the polar foci disappeared (Fig. 2D). Altogether, this argues that FimW reversibly re locates from the cytoplasm to the cell poles upon c-di-GMP binding.

FimW rapidly relocates to the cells poles upon surface contact. In the previous microscopy experiments, the cells were always in contact with a surface (agar pad - glass coverslip interface). We looked at the localization of FimW in planktonic cells. As *P. aeruginosa* is swimming too fast to acquire efficiently fluorescence pictures, we fixed planktonic cells with 250 mM Formaldehyde before imaging. While FimW had a polar localization in 65% of surface associated cells, it had a cytoplasmic distribution in planktonic cells (fig. 3A, B). We hypothesized that FimW relocation to the poles, when *P. aeruginosa* is surface-associated, is due to surface-driven increase in c-di-GMP concentration. Alternatively, FimW localization may require another surface-induced signal in addition to c-di-GMP. To test whether surface and / or c-di-GMP are required for FimW polar localization, we artificially increased the c-di-GMP concentration in planktonic cells by overexpressing the diguanylate cyclase SadC. Planktonic cells with increased c-di-GMP

concentration displayed polar foci (21% of the cells), showing that c-di-GMP can partially restore the polar localization in absence of surface (fig. 3B). This argues that FimW localization depends on both c-di-GMP levels and on surface sensing. We then looked at FimW localization directly during landing of *P. aeruginosa* on the glass surface using a microfluidic device. Astonishingly FimW can relocate to the cell poles upon surface contact as fast as within 20 seconds (Fig. 3C). As FimW localization is c-di-GMP dependent, our data suggest that there is an extremely rapid c-di-GMP concentration increase immediately after surface contact.

FimW polar localization requires the flagellar and T4P machineries. An emerging model proposes that bacteria achieve surface sensing by flagellar mechanosensing, consequently altering the ion flux through the flagellar motor (Hug et al., 2017). The local membrane potential alteration could initiate a surface adaptation program. Pili may indirectly play a role as adhesins, to help immobilizing the flagellum while establishing a firm contact with the surface, or even directly by sensing the tension state of T4P when pulling (O'Toole and Wong, 2016; Persat et al., 2015). Nevertheless, this model remains controversial and needs further investigation. As FimW is a molecular switch reacting to surfaces, we tested the requirement of the flagellar and T4P machineries within 20 min of surface exposure. Mutations of the flagellum (Δ*fliC*), the hook (Δ*flgE*) or the 2 stator pairs of the motor (Δ*motABCD*) all led to a severely reduced FimW polar re-localization, with only 1.6% of cells displaying polar foci for the Δ*motABCD* mutant (as opposed to 74% for the WT). *P. aeruginosa* possesses two specialized stators pairs. While both are involved in swimming motility, MotA/MotB participates in the transition from reversible to irreversible attachment, where MotC/MotD is essential for near-surface swarming motility (Baker et al., 2016; Toutain et al., 2007). Interestingly, a Δ*motAB* strain recapitulates the Δ*motABCD* mutant strain phenotype (14-fold less cells with polar foci than WT), but a Δ*motCD* strain has a milder surface response defect (only 2.5-fold less). Moreover, *motA*/*motB* (PA4954/PA4953) are encoded only 4 genes upstream of *fimW* (PA4958).
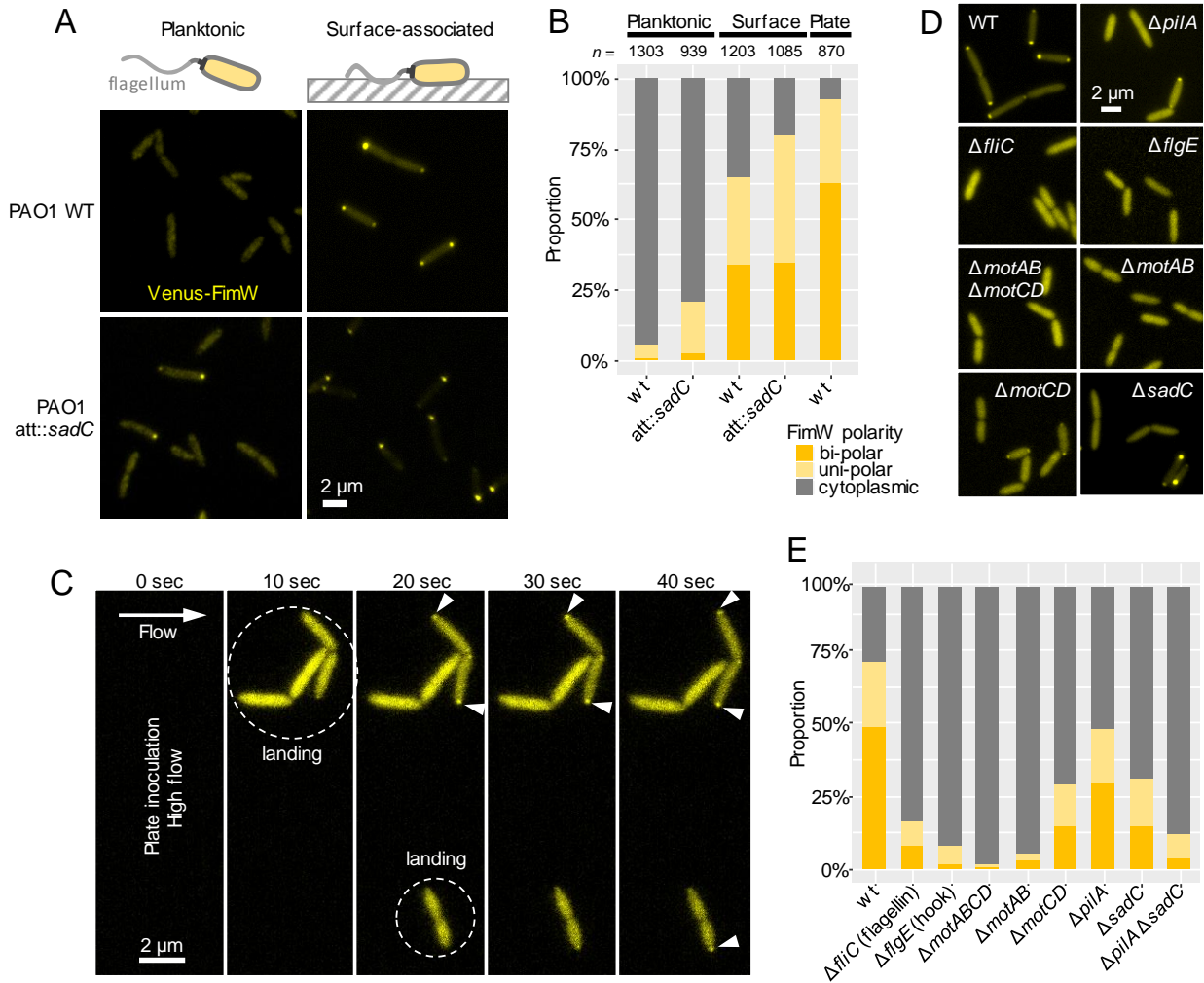
FIG. 3. FIMW LOCALIZATION IN PLANKTONIC CELLS AND SURFACE ASSOCIATED CELLS.
(A) Representative fluorescence microscopy pictures of PAO1 in the free swimming planktonic state after fixation with Formaldehyde (left column) or on a surface (agar pad-glass interface, not fixed, right column). Upper picture: PAO1 WT. Lower pictures: PAO1 with additional chromosomal copy of the DGC SadC under the control of the P$_{BAD}$ promoter, induced with 1% arabinose. (B) Quantification of the microscopy data for the percentage of cells with a polar localization of Venus-FimW. (C) Example of Venus-FimW cytoplasmic-to-polar localization switch during cell landing using a CellASIC microfluidic device (bacterial plates). (D, E) Venus-FimW localization after surface contact in T4P and flagellar machinery mutants. The number of cells counted is indicated above each bar.

A T4P pili mutant (lacking the major pilin PilA) mildly affected FimW relocalization after surface contact (1.5-fold less than WT, Fig. 3D-E). Genetic evidence argue that surface grown cells use the T4P machinery to activate c-di-GMP production by the diguanylate cyclase SadC (Luo et al., 2015). SadC promotes biofilm formation and represses flagellar based-swarming motility. But it is not clear how early after surface contact SadC is active. We tested whether the ΔpilA reduced surface response is caused by the lack of activation of SadC and resulting in a reduction of c-di-GMP synthesis. Surprisingly, FimW polar relocalization on surfaces was halved in a ΔsadC strain, surpassing the ΔpilA phenotype, and ΔsadC and ΔpilA deletions have additive effects (Fig. 3E). This argues that SadC intervene rapidly after surface contact to rise c-di-GMP levels, but also that other DGC(s) or

PDE(s) participate in this response. The hierarchy and timing of activation of DGCs upon surface sensing remains to decipher, and is complicated by a very diverse and intricate c-di-GMP network in *P. aeruginosa*, and the very short timescale of the events to observe. **FimW regulates type IV pili dynamics.** FimW is a surface activated molecular switch, but FimW has no predicted function nor any predicted domain to point at the switch purpose. Nevertheless *fimX*, the second gene of *fimW*'s two-gene operon, is well characterized and plays an important role in the regulation of the T4P dynamics. Alike FimW, FimX is a c-di-GMP effector, although it has a distinct architecture and binds c-di-GMP through its degenerated EAL domain (Kazmierczak et al., 2006). FimX promotes T4P elongation and a type of T4P-driven surface motility called twitching motility. We hypothesized that FimW could also play a role in T4P regulation. This is supported by: 1) T4P dynamics is regulated by c-di-GMP, at least via FimX (Jain et al., 2012), 2) the identical sub-cellular localization of the T4P machineries and FimW at both cells poles (Chiang et al., 2005), and 3) T4P are deployed on surfaces and used for surface behaviors/motility (Cowles and Gitai, 2010). Moreover, a co-occurrence analysis of *fimW* revealed that 16 of the top 50 hits are genes involved in T4P regulation or assembly (Suppl. Table S3). To test this hypothesis, we looked at the piliation of *P. aeruginosa* PAO1 by western blot of sheared surface pili. Interestingly, a Δ*fimW* strain has dramatically decreased levels of surface piliation compared to the WT strain (Fig. 4A). Consistent with the literature, a Δ*fimX* strain shares the same phenotype. The total amount of the major pilin PilA remains unchanged, which excludes an effect on PilA expression.

We then used a T4P-specific phage (DMS3) to look at the pili dynamics. Bacteria are killed by the DMS3 bacteriophage only when T4P are assembled and retracted (Budzik et al., 2004). After a short growth phase, WT PAO1 lyses, while a Δ*pilA* strain is fully phage resistant (Suppl. Fig. S4). Although single deletions of *fimW* or *fimX* dramatically decrease surface piliation, they only confer a partial resistance this T4P-specific phage, nevertheless pointing at a decrease of T4P extension/retraction rate. This can be explained by the high sensitivity of this assay, as even a very low T4P activity is enough for the DMS3 phage to infect and kill *P. aeruginosa*. Interestingly, a Δ*fimW* Δ*fimX* double knockout confers a greatly enhanced protection against the phage, arguing that not only FimW and FimX both play a role in T4P dynamics, but also that they are the two major players and can to some extent complement each other's piliation defect.
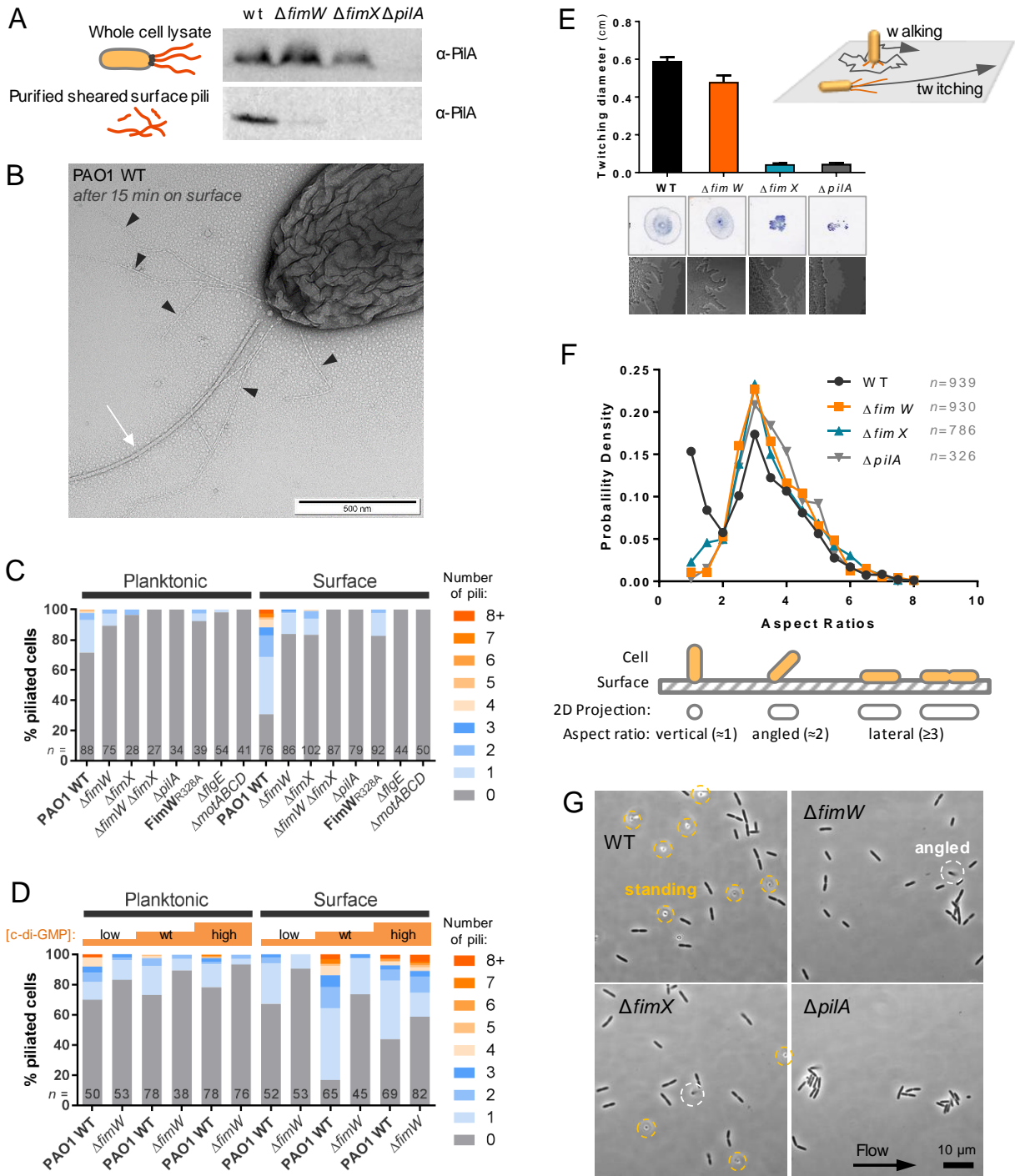
FIG. 4. FIMW REGULATES PILIATION AND PILI-DEPENDENT STANDING/WALKING.

(A) Piliation at the population level, quantified by western blot of purified sheared surface-pili. (B-D) Piliation at the single cell level by Transmission Electron Microscopy (TEM) (B-D). (C) The percentage of piliated cells and the number of pili/cell were quantified from TEM pictures for *P. aeruginosa* mutants. Cells fixed in the planktonic are compared to cells exposed to a surface (the TEM grid) for 15 min before fixation. The number of cell quantified is indicated for each strain. (D) TEM with low/high c-di-GMP concentrations. Low c-di-GMP condition: PDE PA5295 induced with 1 mM vanillate from a pBV-PA5295 vector. High c-di-GMP condition: chromosomally integrated DGC SadC (PA4332) induced with 1% (w/v) arabinose. (E) Twitching motility assayed by microscopy (lower panel) and in a stab inoculation twitching motility assay (middle panel: representative example of the area colonized by twitching, bar chart: quantification of the twitching diameters, *n* = 3). Error bars represent the SEM. (F) Histogram of the aspect ratios plotted as probability densities, with a bin size = 0.5. The number of cells quantified for each strain is indicated on the histogram. Cells were imaged in flow condition using the CellAsic ONIX microfluidic system. (G) Representative microscopy picture of *P. aeruginosa* WT and mutants illustrating the position of cells

relative to the surface. Images were acquired using CellAsic bacterial plates. Standing cells are circled in orange, angled cells are circled in white.

We confirmed this observation when looking at the single cell level piliation using Transmission Electron Microscopy (TEM). In the free-swimming planktonic state, less than 30% of WT *P. aeruginosa* displayed piliation, with usually only 1 polar pilus (Fig. 4C). But after 15 min of surface exposure, piliation significantly increases with both more piliated cells (69%) and more pili per cell (2.3 pili/piliated cells, Fig. 4B, C). But Δ*fimW* and Δ*fimX* strains are not able to increase their piliation when exposed to the surface (Fig. 4B, D). Interestingly, a strain expressing a c-di-GMP blind FimW$_{R328A}$ mutant mimics the Δ*fimW* strain phenotype, showing that the ability of FimW to bind c-di-GMP is essential to drive the surface-induced increase of piliation. Moreover, a Δ*fimW* Δ*fimX* double knockout has an even more dramatic phenotype as is never shows piliation in any condition. We also looked at the single cell level piliation over a broad range of c-di-GMP concentrations. An artificial increase in c-di-GMP level in planktonic cells is not enough to bypass the requirement for a surface to activate piliation (Fig 4D). At the opposite, counteracting the surface induced increase of c-di-GMP levels by overexpressing a Phosphodiesterase, prevents the surface-induced piliation increase (Fig 4E). In the same way as FimW polar localization, these data show that both the surface and an increase of c-di-GMP levels are required for piliation.

FimW is required for T4P based walking motility but dispensable for T4P based twitching motility. *P. aeruginosa* employs T4P to tether to and move across solid surfaces, with several motility types such as twitching and walking (Brill-Karniely et al., 2017; Conrad et al., 2011). FimX is essential for twitching motility (Huang et al., 2003; Kazmierczak et al., 2006), and a Δ*fimX* strain was unable to twitch, as well as a strain missing the major pilin PilA (Fig. 4E). Unexpectedly, although a Δ*fimW* strain has a greatly decreased piliation, it has only a minor twitching motility defect. This small difference is nevertheless consistently observed, and a twitching competition between WT and Δ*fimW* strains showed that WT twitches farther. This could be rationalized by the T4P machinery lacking the positive input of FimW, although FimW seems to not regulate twitching motility.

Besides twitching, *P. aeruginosa* uses T4P to stand vertically on the surface. To quantify the bacterial orientation on the surface, we used the method described by Conrad *et al.* consisting in measuring the bacterial lengths projected onto the surface. Consistent with their observations, the WT *P. aeruginosa* displayed 2 distinct peaks corresponding to standing cells (aspect ratio ≈ 1, Fig. 4F, G) and horizontally oriented cells (aspect ratio ≥3). The Δ*fimW* strain was distinctly unable to stand upright on the surface. The Δ*fimX* was also affected, but with a milder phenotype as some standing bacteria could be observed (Fig. 4F, G). Standing being a prerequisite for walking, unsurprisingly the Δ*fimW* strain was never observed walking upstream in a microfluidic device.
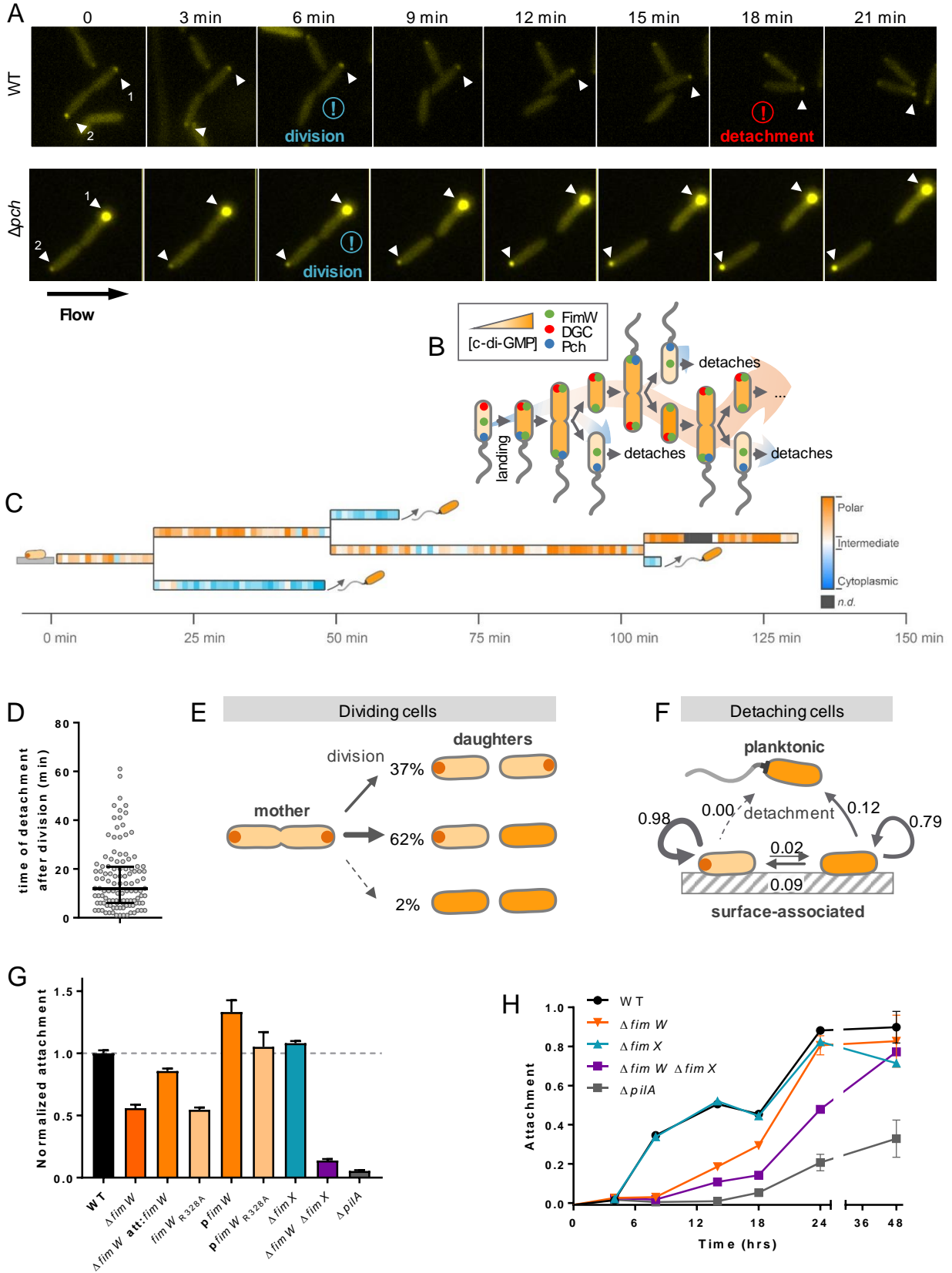
FIG. 5. FIMW LOCALIZATION ASYMMETRY AFTER CELL DIVISION AND CONSEQUENCES ON DETACHMENT AND EARLY SURFACE ATTACHMENT.

(A) Comparison of Venus-FimW localization in *P. aeruginosa* WT and Δ*pch*. Frames corresponding to division or detachment of cells are highlighted with an exclamation mark. (B) Model of localization of FimW and c-di-GMP producing/degrading enzymes and polarity switch during cell division. (C) Representative family tree of *P. aeruginosa* first generations after landing on a surface. The color represents FimW localization and arrows with a swimming bacteria represent detachment events. Tree generated by a custom made Matlab program. (D-F) Quantification of FimW localization and cells behavior over time for up to 3 generations on the glass surface in a CellAsic microfluidic device. (D) Quantification of the average time of detachment after cell division (only cells observed to detach are considered). The bars represent the median with interquartile range, while each dot represents the detachment time of 1 cell (n = 113). (E) Quantification of the Venus-FimW localization asymmetry after division for 227 dividing cells. FimW localization was considered polar when it remained polar for >5 min after division. (F) Frequency of state change for 200 tracks, representing 8640 transitions with a bin time of 2 minutes (*i.e.* a frequency of "0.1" means there is a 10% chance of state change after 2 min). The 3 states considered are: polar localization of Venus-FimW, cytoplasmic distribution of Venus-FimW, detachment of the bacteria. The cell division step was excluded. (G) Attachment assay at 18hrs (at least 6 replicates) and (H) time course attachment assay (n = 3). (96-well plate, static, 37°C, LB). Error bars represent the SEM

Note that while swimming was unaffected, the piliation defect increased swarming motility in Δ*fimW*, Δ*fimX* and Δ*pilA* strains, consistent with previous reports showing that T4P moderate swarming in *P. aeruginosa* (Suppl. Fig. S4) (Anyan et al., 2014). In short, the Δ*fimW* strain the piliation defect does not affect twitching but dramatically affects standing and walking.

The c-di-GMP degrading enzyme Pch creates a FimW localization asymmetry after cell division on surfaces. Remarkably, after the first divisions on a surface, FimW localization is asymmetric. While it segregates equally in the 2 daughter cells (the overall fluorescence level is identical in the 2 siblings), its localization remains polar in one daughter cell, and reverts to a cytoplasmic distribution in the other sibling (Fig. 5A). As FimW localization depends on c-di-GMP levels, this asymmetry could rely on a c-di-GMP asymmetry after division. In line with this hypothesis, the phosphodiesterase Pch (PA5017, also known as DipA) was reported to generate a c-di-GMP heterogeneity after cell division in planktonic cells (Kulasekara et al., 2013). Pch is asymmetrically inherited with central chemotaxis protein CheA in the flagellated daughter, driving the c-di-GMP concentration down; while a set of diguanylate cyclases drive c-di-GMP concentration up in the other daughter cell. Kulasekara and colleagues described that, when *P. aeruginosa* cells are spotted on an agar patch, they observe 20% of cells with a low c-di-GMP concentration, for an early log phase culture. This matches our observation that, in the same conditions, *c.a.* 20-30% of the cells have a cytoplasmic distribution of FimW. The disruption of the *pch* gene abolishes the FimW localization asymmetry: the 2 daughter cells always display polar foci (Fig. 5A), strongly arguing that Pch regulates the c-di-GMP pool responsible for FimW polar localization.

Seed and go: after division on the surface, the flagellated cell daughter flies off while the other sibling stays on the surface. We asked what could be the phenotypic meaning of this molecular feature. In a flow channel, cells that reverted the FimW localization from polar to cytoplasmic after division were observed to detach, after a median time of 12 min (Fig 5A, C, D). The tracking of 200 cell lineages showed that, following division, 62% of the cells showed an asymmetric localization of

FimW, and the others displayed polar foci in bother siblings (Fig. 5E). The post-division detachment was not observed for the Δ*pch* mutant, consistent with the fact that both siblings always display polar foci in this strain. The quantification of the change of FimW localization over time showed that cells with a cytoplasmic distribution of FimW are in an unstable state, and are prone to either detach, or revert again to show polar foci (Fig. 5F). At the opposite, cells displaying polar FimW foci are in a stable state, rarely switch to a cytoplasmic distribution, and were not observed to detach in 200 cell tracks, as summarized by a representative family tree in Fig. 5C. Our data provide molecular insights to observations by Conrad and colleagues that *P. aeruginosa* displays an asymmetric behavior after division in surfaces: while one sibling stays on the surface, the other sibling may detach, move horizontally (twitching motility) or walk upright (Conrad et al., 2011).

FimW is involved in early attachment to surfaces. FimW mediates the surface-induced c-di-GMP signal to the T4P machinery to adapt quickly to the surface, and the Δ*fimW* strain is unable to operate T4P-walking. But T4P also play an important role at later stages in biofilm formation: they serve as adhesin, promote the transition from reversible to irreversible attachment, and shape the biofilm 3D architecture (Chiang and Burrows, 2003; Klausen et al., 2003). The biofilm produced by a Δ*fimW* strain halved at 16 hrs (Fig. 5G). This phenotype can be complemented by re-introducing a copy of *fimW* in *cis*, in the "att" neutral locus, under control of its own promoter. The *fimW*R328A c-di-GMP blind mutant mimics a *fimW* deletion, arguing that an intact c-di-GMP binding site is essential for FimW function in attachment. Vice versa, FimW overexpression led to an increase in biofilm formation, but not the overexpression of the c-di-GMP blind FimWR328A mutant (Fig. 5G). Conversely, a Δ*fimX* strain formed biofilm biomass undistinguishable from the WT. FimX, while essential for twitching motility, is dispensable for the control of T4P for attachment to surfaces. A Δ*fimW* Δ*fimX* double deletion strain has an attachment phenotype close to a Δ*pilA* strain, suggesting that the positive input of FimX on the T4P machinery can contribute to attachment when FimW is missing. A time course attachment assay revealed that the attachment defect of the Δ*fimW* strain occurs during the first hours after inoculation, but at 24 hrs attachment returns to WT levels (Fig. 5H). This corresponds to the first attachment phase, when a Δ*pilA* strain does not attach, suggesting that FimW is essential during the pili dependent phase of attachment, but dispensable at later stages. After 14 hours, even the Δ*pilA* strains starts to form a biofilm, which may be due to the increased cell density and bacteria becoming able to adhere non-reversibly to the surface without pili by producing exopolysaccharides or other adhesion factors. Besides, Kulasekara and colleagues showed that a *pch* knock out in the *P. aeruginosa* strain PA14 increases initial attachment (at 6hrs) in a static biofilm assay, and the overexpression of Pch decreases initial attachment, while both have no phenotype for late attachment (at 24hrs)(Kulasekara et al., 2013). This is comparable to the phenotype of a FimW overexpression and deletion in PAO1, respectively (Fig. 5H), and could be explained by the improper subcellular localization of FimW in Pch mutants due to the altered c-di-GMP concentration.

Discussions

We summarized our Touch, Seed and Go model in Fig. 7. To establish a successful infection, *P. aeruginosa* must quickly activate its surface-virulence program and find the best niches by optimizing its colonization strategies. We present evidence that the flagellar machinery is essential to translate the surface signal into a second messenger signal that can be interpreted by different effectors, including the T4P machinery. The fact that the filament and the motor MotAB are both required suggest that the surface signal could originate from a slowing of the flagellar filament by an increased load, stalling the motor. Interestingly, only the stator MotAB is absolutely required. *P. aeruginosa* seems to have specialized its 2 pairs of stators: one for swarming (MotCD), and one for surface sensing and promotion of early biofilm formation (MotAB) (Baker et al., 2016). This matches the previous observation that while a deletion of the *motAB* stator does not affect swimming, it affects the transition from reversible- to irreversible-attachment and delays biofilm formation (Toutain et al., 2007; Toutain et al., 2005). We also observed that T4P pili play an important role in surface sensing, but we cannot differentiate whether: A) T4P promote the flagellar arrest by ensuring a close proximity to the surface, or B) or if T4P directly sense and transduce the surface signal independently of the flagellum, as suggested by other groups (Luo et al., 2015; Persat et al., 2015). Although the T4P and flagellar machinery are both playing a role, it is clear that the flagellar machinery is has a critical function, while we hypothesize that T4P evolved as a non-essential surface-sensing optimization
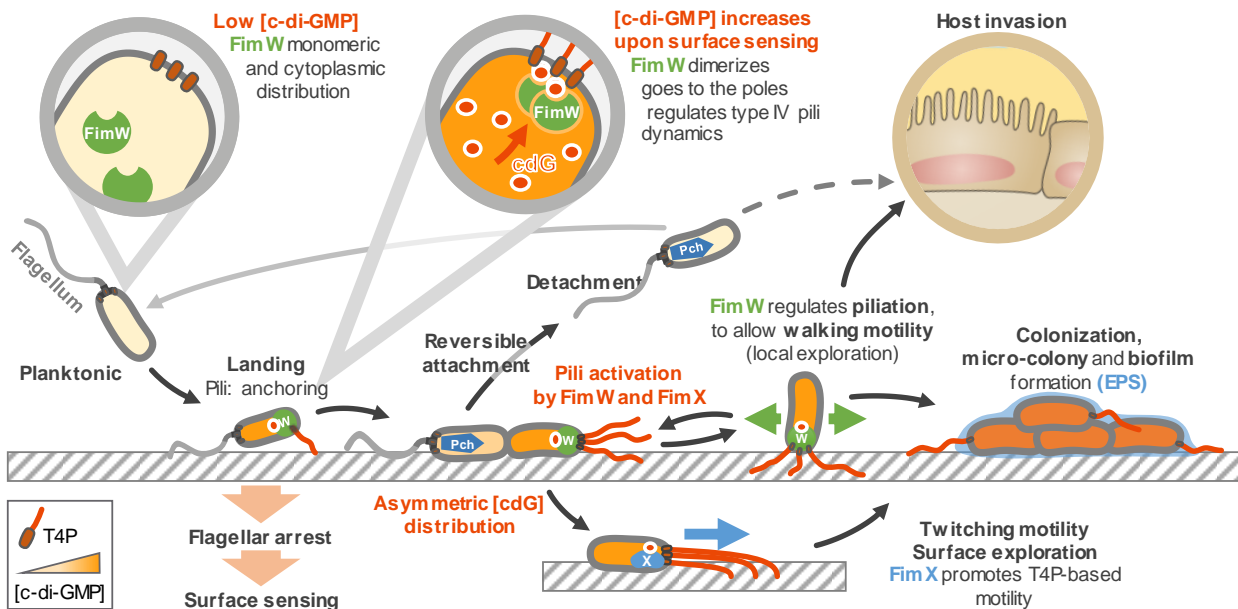

FIG. 7. THE TOUCH, SEED AND GO MODEL.

In planktonic cells, the c-di-GMP concentration is below detection limit by Mass spectrometry (<50 nM), FimW in not bound to c-di-GMP, therefore monomeric, and has a cytoplasmic distribution. When *P. aeruginosa* touches a surface, the c-di-GMP concentration increases very rapidly (how the surface is sensed is unclear). FimW binds to c-di-GMP, dimerizes, and go the cell poles when it positively regulates Type IV pili elongation. It stabilizes the attachment of cells to the surface, that otherwise can detach. Preliminary evidences point at a regulation by FimW of walking motility, which is type of motility used by *P. aeruginosa* to explore quickly the local environment on the surface.

system, bringing speed and efficiency. Consistent with previous reports, we observed a small, but non-zero, number of T4P in free-swimming *P. aeruginosa* (Cowles and Gitai, 2010). One hypothesis is that, together with the flagellar filament, these pre-existing T4P help making contact and sense the surface. A Δ*pilA* strain is still able to increase its c-di-GMP intracellular concentration in response to the surface, although in a lesser extent that WT.

Previous reports argue that increase of c-di-GMP after surface contact takes hours in *P. aeruginosa* (O'Toole and Wong, 2016; Rybtke et al., 2012). This idea is probably a consequence of the lack of fast and sensitive c-di-GMP reporters. The most widely used c-di-GMP reporter is based on the de-repression of GFP transcription, under the control of the *cdrA* promoter, by binding of c-di-GMP to the repressor FleQ. Nevertheless, FleQ has a weak binding affinity ($K_d \approx 4 - 7$ µM) (Baraquet and Harwood, 2013; Matsuyama et al., 2016) and probably lacks sensitivity and speed to sense small and rapid c-di-GMP increase upon surface contact. Also, surface contact induces the increase of cAMP levels, that drives virulence genes expression. Particularly, during the first hours on a surfaces, the adhesins PilY1 is upregulated, and is shown to signal through the DGC SadC to boost c-di-GMP production (Kuchma et al., 2015). Although this argues for a cascade of second messengers occurring on the surface, it could be a positive feedback on c-di-GMP synthesis by SadC, which does not exclude earlier c-di-GMP synthesis by SadC or other DGCs. Our data suggest that initial surface sensing is very rapid (seconds) in *P. aeruginosa*, similar to *Caulobacter crescentus* (Hoffman et al., 2015). Venus-FimW subcellular localization, used as a readout for [c-di-GMP], clearly show that c-di-GMP can increase within seconds after surface contact (Fig. 2C). This is made possible by the high sensitivity of FimW for c-di-GMP, and the superior time resolution of FimW subcellular localization changes over c-di-GMP transcriptional reporters.

Free swimming *P. aeruginosa* have intracellular c-di-GMP concentration below detection limit (<50 nM), while surface associated cells have low c-di-GMP concentration in the range of 300 - 600 nM, which will increase to the low µM range during biofilm formation (Jain et al., 2012; Kulasekara et al., 2013). C-di-GMP receptors bind c-di-GMP in a hierarchical order based on their affinity as c-di-GMP levels cranks up (Pultz et al., 2012). As FimW is one of the highest affinity effector described to date ($K_d = 50$ nM), it is expected to be a first line effector in the surface program. FimW is activated in the low nM range, matching the reported rise of c-di-GMP between planktonic and surface-associated cells. Its noteworthy that FimW and FimX have very close affinities for c-di-GMP (FimX: $K_d \approx 100 - 125$ nM), and therefore should both be activated upon surface contact with a similar timing (Jain et al., 2012; Navarro et al., 2009). Unexpectedly, artificially increasing the c-di-GMP concentration in planktonic cell is not triggering FimW polar delocalization (Fig. 3B), nor activates piliation (Fig. 4D) to the same extent than in surface-associated cells. Although c-di-GMP is essential for FimW polar localization and piliation, it seems that the surface itself is required, by a mechanism that remains elusive.

Upon c-di-GMP binding, FimW dimerizes and relocalizes to the cell poles, where it regulates positively T4P elongation together with FimX. This allows a rapid surface adaptation by promoting attachment stabilization, walking and twitching motility. Subsequently, *P. aeruginosa* will redistribute on the surface to optimize the colonization and to later allow the formation of 3D structured biofilms (Klausen et al., 2003; O'Toole and Kolter, 1998). Interestingly, while FimW and FimX are both c-di-GMP effectors and both activate piliation, they elicit different T4P-based phenotypes, *i.e.* FimW promotes walking and attachment, and FimW controls twitching (Fig. 4 E-G, Fig. 5H-I). This may rely on subtle differences in the way they regulate the T4P machinery at the molecular level. For instance, FimX may trigger a more processive T4P elongation than FimW (to allow twitching) by playing with the exchange rate of ATPases responsible for T4P elongation (PilB) and retraction (PilT and PilU). Also, not all *Pseudomonas* species encode both *fimW* and *fimX*. Although almost 60% of *Pseudomonas* species encode a *fimW* ortholog (47/79 genomes, KEGG best-best blast hit, with threshold=150), only 44% (35/79) harbor a *fimX* ortholog and *fimX* is always associated with *fimW* (Suppl. Fig. S5).

Our data argue that cell division on surfaces is a critical process to generate phenotypic diversity. The c-di-GMP asymmetry created by Pch is a deterministic program ensuring that one sibling stays on the surface, where it can start infecting host cells and establish a micro-colony, while it triggers the detachment of the other sibling. As the "residing" daughter is devoid of Pch, increased c-di-GMP concentration will activate FimW and FimX to regulate the T4P machinery. Also, as Pch is partitioned asymmetrically together with the CheA and the flagellum, this program ensures that the cell flying off is the one that has the propeller and the chemotaxis machinery. This detachment program may have an important role for long-range colonization of remote sites by the newly born planktonic cell, that could not be achieved if the 2 daughter cells could have been limited to "short range" surface motility. Nevertheless, we observed only the first 5 generations after landing, and this asymmetry game could not last forever. As c-di-GMP increases over time spent on the surface, after >5 generations new descendants may start to commit to the surface program.

FimW is a surface-activated molecular switch that allows rapid surface adaptation within seconds after landing. This illustrate how fast a second-messenger network can be put in motion to adapt to new conditions. Combined with a generator of asymmetry after division, *Pseudomonas* is using a deterministic program to diversify, rather than a bet-hedging strategy, by committing a part of the population to the surface while returning the seeding cell to its initial planktonic state. This shed light on new virulence and colonization strategies, and raises questions about the role of c-di-GMP in promoting virulence.

Material & method

Strains and mediums

Strains and plasmids used in this study are listed in Supplementary Table 1 and 2. Unless otherwise stated, *P. aeruginosa* PAO1 and all *E. coli* strains were grown at 37°C in Luria Bertani (LB) medium (Miller, 1972), solidified with 1.3% agar where appropriate. For *P. aeruginosa*, antibiotics were used at the following concentrations: 30 μg/mL gentamycin, 100 μg/mL tetracycline, and 200 μg/mL carbenicillin. For *E. coli*: 20 μg/mL gentamycin, 12.5 μg/mL tetracycline, was 50 μg/mL kanamycin and 100 μg/mL ampicillin. For inducible plasmids, vanillate was added to a final concentration 1 mM, arabinose from 0.2 to 1% and IPTG from 0.1 to 0.5 mM, as appropriate.

Molecular biology procedures

Cloning was carried out as previously described in Malone *et al*. 2012 (Malone et al., 2012) and details for each construct are provided in Supplementary Table 2. Primers used in this study are listed in the Supplementary Table 3.

Deletion of genes by homologous recombination

The clean knock out PAO1 strains were generated by two-step allelic exchange as previously described (Malone et al., 2012). The deletion vectors, containing homologous flanking regions to the target gene, and details about their construction are provided in Supplementary Table 2.

Site directed mutagenesis

FimW mutants were constructed by means of the Quick-Change mutagenesis protocol (Stratagene) using Phusion DNA polymerase (Finnzyme) and dedicated oligonucleotides according to manufacturer's instructions (GE Healthcare). All mutated genes were verified by DNA sequencing.

FimW purification

N-ter His_6 FimW fusions were cloned in pET28a and expressed in *Escherichia coli* BL21 (DE3). After incubating the cultures at 37°C in LB medium supplemented with kanamycin to an OD_{600} of 0.5, expression was induced for 2h at 37°C by adding 0.5mM IPTG. Proteins were 2-steps purified on a ÄKTA purifier using 1 ml HisTrap HP column (GE Healthcare) followed by size-exclusion chromatography (HiLoad 16/60 Superdex 200) in 100 mM Tris-Hcl, 100 mM NaCl, 1 mM DTT, pH 8.5.

Isothermal titration calorimetry

His_6-FimW (10 μM) was titrated with c-di-GMP (up to 200 μM over a set of 30 injections) at 25°C, in purification buffer (100 mM Tris-Hcl, 100 mM NaCl, 1 mM DTT, pH 8.5). Measurements were carried using a Microcal VP-ITC isothermal titration calorimeter (MicroCal, Northampton, MA-USA). Background was subtracted using Origin 7, and replicates were fitted using Prism 7 for Windows (GraphPad softwares).

Differential scanning fluorimetry

Differential scanning fluorimetry was used to semi-quantitatively measure ligand binding by looking at the increase of the thermal stability of FimW (Niesen et al., 2007; Vivoli et al., 2014). Ten micromolars of purified proteins were mixed with 1 to 1.000 µM nucleotide and 5X SYPRO orange (final concentration) in PBS into 96-well PCR plates (#HSP-9655, Bio-Rad). SYPRO orange fluorescence intensity was measured along a temperature gradient ranging from 10 to 90°C, with 0.5°C steps, using a CFX96 Real-Time PCR System (Bio-Rad). Melting temperatures (Tm) were calculated with CFX Manager 2.1 (Bio-Rad) from the melting curves.

Microscale thermophoresis

Microscale thermophoresis was used to quantitatively measure FimW:c-di-GMP binding affinity by looking at the directed movement of fluorescently labelled c-di-GMP in a temperature gradient. This movement is affected by changes in the hydration shell such as conformational rearrangements and ligand binding. A 16-steps serial dilution with a 2:1 pattern of purified His_6-FimW and mutants (ranging *c.a.* 20 µm to 50 nM) was prepared in 200 µL tubes in the protein purification buffer (Tris 100 mM, NaCl 100 mM, DTT 1 mM, pH 8.5) supplemented with 0.05-0.1% (v/v) Tween20. Fluorescein Labelled c-di-GMP (2'-Fluo-AHC-c-di-GMP, ref F009-001, Biolog, Bremen, Germany) was added to a final concentration of 100 nM. After 10 min incubation at room temperature, 16 un-treated glass capillaries Monolith NT™ Standard Treated Capillaries (NanoTemper, Munich, Germany) were loaded with the dilution series. Fluorescence of the 2'-Fluo-AHC-c-di-GMP was measured with a Monolith NT115 (NanoTemper), at 25°C, with a LED power of 100% and a laser power of 60 % (ON time 30 sec, OFF time 5 sec). Data were exported with the NanoTemper Analysis software, then plotted and fitted with Graphpad PRISM 7, using the One-site Total binding equation, to calculate dissociation constants (K_d).

Multi Angle Light Scattering

MALS was used to assess the oligomeric state of FimW. SEC-MALS measurements for His6-FimW were performed at a sample loading concentration of 2 mg/mL in the presence or absence of 300 µM c-di-GMP (≈ 10-fold molar excess) at 6 C in 100 mM Tris, 100 mM NaCl, 1 mM DTT, pH 8.5. Chromatographic separation was achieved using a Wyatt silica SEC column (4.6 × 300 mm, 5 µm bead, 300 Å pore) on an Agilent 1100 HPLC. Elution was monitored using an Agilent absorbance detector (data collected at 280 nm), a Wyatt miniDawn TriStar multi-angle light scattering detector and a Wyatt Optilab rEX differential refractive index detector. The column was equilibrated overnight in the running buffer to obtain stable baseline signals from the detectors before data collection. Inter-detector delay volumes, band broadening corrections, and light-scattering detector normalization were calibrated using an injection of 2 mg/mL BSA solution (ThermoPierce) and standard protocols in ASTRA 5 (Wyatt Technology). Weight-averaged molar mass (Mw), elution concentration, and mass distributions of the samples were calculated using the ASTRA 6 software (Wyatt Technology).

Twitching assays

Twitching motility was assayed using TB plates containing 1% agar as previously described (Huang et al., 2003). Bacteria were picked from fresh plates and stabbed-inoculated through the agar using 200 μL pipet tips and plates incubated 24hrs at 37°C. Twitching rings were visualized by staining with 0.1% Crystal Violet following removal of the agar. Assays were repeated at least 3 times independently.

Piliation assay

The pili purification was performed as previously described with minor modification (Bucior et al., 2012). Briefly, bacteria were grown on LB Agar 1.3% plates at 37°C for 16 hrs, then scrapped and resuspended in PBS (pH 7.4). After adjusting the OD_{600} to 20 and sparing an aliquot for the whole cell piliation control, 1 mL of cells was vortexed for 30 min in 1.5 mL tubes to shear pili off. After centrifugation at 20,000 x g for 10 min to remove the cells and large debris, 850 μL of supernatant was transferred to a fresh tube, and the centrifugation process repeated once. $MgCl_2$ was added to a final concentration of 100 mM, and pili were precipitated overnight at 4°C. Precipitates were pelleted at 16 000 x g for 40 min at 4°C, then resuspended in 100 μL PBS before western blot analysis.

Western blot samples were boiled at 100°C for 5 min in presence of 1% beta-mercaptoethanol and 2% SDS. Proteins were separated on a 15% SDS-PAGE, then semi-dry transferred on a nitrocellulose membrane (Amersham Protan 0.2μm). Membranes were blocked overnight in PMT (PBS, 0.1% v/v Tween 20, 5% w/v dry milk). Primary polyclonal anti-PilA rabbit antibodies (1:5,000) were generously provided by Barbara Kazmierczak (Yale University)(Jain et al., 2012), and were detected with polyclonal swine anti-rabbit-HRP antibodies (1:10,000, Dako, Denmark). After addition of ECL, chemiluminescence was detected with a LAS4000 imager using ImageQuant LAS4000 version 1.3.

Static biofilm assay

Assays were adapted from Merritt *et al*., 2005 (Merritt et al., 2005). Overnight cultures were washed once with LB medium, adjusted to an OD600 of 0.02. 96-well plates containing 190 μL LB medium/well (and antibiotic or inducers when appropriate) were inoculated with 10 μL of the washed bacteria, and incubated at 37°C without shaking for 4, 8, 14, 18, 24 or 48hrs. Plates were washed three times with distilled water. Remaining cell material was then stained with 0.1% Crystal Violet solution (5% methanol, 5% isopropanol in ddH_2O) and washed three times with distilled water to remove excess dye. Crystal Violet was dissolved in 20% acetic acid solution and absorbance measured at 600 nm. Assays were performed with at least 4 wells/strain and repeated independently at least 3 times.

Microscopy

Microscopy images were acquired using a DeltaVision system (GE Healthcare), equipped with a pco.edge sCMOS camera, and a UPlan FL N 100x/1.30 oil objective (Olympus). Images were acquired using softWoRx 6.0 (GE Healthcare). Unless otherwise stated, cells were grown overnight in LB supplemented with the appropriate antibiotic, then diluted 1:100 and grown to an OD_{600} of 0.2 to 0.5.

Venus-FimW was expressed from plasmid pME6032::*venus-fimW* by induction with 100 μM IPTG. For imaging cells in the planktonic state, *P. aeruginosa* was fixed for 5 min with 0.5 M Formaldehyde (F-1268, Sigma) before surface exposure. Bacteria were then spotted on 1% agar LB pads containing IPTG, arabinose or antibiotics when appropriate, and imaged within 20 minutes of surface exposure, at 33°C. Images were analysed with SoftWoRx explorer 1.3 (Applied Precision, USA) and Fiji 1.51k (Schindelin et al., 2012).

Super-resolution three-dimensional structured illumination microscopy (3D-SIM) imaging was performed on a DeltaVision OMX62 Blaze version 4 microscope (Applied Precision, USA) as previously described (Sprecher et al., 2017).

Microfluidics

For the observation of bacteria under flow conditions, we used the CellAsic ONIX system with CellAsic Microfluidic Bacterial Plates (ref. B04A-03-5PK, Merck-Millipore). The microfluidic plate was operated with the CellAsic ONIX Microfluidic Platform controlled by the CellAsic ONIX FG Software 5.0.2.0. Plates were washed with LB, then inoculated with exponentially growing cells (OD_{600} 0.2-0.5) and run at 5 PSI at 33°C. Note that although the CellAsic Bacterial plates are usually used for trapping bacteria, *P. aeruginosa* PAO1 was too small to be properly trapped, but the CellAsic allowed to constraint the cells in a 2D plan when imaging in the lowest trap region (step 5, height: 0.7μm). The inlet region was used as a linear channel.

Microscopy image analysis

To quantify FimW subcellular localization in a reproducible and unbiased manner, we created a foci detection 2-step pipeline. First, the software Oufti (Paintdakhi et al., 2016) was used to detect cells from the bright field images. Second, the custom-made MatLab R2016b program named "WHISIT" which was used to detect polar foci and calculate the pole/cytoplasm fluorescence ratio for each pole. To determine the pole/cytoplasm fluorescence ratio corresponding to the appearance of a foci and translate the ratio into discrete categories (*i.e.*: cytoplasmic distribution, uni- or bi-polar foci), we used as a negative control the Venus-FimW$_{R328A}$ mutant that has a cytoplasmic distribution. Cells were considered to display a polar focus when the pole/cytoplasm fluorescence ratio was above 1.5. Data were plotted with R and RStudio 0.99.489.

The positioning *P. aeruginosa* cells in a flow (standing, angled, parallel to the surface) was measured as the projected length/width ratio for each cell using CellProfiler 2.2.0, as previously described (Luo et al., 2015). The probability of each aspect ratio was plotted with PRISM with a bin size = 0.5.

Transmission electron microscopy

Log phase cultures (OD_{600} 0.25 to 0.5) were fixed in the planktonic state with 0.1% glutaraldehyde and then spotted on a 400 mesh copper grid covered with a parlodion and carbon film. Alternatively, cells were first spotted on a grid, incubated for 15 min at room temperature, and then fixed in a surface-associated state with 0.1% glutaraldehyde. Preparations were then washed 4 times with

water and negatively-stained twice with 0.5% uranyl acetate. Images were taken with a Morgagni 268D FEI (80kV) and a FEI T12 (120kV) - TVIPS F416 electron microscope.

Acknowledgements

Supplementary data

SUPPLEMENTAL METHODS

c-di-GMP effector screen

FimW was identified as a putative c-di-GMP effector using a biochemical approach taking advantage of a c-di-GMP-Capture Compound technology coupled to Mass Spectrometry (CCMS). Briefly, following capture with a c-di-GMP capture compound, washing, digestion with Trypsin, LC-MS/MS analysis and label-free quantification, proteins were sorted as detailed in a video format in Laventie *et al* 2015 (Laventie et al., 2015). The 4 replicates for the soluble fraction were performed in the presence of 5 µM c-di-GMP-CC, and the competition experiment with 1 mM c-di-GMP.

Pili-specific phage sensitivity assay

P. aeruginosa was grown in LB overnight at 37°C, then washed once in LB and diluted in LB to a final OD_{600} of 0.05 in a 96-well plate. The pili-specific DMS3 bacteriophage (Budzik et al., 2004) was added to obtain a final titer of 10^3 phage/mL. The 96-well plate was incubated in a Synergy2 plate reader (BioTek) at 37°C with shaking, and the OD_{600} was measured every 30 min for 24hrs.

Motility assays

Motility plates consisted in 25 mL M9G (M9 salts, glucose 0.2% w/v, casamino acids 0.5% w/v, $MgSO_4$ 1mM) solidified with 0.8% agar for swarming assays and 0.8% agar for swimming assays swarm plates were inoculated by spotting 2.5µL overnight culture and incubated 24hrs at 37°C. Swimming plates were stab inoculated using toothpicks from an overnight culture and plates incubated 24hrs at 37°C. Swarm diameters measured with ImageJ. Assays were repeated 3 times independently. Error bars are representing the SEM.

Phylogenetic analysis

The microbial Tree of Life was obtained from the Huttenhower Lab (1, https://huttenhower.sph.harvard.edu/phylophlan). The original bacterial phylogeny per species was restricted to taxa encoding for either FimW or FimX homologs according to the OMA database of orthologues (2, https://omabrowser.org/oma/home/). The tree was then further simplified in order to retain a single representative leaflet per species (72 terminal branches). Co-occurrences of additional group of homologs was inferred from OMA and marked on the phylogeny.

1- PhyloPhlAn is a new method for improved phylogenetic and taxonomic placement of microbes, Nicola Segata, Daniela Börnigen, Xochitl C. Morgan, and Curtis Huttenhower. Nature Communications 4, 2013.
2- Altenhoff A et al., The OMA orthology database in 2015: function predictions, better plant support, synteny view and other improvements, Nucleic Acids Research, 2015, 43 (D1): D240-D249 (doi:10.1093/nar/gku1158).

SUPPLEMENTAL TABLES

Supplementary Table S1. Bacterial strains used in this study.

**Supplementary Table S2. Plasmids used in this study.**

Supplementary Table S3. Primers used in this study.

Supplementary Table S4. Genes co-occurring with *fimW*.

List of genes co-occurring with fimW (PA4958, from *P. aeruginosa* PAO1) computed by online tool MicroScope (hosted on the Microbial Genome Annotation & Analysis Platform, https://www.genoscope.cns.fr/). The list contains the 500 best hits, and the T4P related genes are highlighted in orange.

FIG. S1. VOLCANOPLOTS OF *P. AERUGINOSA* PROTEINS ENRICHED BY CCMS.

SUPPLEMENTAL FIGURES
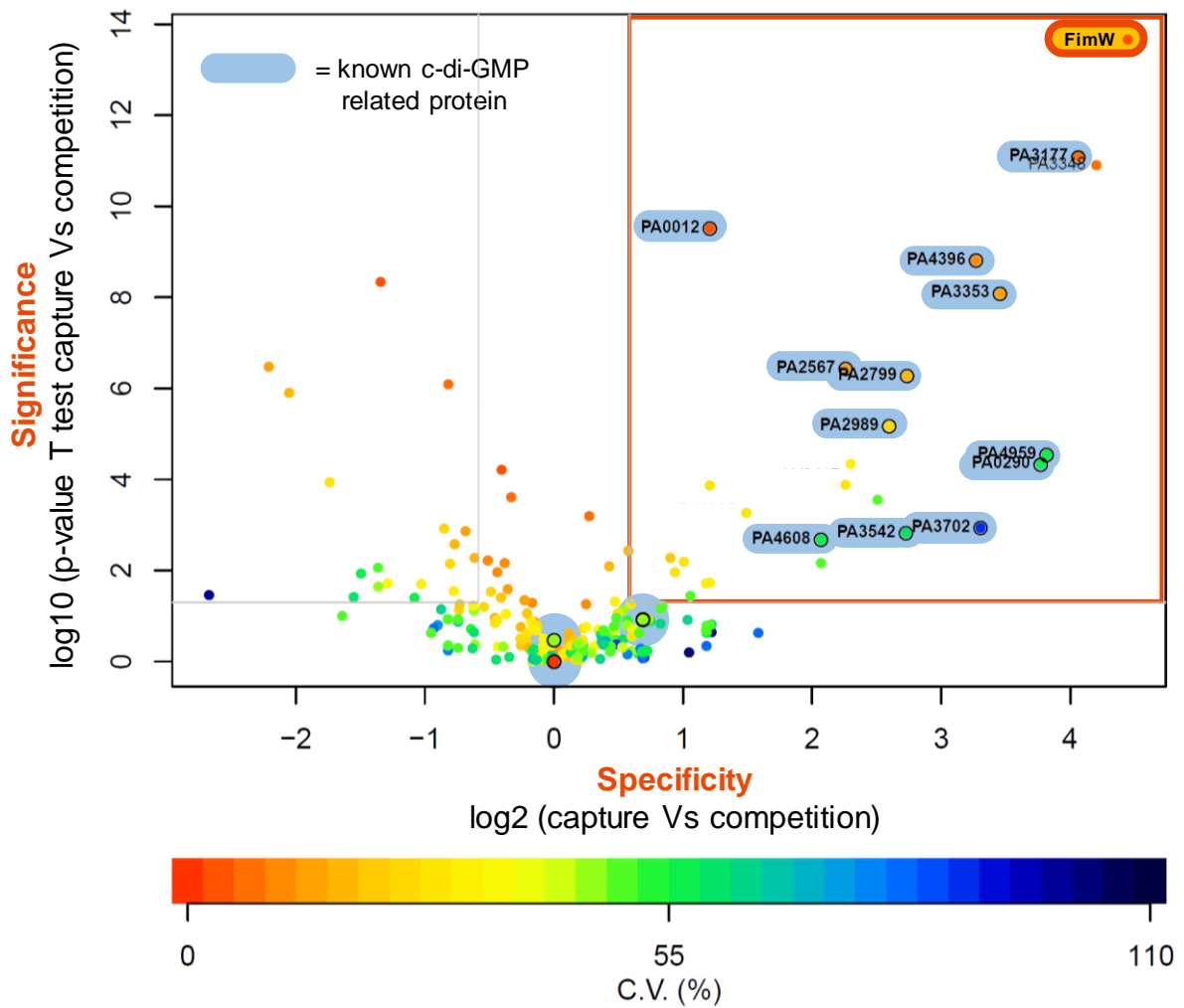
Log2-intensity ratio of detected peptide between the capture and competition experiments were calculated and plotted versus values derived from significance analysis (modified t-statistic, empirical Bayes method). Proteins significantly enriched are indicated in the orange box (within the significance thresholds for *p*-values <0.05 and intensity ratios >1.5-fold). FimW was enriched 22-fold in the capture experiment compared to the competition experiment, with a *p*-value < 0.0001. The circled dots correspond to known c-di-GMP binding proteins.

Misprediction of the *fimW* (PA4958) ORF in F<small>IG</small>. S2. *Pseudomonas aeruginosa* PAO1 in databases

The predicted *fimW* ORF (1464 nt) starts with the infrequent bacterial start codon GTG. A *fimW* ORF longer on the 3' end (1824 nt) was predicted by the Geneious 10.0.7 ORF finder, starting with a classic ATG start codon (Suppl. Fig. S2A). The protein coding prediction based on EMBOSS 6.5.7 tool tcode also favors the long ORF. Additionally, in the *Pseudomonas* Ortholog Group POG004573, 22 of 27 *fimW* orthologs are predicted as the long ORF and only 5 with a short ORF (http://www.pseudomonas.com). Western blot analysis of PAO1 carrying a C-ter flag tagged FimW (tagged chromosomally at the original locus) showed a measured protein molecular weight of *c.a.* 70 kDa, corresponding the predicted mass of the long ORF (70.5 kDa, Suppl. Fig. S2B). Finally, the expression *in trans* from a pME6032 vector of the short FimW form doesn't complement the attachment defect of a ΔfimW strain, while the long form does (Suppl. Fig. S2C).
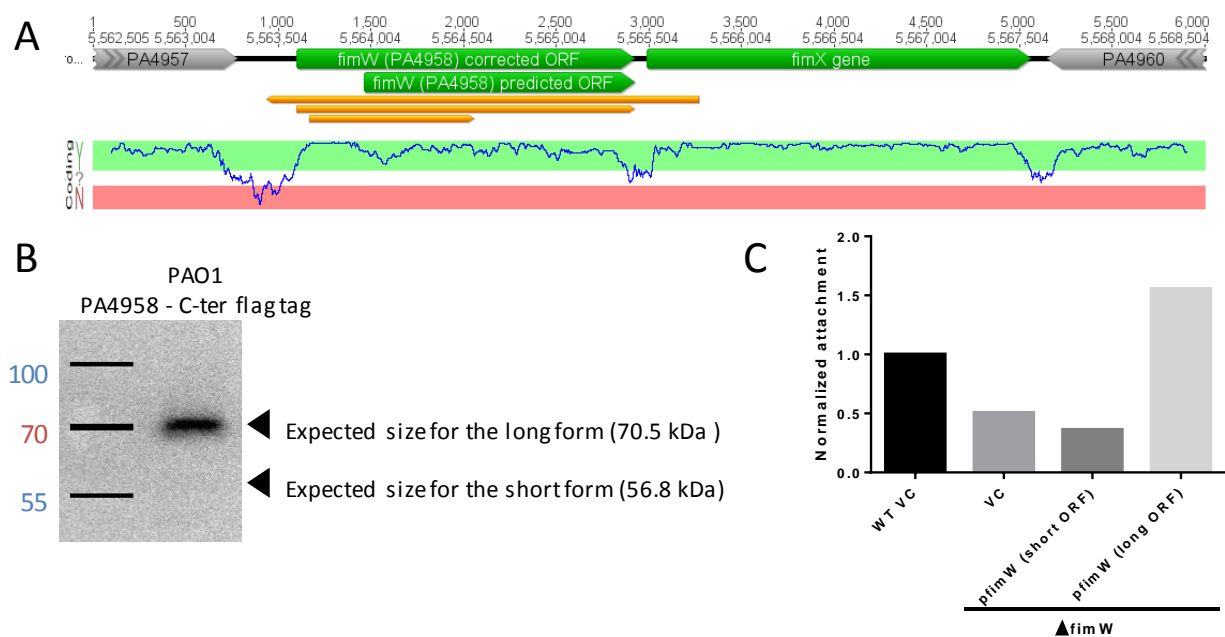
(**A**) PA4958 ORF prediction (> 500bp; start codons considered: CTG, TTG, ATG; protein coding prediction based on EMBOSS 6.5.7 tool tcode using a window size of 200 and a step size of 3, green = coding, red = non coding ; generated with Geneious 6.1.2). (**B**) Chromosomal C-terminal fusion of a Flag tag after PA4958 to measure the size of the expressed protein (anti-flag western blot). (**C**) Complementation of the attachment defect of a ΔfimW strain with either the predicted (short) or corrected (long) form of FimW.

A

B
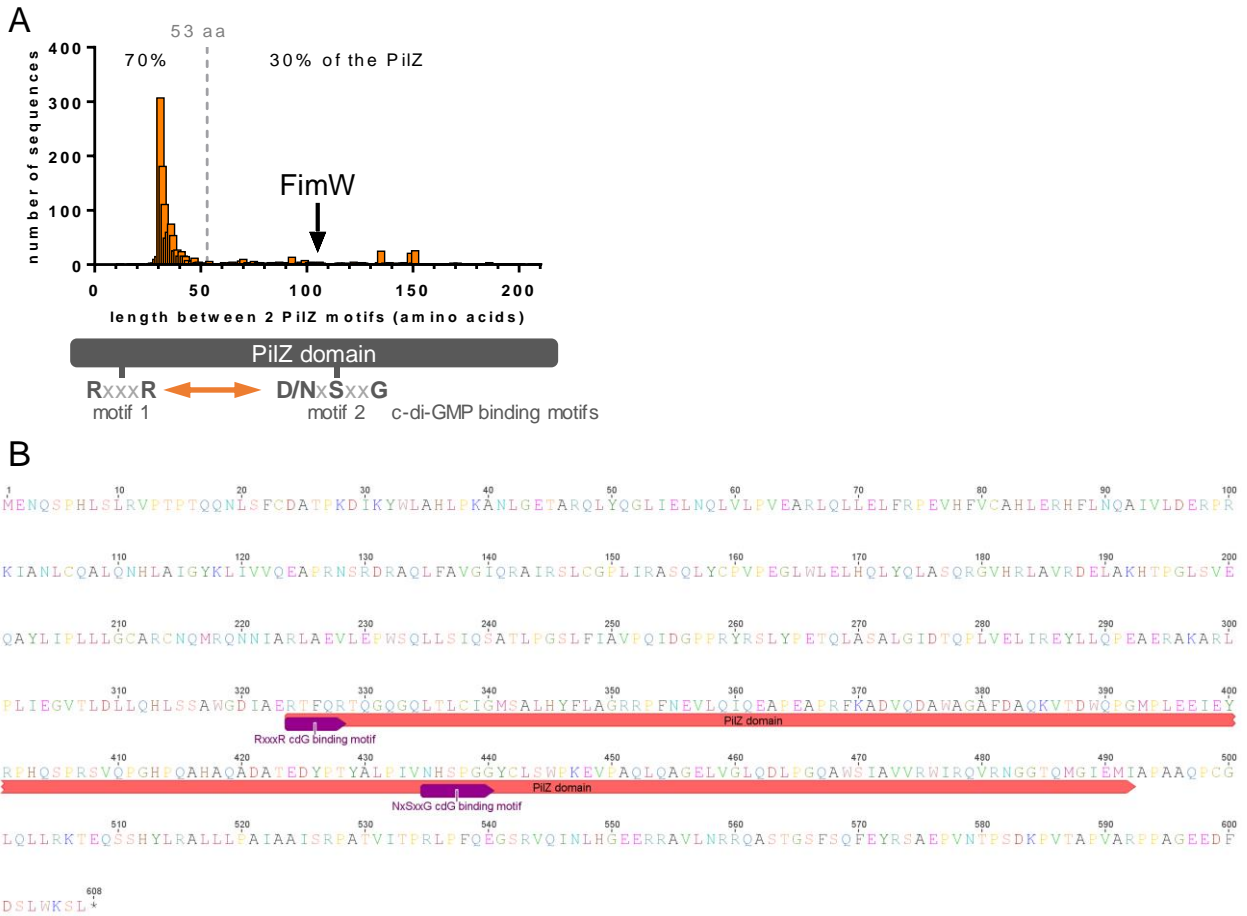
(A) Length in amino acid binding motifs (RxxxR domains. All the PilZ

FIG. S3. FIMW PILZ DOMAIN AND C-DI-GMP BINDING MOTIFS.

between the 2 c-di-GMP and D/NxSxxG) in PilZ domains in PFAM (RP75)

were considered (1531 sequences, http://pfam.xfam.org/). Most PilZ domains have a distance centered around 31 amino acids (median distance: 36 amino acids), and 70% of the sequences displays a linker between the 2 motifs ranging from 12 to 53 amino acids long. FimW's PilZ domain has an unusually long 106 amino acid linker. Among *P. aeruginosa* PilZ domain containing proteins, this feature is shared only by PA2989 which has an 87 amino acids long linker. (B) PilZ domain and c-di-GMP binding motifs annotated on the sequence of FimW (PA4958) from *Pseudomonas aeruginosa* PAO1. The FimW PilZ domain limits correspond to the limits of the PilZ domain of PA4608 (from *Pseudomonas aeruginosa* PAO1), as predicted by HHPRED (https://toolkit.tuebingen.mpg.de/hhpred# (Soding et al., 2005)). Created with Geneious 10.0.7.
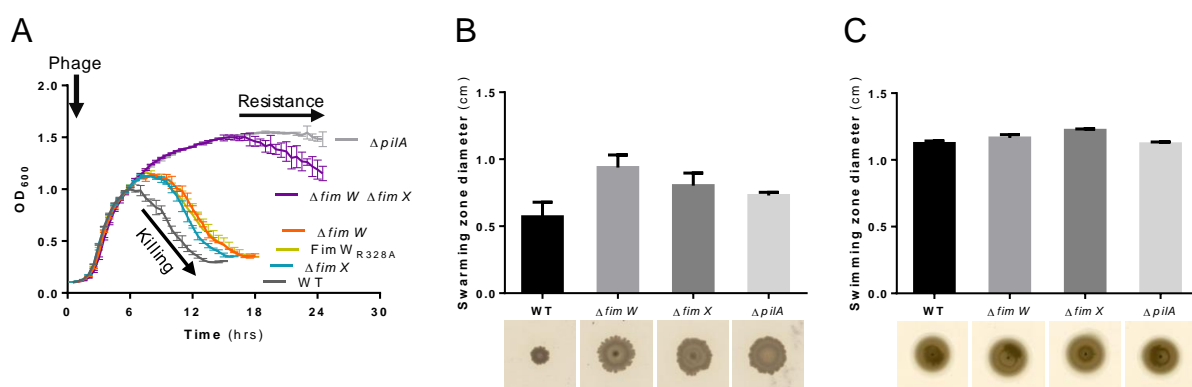
FIG. S4. FIMW T4P REGULATION AND CONSEQUENCE ON T4P-SPEFCIFIC PHAGE RESISTANCE AND MOTILITY.

(A) T4P-specific phage (DMS3) bacterial killing (n = 2). FimW does not control swarming or swimming. (B) Swarming and (C) swimming motility assays. Images below the bar chart represent typical swarming or swimming zones. Error bars represent the SEM (n = 3).
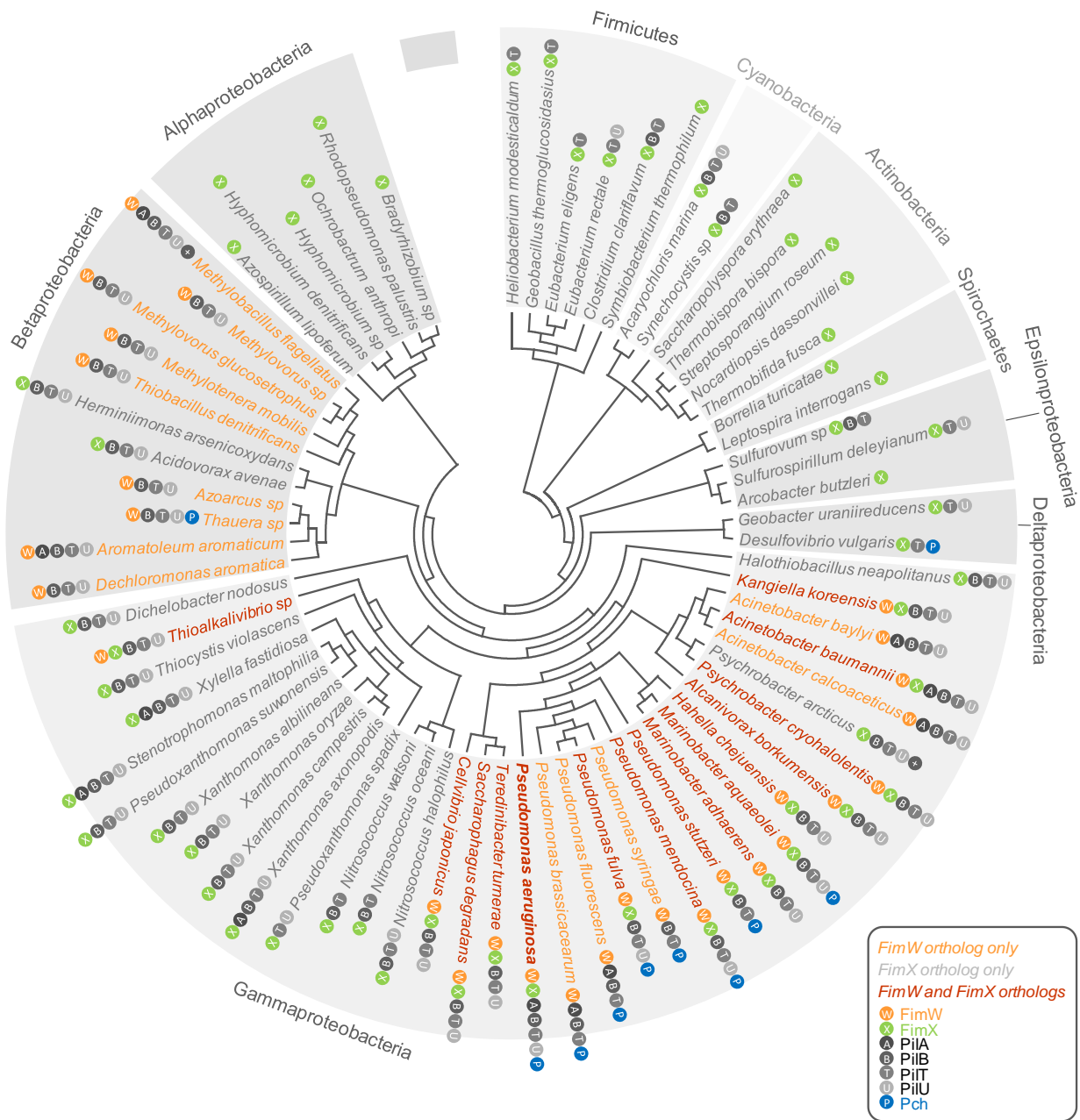
FIG. S5. PHYLOGENETIC TREE OF ALL BACTERIAL SPECIES HARBORING FIMW (ORANGE NAMES) OR FIMX (GREY NAMES) ORTHOLOGS.

The circles attached to species names indicate when orthologs of the following genes where found: *pch*, *fimW*, *fimX*, *pilA* (major pilin), and the T4P ATPases *pilB*, *pilT*, and *pilU* as markers of the presence of T4P machineries.

References

Almblad, H., Harrison, J.J., Rybtke, M., Groizeleau, J., Givskov, M., Parsek, M.R., and Tolker-Nielsen, T. (2015). The Cyclic AMP-Vfr Signaling Pathway in Pseudomonas aeruginosa Is Inhibited by Cyclic Di-GMP. Journal of Bacteriology *197*, 2190-2200.

Amikam, D., and Galperin, M.Y. (2006). PilZ domain is part of the bacterial c-di-GMP binding protein. Bioinformatics *22*, 3-6.

Anyan, M.E., Amiri, A., Harvey, C.W., Tierra, G., Morales-Soto, N., Driscoll, C.M., Alber, M.S., and Shrout, J.D. (2014). Type IV pili interactions promote intercellular association and moderate swarming of Pseudomonas aeruginosa. Proceedings of the National Academy of Sciences of the United States of America *111*, 18013-18018.

Baker, A.E., Diepold, A., Kuchma, S.L., Scott, J.E., Ha, D.G., Orazi, G., Armitage, J.P., and O'Toole, G.A. (2016). PilZ Domain Protein FlgZ Mediates Cyclic Di-GMP-Dependent Swarming Motility Control in Pseudomonas aeruginosa. Journal of Bacteriology *198*, 1837-1846.

Baraquet, C., and Harwood, C.S. (2013). Cyclic diguanosine monophosphate represses bacterial flagella synthesis by interacting with the Walker A motif of the enhancer-binding protein FleQ. Proceedings of the National Academy of Sciences of the United States of America *110*, 18478-18483.

Baraquet, C., Murakami, K., Parsek, M.R., and Harwood, C.S. (2012). The FleQ protein from Pseudomonas aeruginosa functions as both a repressor and an activator to control gene expression from the pel operon promoter in response to c-di-GMP. Nucleic acids research *40*, 7207-7218.

Basso, P., Ragno, M., Elsen, S., Reboud, E., Golovkine, G., Bouillot, S., Huber, P., Lory, S., Faudry, E., and Attree, I. (2017). Pseudomonas aeruginosa Pore-Forming Exolysin and Type IV Pili Cooperate To Induce Host Cell Lysis. MBio *8*.

Belas, R. (2014). Biofilms, flagella, and mechanosensing of surfaces by bacteria. Trends in Microbiology *22*, 517-527.

Benach, J., Swaminathan, S.S., Tamayo, R., Handelman, S.K., Folta-Stogniew, E., Ramos, J.E., Forouhar, F., Neely, H., Seetharaman, J., Camilli, A., *et al.* (2007). The structural basis of cyclic diguanylate signal transduction by PilZ domains. The EMBO Journal *26*, 5153-5166.

Brill-Karniely, Y., Jin, F., Wong, G.C., Frenkel, D., and Dobnikar, J. (2017). Emergence of complex behavior in pili-based motility in early stages of P. aeruginosa surface adaptation. Sci Rep *7*, 45467.

Bruzaud, J., Tarrade, J., Coudreuse, A., Canette, A., Herry, J.M., Taffin de Givenchy, E., Darmanin, T., Guittard, F., Guilbaud, M., and Bellon-Fontaine, M.N. (2015). Flagella but not type IV pili are involved in the initial adhesion of Pseudomonas aeruginosa PAO1 to hydrophobic or superhydrophobic surfaces. Colloids Surf B Biointerfaces *131*, 59-66.

Bucior, I., Pielage, J.F., and Engel, J.N. (2012). Pseudomonas aeruginosa pili and flagella mediate distinct binding and signaling events at the apical and basolateral surface of airway epithelium. PLoS Pathogens *8*, e1002616.

Budzik, J.M., Rosche, W.A., Rietsch, A., and O'Toole, G.A. (2004). Isolation and characterization of a generalized transducing phage for Pseudomonas aeruginosa strains PAO1 and PA14. Journal of Bacteriology *186*, 3270-3273.

Burrows, L.L. (2012). Twitching Motility: Type IV Pili in Action. Annual review of microbiology *66*, 493-520.

Chiang, P., and Burrows, L.L. (2003). Biofilm formation by hyperpiliated mutants of Pseudomonas aeruginosa. Journal of Bacteriology *185*, 2374-2378.

Chiang, P., Habash, M., and Burrows, L.L. (2005). Disparate subcellular localization patterns of Pseudomonas aeruginosa Type IV pilus ATPases involved in twitching motility. Journal of Bacteriology *187*, 829-839.

Conrad, J.C., Gibiansky, M.L., Jin, F., Gordon, V.D., Motto, D.A., Mathewson, M.A., Stopka, W.G., Zelasko, D.C., Shrout, J.D., and Wong, G.C. (2011). Flagella and pili-mediated near-surface single-cell motility mechanisms in P. aeruginosa. Biophys J *100*, 1608-1616.

Cowles, K.N., and Gitai, Z. (2010). Surface association and the MreB cytoskeleton regulate pilus production, localization and function in Pseudomonas aeruginosa. Molecular Microbiology *76*, 1411-1426.

Ellison, C.K., Kan, J., Dillard, R.S., Kysela, D.T., Ducret, A., Berne, C., Hampton, C.M., Ke, Z., Wright, E.R., Biais, N., *et al.* (2017). Obstruction of pilus retraction stimulates bacterial surface sensing. Science *358*, 535-538.

Fulcher, N.B., Holliday, P.M., Klem, E., Cann, M.J., and Wolfgang, M.C. (2010). The Pseudomonas aeruginosa Chp chemosensory system regulates intracellular cAMP levels by modulating adenylate cyclase activity. Molecular Microbiology *76*, 889-904.

Habazettl, J., Allan, M.G., Jenal, U., and Grzesiek, S. (2011). Solution structure of the PilZ domain protein PA4608 complex with cyclic di-GMP identifies charge clustering as molecular readout. The Journal of biological chemistry *286*, 14304-14314.

Hoffman, M.D., Zucker, L.I., Brown, P.J., Kysela, D.T., Brun, Y.V., and Jacobson, S.C. (2015). Timescales and Frequencies of Reversible and Irreversible Adhesion Events of Single Bacterial Cells. Anal Chem *87*, 12032-12039.

Huang, B., Whitchurch, C.B., and Mattick, J.S. (2003). FimX, a Multidomain Protein Connecting Environmental Signals to Twitching Motility in Pseudomonas aeruginosa. Journal of Bacteriology *185*, 7068-7076.

Hug, I., Deshpande, S., Sprecher, K.S., Pfohl, T., and Jenal, U. (2017). Second messenger-mediated tactile response by a bacterial rotary motor. Science *358*, 531-534.

Jain, R., Behrens, A., Kaever, V., and Kazmierczak, B.I. (2012). Type IV pilus assembly in Pseudomonas aeruginosa over a broad range of cyclic di-GMP concentrations. Journal of Bacteriology *194*, 4285-4294.

Jenal, U., Reinders, A., and Lori, C. (2017). Cyclic di-GMP: second messenger extraordinaire. Nat Rev Microbiol *15*, 271-284.

Jones, C.J., Utada, A., Davis, K.R., Thongsomboon, W., Zamorano Sanchez, D., Banakar, V., Cegelski, L., Wong, G.C., and Yildiz, F.H. (2015). C-di-GMP Regulates Motile to Sessile Transition by Modulating MshA Pili Biogenesis and Near-Surface Motility Behavior in Vibrio cholerae. PLoS Pathogens *11*, e1005068.

Kazmierczak, B.I., Lebron, M.B., and Murray, T.S. (2006). Analysis of FimX, a phosphodiesterase that governs twitching motility in Pseudomonas aeruginosa. Molecular Microbiology *60*, 1026-1043.

Klausen, M., Aaes-Jorgensen, A., Molin, S., and Tolker-Nielsen, T. (2003). Involvement of bacterial migration in the development of complex multicellular structures in Pseudomonas aeruginosa biofilms. Molecular Microbiology *50*, 61-68.

Kuchma, S.L., Delalez, N.J., Filkins, L.M., Snavely, E.A., Armitage, J.P., and O'Toole, G.A. (2015). Cyclic Di-GMP-Mediated Repression of Swarming Motility by Pseudomonas aeruginosa PA14 Requires the MotAB Stator. Journal of Bacteriology *197*, 420-430.

Kulasekara, B.R., Kamischke, C., Kulasekara, H.D., Christen, M., Wiggins, P.A., and Miller, S.I. (2013). c-di-GMP heterogeneity is generated by the chemotaxis machinery to regulate flagellar motility. Elife *2*, e01402.

Laventie, B.J., Nesper, J., Ahrne, E., Glatter, T., Schmidt, A., and Jenal, U. (2015). Capture compound mass spectrometry--a powerful tool to identify novel c-di-GMP effector proteins. Journal of visualized experiments : JoVE.

Lele, P.P., Hosu, B.G., and Berg, H.C. (2013). Dynamics of mechanosensing in the bacterial flagellar motor. Proceedings of the National Academy of Sciences of the United States of America *110*, 11839-11844.

Luo, Y., Zhao, K., Baker, A.E., Kuchma, S.L., Coggan, K.A., Wolfgang, M.C., Wong, G.C., and O'Toole, G.A. (2015). A Hierarchical Cascade of Second Messengers Regulates Pseudomonas aeruginosa Surface Behaviors. mBio *6*.

Malone, J.G., Jaeger, T., Manfredi, P., Dotsch, A., Blanka, A., Bos, R., Cornelis, G.R., Haussler, S., and Jenal, U. (2012). The YfiBNR signal transduction mechanism reveals novel targets for the evolution of persistent Pseudomonas aeruginosa in cystic fibrosis airways. PLoS Pathogens *8*, e1002760.

Matsuyama, B.Y., Krasteva, P.V., Baraquet, C., Harwood, C.S., Sondermann, H., and Navarro, M.V. (2016). Mechanistic insights into c-di-GMP-dependent control of the biofilm regulator FleQ from Pseudomonas aeruginosa.

Proceedings of the National Academy of Sciences of the United States of America *113*, E209-218.

McCarter, L., Hilmen, M., and Silverman, M. (1988). Flagellar dynamometer controls swarmer cell differentiation of V. parahaemolyticus. Cell *54*, 345-351.

Merighi, M., Lee, V.T., Hyodo, M., Hayakawa, Y., and Lory, S. (2007). The second messenger bis-(3'-5')-cyclic-GMP and its PilZ domain-containing receptor Alg44 are required for alginate biosynthesis in Pseudomonas aeruginosa. Molecular Microbiology *65*, 876-895.

Merritt, J.H., Kadouri, D.E., and O'Toole, G.A. (2005). Growing and analyzing static biofilms. Curr Protoc Microbiol *Chapter 1*, Unit 1B 1.

Miller, J.H. (1972). Experiments in molecular genetics (Cold Spring Harbor Laboratory).

Navarro, M.V., Nabanita, Bae, N., Wang, Q., and Sondermann, H. (2009). Structural analysis of the GGDEF-EAL domain-containing c-di-GMP receptor FimX. Structure (London, England : 1993) *17*, 1104-1116.

Nesper, J., Reinders, A., Glatter, T., Schmidt, A., and Jenal, U. (2012). A novel capture compound for the identification and analysis of cyclic di-GMP binding proteins. Journal of Proteomics *75*, 4874-4878.

Niesen, F.H., Berglund, H., and Vedadi, M. (2007). The use of differential scanning fluorimetry to detect ligand interactions that promote protein stability. Nature protocols *2*, 2212-2221.

O'Toole, G.A., and Kolter, R. (1998). Flagellar and twitching motility are necessary for Pseudomonas aeruginosa biofilm development. Molecular Microbiology *30*, 295-304.

O'Toole, G.A., and Wong, G.C. (2016). Sensational biofilms: surface sensing in bacteria. Current Opinion in Microbiology *30*, 139-146.

Paintdakhi, A., Parry, B., Campos, M., Irnov, I., Elf, J., Surovtsev, I., and Jacobs-Wagner, C. (2016). Oufti: an integrated software package for high-accuracy, high-throughput quantitative microscopy analysis. Mol Microbiol *99*, 767-777.

Persat, A., Inclan, Y.F., Engel, J.N., Stone, H.A., and Gitai, Z. (2015). Type IV pili mechanochemically regulate virulence factors in Pseudomonas aeruginosa. Proceedings of the National Academy of Sciences of the United States of America.

Pultz, I.S., Christen, M., Kulasekara, H.D., Kennard, A., Kulasekara, B., and Miller, S.I. (2012). The response threshold of Salmonella PilZ domain proteins is determined by their binding affinities for c-di-GMP. Molecular Microbiology *86*, 1424-1440.

Rodesney, C.A., Roman, B., Dhamani, N., Cooley, B.J., Touhami, A., and Gordon, V.D. (2017). Mechanosensing of shear by Pseudomonas aeruginosa leads to increased levels of the cyclic-di-GMP signal initiating biofilm development. Proc Natl Acad Sci U S A *114*, 5906-5911.

Russell, M.H., Bible, A.N., Fang, X., Gooding, J.R., Campagna, S.R., Gomelsky, M., and Alexandre, G. (2013). Integration of the Second Messenger c-di-GMP into the Chemotactic Signaling Pathway. mBio *4*.

Rybtke, M.T., Borlee, B.R., Murakami, K., Irie, Y., Hentzer, M., Nielsen, T.E., Givskov, M., Parsek, M.R., and Tolker-Nielsen, T. (2012). Fluorescence-based reporter for gauging cyclic di-GMP levels in Pseudomonas aeruginosa. Applied and Environmental Microbiology *78*, 5060-5069.

Schindelin, J., Arganda-Carreras, I., Frise, E., Kaynig, V., Longair, M., Pietzsch, T., Preibisch, S., Rueden, C., Saalfeld, S., Schmid, B., *et al.* (2012). Fiji: an open-source platform for biological-image analysis. Nat Methods *9*, 676-682.

Shikata, M., Hayashi, N., Fujimoto, A., Nakamura, T., Matsui, N., Ishiyama, A., Maekawa, Y., and Gotoh, N. (2016). The pilT gene contributes to type III ExoS effector injection into epithelial cells in Pseudomonas aeruginosa. J Infect Chemother.

Siryaporn, A., Kuchma, S.L., O'Toole, G.A., and Gitai, Z. (2014). Surface attachment induces Pseudomonas aeruginosa virulence. Proceedings of the National Academy of Sciences of the United States of America.

Soding, J., Biegert, A., and Lupas, A.N. (2005). The HHpred interactive server for protein homology detection and structure prediction. Nucleic Acids Res *33*, W244-248.

Sprecher, K.S., Hug, I., Nesper, J., Potthoff, E., Mahi, M.A., Sangermani, M., Kaever, V., Schwede, T., Vorholt, J., and Jenal, U. (2017). Cohesive Properties of the Caulobacter crescentus Holdfast Adhesin Are Regulated by a Novel c-di-GMP Effector Protein. MBio *8*.

Toutain, C.M., Caizza, N.C., Zegans, M.E., and O'Toole, G.A. (2007). Roles for flagellar stators in biofilm formation by Pseudomonas aeruginosa. Research in Microbiology *158*, 471-477.

Toutain, C.M., Zegans, M.E., and O'Toole, G.A. (2005). Evidence for two flagellar stators and their role in the motility of Pseudomonas aeruginosa. Journal of Bacteriology *187*, 771-777.

Van Dellen, K.L., Houot, L., and Watnick, P.I. (2008). Genetic analysis of Vibrio cholerae monolayer formation reveals a key role for DeltaPsi in the transition to permanent attachment. J Bacteriol *190*, 8185-8196.

Vivoli, M., Novak, H.R., Littlechild, J.A., and Harmer, N.J. (2014). Determination of protein-ligand interactions using differential scanning fluorimetry. Journal of visualized experiments : JoVE, 51809.

Wolfgang, M.C., Lee, V.T., Gilmore, M.E., and Lory, S. (2003). Coordinate regulation of bacterial virulence genes by a novel adenylate cyclase-dependent signaling pathway. Dev Cell *4*, 253-263.

Xu, L., Venkataramani, P., Ding, Y., Liu, Y., Deng, Y., Yong, G.L., Xin, L., Ye, R., Zhang, L., Yang, L., *et al.* (2016a). A Cyclic di-GMP-binding Adaptor Protein Interacts with Histidine Kinase to Regulate Two-Component Signaling. The Journal of biological chemistry.

Xu, L., Xin, L., Zeng, Y., Yam, J.K., Ding, Y., Venkataramani, P., Cheang, Q.W., Yang, X., Tang, X., Zhang, L.H., *et al.* (2016b). A cyclic di-GMP-binding adaptor protein interacts with a chemotaxis methyltransferase to control flagellar motor switching. Sci Signal *9*, ra102.

CHAPTER 4

_____

SPRECHER K.S. ET AL., 2017

Cohesive Properties of the Caulobacter crescentus Holdfast Adhesin Are Regulated by a Novel c-di-GMP Effector Protein

Kathrin S. Sprecher,[a] Isabelle Hug,[a] Jutta Nesper,[a †] Eva Potthoff,[b *] Mohamed-Ali Mahi,[c]

Matteo Sangermani,[a] Volkhard Kaever,[d] Torsten Schwede,[c] Julia Vorholt,[b] Urs Jenal [a]

[a] - Focal Area of Infection Biology, Biozentrum, University of Basel, Basel, Switzerlanda

[b] - Institute of Microbiology, ETH Zurich, Zurich, Switzerland

[c] - Focal Area of Computational & Systems Biology, Biozentrum, University of Basel, Basel, Switzerland

[d] - Research Core Unit Metabolomics and Institute of Pharmacology, Hannover Medical School, Hannover, Germany

Cohesive Properties of the *Caulobacter crescentus* Holdfast Adhesin Are Regulated by a Novel c-di-GMP Effector Protein

Kathrin S. Sprecher,[a] Isabelle Hug,[a] Jutta Nesper,[a]† Eva Potthoff,[b]*
Mohamed-Ali Mahi,[c] Matteo Sangermani,[a] Volkhard Kaever,[d] Torsten Schwede,[c]
Julia Vorholt,[b] Urs Jenal[a]

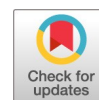Focal Area of Infection Biology, Biozentrum, University of Basel, Basel, Switzerland[a]; Institute of Microbiology, ETH Zurich, Zurich, Switzerland[b]; Focal Area of Computational & Systems Biology, Biozentrum, University of Basel, Basel, Switzerland[c]; Research Core Unit Metabolomics and Institute of Pharmacology, Hannover Medical School, Hannover, Germany[d]

ABSTRACT When encountering surfaces, many bacteria produce adhesins to facilitate their initial attachment and to irreversibly glue themselves to the solid substrate. A central molecule regulating the processes of this motile-sessile transition is the second messenger c-di-GMP, which stimulates the production of a variety of exopolysaccharide adhesins in different bacterial model organisms. In *Caulobacter crescentus*, c-di-GMP regulates the synthesis of the polar holdfast adhesin during the cell cycle, yet the molecular and cellular details of this control are currently unknown. Here we identify HfsK, a member of a versatile *N*-acetyltransferase family, as a novel c-di-GMP effector involved in holdfast biogenesis. Cells lacking HfsK form highly malleable holdfast structures with reduced adhesive strength that cannot support surface colonization. We present indirect evidence that HfsK modifies the polysaccharide component of holdfast to buttress its cohesive properties. HfsK is a soluble protein but associates with the cell membrane during most of the cell cycle. Coincident with peak c-di-GMP levels during the *C. crescentus* cell cycle, HfsK relocalizes to the cytosol in a c-di-GMP-dependent manner. Our results indicate that this c-di-GMP-mediated dynamic positioning controls HfsK activity, leading to its inactivation at high c-di-GMP levels. A short C-terminal extension is essential for the membrane association, c-di-GMP binding, and activity of HfsK. We propose a model in which c-di-GMP binding leads to the dispersal and inactivation of HfsK as part of holdfast biogenesis progression.

IMPORTANCE Exopolysaccharide (EPS) adhesins are important determinants of bacterial surface colonization and biofilm formation. Biofilms are a major cause of chronic infections and are responsible for biofouling on water-exposed surfaces. To tackle these problems, it is essential to dissect the processes leading to surface colonization at the molecular and cellular levels. Here we describe a novel c-di-GMP effector, HfsK, that contributes to the cohesive properties and stability of the holdfast adhesin in *C. crescentus*. We demonstrate for the first time that c-di-GMP, in addition to its role in the regulation of the rate of EPS production, also modulates the physicochemical properties of bacterial adhesins. By demonstrating how c-di-GMP coordinates the activity and subcellular localization of HfsK, we provide a novel understanding of the cellular processes involved in adhesin biogenesis control. Homologs of HfsK are found in representatives of different bacterial phyla, suggesting that they play important roles in various EPS synthesis systems.

Microorganisms are predominantly surface associated and often grow in complex multicellular structures called biofilm (1, 2). At the same time, they are able to disperse as motile single cells and explore their environment (3, 4). To effectively switch between these fundamentally different lifestyles, many bacteria have evolved regulatory mechanisms that robustly promote cellular processes associated with motility and sessility, respectively. The ubiquitous second messenger c-di-GMP plays a central role in this transition (5). While c-di-GMP interferes with flagellum- and pilus-based motility (6, 7), it stimulates the synthesis of adhesion factors and extracellular matrix components like curli fibers or exopolysaccharides (EPSs) (8–10). A prime example of c-di-GMP-mediated control is the production of cellulose, a secreted glucose polymer mediating surface attachment and biofilm stability in many bacteria (11). Cellulose is synthesized and translocated through the cell envelope by the membrane-integral BcsAB complex (12). The synthase BcsA is held in an autoinhibitory state by a gating loop that blocks the access of glucose monomers to the catalytic site and that is released upon c-di-GMP binding (13, 14). Similarly, the synthesis of poly-β-1,6-N-acetylglucosamine in *Escherichia coli* requires the simultaneous binding of c-di-GMP to the synthase PgaC and to its cosynthase PgaD to stabilize their interaction and boost their activity (15).

We use *Caulobacter crescentus* as a model to study the regulatory mechanisms of the motile-to-sessile transition of bacteria. This Gram-negative freshwater bacterium has a biphasic cell cycle with an asymmetric division producing motile, replication-inert swarmer (SW) cells and sessile, replication-competent stalked (ST) cells (16). SW cells are equipped with a flagellar motor and adhesive pili and remain motile for an extended period before differentiating into ST cells. During this process, they replace their flagellum and pili with an EPS adhesin, the holdfast, which is located at the tip of a cell extension, the stalk. The holdfast, which consists of EPS (17, 18) and additional, undefined components (18–20), mediates strong and permanent attachment of ST cells to surfaces (21–23). The holdfast EPS is composed of oligomers of N-acetylglucosamine and is synthesized and anchored by the holdfast synthesis (Hfs) and holdfast anchoring (Hfa) proteins, most of which are encoded in two separate operons in the *C. crescentus* genome (23–25). On the basis of homology models and deletion studies, several glycosyltransferases were predicted to participate in the assembly of a glycosyl oligomer onto a lipid anchor (23, 26, 27). The sugar moieties were proposed to be chemically modified. For example, HfsH is thought to deacetylate a glycosyl subunit(s) of the growing polymer (19). The lipid-linked oligomers are then flipped through the cytoplasmic membrane into the periplasm, further polymerized, and exported to the cell surface (23). Mutants that lack the anchor protein HfaA, -B, or -D shed their holdfast. How these proteins contribute to EPS anchoring is not understood (25, 28).

C. crescentus cell morphogenesis and behavior are regulated by c-di-GMP, the levels of which oscillate through the cell cycle (29, 30). The c-di-GMP concentration is low in SW cells, peaks during the SW-to-ST-cell transition, and later becomes intermediate in dividing cells (29, 31). Changes in the c-di-GMP concentration are mediated by cell type-specific diguanylate cyclases (DGCs) and phosphodiesterases (PDEs). While c-di-GMP levels are kept low in SW cells by the PDE PdeA, the c-di-GMP upshift during cell differentiation is mediated by the specific degradation of PdeA (32) and the consecutive activation of PleD, a DGC that is active only in the sessile cell type (33, 34). The upshift of c-di-GMP during cell differentiation leads to ejection of the flagellum (35), stimulates the assembly of the stalk, and prompts the biogenesis of the holdfast adhesin (29). However, how c-di-GMP stimulates these processes has remained unclear.

Here we identify the acetyltransferase HfsK as a novel c-di-GMP effector protein that is required for the formation of a cohesive and stably anchored holdfast. Cells harboring an *hfsK* deletion shed abnormal holdfasts that formed elastic filamentous structures when subjected to shear stress. We show that HfsK activity depends on its association with the cytoplasmic membrane. HfsK remains membrane associated throughout most of the cell cycle but is released into the cytoplasm in a c-di-GMP-dependent manner during the SW-to-ST transition, coinciding with peak c-di-GMP concentrations and with holdfast assembly. We identify a short 25-amino-acid stretch at the C terminus of HfsK

TABLE 1 HfsK and CC1244 detection by CCMS screening for c-di-GMP effectors

Protein and expt[a]	No. of spectral counts of identified peptides (CCMS experiment/CCMS competition)[b]	
	Soluble fraction	Membrane fraction
HfsK (CC3689)		
1	9/0	14/5
2	8/0	13/4
3	10/0	14/4
CC1244		
1	4/0	1/0
2	0/0	2/1
3	0/0	8/3

[a]Results of three independent experiments using 10 μM (soluble fraction) or 8 μM (membrane fraction) c-di-GMP capture compound are shown.
[b]Competition experiments were performed in the presence of 1 mM c-di-GMP.

as a critical determinant of c-di-GMP binding, membrane association, and protein function. On the basis of our data, we propose that c-di-GMP controls HfsK by coupling its activity to its membrane compartmentalization.

RESULTS

CC3689 is a novel c-di-GMP binding protein. We have recently described capture compound-coupled mass spectrometry (CCMS) technology, a biochemical method to isolate c-di-GMP binding proteins (36). Using CCMS, we isolated an uncharacterized protein (CC3689) directly from *C. crescentus* cell extracts (Table 1). Structure-based homology searches with HHpred (37) revealed that CC3689 belongs to the Gcn5-related *N*-acetyltransferase (GNAT) family, a ubiquitous group of *N*-acyltransferases that acylate a variety of different substrates, ranging from proteins to polyamines and aminoglycosides (38).

To confirm the binding of c-di-GMP to CC3689, we affinity purified a His-CC3689 fusion protein and used it for isothermal titration calorimetry (ITC). His-CC3689 bound c-di-GMP in a concentration-dependent manner with an equilibrium disassociation constant (K_d) of 724 nM and a binding stoichiometry of 2:1 (c-di-GMP to CC3689) (Fig. 1A). To test binding specificity, we performed UV cross-linking assays (5). His-CC3689 binding to ^{33}P-labeled c-di-GMP was effectively outcompeted by the addition of unlabeled c-di-GMP but not by the addition of other nucleotides (Fig. 1B). From this, we concluded that CC3689 is a *bona fide* c-di-GMP binding protein.

HfsK and its paralogs contribute to *C. crescentus* surface attachment by modifying the holdfast adhesin. *C. crescentus* encodes two additional paralogs of *cc3689* (*cc2278* and *cc1244*) with sequence identities of around 30% (see Fig. S1A and B in the supplemental material). While the neighboring genes gave no hints about a possible function of *cc3689*, *cc2278* lies in an operon containing a gene for a predicted glycosyltransferase that is required for holdfast synthesis (27). In addition, when analyzing the genomic context of *cc3689* orthologs, we found that many of them cluster with genes predicted to function in EPS biogenesis (see Fig. S1C). Strains encoding such orthologs belong to different phyla, indicating that the connection of this protein class with EPS synthesis is of ancient evolutionary origin. Interestingly, in three closely related marine species, namely, *Maricaulis maris*, *Oceanicaulis alexandrii*, and *Woodsholea maritima* (39), orthologs of *cc3689* cluster with homologs of *C. crescentus* holdfast synthesis genes (40) (see Fig. S1D). On the basis of these observations and the results presented below, we renamed CC3689 holdfast synthesis protein K (HfsK).

To test whether *hfsK* and its paralogs *cc2278* and *cc1244* are involved in holdfast biogenesis, we engineered deletions of all three genes in the chromosome of *C. crescentus* wild-type strain CB15 and investigated surface colonization by the resulting mutant strains as a proxy for their ability to form a functional holdfast. The Δ*hfsK* mutant showed a 90% reduction in surface colonization after 30 min and after 24 h of
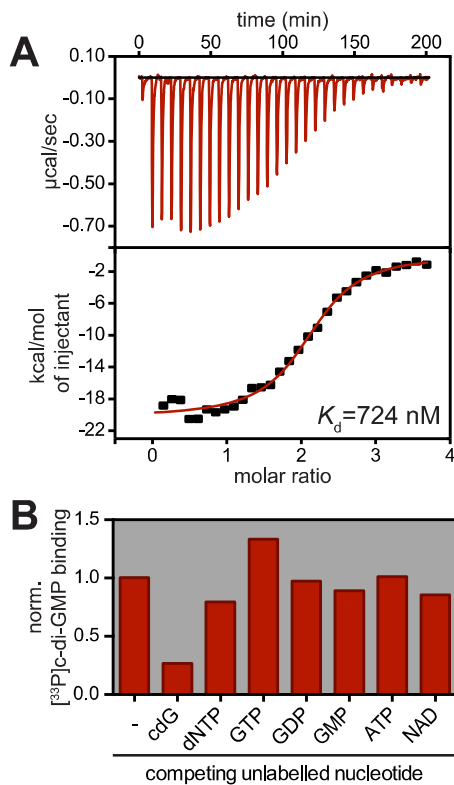
FIG 1 HfsK specifically binds c-di-GMP. (A) ITC measuring the interaction of His-HfsK with c-di-GMP. Heat release upon ligand injection (top), integrated heat plotted against the molar ratio of ligand and protein (bottom), and the resulting disassociation constant (K_d) are shown. (B) Quantified autoradiographs of 1 μM purified His-HfsK that has been UV cross-linked to 10 μM [^{33}P]c-di-GMP in the presence or absence of a 10-fold excess of nonlabeled nucleotides to test competition. norm., normalized.

growth compared to the wild type. In contrast, the Δ*cc2278* mutant showed only minor defects in surface colonization during the initial phase of growth (Fig. 2A; see Fig. S2A). Surface colonization was fully restored when the *hfsK* and *cc2278* mutants were complemented with a wild-type copy of the respective gene in *trans*, but the two proteins failed to cross-complement each other (see Fig. S2B). A Δ*hfsK* Δ*cc2278* double mutant showed lower surface colonization than the *hfsK* single mutant, indicating additive contributions of both proteins to surface attachment (Fig. 2A). Finally, deletion of the third paralog, *cc1244*, revealed no obvious phenotype alone or in combination with deletions of *hfsK* or *cc2278*. However, the Δ*hfsK* Δ*cc2278* Δ*cc1244* triple mutant failed to adhere completely (Fig. 2A; see Fig. S2A).

In line with the strong surface colonization defect, the Δ*hfsK* mutant showed a severe reduction in holdfast biogenesis. Upon staining of holdfast with the Oregon green-labeled lectin wheat germ agglutinin (OG-WGA), 63% of the wild-type ST cells carried a holdfast while only 4% of the Δ*hfsK* mutant cells were holdfast positive (see Fig. S2C). Whereas strains carrying deletions of *cc2278* or *cc1244* showed normal holdfast formation, holdfast formation was completely abolished in a triple mutant lacking HfsK and its paralogs.

The observed reduction of Δ*hfsK* mutant cells bearing an adhesive holdfast could be explained by either diminished holdfast production or defective anchoring and increased shedding of holdfast material (28). To distinguish between these possibilities, wild-type and mutant strains were allowed to adsorb to glass surfaces for 2 h before the glass was washed, stained with OG-WGA, and analyzed by fluorescence microscopy. Glass surfaces incubated with the wild-type strain were covered with cells adhering via their holdfasts. In contrast, only a few cells of the Δ*hfsK* mutant remained attached after washing, yet the amount of holdfast material observed was comparable to that of the
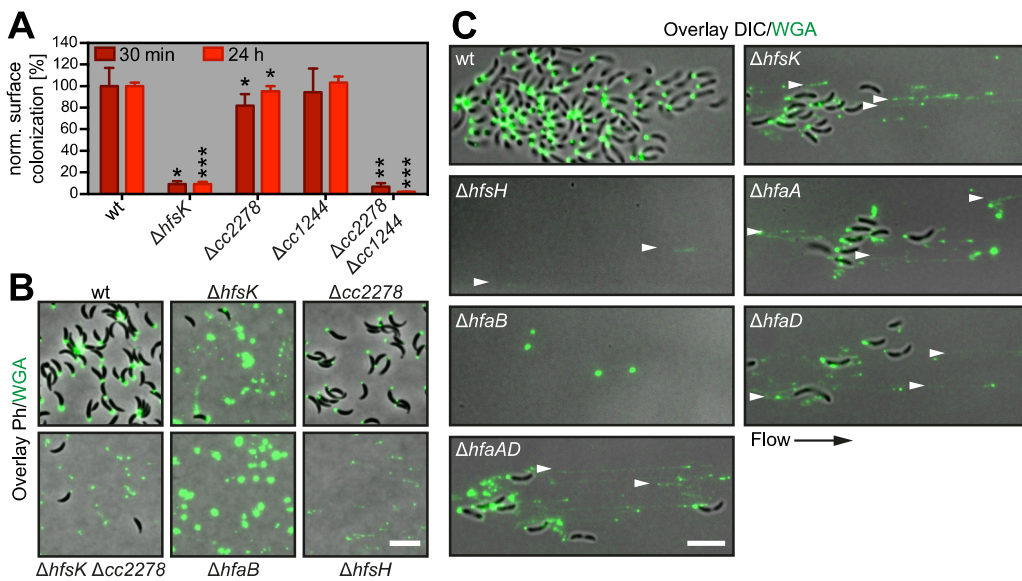
FIG 2 HfsK deletion leads to an incoherent holdfast that does not support surface colonization. (A) Surface colonization by the wild type (wt) and mutants lacking the *hfsK* paralog family determined by crystal violet staining of adherent cells after 30 min (dark red bars) and 24 h (light red bars) of growth in microtiter plates. norm, normalized per condition. Error bars show standard deviations (SD) of three independent experiments. *, **, and *** represent P values of <0.1, <0.01, and <0.001, respectively. (B) Analysis of holdfast shedding in *hfsK* and *cc2278* mutants, as well as in strains that shed (Δ*hfaB*) or form incoherent (Δ*hfsH*) holdfast. Shown are overlays of phase-contrast (Ph) and fluorescence images of adhered WGA-stained holdfast on glass coverslips after 2 h of cell adsorption. (C) Holdfasts analyzed under shear stress after 15 h of growth in a microfluidic channel with a constant flow of fresh medium containing OG-WGA. Shown is an overlay of fluorescence and inverted differential interference contrast (DIC) images. Arrowheads point to holdfast filaments. Scale bars in panels B and C, 5 μm.

wild type (Fig. 2B; see Fig. S2C). Of note, this is similar to the shedding phenotype observed in a strain lacking the holdfast anchor protein HfaB (25, 28). Cells lacking CC2278 did not shed their holdfast but produced smaller, less intensely stained adhesins. A Δ*hfsK* Δ*cc2278* double mutant shed small holdfasts, again indicating that the two proteins affect holdfast properties independently. Intriguingly, the Δ*cc2278* Δ*cc1244* double mutant and the triple mutant completely failed to adhere to glass (see Fig. S2C and D). This and the observation that surface colonization of the Δ*cc2278* Δ*cc1244* double mutant was barely affected in polystyrene microtiter plates (see Fig. S2A) indicated that distinct members of this family of proteins might optimize the attachment to different surface chemistry.

Mutants with mutations in *hfsK* or its paralogs retained normal surface-adherent pili and active flagellar motors (see Fig. S2E and F), two c-di-GMP-dependent cellular appendages that are required for optimal surface attachment (22, 27, 29, 41). On the basis of these data, we propose that the reduction in surface colonization observed in *hfsK*, *cc2278*, and *cc1244* mutants can be attributed to defective holdfast biogenesis or, in the case of an *hfsK* mutant, possibly defective holdfast anchoring.

HfsK contributes to holdfast cohesion and adhesion strength. Recently, Wan and colleagues showed that a mutant lacking the polysaccharide deacetylase HfsH sheds holdfast material that is less cohesive and forms fiber-like structures when exposed to shear forces (19). The authors suggested that the degree of acetylation might be critical for the physical properties of holdfast. Similarly, the *N*-acyltransferase HfsK might influence the acetylation state of holdfast. To analyze holdfast performance under shear stress, wild-type and mutant bacteria were grown in a microfluidic device under permanent flow of fresh medium. After overnight growth, individual wild-type cells formed microcolonies with discrete foci of WGA-stained holdfast material at the adherent cell poles (Fig. 2C). Mutants lacking HfaB or HfsH were unable to attach but shed compact holdfast structures and faint holdfast fibers, respectively. In contrast, the *hfsK* mutant formed microcolonies smaller than those of the wild type

with fluorescent trails of abraded, filamentous holdfast structures. Holdfast trails were generated by mutant cells that secreted holdfast material onto the surface while slowly drifting with the medium flow (see Movies S1 and S2). Some holdfast structures elongated into extended filaments from which cells were dangling for some time before the connection ruptured. Upon rupturing, several holdfast filaments bounced back like a released rubber band (see Movie S3), indicating that the cohesive and elastic properties of the holdfast are severely altered in the ΔhfsK mutant.

To analyze the adhesive forces of wild-type and mutant holdfasts more precisely, we used a single-cell force spectroscopy (SCFS) approach and fluidic force microscopy (FluidFM) technology. This setup enables single-cell manipulation by combining the precise force control of an atomic force microscope with a microfluidic device (42, 43) (see Fig. S2G). Comparison of detachment forces revealed that, on average, wild-type cells showed approximately five times stronger adherence than ΔhfsK mutant cells (see Fig. S2H). Of note, in several cases, cells could not be detached at all and were not included in the analysis. During holdfast biogenesis, the dimensions of the secreted structures increase over time (44). Thus, we next compared the adherence of ΔhfsK mutant cells with that of weaker (young holdfast) and more intense holdfast staining (mature holdfast). Larger holdfasts were indeed more likely to remain surface bound, with ruptures often occurring between the adhesin and the cell body (see Fig. S2I). These results indicated that holdfast from the ΔhfsK mutant, although more fragile and less cohesive, can still gain adhesion strength over time, as observed in holdfasts of wild-type cells (20).

The above-described experiments argued that holdfasts of ΔhfsK mutant cells, similar to those of ΔhfsH mutant cells, show altered cohesive or adhesive properties. However, it is unclear if the observed changes influence the overall properties of the holdfast material or its anchoring in the cell envelope. In line with the latter, microfluidic experiments exposed similar phenotypes of ΔhfsK mutant cells and mutants lacking the holdfast anchor protein HfaA or HfaD. When growing ΔhfaA mutants, ΔhfaD mutants, or double mutants in microfluidic devices, trails of WGA-stained material were observed, similar to the structures formed by ΔhfsK mutants (Fig. 2C). Thus, we asked whether the holdfast anchoring process is still functional in ΔhfsK mutant cells. For this, we took advantage of the observation that hfs, but not hfa, mutants, are able adhere to holdfasts shed by anchor mutants (21). We combined the ΔhfsK deletion with a ΔhfsJ deletion, which completely abolishes holdfast EPS formation (26), and tested the coattachment of these cells with a ΔhfaB mutant strain. Deletion of hfsK did not change the coattachment capacity of the holdfast-deficient strain (see Fig. S2J), suggesting that this strain produces an intact holdfast anchor.

Together, these results demonstrate that HfsK contributes to the effective surface adherence of C. crescentus by modulating the cohesive properties of the holdfast material and/or by facilitating the efficient anchoring of the adhesin in the cell envelope that is necessary to withstand strong shear forces.

c-di-GMP controls HfsK compartmentalization. Holdfast production is controlled by c-di-GMP and coincides with an upshift of c-di-GMP levels during the SW-to-ST-cell transition (27, 29). From this and from the observation that HfsK binds c-di-GMP, we anticipated that the activity of this protein might be controlled by c-di-GMP during the cell cycle, akin to other c-di-GMP effector proteins (30, 45, 46). Similar to the expression of other hfs genes (26), that of hfsK is specific to the late predivisional stage of the cell cycle (47). However, this does not result in significant changes in HfsK protein levels during the cell cycle (see Fig. S3A). Accordingly, HfsK levels showed only minor changes in engineered strains with different c-di-GMP levels (see Fig. S3B and C). Thus, c-di-GMP affects HfsK abundance only marginally, making it unlikely that holdfast maturation is controlled by c-di-GMP at the level of HfsK expression or stability.

Although assembly and maturation of EPS generally occur in or at the cytoplasmic membrane (48), HfsK is predicted to be a cytosolic protein (49). We used cell fractionation experiments to determine HfsK localization. After the ultracentrifugation of cell
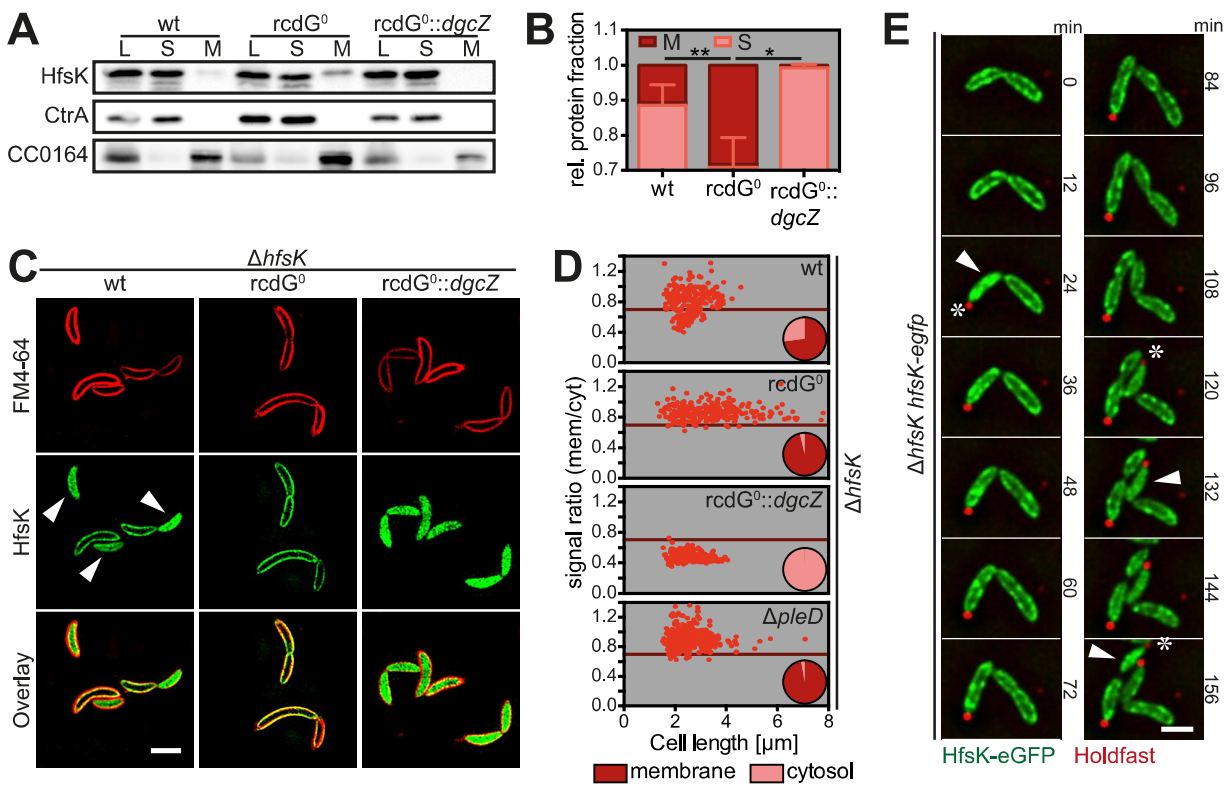
FIG 3 c-di-GMP controls HfsK localization. (A, B) HfsK localization in wild-type (wt), rcdG0 (c-di-GMP low), and rcdG0::*dgcZ* (c-di-GMP high) cells analyzed by cell fractionation, followed by immunoblotting. CtrA (cytosolic) and CC0164 (inner membrane) were used as controls. (A) Lanes: cell lysates, L; soluble fraction, S; membrane fraction, M. (B) Quantification of three independent cell fractionations showing the fractions of soluble (light red) and membrane-associated (dark red) HfsK. Error bars show the SD, * and ** represent *P* values of <0.1 and <0.01, respectively. (C) 3D-SIM images of HfsK-eGFP in cells with different c-di-GMP levels. Staining was done with the membrane dye FM4-64. Arrowheads indicate cells with cytosolic HfsK-eGFP. Scale bar, 2 μm. (D) Quantification of HfsK-eGFP localization in standard fluorescence microscopy images. The ratio of the average signal intensities in the membrane and cytosolic compartments is correlated with cell length. The pie chart inset shows the fraction of cells with a membrane-associated (ratio$_{membrane-cytosol}$ > 0.7; dark red) or cytosolic (ratio, ≤0.7; light red) GFP signal. *n* = 250 cells per strain in two independent experiments. (E) Time-lapse video of Δ*hfsK* P$_{van}$-*hfsK-egfp* mutant cells grown on PYE agarose pads supplemented with rhodamine-WGA and vanillic acid at 30°C. Cells with dispersed HfsK-eGFP (arrowheads) and the first appearance of holdfast in each cell (asterisks) are indicated. Scale bar, 1 μm. In all of the images, expression of *egfp* constructs and *dgcZ* was induced with 0.55 mM vanillic acid and 0.5 mM IPTG, respectively.

lysates, about 90% of the HfsK remained in the soluble fraction, while 10% was retained in the pellet (Fig. 3A and B). This indicated that HfsK is at least partially membrane associated, possibly by binding to an interaction partner in the membrane. In agreement with this idea, HfsK was lost from the membrane fraction when lysates were treated with increasing salt concentrations that are known to disturb such interactions (50) (see Fig. S4A). Importantly, none of the known inner membrane components of the holdfast synthesis machinery was required for sequestration of HfsK to the membrane (see Fig. S4B).

To test if the membrane association of HfsK is c-di-GMP controlled, cell fractionation was carried out with a newly constructed strain that lacks all of the genes encoding DGCs and PGEs (rcdG0) and with the same strain harboring a P$_{lac}$-driven copy of *dgcZ* from *E. coli* (rcdG0::*dgcZ*), which allows tuning of intracellular c-di-GMP levels. Expression of the DgcZ DGC (51) in this background produced c-di-GMP levels 6-fold higher than those of the wild type (see Fig. S3B). In the rcdG0 strain, the fraction of membrane-associated HfsK increased to about 30%, while the rcdG0::*dgcZ* strain had lost the HfsK protein from the membrane fraction almost entirely (Fig. 3A and B). Likewise, when c-di-GMP was added to cell extracts of the rcdG0 strain before fractionation, HfsK primarily localized to the cytosol (see Fig. S4C). These results indicated that c-di-GMP modulates HfsK membrane interaction, with high levels of c-di-GMP promoting its cytosolic state and low levels of c-di-GMP stimulating its association with the membrane.

HfsK dynamically repositions to the cytoplasm during the cell cycle. To more carefully analyze HfsK localization and its association with the cytoplasmic membrane, we expressed a P_{van}-driven chromosomal copy of *hfsK-eGFP* in the Δ*hfsK* mutant strain (see Fig. S4D). Localization of HfsK-enhanced green fluorescent protein (eGFP) relative to the membrane was visualized by superresolution three-dimensional structured illumination microscopy (3D-SIM) after cells were stained with the membrane-specific dye FM4-64. While the majority of cells showed peripheral HfsK-eGFP colocalizing with the membrane stain, HfsK-eGFP was dispersed in the cytosol in a subfraction of the population (Fig. 3C and D). Of note, with the exception of HfsH, which was reported to be cytosolic (19), all functional mCherry fusions of proteins catalyzing early steps of holdfast biogenesis (see Fig. S4E) localized to the membrane but lacked the cytosolic subfraction characteristic of HfsK (see Fig. S4F).

To investigate if these changes are driven by c-di-GMP, HfsK-eGFP localization was analyzed in cells harboring different c-di-GMP levels. Strikingly, in the rcdG0 strain, HfsK-eGFP showed strong membrane localization in a large majority of the cells, while HfsK-eGFP was entirely cytosolic in the rcdG0::*dgcZ* strain (Fig. 3C and D). Note that the rcdG0 strain constructed in this study shows a filamentous morphology similar to that of the cdG0 strain lacking all DGCs (29). To carefully quantify HfsK-eGFP localization at the single-cell level, averages of the fluorescent signals at the cell periphery and in the cytosol were determined and ratios were calibrated by using soluble eGFP and the membrane dye FM4-64 (see Fig. S4G). The fraction of cells with membrane-associated HfsK-eGFP ranged from 0% in the rcdG0::*dgcZ* strain to roughly 70% in the wild-type background and 96% in the rcdG0 background (Fig. 3D). Importantly, wild-type cells with membrane-associated HfsK-eGFP included the entire spectrum of measured cell length, while cells with a cytosolic signal were all short. This suggested that HfsK distribution changes during the cell cycle. To test this, time-lapse experiments were carried out with a Δ*hfsK* mutant strain expressing HfsK-eGFP. HfsK-eGFP was membrane associated in newborn SW cells but became cytosolic about 24 min after division and shortly after the appearance of holdfast (Fig. 3E; see Fig. S4H). About 12 min after its dispersal, HfsK-eGFP gradually relocalized to the membrane, coincident with cells starting to elongate and divide. These observations indicated that HfsK transiently delocalizes in newly differentiated ST cells, coincident with peak c-di-GMP levels during the cell cycle. In line with this idea, HfsK-eGFP was not discharged from the membrane fraction in a strain lacking PleD, the main DGC responsible for the upshift of c-di-GMP during the SW-to-ST transition (29, 52) (Fig. 3D).

Together, these results demonstrated that HfsK localization is dynamic and indicated that its repositioning to the cytoplasm during the SW-to-ST transition is driven by peak levels of c-di-GMP.

The C terminus is required for the activity and membrane localization of HfsK. Despite low sequence homology, GNAT proteins have a remarkably conserved core fold (38). The closest homolog of HfsK with a solved 3D structure is FemX, an enzyme involved in peptidoglycan synthesis in Gram-positive bacteria (53, 54). Both proteins have two GNAT domains in tandem. Sequence comparisons revealed that HfsK has a short C-terminal extension of 25 amino acids that is absent in FemX (see Fig. S5A). Surprisingly, an eGFP fusion protein with truncated HfsK (HfsK$_{trnc}$) that lacks this extension, although being stable, lost its characteristic membrane association and, in contrast to full-length HfsK-eGFP, failed to complement the Δ*hfsK* phenotype (Fig. 4A to C; see Fig. S4C). HfsK and HfsK$_{trnc}$ localized exclusively to the membrane when fused to the transmembrane (TM) helix of *C. crescentus* SecE, which is sufficient to restrict reporter proteins to the membrane (55) (Fig. 4A and B). However, these proteins harboring the TM from SecE failed to respond to changes in c-di-GMP (see Fig. S5B). Whereas TM-tagged wild-type HfsK was fully functional, cells expressing HfsK$_{trnc}$ did not support surface colonization even if shuttled to the cytoplasmic membrane by the exogenous TM segment (Fig. 4C). Thus, the C terminus of HfsK is required for its membrane localization and for its function. These experiments also indicated that
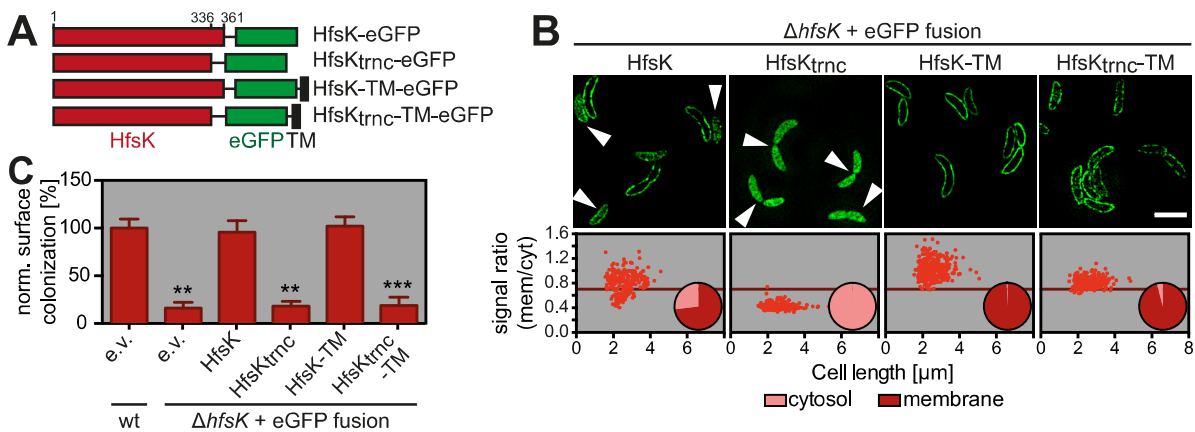
FIG 4 The C terminus of HfsK is an important determinant of its localization and function. (A) Schematic representation of the HfsK-eGFP mutants used in this experiment. Amino acid positions are indicated at the top. The drawing is not to scale. TM, transmembrane domain of SecE. (B) Localization quantification of different HfsK-eGFP mutants expressed by the addition of 0.55 mM vanillic acid as described in the legend to Fig. 3D. *n* = 260 cells per strain from two independent experiments. Representative 3D-SIM images for visualization are shown at the top. Arrowheads indicate cells with dispersed HfsK-eGFP. Note that because of the weak signal intensity of HfsK$_{trnc}$-TM, the 3D-SIM image recreation resulted in images with a high background signal level. Scale bar, 3 μm. (C) Functionality of HfsK-eGFP mutants compared to that of a wild-type strain harboring the control empty vector (e.v.) in surface colonization after 24 h of growth in microtiter plates in the presence of 0.1 mM vanillic acid. Error bars show the SD of three independent experiments. ** and *** represent *P* values of <0.01 and <0.001, respectively.

membrane-associated HfsK represents the active species of the protein and that release of HfsK from the membrane at high levels of c-di-GMP might lead to its inactivation.

c-di-GMP drives HfsK to the cytosol but is dispensable for its activity. We have shown above that both c-di-GMP and the C terminus of HfsK are important for the localization of the protein during the cell cycle. This indicated that the C terminus of HfsK itself could be targeted by c-di-GMP and could contribute to c-di-GMP binding. In agreement with this, we found that a StrepII-HfsK fusion lacking the 25 C-terminal amino acids (HfsK$_{trnc}$) bound c-di-GMP more weakly than wild-type HfsK did (Fig. 5A). Structural examination of c-di-GMP binding proteins had revealed important roles for arginine residues in ligand binding (56). We thus generated the mutant protein HfsK(RR352AA) that had two central arginine residues of the C terminus (see Fig. S1A) changed to alanine. Similar to shortened HfsK$_{trnc}$, this mutation reduced the affinity for c-di-GMP (Fig. 5A). To identify residues located in the core region of HfsK that are involved in c-di-GMP binding, we compared the sequences of HfsK and its two *C. crescentus* paralogs. Because HfsK and CC1244, but not CC2278, were identified by CCMS, we searched for arginine residues that are conserved in HfsK and CC1244 but not in CC2278 (see Fig. S1A). Several of these residues of HfsK (R102, R112, R151, R240, and R267) were replaced with alanine, and the resulting mutant proteins were expressed as StrepII-tagged fusions in *E. coli*. Binding studies with radiolabeled c-di-GMP identified HfsK$_{R112a}$ as the only mutant variant with reduced binding affinity for c-di-GMP (Fig. 5A). These results suggested that R112, as well as arginine residues located in the HfsK C terminus, may contribute to c-di-GMP binding.

Importantly, HfsK-eGFP fusions containing R112A or RR352AA point mutations remained membrane associated even in strains harboring high levels of c-di-GMP, arguing that they no longer respond to the second messenger *in vivo* (Fig. 5B). Functional analysis revealed that the HfsK$_{RR352AA}$-eGFP fusion failed to restore the Δ*hfsK* phenotype, underlining the importance of the C terminus for protein function. In contrast, expression of the HfsK$_{R112a}$-eGFP fusion was able to substitute for HfsK in surface colonization and holdfast biogenesis (Fig. 5C and D; see Fig. S5C). Together, these data support a model in which c-di-GMP binding determines HfsK subcellular localization and possibly HfsK activity. Our data are in line with the view that binding of c-di-GMP inactivates HfsK by sequestering the protein away from a membrane-associated active conformation. In agreement with this view, we found that unphysi-
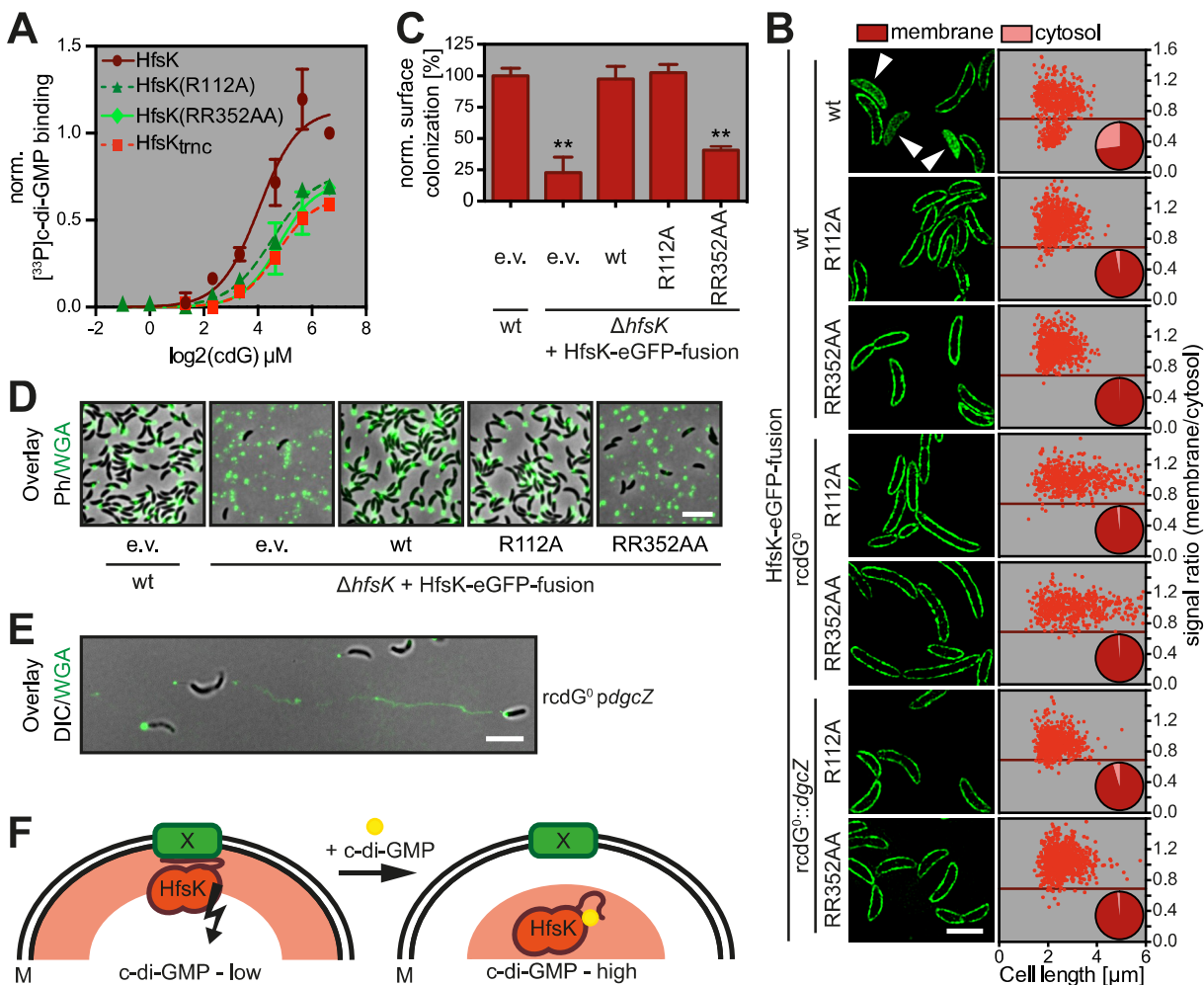
Sprecher et al.

mBio®

FIG 5 c-di-GMP binding is required for HfsK delocalization but not for HfsK-mediated surface colonization. (A) Quantified autoradiographs of 1 μM purified StrepII-HfsK mutants that were UV cross-linked to increasing concentrations of [³³P]c-di-GMP. (B) Localization analysis of different arginine mutants fused to GFP expressed by the addition of 0.55 mM vanillic acid. Representative 3D-SIM images for visualization (left) and localization quantification, as described in the legend to Fig. 3D, are shown. n = 575 cells per strain from two independent experiments. Expression of *dgcZ* was induced with 0.5 mM IPTG. Scale bar, 3 μm. (C) Functionality of HfsK arginine mutants compared to that of a wild-type (wt) strain harboring the control empty vector (e.v.) in surface colonization after 24 h of growth in microtiter plates in the presence of 0.1 mM vanillic acid. (D) Analysis of adhered OG-WGA-stained holdfast on coverslips after 2 h of cell adsorption. Representative overlays of fluorescence and phase-contrast (Ph) images are shown. Scale bar, 5 μm. (E) Holdfasts of a strain with high c-di-GMP levels analyzed under shear stress after 15 h of growth in a microfluidic channel with a constant flow of fresh medium containing OG-WGA. Shown is an overlay of fluorescence and inverted differential interference contrast (DIC) images. Scale bar, 5 μm. (F) Model of HfsK regulation. General protein localization is represented by red shades. Active HfsK binds to membrane component X in the absence of c-di-GMP via its C terminus. Upon c-di-GMP binding, the C terminus rearranges to accommodate the nucleotide and the protein is inactivated and disperses in the cytosol. M, membrane. The error bars in panels A and B show the SD of three independent experiments. **, P < 0.01.

ologically high levels of c-di-GMP not only severely reduced surface colonization but, akin to the Δ*hfsK* mutant, changed the cohesive properties of holdfast structures (Fig. 5E; see Fig. S6A to C). The finding that the C terminus of HfsK is essential for its function and for its subcellular localization and contributes to c-di-GMP binding implies that this part of the protein is the central regulatory hub controlling HfsK dynamics and activity in response to the second messenger.

DISCUSSION

The second messenger c-di-GMP controls EPS production in a wide range of bacteria by stimulating the activity of glycosyltransferases directly or via adaptor proteins (15, 57–59). By this means, c-di-GMP directly affects the polymerization and rate of secretion of EPS across the inner membrane. Here we describe the first c-di-GMP effector that is not required to adjust the amount of EPS produced but rather controls EPS adhesin

modification and thus changes its physical properties and strength. However, HfsK activity does not seem to depend on c-di-GMP. Rather, our data argue that c-di-GMP affects HfsK negatively, possibly to adjust or coordinate its activity with other processes of holdfast biogenesis. Because cells that lack c-di-GMP are unable to produce holdfast (29), additional c-di-GMP-controlled catalytic components must contribute to this process. This example nicely illustrates that c-di-GMP can influence EPS production both quantitatively and qualitatively.

Cells lacking HfsK produce normal amounts of holdfast material. However, mutant holdfasts form elastic and abrasive filaments that are unable to withstand strong shear forces, suggesting that they have reduced cohesiveness and stability. A similar change in the physical properties of the holdfast adhesin was described for mutants deficient in HfsH. HfsH was proposed to deacetylate holdfast EPS precursors and, by doing that, unmask amine groups that might serve as holdfast anchoring sites (19). This is consistent with our findings that cells lacking the holdfast anchoring protein HfaA or HfaD display comparable holdfast behavior under shear stress. In contrast to the ΔhfaA ΔhfaD double mutant, shed holdfasts of ΔhfaB mutant cells did not deform under shear stress and retained a globular shape. Because HfaA and HfaD are thought to be exported and inserted into the outer membrane by the action of HfaB, these factors should, in principle, behave epistatically. However, similar observations were made by Hardy and colleagues indicating that HfaB likely adopts additional roles (28). For instance, it is possible that HfaB directly contributes to EPS anchoring and that in its absence shedding of the holdfast is unrestrained. Altogether, the similarity of the mutant phenotypes suggested that the putative acyltransferase HfsK, the deacetylase HfsH, and the holdfast anchor proteins HfaD and HfaA may be part of the same pathway that is required for holdfast anchoring and proper holdfast cohesion—two aspects that seem to be interdependent.

The exact role of HfsK in this pathway remains unclear. The closest homologs with known structure are the Fem proteins of Gram-positive bacteria that transfer aminoacyl moieties to peptidoglycan sugar precursors (53, 54). Given the low overall sequence similarity, the functional versatility of GNAT proteins, and their diversity in terms of acyl donors and acceptors (38), it is difficult to make predictions about the catalytic role of HfsK. It might transfer an acyl group to amines exposed by the action of HfsH (19). Depending on the nature of this acyl group, it could be involved in the covalent linkage of polysaccharide moieties to anchor proteins (60) or participate in electrostatic interactions required for adhesion, cohesion, or anchoring. This is in line with the observation that isolated holdfasts from a ΔhfsH mutant showed reduced electrostatic interactions with the substrate (20). While we cannot fully exclude the possibility that HfsK acylates an anchor protein to provide cross-linking sites, several observations indicated that HfsK chemically modifies holdfast EPS precursors directly (1). HfsK homologs are genetically coupled to various EPS synthesis systems (2). Deletion of the paralogs *cc2278* and *cc1244* affects the adhesin without an observable shedding phenotype (3). Cells lacking HfsK are able to adhere to shed holdfasts of a ΔhfaB mutant, indicating an intact anchor mechanism (4). HfsK colocalizes with other holdfast components involved in EPS precursor biogenesis. This is in contrast to holdfast export and anchoring proteins that localize to the cell pole where holdfast is assembled (25, 28, 61). On the basis of these arguments, we propose that HfsK acylates the EPS component of the holdfast and that this modification is necessary for proper holdfast cohesion and anchoring.

HfsK was originally isolated by a c-di-GMP-specific capture method and was shown to specifically bind c-di-GMP *in vitro*. The binding affinity of HfsK lies in the submicromolar range, which correlates well with the peak concentrations of c-di-GMP during *C. crescentus* SW-to-ST differentiation (29, 31). These values are in line with our findings that the protein delocalizes in a c-di-GMP-dependent manner coincident with holdfast formation during the cell cycle. HfsK may thus be retained at the cytosolic membrane when c-di-GMP levels are low or intermediate and be transiently released from the membrane during a short period of the cell cycle, when c-di-GMP reaches a high

concentration. Our data also suggest that the membrane-associated form of HfsK is catalytically active, while membrane release results in its inactivation. In line with this, we found that the R112A mutant c-di-GMP binding protein permanently localized to the membrane while retaining its activity for holdfast formation. Several observations point to the C terminus as a central determinant of HfsK localization and catalytic activity. Mutants lacking the C terminus failed to localize to the membrane and were inactive even when forced to bind to the membrane artificially. Moreover, the C terminus is also involved in c-di-GMP binding. A mutant protein lacking two central arginine residues within this region failed to efficiently bind c-di-GMP and remained membrane associated throughout the cell cycle irrespective of the c-di-GMP concentration. Unlike the R112A mutant protein, the RR352AA variant was inactive, indicating that this site may be the core of HfsK control. We propose a model in which the C terminus of HfsK serves as an interaction site for a putative membrane partner (Fig. 5F). In this model, membrane tethering is necessary for HfsK activity while c-di-GMP binding interferes with the tether and leads to delocalization and inactivation of HfsK. On the basis of our data, we envisage that the arginine residues in the C terminus are involved in the c-di-GMP binding and activity of HfsK, offering a simple switch through which c-di-GMP can control conformation, membrane association, and catalytic activity. A FemX-derived structure model of HfsK could provide a molecular frame for this c-di-GMP-mediated switch (see Fig. S6D). Residue R112, which is localized on the surface of one of the GNAT domains, and R352 and/or R353 in the C terminus might jointly contribute to c-di-GMP binding. Accordingly, ligand binding would provoke the C terminus to swing back and interact with the GNAT core. To clarify such mechanistic details, additional biochemical and structural studies with HfsK and c-di-GMP are needed.

This study represents one of few examples of a c-di-GMP effector protein that is inactivated by ligand binding (30, 62). It remains unclear why HfsK activity would need to be turned off during the cell cycle and why this process is linked to peak levels of c-di-GMP. Given the timing of HfsK delocalization, it is possible that it is involved in some early step of holdfast biogenesis, catalyzing a reaction that is detrimental for later steps of holdfast export or maturation. If so, C. crescentus may elegantly use c-di-GMP for dual control of holdfast biogenesis. During the SW-to-ST transition, when c-di-GMP levels begin to increase, one or several key enzymes may be turned on to initiate holdfast biogenesis, but when c-di-GMP levels peak, the cell might turn off an enzyme(s) that is no longer needed or damaging. Alternatively, HfsK may engage in additional processes. For several holdfast synthesis steps, redundant functional equivalents exist, with one copy being encoded in the *hfs* operons and its paralog(s) being encoded elsewhere. It was proposed that paralogs may act in other pathways but can contribute to holdfast synthesis because of substrate similarities (23). It is plausible that HfsK interferes with related cellular pathways required for capsule, lipopolysaccharide, O-antigen, or possibly even peptidoglycan synthesis. In this case, proper timing of enzyme activity during the cell cycle could help prevent substrate depletion or leakage, thereby providing a rationale for c-di-GMP-mediated control.

MATERIALS AND METHODS

Bacterial strains and growth conditions. The bacterial strains and plasmids used in this study are described in Text S1. *E. coli* strains were grown at 37°C or 30°C in Luria broth, and *C. crescentus* strains were grown at 30°C in peptone yeast extract (PYE) or M2 minimal medium supplemented with 0.1% glucose (M2G) under aeration or on the respective 1.5% agar medium plates. If required, media were supplemented with the appropriate antibiotics (*E. coli*, 50/30 [solid/liquid in μg/ml] kanamycin and 30/20 chloramphenicol; *C. crescentus*, 20/5 kanamycin and 20/0 nalidixic acid); the inducer isopropyl-β-D-thiogalactopyranoside (IPTG) at 0.3 0.5, or 0.75 mM; xylose at 0.1%; and vanillic acid at 0.1 or 0.55 mM. If required, cell cultures were synchronized by density gradient centrifugation (63) (see Text S1).

Attachment assay. Overnight (24-h) or mid-log-phase (30-min) cultures were diluted 1:32 or to an optical density at 600 nm (OD_{660}) of 0.3, respectively, and grown in 96-well polystyrene microtiter plates at 30°C under aeration for the times indicated. Plates were then rinsed thoroughly with water, incubated for 30 min with 0.1% (wt/vol) crystal violet–1% methanol–isopropanol, rinsed again, and dried, and the adherent crystal violet was dissolved in 20% acetic acid before absorption at 600 nm was measured (see Text S1).

Fluorescence microscopy. Bacteria in mid-log phase were mounted on 1% agarose pads containing water (snapshots) or PYE containing appropriate supplements (time-lapse videos). The specifications of the microscopes used can be found in Text S1. Images showing protein localization were deconvolved with softWoRx or Huygens software.

Holdfast and membrane stain. Membranes were visualized on 1% agarose pads containing 0.66 μg/ml FM4-64 dye (Molecular Probes, USA). To visualize holdfast, cultures were incubated with 1 μg/ml OG-WGA (Invitrogen, USA) before microscopy or 2.66 μg/ml tetramethylrhodamine-WGA was added to the agarose pads directly. Adherent holdfast visualization on glass was adapted from reference 25. Overnight cultures or, if required, preinduced mid-log-phase cultures were diluted to an OD_{660} of 0.15 and grown in polystyrene plates containing round 12-mm borosilicate coverslips for 2 h at 30°C under aeration. The coverslips were then stained for 15 min with 2.5 μg/ml WGA coupled to Oregon green, tetramethylrhodamine, or Alexa Fluor 350 (Invitrogen); rinsed with water; and mounted on 1% agarose pads. For quantification, the mean gray value was measured with the FIJI software (64), and the measured background fluorescence of the holdfast-minus NA1000 strain was subtracted (see Text S1).

Quantification of protein localization. Quantitative fluorescent signal measurements were performed with a MatLab-based program developed by our group (WHISIT; available from MathWorks, Natick, MA). WHISIT calculated the average pixel fluorescent signal intensity of the membrane and cytoplasmic compartments. The membrane compartment was defined to enclose the first four intracellular pixels flanking the cell outline that was computed by Oufti (65) on phase-contrast images, while the remaining intracellular pixels were defined as the cytoplasmic compartment (see Text S1).

Microfluidics. Mid-log-phase cells were used to fill polydimethylsiloxane-based microfluidic devices (66) consisting of a single channel 10 mm long, 40 μm wide, and 25 μm high before a constant flow (0.002 μl/s) of PYE medium supplemented with 1 μg/ml OG-WGA was installed to allow growth (see Text S1).

Cell fractionation. Cells were lysed in CellFrac buffer (phosphate-buffered saline, 1× cOmplete mini EDTA-free protease inhibitor [Roche], 2.5 μg/ml DNase I [Roche]) with a French pressure cell and centrifuged to remove cell debris (10 min, 18,000 $\times$ g, 4°C). The cleared lysate was then centrifuged at high speed (1 h, 100,000 $\times$ g, 4°C) to separate soluble from insoluble proteins. The supernatant was removed and kept as the soluble fraction, whereas the pellet was washed and resuspended in the original volume of CellFrac buffer. The cleared lysate and soluble and pellet fractions were further analyzed by immunoblotting (see Text S1).

Protein purification. Proteins expressed from pET28aStrepII plasmids were purified from cleared lysates with Strep-Tactin Superflow plus resins (Qiagen) in accordance with the manufacturer's protocol. HfsK-His was purified on a 5-ml HisTrap HP column (GE Healthcare), and the His-tagged protein was eluted with a gradient of elution buffer containing 20 mM Tris (pH 8.5), 0.5 M NaCl, 3 mM β-mercaptoethanol, 0.1%Tween 20, and 500 mM imidazole and concentrated on a Superdex 200 10/300 GL Increase gel filtration column (GE Healthcare) equilibrated with 30 mM HEPES (pH 7.4), 0.3 M NaCl, 3 mM β-mercaptoethanol, and 5 mM $MgCl_2$ (see Text S1).

ITC. ITC measurements were performed with a VP-ITC isothermal titration calorimeter (MicroCal) with 13 μM HfsK in the cell and 211 μM c-di-GMP in the syringe (buffer: 30 mM HEPES [pH 7.4], 0.3 M NaCl, 5 mM $MgCl_2$, and 3 mM β-mercaptoethanol) at 22°C. The first injection of 3 μl was followed by 29 injections of 10 μl. The data were analyzed with the MicroCal version of ORIGIN and fitted with the "One binding site model" of ORIGIN (see Text S1).

UV cross-linking with [^{33}P]c-di-GMP. Cross-linking experiments were performed with 1 μM purified protein, an appropriate concentration of [^{33}P]c-di-GMP (51, 67), and reaction buffer (50 mM NaH_2PO_4 [pH 6.5], 200 mM NaCl, and 1 mM dithiothreitol [DTT] or 20 mM Tris [pH 8.5], 200 mM NaCl, and mM DTT) as described in references 68 and 69 (see Text S1).

Statistics. For statistical comparisons, paired t tests were used if not stated otherwise. Calculations were performed with GraphPad Prism. Full experimental details are available in Text S1.

SUPPLEMENTAL MATERIAL

Supplemental material for this article may be found at https://doi.org/10.1128/mBio.00294-17.

MOVIE S1, AVI file, 0.8 MB.
MOVIE S2, AVI file, 2.5 MB.
MOVIE S3, AVI file, 1.7 MB.
TEXT S1, PDF file, 0.3 MB.
FIG S1, TIF file, 1 MB.
FIG S2, TIF file, 1.6 MB.
FIG S3, TIF file, 1 MB.
FIG S4, TIF file, 0.9 MB.
FIG S5, TIF file, 1.9 MB.
FIG S6, TIF file, 2.3 MB.

REFERENCES

1. Costerton JW, Cheng KJ, Geesey GG, Ladd TI, Nickel JC, Dasgupta M, Marrie TJ. 1987. Bacterial biofilms in nature and disease. Annu Rev Microbiol 41:435–464. https://doi.org/10.1146/annurev.mi.41.100187.002251.

2. Zobell CE. 1943. The effect of solid surfaces upon bacterial activity. J Bacteriol 46:39–56.

3. Thormann KM, Saville RM, Shukla S, Spormann AM. 2005. Induction of rapid detachment in Shewanella oneidensis MR-1 biofilms. J Bacteriol 187:1014–1021. https://doi.org/10.1128/JB.187.3.1014-1021.2005.

4. Sauer K, Cullen MC, Rickard AH, Zeef LAH, Davies DG, Gilbert P. 2004. Characterization of nutrient-induced dispersion in Pseudomonas aeruginosa PAO1 biofilm. J Bacteriol 186:7312–7326. https://doi.org/10.1128/JB.186.21.7312-7326.2004.

5. Jenal U, Reinders A, Lori C. 2017. Cyclic di-GMP: second messenger extraordinaire. Nat Rev Microbiol. https://doi.org/10.1038/nrmicro.2016.190.

6. Kazmierczak BI, Lebron MB, Murray TS. 2006. Analysis of FimX, a phosphodiesterase that governs twitching motility in Pseudomonas aeruginosa. Mol Microbiol 60:1026–1043. https://doi.org/10.1111/j.1365-2958.2006.05156.x.

7. Boehm A, Kaiser M, Li H, Spangler C, Kasper CA, Ackermann M, Kaever V, Sourjik V, Roth V, Jenal U. 2010. Second messenger-mediated adjustment of bacterial swimming velocity. Cell 141:107–116. https://doi.org/10.1016/j.cell.2010.01.018.

8. Pérez-Mendoza D, Sanjuán J. 2016. Exploiting the commons: cyclic diguanylate regulation of bacterial exopolysaccharide production. Curr Opin Microbiol 30:36–43. https://doi.org/10.1016/j.mib.2015.12.004.

9. Monds RD, Newell PD, Gross RH, O'Toole GA. 2007. Phosphate-dependent modulation of c-di-GMP levels regulates Pseudomonas fluorescens Pf0-1 biofilm formation by controlling secretion of the adhesin LapA. Mol Microbiol 63:656–679. https://doi.org/10.1111/j.1365-2958.2006.05539.x.

10. Sommerfeldt N, Possling A, Becker G, Pesavento C, Tschowri N, Hengge R. 2009. Gene expression patterns and differential input into curli fimbriae regulation of all GGDEF/EAL domain proteins in Escherichia coli. Microbiology 155:1318–1331. https://doi.org/10.1099/mic.0.024257-0.

11. Römling U, Galperin MY. 2015. Bacterial cellulose biosynthesis: diversity of operons, subunits, products, and functions. Trends Microbiol 23:545–557. https://doi.org/10.1016/j.tim.2015.05.005.

12. Morgan JLW, McNamara JT, Fischer M, Rich J, Chen HM, Withers SG, Zimmer J. 2016. Observing cellulose biosynthesis and membrane translocation in crystallo. Nature 531:329–334. https://doi.org/10.1038/nature16966.

13. Morgan JLW, McNamara JT, Zimmer J. 2014. Mechanism of activation of bacterial cellulose synthase by cyclic di-GMP. Nat Struct Mol Biol 21:489–496. https://doi.org/10.1038/nsmb.2803.

14. Morgan JLW, Strumillo J, Zimmer J. 2013. Crystallographic snapshot of cellulose synthesis and membrane translocation. Nature 493:181–186. https://doi.org/10.1038/nature11744.

15. Steiner S, Lori C, Boehm A, Jenal U. 2013. Allosteric activation of exopolysaccharide synthesis through cyclic di-GMP-stimulated protein-protein interaction. EMBO J 32:354–368. https://doi.org/10.1038/emboj.2012.315.

16. Poindexter JS. 1981. The caulobacters: ubiquitous unusual bacteria. Microbiol Rev 45:123–179.

17. Merker RI, Smit J. 1988. Characterization of the adhesive holdfast of

marine and freshwater caulobacters. Appl Environ Microbiol 54:2078–2085.

18. Li G, Smith CS, Brun YV, Tang JX. 2005. The elastic properties of the Caulobacter crescentus adhesive holdfast are dependent on oligomers of N-acetylglucosamine. J Bacteriol 187:257–265. https://doi.org/10.1128/JB.187.1.257-265.2005.

19. Wan Z, Brown PJB, Elliott EN, Brun YV. 2013. The adhesive and cohesive properties of a bacterial polysaccharide adhesin are modulated by a deacetylase. Mol Microbiol 88:486–500. https://doi.org/10.1111/mmi.12199.

20. Berne C, Ma X, Licata NA, Neves BRA, Setayeshgar S, Brun YV, Dragnea B. 2013. Physiochemical properties of Caulobacter crescentus holdfast: a localized bacterial adhesive. J Phys Chem B 117:10492–10503. https://doi.org/10.1021/jp405802e.

21. Ong CJ, Wong ML, Smit J. 1990. Attachment of the adhesive holdfast organelle to the cellular stalk of Caulobacter crescentus. J Bacteriol 172:1448–1456. https://doi.org/10.1128/jb.172.3.1448-1456.1990.

22. Bodenmiller D, Toh E, Brun YV. 2004. Development of surface adhesion in Caulobacter crescentus. J Bacteriol 186:1438–1447. https://doi.org/10.1128/JB.186.5.1438-1447.2004.

23. Toh E, Kurtz HD, Brun YV. 2008. Characterization of the Caulobacter crescentus holdfast polysaccharide biosynthesis pathway reveals significant redundancy in the initiating glycosyltransferase and polymerase steps. J Bacteriol 190:7219–7231. https://doi.org/10.1128/JB.01003-08.

24. Smith CS, Hinz A, Bodenmiller D, Larson DE, Brun YV. 2003. Identification of genes required for synthesis of the adhesive holdfast in Caulobacter crescentus. J Bacteriol 185:1432–1442. https://doi.org/10.1128/JB.185.4.1432-1442.2003.

25. Cole JL, Hardy GG, Bodenmiller D, Toh E, Hinz A, Brun YV. 2003. The HfaB and HfaD adhesion proteins of Caulobacter crescentus are localized in the stalk. Mol Microbiol 49:1671–1683. https://doi.org/10.1046/j.1365-2958.2003.03664.x.

26. Fiebig A, Herrou J, Fumeaux C, Radhakrishnan SK, Viollier PH, Crosson S. 2014. A cell cycle and nutritional checkpoint controlling bacterial surface adhesion. PLoS Genet 10:e1004101. https://doi.org/10.1371/journal.pgen.1004101.

27. Levi A, Jenal U. 2006. Holdfast formation in motile swarmer cells optimizes surface attachment during Caulobacter crescentus development. J Bacteriol 188:5315–5318. https://doi.org/10.1128/JB.01725-05.

28. Hardy GG, Allen RC, Toh E, Long M, Brown PJB, Cole-Tobian JL, Brun YV. 2010. A localized multimeric anchor attaches the Caulobacter holdfast to the cell pole. Mol Microbiol 76:409–427. https://doi.org/10.1111/j.1365-2958.2010.07106.x.

29. Abel S, Bucher T, Nicollier M, Hug I, Kaever V, Abel Zur Wiesch P, Jenal U. 2013. Bi-modal distribution of the second messenger c-di-GMP controls cell fate and asymmetry during the Caulobacter cell cycle. PLoS Genet 9:e1003744. https://doi.org/10.1371/journal.pgen.1003744.

30. Lori C, Ozaki S, Steiner S, Böhm R, Abel S, Dubey BN, Schirmer T, Hiller S, Jenal U. 2015. Cyclic di-GMP acts as a cell cycle oscillator to drive chromosome replication. Nature 523:236–239. https://doi.org/10.1038/nature14473.

31. Christen M, Kulasekara HD, Christen B, Kulasekara BR, Hoffman LR, Miller SI. 2010. Asymmetrical distribution of the second messenger c-di-GMP upon bacterial cell division. Science 328:1295–1297. https://doi.org/10.1126/science.1188658.

32. Abel S, Chien P, Wassmann P, Schirmer T, Kaever V, Laub MT, Baker TA, Jenal U. 2011. Regulatory cohesion of cell cycle and cell differentiation

through interlinked phosphorylation and second messenger networks. Mol Cell 43:550–560. https://doi.org/10.1016/j.molcel.2011.07.018.

33. Paul R, Weiser S, Amiot NC, Chan C, Schirmer T, Giese B, Jenal U. 2004. Cell cycle-dependent dynamic localization of a bacterial response regulator with a novel di-guanylate cyclase output domain. Genes Dev 18:715–727. https://doi.org/10.1101/gad.289504.

34. Wassmann P, Chan C, Paul R, Beck A, Heerklotz H, Jenal U, Schirmer T. 2007. Structure of BeF$_3$$^-$-modified response regulator PleD: implications for diguanylate cyclase activation, catalysis, and feedback inhibition. Structure 15:915–927. https://doi.org/10.1016/j.str.2007.06.016.

35. Aldridge P, Jenal U. 1999. Cell cycle-dependent degradation of a flagellar motor component requires a novel-type response regulator. Mol Microbiol 32:379–391. https://doi.org/10.1046/j.1365-2958.1999.01358.x.

36. Nesper J, Reinders A, Glatter T, Schmidt A, Jenal U. 2012. A novel capture compound for the identification and analysis of cyclic di-GMP binding proteins. J Proteomics 75:4874–4878. https://doi.org/10.1016/j.jprot.2012.05.033.

37. Söding J, Biegert A, Lupas AN. 2005. The HHpred interactive server for protein homology detection and structure prediction. Nucleic Acids Res 33:W244–W248. https://doi.org/10.1093/nar/gki408.

38. Salah Ud-Din AI, Tikhomirova A, Roujeinikova A. 2016. Structure and functional diversity of GCN5-related N-acetyltransferases (GNAT). Int J Mol Sci 17:E1018. https://doi.org/10.3390/ijms17071018.

39. Abraham WR, Strömpl C, Vancanneyt M, Bennasar A, Swings J, Lünsdorf H, Smit J, Moore ERB. 2004. Woodsholea maritima gen. nov., sp. nov., a marine bacterium with a low diversity of polar lipids. Int J Syst Evol Microbiol 54:1227–1234. https://doi.org/10.1099/ijs.0.02943-0.

40. Brown PJB, Hardy GG, Trimble MJ, Brun YV. 2009. Complex regulatory pathways coordinate cell-cycle progression and development in Caulobacter crescentus. Adv Microb Physiol 54:1–101. https://doi.org/10.1016/S0065-2911(08)00001-5.

41. Entcheva-Dimitrov P, Spormann AM. 2004. Dynamics and control of biofilms of the oligotrophic bacterium Caulobacter crescentus. J Bacteriol 186:8254–8266. https://doi.org/10.1128/JB.186.24.8254-8266.2004.

42. Potthoff E, Ossola D, Zambelli T, Vorholt JA. 2015. Bacterial adhesion force quantification by fluidic force microscopy. Nanoscale 7:4070–4079. https://doi.org/10.1039/c4nr06495j.

43. Guillaume-Gentil O, Potthoff E, Ossola D, Franz CM, Zambelli T, Vorholt JA. 2014. Force-controlled manipulation of single cells: from AFM to FluidFM. Trends Biotechnol 32:381–388. https://doi.org/10.1016/j.tibtech.2014.04.008.

44. Li G, Brun YV, Tang JX. 2013. Holdfast spreading and thickening during Caulobacter crescentus attachment to surfaces. BMC Microbiol 13:139. https://doi.org/10.1186/1471-2180-13-139.

45. Davis NJ, Cohen Y, Sanselicio S, Fumeaux C, Ozaki S, Luciano J, Guerrero-Ferreira RC, Wright ER, Jenal U, Viollier PH. 2013. De- and repolarization mechanism of flagellar morphogenesis during a bacterial cell cycle. Genes Dev 27:2049–2062. https://doi.org/10.1101/gad.222679.113.

46. Ozaki S, Schalch-Moser A, Zumthor L, Manfredi P, Ebbensgaard A, Schirmer T, Jenal U. 2014. Activation and polar sequestration of PopA, a c-di-GMP effector protein involved in Caulobacter crescentus cell cycle control. Mol Microbiol 94:580–594. https://doi.org/10.1111/mmi.12777.

47. Fang G, Passalacqua KD, Hocking J, Llopis PM, Gerstein M, Bergman NH, Jacobs-Wagner C. 2013. Transcriptomic and phylogenetic analysis of a bacterial cell cycle reveals strong associations between gene co-expression and evolution. BMC Genomics 14:450. https://doi.org/10.1186/1471-2164-14-450.

48. Schmid J, Sieber V, Rehm B. 2015. Bacterial exopolysaccharides: biosynthesis pathways and engineering strategies. Front Microbiol 6:496. https://doi.org/10.3389/fmicb.2015.00496.

49. Yu NY, Wagner JR, Laird MR, Melli G, Rey S, Lo R, Dao P, Sahinalp SC, Ester M, Foster LJ, Brinkman FSL. 2010. PSORTb 3.0: improved protein subcellular localization prediction with refined localization subcategories and predictive capabilities for all prokaryotes. Bioinformatics 26:1608–1615. https://doi.org/10.1093/bioinformatics/btq249.

50. Speers AE, Wu CC. 2007. Proteomics of integral membrane proteins—theory and application. Chem Rev 107:3687–3714. https://doi.org/10.1021/cr068286z.

51. Boehm A, Steiner S, Zaehringer F, Casanova A, Hamburger F, Ritz D, Keck W, Ackermann M, Schirmer T, Jenal U. 2009. Second messenger signalling governs Escherichia coli biofilm induction upon ribosomal stress.

52. Jenal U, Malone J. 2006. Mechanisms of cyclic-di-GMP signaling in bacteria. Annu Rev Genet 40:385–407. https://doi.org/10.1146/annurev.genet.40.110405.090423.

53. Biarrotte-Sorin S, Maillard AP, Delettré J, Sougakoff W, Arthur M, Mayer C. 2004. Crystal structures of Weissella viridescens FemX and its complex with UDP-MurNAc-pentapeptide: insights into FemABX family substrates [sic] recognition. Structure 12:257–267. https://doi.org/10.1016/j.str.2004.01.006.

54. Hegde SS, Shrader TE. 2001. FemABX family members are novel nonribosomal peptidyltransferases and important pathogen-specific drug targets. J Biol Chem 276:6998–7003. https://doi.org/10.1074/jbc.M008591200.

55. Craney A, Tahlan K, Andrews D, Nodwell J. 2011. Bacterial transmembrane proteins that lack N-terminal signal sequences. PLoS One 6:e19421. https://doi.org/10.1371/journal.pone.0019421.

56. Chou SH, Galperin MYY. 2016. Diversity of cyclic di-GMP-binding proteins and mechanisms. J Bacteriol 198:32–46. https://doi.org/10.1128/JB.00333-15.

57. Pérez-Mendoza D, Rodríguez-Carvajal MÁ, Romero-Jiménez L, Farias Gde A, Lloret J, Gallegos MT, Sanjuán J. 2015. Novel mixed-linkage β-glucan activated by c-di-GMP in Sinorhizobium meliloti. Proc Natl Acad Sci U S A 112:E757–E765. https://doi.org/10.1073/pnas.1421748112.

58. Merighi M, Lee VT, Hyodo M, Hayakawa Y, Lory S. 2007. The second messenger bis-(3′-5′)-cyclic-GMP and its PilZ domain-containing receptor Alg44 are required for alginate biosynthesis in Pseudomonas aeruginosa. Mol Microbiol 65:876–895. https://doi.org/10.1111/j.1365-2958.2007.05817.x.

59. Whitney JC, Howell PL. 2013. Synthase-dependent exopolysaccharide secretion in Gram-negative bacteria. Trends Microbiol 21:63–72. https://doi.org/10.1016/j.tim.2012.10.001.

60. Ton-That H, Labischinski H, Berger-Bächi B, Schneewind O. 1998. Anchor structure of staphylococcal surface proteins. III. Role of the FemA, FemB, and FemX factors in anchoring surface proteins to the bacterial cell wall. J Biol Chem 273:29143–29149. https://doi.org/10.1074/jbc.273.44.29143.

61. Javens J, Wan Z, Hardy GG, Brun YV. 2013. Bypassing the need for subcellular localization of a polysaccharide export-anchor complex by overexpressing its protein subunits. Mol Microbiol 89:350–371. https://doi.org/10.1111/mmi.12281.

62. Trampari E, Stevenson CEM, Little RH, Wilhelm T, Lawson DM, Malone JG. 2015. Bacterial rotary export ATPases are allosterically regulated by the nucleotide second messenger cyclic-di-GMP. J Biol Chem 290:24470–24483. https://doi.org/10.1074/jbc.M115.661439.

63. Jenal U, Shapiro L. 1996. Cell cycle-controlled proteolysis of a flagellar motor protein that is asymmetrically distributed in the Caulobacter predivisional cell. EMBO J 15:2393–2406.

64. Schindelin J, Arganda-Carreras I, Frise E, Kaynig V, Longair M, Pietzsch T, Preibisch S, Rueden C, Saalfeld S, Schmid B, Tinevez JY, White DJ, Hartenstein V, Eliceiri K, Tomancak P, Cardona A. 2012. Fiji: an open-source platform for biological-image analysis. Nat Methods 9:676–682. https://doi.org/10.1038/nmeth.2019.

65. Paintdakhi A, Parry B, Campos M, Irnov I, Elf J, Surovtsev I, Jacobs-Wagner C. 2016. Oufti: an integrated software package for high-accuracy, high-throughput quantitative microscopy analysis. Mol Microbiol 99:767–777. https://doi.org/10.1111/mmi.13264.

66. Deshpande S, Pfohl T. 2012. Hierarchical self-assembly of actin in micro-confinements using microfluidics. Biomicrofluidics 6:34120. https://doi.org/10.1063/1.4752245.

67. Zähringer F, Massa C, Schirmer T. 2011. Efficient enzymatic production of the bacterial second messenger c-di-GMP by the diguanylate cyclase YdeH from E. coli. Appl Biochem Biotechnol 163:71–79. https://doi.org/10.1007/s12010-010-9017-x.

68. Christen M, Christen B, Folcher M, Schauerte A, Jenal U. 2005. Identification and characterization of a cyclic di-GMP-specific phosphodiesterase and its allosteric control by GTP. J Biol Chem 280:30829–30837. https://doi.org/10.1074/jbc.M504429200.

69. Christen B, Christen M, Paul R, Schmid F, Folcher M, Jenoe P, Meuwly M, Jenal U. 2006. Allosteric control of cyclic di-GMP signaling. J Biol Chem 281:32015–32024. https://doi.org/10.1074/jbc.M603589200.

Mol Microbiol 72:1500–1516. https://doi.org/10.1111/j.1365-2958.2009.06739.x.

CHAPTER 5

_____

Reinders A. et al., 2018

Stay or go? A bistable molecular switch facilitating bacterial lifestyle transitions

Alberto Reinders, Shogo Ozaki[±], Johanna Rueher[±], Benjamin Sellner[±], Matteo Sangermani[±], Tilman Schirmer, and Urs Jenal*

Biozentrum of the University of Basel, Klingelbergstrasse 50/70, 4056 Basel, Switzerland

*for correspondence: urs.jenal@unibas.ch

[±]equal contribution

Abstract

Bacteria preferentially colonize surfaces and air-liquid interfaces as matrix embedded communities called biofilms. Biofilms exhibit specific physiological properties, including general stress tolerance, increased antibiotic recalcitrance and tolerance against phagocytic clearance. Together this largely accounts for increased biofilm persistence, chronic infections and infection relapses. One of the principle regulators of biofilm formation is c-di-GMP, a bacterial second messenger controlling various cellular processes. Cellular levels of c-di-GMP are controlled by two antagonistic enzyme families, diguanylate cyclases and phosphodiesterases. But despite the identification and characterization of an increasing number of components of the c-di-GMP network in different bacterial model organisms, details of c-di-GMP mediated decision-making have remained unclear. In particular, how cells shuttle between specific c-di-GMP regimes at the population and single cell level is largely unknown and moreover how these transitions are deterministically made in time and space, given that bacterial networks of diguanylate cyclases and phosphodiesterases show a high degree of complexity.

Here we describe a novel mechanism regulating c-di-GMP mediated biofilm formation in *E. coli*. This mechanism relies on the bi-stable expression of a key phosphodiesterase that acts both as catalyst for c-di-GMP degradation and as a transcription factor promoting its own production. Bi-stability results from two interconnected positive feedback loops operating on the catalytic and gene expression level. Based on structural, biochemical and *in silico* analyses we postulate a simple substrate-induced switch mechanism through which this enzyme can sense changing concentration of c-di-GMP and convert this information into a bistable c-di-GMP response. This mechanism may explain how cellular heterogeneity of small signaling molecules is generated in bacteria and used as a bet hedging strategy for important lifestyle transitions.

Introduction

To maintain their own integrity and fitness, all living organisms need to be able to effectively change the cellular program in order to take over specialized functions or to respond to changes in the environment. To provide directionality to key cellular decisions such as changing cell shape and/or behavior, the respective regulatory networks need to be deterministic and robust. For example, stem cells need to stably maintain their replicative program but at the same time be capable to rapidly induce cell differentiation in response to external signals (Blanpain and Simons, 2013; Hindley and Philpott, 2012). This is mainly achieved through positive feedback regulation and mutual cross-inhibition of master regulators activating downstream feedforward regulatory cascades (Holmberg and Perlmann, 2012). Thus, although differentiation of cells is not terminal, reversion of this highly coordinated and robust process becomes harder, the more differentiation has proceeded (Pasque et al., 2011).

In analogy, bacteria can transit between two different forms of behavior, a motile single cell and a sessile, community-based lifestyle called biofilm (Hengge, 2009; Jenal and Malone, 2006; Jenal et al., 2017). These two lifestyles are fundamentally different with respect to gene expression patterns and the overall physiological state of the cell (Patell et al., 2010; Pratt and Kolter, 1999; Southey-Pillig et al., 2005; Waite et al., 2005). Consequently, both the transition between and the stable maintenance of these two physiological states come with substantial costs. Thus, the decision to transit from single cell to community behavior requires fine-tuned regulatory processes that integrate environmental signals and – in response – establish robust and stable programs at the right time and space. While several aspects of cellular control mechanisms of this switch have been uncovered, it has remained unclear which factors contribute to the directionality and stability of this important bi- or multimodal program (Lopez et al., 2009).

One of the central regulators of this physiological adaptation is the second messenger c-di-GMP. Discovered as a small signaling molecule stimulating cellulose production in *Gluconacetoacter xylinus* (Ross et al., 1987), c-di-GMP controls important behavioral processes such as motility (Boehm et al., 2010), virulence (Tischler and Camilli, 2004), biofilm formation (Steiner et al., 2013) or cell-cycle regulation (Lori et al., 2015). Planktonic cells are associated with low intracellular c-di-GMP concentrations (Boehm et al., 2010; Reinders et al., 2015), whereas sessile communities generally display high levels of c-di-GMP (Jenal et al., 2017). Most bacteria harbor large arrays of enzymes that synthesize (diguanylate-cyclases, DGC) or degrade c-di-GMP (phosphodiesterases PDE) to adjust their internal concentration of the second messenger in response to specific intrinsic or extrinsic signals (Hengge, 2009). The internal c-di-GMP concentration is then sensed by downstream effectors, which ultimately elicit a cellular function (Hengge, 2009; Jenal et al., 2017). The co-occurrence of multiple DGCs and PDEs, combined with hypersensitive downstream effectors (nM affinities) poses the problem of stochastic noise and network stability (Hengge, 2009; Jenal and Malone, 2006). While in eukaryotic cells, compartmentalization can potentially shield cellular components from such

effects, bacteria cannot rely on physical barriers. Thus, there is a necessity for systems that buffer stochastic fluctuations and establish precise threshold concentrations of c-di-GMP to initiate rapid program switch. We postulate that in order to install stable programs, cells harbor specialized enzymes with the ability to "sense" the prevailing c-di-GMP levels and are equipped with feedback control and non-linear behavior. In principle such a cellular component could generate populations with bistable c-di-GMP steady states, where intermediate levels would be highly instable (Ferrell, 2002).

Here we characterize the c-di-GMP-specific phosphodiesterase and transcription factor PdeL from *Eschericia coli* K-12. We show that PdeL is feedback regulated both on the transcriptional and on the enzymatic level and that these properties install bistable c-di-GMP regimes in *E. coli* cells. PdeL transcription is under superordinate control by the central metabolic regulator Cra, which binds to the *pdeL* promoter region to recruit PdeL. PdeL stimulates its own expression in a c-di-GMP-dependent manner. This positive feedback loop on the transcriptional level is assisted by a double-negative feedback loop at the enzymatic level where c-di-GMP inhibits PdeL activity and PdeL itself negatively contributes to the c-di-GMP pool. As a consequence, PdeL shows high catalytic and transcription activity at low c-di-GMP levels, while the protein is catalytically and transcriptionally inert when c-di-GMP levels are high. We present structural, biochemical and genetic evidence that PdeL catalysis and transcription are directly interlinked through a c-di-GMP-driven non-linear conformational switch of PdeL. This system generates bistable populations with a high degree of cellular memory that buffers against noise in c-di-GMP distribution and establishes self-sustained heritable regimes of a potent small signaling molecule.

Results

CRA AND PDEL ARE ACTIVATORS OF *PDEL* TRANSCRIPTION

To understand the determinants of *pdeL* auto-regulation, we set out to dissect the regulatory elements of the *pdeL* promoter region (Figure 1A). This region contains a σ^{70}-dependent promoter, 341 bp upstream of the *pdeL* start codon (Shimada et al., 2005), a binding site for the central metabolic regulator Cra (**c**atabolite **r**epressor **a**ctivator) (Shimada et al., 2005; 2011), and a palindromic binding site for PdeL 675 bp upstream of the *pdeL* start codon (Reinders et al., 2015). We first confirmed that Cra binds with high affinity (K$_D$ = 49 nM) to a site 114 bp upstream of the *pdeL* promoter, which shows strong similarity to other Cra binding sites (Shimada et al., 2011) (Figure 1A, B and Figure S1A). EMSA experiments with different DNA fragments and oligonucleotides spanning the promoter region revealed an additional binding site for PdeL in the immediate vicinity of the Cra binding site (Figure 1A, B). PdeL binding to this site was dependent on the presence of Cra, indicating that Cra is able to recruit PdeL to this site upstream of the promoter. We thus termed this binding site **C**ra-**d**ependent PdeL-**b**ox (CDB). Titration experiments revealed that PdeL binds to this DNA site with an affinity similar to Cra (K$_D$ = 76 nM) (Figure S1B). In contrast, PdeL binds to the upstream **C**ra-**i**ndependent **b**inding site (CIB) with significantly lower affinity (K$_D$ = 573 nM) (Figure 1B and Figure S1C). While c-di-GMP negatively impacts *pdeL* transcription (Reinders et al., 2015), *in vitro* binding of PdeL to the CDB and CIB sites was not modulated by c-di-GMP (Figure 1B).

Strains lacking Cra or PdeL showed strongly reduced *pdeL* promoter activity as compared to wild type (Figure 1C), arguing that both proteins help stimulating *pdeL* transcription. Scrambling of the Cra- or PdeL-boxes, resulted in a similar reduction of *pdeL* promoter activity (Figure S1D, C). The observation that the Δ*cra* deletion had a stronger effect as compared to the Δ*pdeL* mutant, together with the observation that Cra is required for PdeL binding to the CDB site indicated that Cra acts upstream of PdeL in stimulating *pdeL* transcription. Scrambling one half-site of the CIB palindrome moderately reduced *pdeL* transcription 1.7-fold (Figure 1C and Figure S1D, E).

A recent study had shown that the histone-like protein H-NS binds to the intergenic region of *pdeL* (Grainger et al., 2006). After recognition of a specific nucleation consensus sequence (Fang and Rimsky, 2008; Lang et al., 2007; Sette et al., 2009), H-NS is described to polymerize across AT-rich DNA-stretches thus facilitating bending or bridging of DNA (Dorman, 2004). The *pdeL* promoter region has a relatively high AT content (66%) and contains several putative H-NS recognition sequences, one of which overlaps the 5'-palindrome half-site of the CIB (Figure 1A). EMSA analyses showed that PdeL competes with H-NS for binding to the CIB (Figure 1D). In agreement with H-NS acting as a transcriptional silencer of *pdeL*, an *hns* mutant showed strong derepression of *pdeL* transcription (Figure 1C).
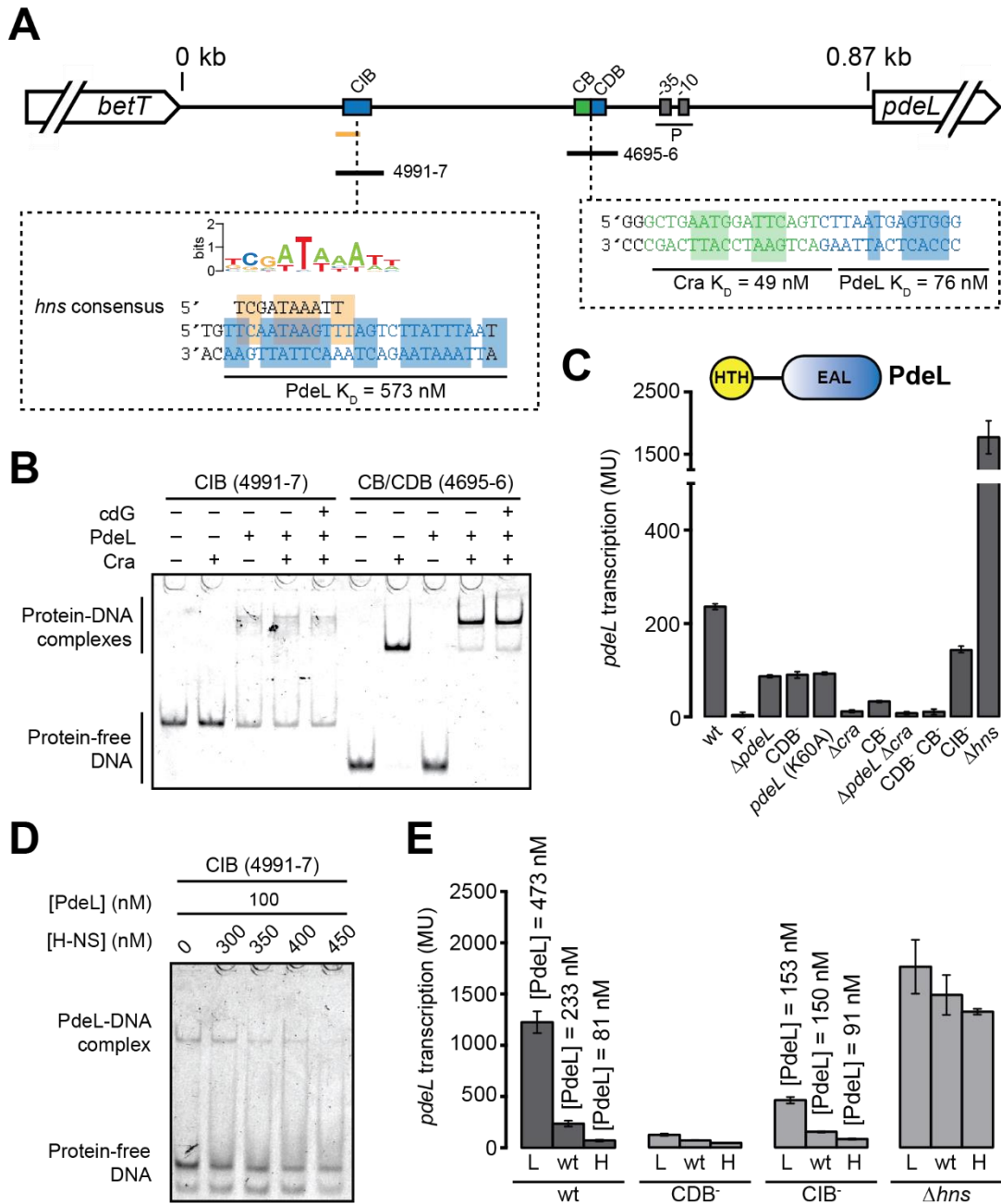
FIGURE 1: REGULATORY ELEMENTS OF PDEL TRANSCRIPTION. (A)

(A) Schematic representation of pdeL intergenic region (not to scale). Minimal binding regions for PdeL- and Cra-binding are shown in blue and green respectively. Palindromes or bases, which were identified to be crucial for transcription factor binding are highlighted in blue or green boxes respectively. Binding affinities for Cra and PdeL to respective binding boxes are shown as determined by EMSA (see Figure S1). H-NS recognition sequence is shown as web logo. Putative H-NS-recognition site overlapping with CIB is highlighted in orange. (B) Electrophoretic mobility shift assay (EMSA) of 5′ Cy3 labeled oligonucleotides, co-incubated with purified Cra-StrepII and PdeL-StrepII. (CDB = Cra-dependent PdeL-box; CB = Cra-box; CIB = Cra-independent PdeL-box). The position of the labeled oligonucleotides (4991-7 & 4695-6) within the intergenic region is depicted in (A). (C) β-galactosidase activity of merodiploid PpdeL-lacZ promoter fusion. Transcription factor recognition sequences were randomized to abolish binding. Mutations abolishing binding of PdeL to CIB were chosen to not affect H-NS recognition sequence. Inset shows domain architecture of PdeL. (D) Competition of PdeL and HN-S for CIB as

determined by EMSA. Increasing H-NS-StrepII concentrations were titrated to a fixed PdeL-StrepII concentration of 100 nM. (E) Effect of c-di-GMP on pdeL transcription. pdeL transcription was probed in strains with different c-di-GMP regimes (L = low c-di-GMP levels, which correspond to a ΔpdeH strain with 65 μM IPTG induction of Plac-pdeH. H = high c-di-GMP levels, which correspond to a ΔpdeH strain with uninduced Plac-pdeH). Cellular PdeL protein levels – as determined by protein titration experiment – are shown above corresponding bars. c-di-GMP-dependent pdeL transcription is shown in CDB- and CIB- promoter mutation as well as in an hns mutant background.

Together these data indicated that Cra, PdeL and H-NS are critical regulatory elements of the *pdeL* promoter. The data suggested that H-NS acts as a transcriptional silencer, possibly by protecting large regions of the *pdeL* promoter region.

CRA AND PDEL MEDIATE C-DI-GMP-DEPENDENT TRANSCRIPTION OF PDEL

PdeL autoregulates transcription of the *pdeL* gene in response to the cellular levels of c-di-GMP (Reinders et al., 2015) (Figure 1E). While *pdeL* transcription is maximal at low c-di-GMP concentration, it is strongly reduced at increased c-di-GMP levels. As a result, PdeL protein levels change roughly 10-fold from 81 nM – 473 nM (Figure 1E) in strains with c-di-GMP levels ranging from 0 – ca. 5.7 μM (data not shown). This c-di-GMP mediated response was not only dependent on PdeL itself, but was also abrogated when the PdeL binding sites in the *pdeL* promoter region was mutated (Figure 1E). While scrambling the CDB site abolished *pdeL* transcription, mutation of the CIB strongly diminished the dynamic range of *pdeL* promoter strength. These data suggested that the CDB is the primary control element of c-di-GMP-dependent *pdeL* transcription, while the distal CIB serves as an auxiliary site to enhance the dynamic range of c-di-GMP control. The c-di-GMP mediated control of *pdeL* transcription is completely abolished in an *hns* mutant (Figure 1E), arguing that H-NS acts as a silencer to gauge *pdeL* transcription to a range in which c-di-GMP has the maximal dynamic range effect on *pdeL* transcription.

PDEL IS A C-DI-GMP SENSOR

We previously showed that PdeL acts as a sensor for c-di-GMP by translating the intracellular c-di-GMP concentration into *pdeL* expression (Reinders et al., 2015) (Figure. 1E). To understand this link, we genetically dissected the propertied of PdeL needed for c-di-GMP-dependent *pdeL* transcription.

In our previous study, we introduced a DNA-blind PdeL mutant (K60A), which showed baseline *pdeL* expression, thus concluding that PdeL regulates its own expression (Reinders et al., 2015). In line with these results a *pdeL* (K60A) allele remained transcriptionally insensitive to c-di-GMP (Figure 2). In agreement with our previously published data (Reinders et al., 2015), this reinforces
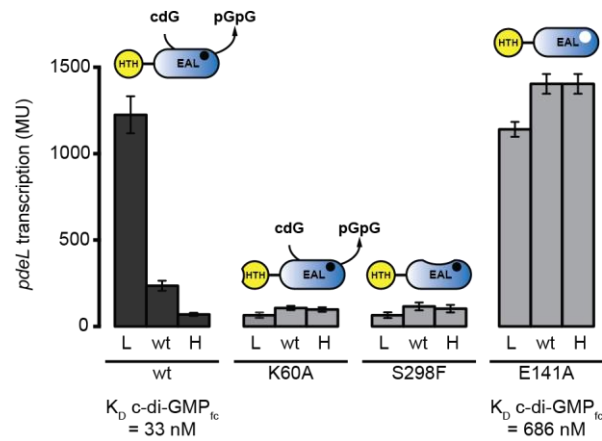
FIGURE 2: DETERMINANTS OF C-DI-GMP-DEPENDENT *PDEL* TRANSCRIPTION AND PDEL ENZYME ACTIVITY.

PdeL promoter activity of PdeL mutant variants (K60A = DNA-binding-deficient, S298F = dimerization-deficient, E141A = c-di-GMP binding-deficient). Specific β-galactosidase activity was determined in different c-di-GMP regimes as introduced in Figure 1. For wild type, as well as variant E141A the binding affinity of fluorescein-labeled c-di-GMP (c-di-GMP$_{fc}$) to PdeL$_{EAL}$ was determined in the presence of Mg^{2+}.

that PdeL itself is strictly required for c-di-GMP-dependent *pdeL* autoregulation by binding to its own promoter region.

In a previous study focusing on structural and biochemical characterization of the EAL-domain of PdeL it was nicely shown that c-di-GMP drives PdeL dimerization (Sundriyal et al., 2014). Moreover, a crucial serine (S298) was identified as a key player for dimerization. Mutation of this serine to a bulky aromatic amino acid fully abrogated dimerization and consequently enzyme activity (Sundriyal et al., 2014). Interestingly, mutation of S298 to phenylalanine mead the *pdeL* promoter irresponsive to c-di-GMP (Figure 2) arguing that c-di-GMP-dependent transcription requires either the enzymatic activity of PdeL, its ability to dimerize or both. To further address this, we focused on conserved active site residues of PdeL crucial for substrate binding, such as the highly-conserved glutamate as part of the EAL motif (Tchigvintsev et al., 2010). Alanine-substitution of this particular glutamate (E141A) lead to derepressed and c-di-GMP-independent *pdeL* transcription (Figure 2).

Given that a dimerization deficient PdeL mutant shows wild-type-like substrate binding constants (Sundriyal et al., 2014) these results suggest that absent c-di-GMP-dependent *pdeL* transcription of a dimerization mutant is a consequence of impaired dimerization, rather that absent enzymatic activity. Form this we conclude that that c-di-GMP is sensed by binding to the active site of PdeL and thereby inducing dimerization to regulate *pdeL* transcription.

TWO DIMER CONFIGURATIONS OF PDEL DRIVE C-DI-GMP-DEPENDENT *PDEL* TRANSCRIPTION

Given that both DNA-binding and dimerization of PdeL are prerequisites for *pdeL* transcription and that substrate binding induces dimerization, it is tempting to hypothesize that substrate-induced dimerization of the EAL-domain facilitates dimerization of the associated HTH-domains and

therefore DNA binding. However, the observation that a dimerization-deficient mutant showed wild-type like binding to DNA (data not shown) lead us to test alternative hypotheses for how PdeL regulates its own transcription in response to c-di-GMP.

Structural studies with the EAL-domain of PdeL revealed that PdeL can adopt two different dimer configurations (Sundriyal et al., 2014). In its apo form, PdeL$_{EAL}$ crystalized as a canonical "open" EAL-dimer (Figure 3A, C), whereas in its c-di-GMP-bound form, PdeL formed a non-canonical "closed" EAL-dimer configuration (Figure 3B, C). For simplicity reason the canonical dimer configuration is termed R-state (relaxed) and the non-canonical configuration T-state (tight) throughout this study.

Formation of the T-state requires the two dimerization helices $\alpha5_A$ and $\alpha6'_B$ face each other via their positively charged N-termini. In order to enable this conformation, intercalation of the negatively charged D295$_B$ residue is strictly required (Figure 3A, B). Moreover formation of the two dimer configurations comes along with large structural movements in a highly conserved loop region, which connects strand $\beta5$ and $\alpha5$ of the EAL TIM-barrel structure and is commonly termed loop 6 (Figure 3A-C) (Sundriyal et al., 2014). Loop 6 was shown to play a central role in PDE enzyme activity and to impact dimerization and the formation of higher oligomers (Rao et al., 2009). In PdeL a striking feature of loop 6 is its ability to adopt two different conformations, which are attributed to the T- and R-state (Sundriyal et al., 2014). Alternative conformations of loop 6 are directed by (i) the dimer configuration, (ii) occupancy of the active site and (iii) E235, the so-called "anchoring glutamate", which interacts either with active-site residue D263 or with T270, a central residue within loop 6 (Figure 3A, B). Thus, it appears that there is a loop 6-mediated bidirectional communication between the active site and the dimerization interface of PdeL.
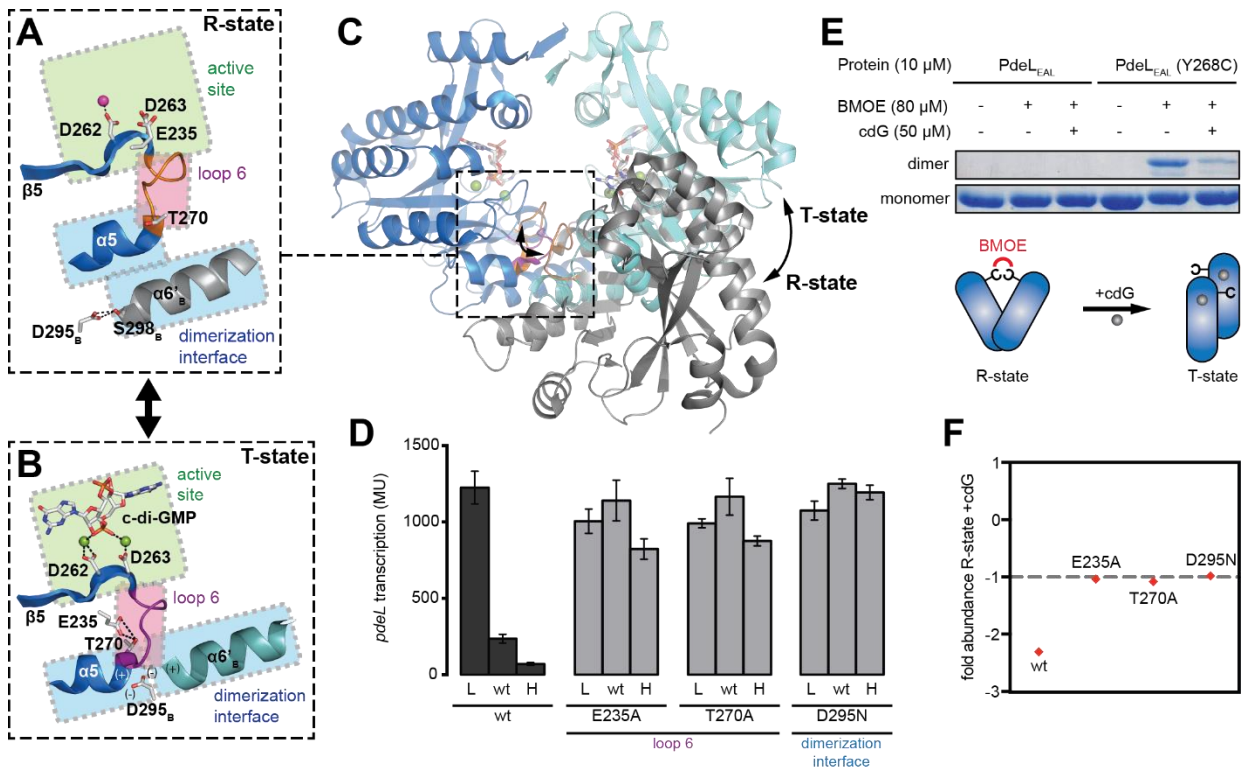
FIGURE 3: CHARACTERIZATION OF PDEL DIMER SPECIES.

(A) Zoom of active site (green), loop 6 (loop itself shown in orange, region in magenta) and dimerization helices (blue) in canonical "open" dimer configuration (R-state) of PdeL EAL-domain as crystalized in apo in presence of Mg^{2+}. **(B)** Zoom of non-canonical "closed" dimer configuration, crystalized in presence of Ca^{2+} and c-di-GMP. Coloring is analogous to (A), with loop 6 here shown in magenta. **(C)** Overlay of T-state dimer (blue hues) and a protomer of the R-state configuration (grey), depicting large quaternary rearrangements and positioning of loop 6. **(D)** c-di-GMP-dependent *pdeL* Promoter activity of PdeL point mutations in the dimerization interface and loop 6. (L = low c-di-GMP levels, H = high c-di-GMP levels). Note that both D295N and T270A were isolated as a motile suppressor allele (Figure S2). **(E)** *In vitro* cysteine-crosslink of PdeL$_{EAL}$ (Y268C)-StrepII with bismaleimidoethane (BMOE). Crosslinks were performed in absence or presence of Ca^{2+} and 50 µM c-di-GMP. As a negative control for Y268C-specific crosslink wild type PdeL$_{EAL}$-StrepII was included. **(F)** Quantification of *in vitro* cysteine-crosslinks of PdeL mutant variants as described in (E). Graph shows ratio of band intensity between cysteine-crosslink in presence and absence of excess c-di-GMP, plotted as fold change.

As a matter of fact, mutating of the anchoring glutamate (E235A) lead to derepressed and c-di-GMP-independent *pdeL* transcription (Figure 3D) arguing that destabilization of loop 6 favors a transcriptionally active species of PdeL. Based on the PdeL$_{EAL}$ structure, mutating the T-state interaction partner of the anchoring glutamate (T270) or the residue stabilizing the T-state conformation of dimerization helices α5 and α6' (D295), should in principle phenocopy the effect of an E235A. This was confirmed by gain of function *pdeL* alleles (T270A & D295N), which were isolated in a selection screen for motile suppressors of a non-motile *ΔpdeH* strain (see (Reinders et al., 2015) and Figure S2). Reassuringly, these mutations indeed fully abrogated c-di-GMP-dependent *pdeL* transcription control (Figure 3D).

Thus, c-di-GMP seems to be sensed via the active site and this information translated via the conserved loop 6 to the dimerization interface in order to dictate the dimer configuration of PdeL, which in turn determines transcriptional activity of PdeL.

C-DI-GMP DRIVES PDEL DIMER-SPECIES CONFIGURATION

The previous section suggested that PdeL can shuttle between a transcriptionally inert T-state and a transcriptionally active R-state dimer. Since *pdeL* transcription is a function of c-di-GMP levels, we postulated that c-di-GMP drives the switch between the two PdeL dimer configurations. In order to test this substrate-dependent regulation we performed cysteine cross-link assays with the catalytic domain of PdeL in presence and absence of c-di-GMP. These experiments were based on a cysteine substitution in residue Y268, which exclusively show close steric proximity to the R-state dimer (Figure S3). Bismaleimidoethane-mediated (BMOE) oxidation of Y268C revealed that in absence of c-di-GMP the R-state variant is predominantly cross-linked (Figure 3E). Further, in line with our transcriptional data, mutations of crucial loop 6 residues or the aspartic acid intercalating between loop α5A and α6′B renders PdeL insensitive to a substrate-induced R- to T-state switch (Figure 3F).

These data evoke a model where PdeL can adopt two alternative confirmations, the equilibrium of which is determined by the concentration of its substrate. While low c-di-GMP concentrations favor the transcriptionally active R-state, PdeL switches into the inert T-state at high substrate concentrations.

PDEL ENZYME ACTIVITY SCALES WITH C-DI-GMP CONCENTRATION

The isolated motile-suppressor mutant alleles of PdeL were isolated in a strain background displaying high c-di-GMP levels (*ΔpdeH*). Under such conditions, wild type PdeL does not show high enough activity to suppress this phenotype. Initial characterization of several motile suppressor alleles (Reinders et al., 2015) & Figure S3 showed enhanced enzymatic activity as well as derepressed *pdeL* transcription indicating that the suppressor mutations lock PdeL in a state in which c-di-GMP can no longer regulate PdeL and therefore displaying high activity even at high c-di-GMP levels. Together with the previous results we hypothesized that the c-di-GMP-driven equilibrium shift from the R-state to the T-state not only switches PdeL off as a transcription factor but also as an enzyme.

To test this, we measured turnover rates of PdeL as a function of increasing substrate concentrations. Indeed, we determined substrate concentration-dependent turnover rates that were nicely fitted with a substrate inhibition Michaelis-Menten model (Figure 4A), thus confirming that PdeL shows low turnover rates at high c-di-GMP levels.

PDEL ENZYME ACTIVITY SCALES WITH PDEL CONCENTRATION

In the previous sections, we showed that c-di-GMP drives *pdeL* transcription by determining the equilibrium between an enzymatically and transcriptionally inert T-state and highly active R-state configuration. As a consequence, within a c-di-GMP concentration range between $0 - 5.7$ µM, PdeL protein levels inversely scale between $81 - 473$nM (Figure 1E). Although this feature is commonly observed in transcription factors that regulate their own expression in response to a ligand (Chen et
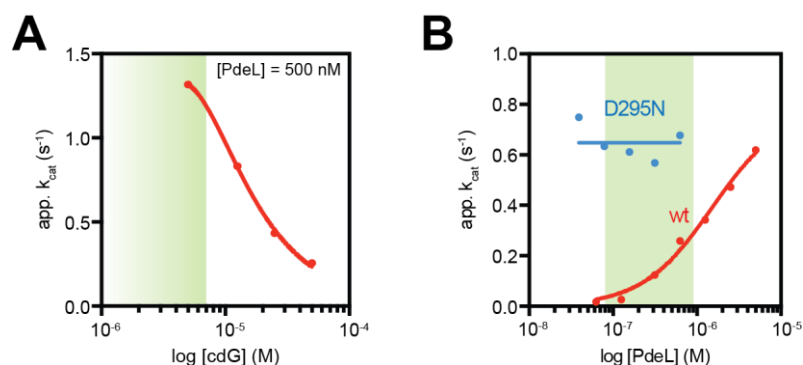
FIGURE 4: PROPERTIES OF PDEL ENZYME ACTIVITY.

(A) Apparent k_{cat} of PdeL-StrepII as a function of PdeL concentration (wt = red, motile suppressor and R-lock mutant S295N = blue). Enzyme activity was measured with phosphate sensor method as previously published in {Reinders:2015bo}. Data points were fitted with a simple Michaelis-Menten model. Green are depicts physiologically relevant PdeL concentration range. **(B)** Apparent k_{cat} at 37°C of 500 nM PdeL-StrepII as a function of increasing substrate concentrations. Enzyme activity was measured with FPLC as published in {Sundriyal:2014ez}. Data points were fitted with a Michaelis-Menten substrate inhibition model. Green area depicts physiologically relevant c-di-GMP concentration range.

al., 2017) this autoregulation is particularly interesting given that PdeL is a *bona fide* c-di-GMP-specific phosphodiesterase. Thus, increasing PdeL levels could in principle also impact PdeL enzyme activity and by that have substantial implications on the feedback loop itself as well as on general cell physiology.

To address this question, we determined turnover rates of PdeL as a function of PdeL concentration. PdeL turnover rates showed a non-linear apparent k_{cat}, with half-maximal activation at ca. 1.5 µM PdeL concentration (Figure 4B). From this we concluded that one reason for building up PdeL levels is a net increase in PdeL enzyme activity.

Since our data reinforce the notion that there is bidirectional communication between the dimer configuration and the active site via loop 6, we hypothesized that – in addition to substrate controlled dimer-state equilibrium – PdeL itself can drive the equilibrium between the inert T-state and highly active R-state. To test this, we measured enzyme activity of the D295N R-lock variant as a function of protein concentrations. We could clearly show that – compared to wild type – an R-lock mutant shows a protein concentration-independent k_{cat}, which is comparable to the highest k_{cat} values measured for wild type PdeL (Figure 4B).

This argues that in addition to substrate-regulated T- to R-state equilibrium, the dimer configurations of PdeL are a function of PdeL levels itself therefore possibly strongly enhancing the equilibrium shift from a transcriptionally and enzymatically inert T-state to a highly active R-state.

PDEL EXPRESSION IS HIGHLY COOPERATIVE

At his stage, the data allow us to place PdeL in the center of two interlinked positive feedback loops. (i) a double-negative enzymatic feedback where c-di-GMP inhibits PdeL enzyme activity and PdeL

negatively affects the c-di-GMP pool and (ii) a positive transcriptional feedback loop where increasing PdeL levels enhance *pdeL* transcription (Figure 5A). When present in noisy systems, positive feedback loops can give rise to bistability (Ackermann, 2015), especially when these feedback loops show strong non-linear or cooperative behavior. The observation that *pdeL* transcription is driven by two intricate positive feedback loops suggests that *pdeL* transcription shows cooperative behavior.

To test whether the *pdeL* promoter responds in a cooperative manner to increasing PdeL levels, we measured *pdeL* transcription in a strain where *pdeL* is driven by a tetracycline-inducible promoter. To exclude the c-di-GMP effect on *pdeL* transcription we performed this experiment in a strain devoid of c-di-GMP (full P_{lac}–*pdeH* induction in a $\Delta pdeH$ background). Here we saw that *pdeL* transcription reacts in a highly cooperative manner ($n_h = 5.2$) to increasing levels of PdeL, with a half-maximal activation constant of 317 nM PdeL (Figure 5B). Interestingly, there is no activation of PdeL transcription in a strain background with high c-di-GMP, which reinforced our previous observation that high levels of c-di-GMP lock PdeL in the inert T-state.

PDEL EXPRESSION SHOWS STRONG TRANSCRIPTIONAL MEMORY

In the previous section, we showed that the *pdeL* promoter reacts in a cooperative manner to PdeL levels. In the light of positive feedback regulation, this property might be the framework for bistable expression of *pdeL*. A hallmark of bistability is hysteresis, which describes the discrepancy in activation energies depending on the initial resting state of a system (Mitrophanov and Groisman, 2008). This feature ultimately endows a system with intrinsic memory. and can lead to the establishment of bistable and bimodal populations (Veening et al., 2008).

To test this, we performed hysteresis experiments *in vivo*. In order to modulate c-di-GMP levels we made use of the previously introduced P_{lac}–*pdeH* expression system, which we introduced in a $\Delta pdeH$ background. Either not inducing or fully inducing the plasmid over-night allowed us to pre-establish a history with high or low levels of c-di-GMP. In these two backgrounds, we finely tuned the c-di-GMP levels and measured *pdeL* transcription as a function of c-di-GMP in exponential growing cells (Figure 5C). From this experiment, we saw a remarkable hysteresis window with a window size of ca. 1 log, within a c-di-GMP concentration range of 44 nM – 1.6 µM.

From this we conclude that – depending on the c-di-GMP history of the cells – there is a certain c-di-GMP concentration range that only allows for two stable c-di-GMP concentration regimes, therefore confirming that c-di-GMP-dependent *pdeL* expression shows remarkable hysteresis.
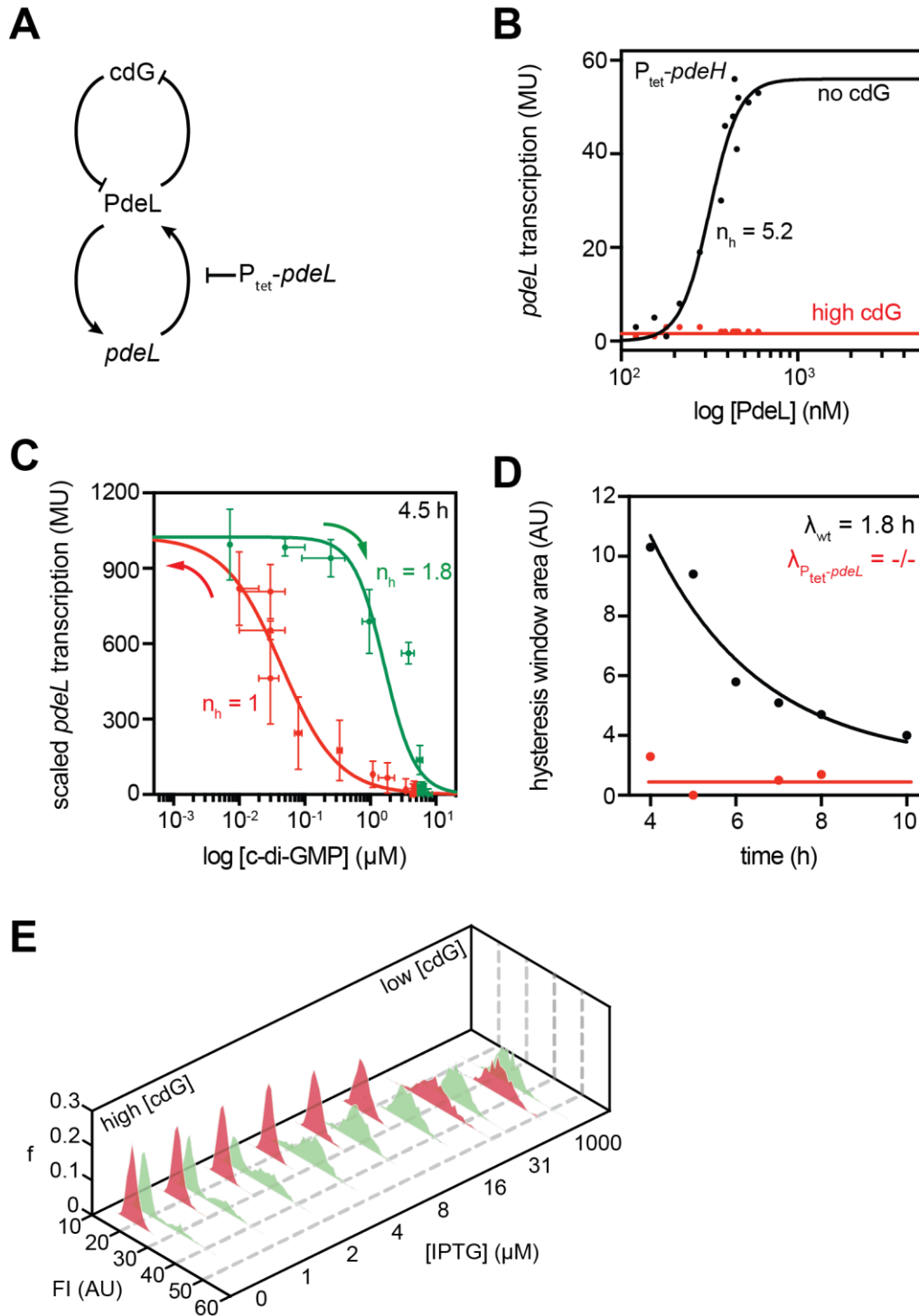
FIGURE 5: BISTABILITY AND BIMODALITY OF *PDEL* EXPRESSION.

(A) Schematic of feedback loops determining *pdeL* transcription. Upper loop = double-negative enzymatic feedback loop. Lower loop = transcriptional feedback loop. Chromosomal construct with P$_{tet}$-driven *pdeL* (P$_{tet}$-*pdeL*) opens transcriptional feedback loop. **(B)** Cooperative behavior of PdeL-dependent *pdeL* transcription. Experiment was performed in a *ΔpdeH* background with chromosomal P$_{tet}$-*pdeL* and plasmid borne P$_{lac}$-*pdeH*. Black curve = Full induction of P$_{lac}$-*pdeH* to generate absent c-di-GMP levels. Red curve = no induction of P$_{lac}$-*pdeH* to generate high c-di-GMP levels. Absolute PdeL levels were quantified by comparing PdeL-3xFlag levels to a purified and quantified PdeL-3xFlag-StrepII titration standard via western blot. Black curve was fitted with Michaelis-Menten equation with Hill-coefficient- Red curve was fitted with horizontal line. **(C)** Hysteresis experiment after 4.5 growth in TB medium at 37°C. Strain background is *ΔpdeH* P$_{lac}$-*pdeH*. Red curve represents strain background grown o/n with no induction of plasmid-borne *pdeH* = initial high c-di-GMP levels. Green curve represents strain background grown

over night with full induction of plasmid-borne *pdeH* = low initial c-di-GMP levels. Through gradual expression of *pdeH*, red curve shows *pdeL* on-kinetics due to reduction of c-di-GMP levels and green curve shows *pdeL* off-kinetics due to increasing c-di-GMP levels. Curves were fitted with Michelis-Menten model with Hill-coefficient. **(D)** Half-life of pdeL transcription memory. Black curve = wild type *pdeL* promoter. Red curve = P$_{tet}$-driven *pdeL*. Data points show area of hysteresis window as a function of time. Black curve was fitted with standard exponential decay curve. Red curve was fitted with horizontal line. **(E)** Quantification of single cell fluorescence of a *pdeL*-[RBS-*mCherry*]$_2$ reporter fusion in a *ΔpdeH* background. Hysteresis experiment was performed analogous to (C) by tuning P$_{lac}$-*pdeH* in a strain where P$_{lac}$-*pdeH* was previously fully induced over night (green) or not induced at all (red).

PDEL TRANSCRIPTION IS BISTABLE

Although c-di-GMP-dependent *pdeL* regulation shows strong hysteresis it might nonetheless be that the memory might quickly collapse as a function of time, which would argue against a highly stable system. Thus, to determine the half-life of *pdeL* transcription memory we measured the hysteresis window area as a function of time.

We measured the hysteresis window area from hysteresis experiments performed within a time-window of 4 – 8 h and observed a long perpetuation of *pdeL* transcription memory with a half-life of nearly 2 h (Figure 5D), which under the growth conditions tested would correspond to roughly 4 cell divisions. This experiment reinforces that c-di-GMP-dependent *pdeL* transcription not only shows strong transcriptional memory but can maintain this memory over long timescales, thus confirming the strong bistable nature of *pdeL* transcription.

BISTABILITY OF *PDEL* FULLY DEPENDS ON THE TRANSCRIPTIONAL FEEDBACK LOOP

At this point we aimed to dissect the requirements for bistable c-di-GMP-dependent *pdeL* transcription. As previously described, *pdeL* transcription depends on two intricate self-amplifying feedback loops (Figure 5A). We therefore asked, which of the two feedback loops has the greatest contribution or is even essential for the establishment of bistability. Since our previous data showed that the transcriptional feedback loop reacts highly cooperative to an increase in PdeL levels, this feedback loop seemed the best candidate for the establishment and maintenance of *pdeL* transcription memory.

In order to open the transcriptional feedback loop, we exchanged the native *pdeL* intergenic region with a tetracycline inducible promoter. To measure the memory half-life of a *pdeL* circuit lacking the transcriptional feedback loop, we performed the same experiment as described in the previous section at PdeL levels similar to a low c-di-GMP background. We observed that *pdeL* transcription memory fully collapsed showing no apparent memory even at the first time-point measured (Figure 5D), arguing that *pdeL* transcription memory and thus establishment of bistability fully depends on the presence of the transcriptional feedback loop.
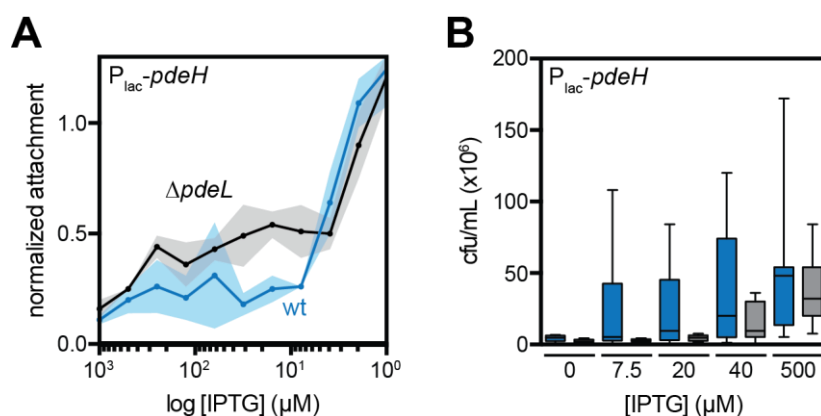
FIGURE 6: PROPERTIES OF PDEL ENZYME ACTIVITY.

(A) Crystal-Violet-based staining of attached biomass during gradual expression of plasmid-borne P$_{lac}$-*pdeH*. Biofilm formation of a P$_{const}$-*pgaA-D* Δ*pdeH* (blue) and P$_{const}$-*pgaA-D* Δ*pdeH* Δ*pdeL* (black). In order to start with low c-di-GMP levels strains were grown over night with full induction of P$_{lac}$-*pdeH*. **(B)** Quantification of planktonic cells escaping a pre-formed biofilm. A *csrA⁻* Δ*pdeH* (black) and *csrA⁻* Δ*pdeH* Δ*pdeL* (blue), equipped with P$_{lac}$-*pdeH* were incubated for 8 h static at 30°C to form a biofilm. After washing, fresh medium supplemented with increasing amounts of IPTG was added to the pre-formed biofilm and incubated static at 30°C for 3 h. Escaped planktonic cells were quantified by dot-spotting serial dilutions and determination of cfu/mL. Black bars represent median cfu/mL, error-bars show upper and lower quartile.

BISTABLE EXPRESSION OF *PDEL* GENERATES BIMODAL POPULATIONS

The behavior of individuals within a clonal population will ultimately determine how a population will adapt to environmental changes, which in this particular case are changes in c-di-GMP levels. It is mostly observed that bistable systems also manifest in bimodality on the single-cell level. These properties help to establish life-strategies such as bet-hedging and/or division of labor, which significantly contribute to the fitness of a whole population (Ackermann, 2015).

In the previous section, we observed strong bistability of *pdeL* expression on the population level. To address how this translates to individual cells we re-performed the hysteresis experiment on the single-cell level by measuring fluorescence of a transcriptional *pdeL*-[RBS-*mCherry*]$_2$ fusion.

Here we observed that while *pdeL* on-kinetics showed a unimodal – yet switch-like – behavior, down-kinetics of PdeL showed clear bimodal split at c-di-GMP concentrations of ca. 2 µM (Figure 5E). Thus, c-di-GMP-dependent and bistable PdeL expression establishes bimodal populations. This bimodality however depends on the c-di-GMP history of the cells.

PDEL IS A GATEKEEPER FOR MOTILE-SESSILE LIFESTYLE TRANSITIONS

The dissection of the feedback loops driving c-di-GMP-dependent *pdeL* transcription, showed that PdeL is in the center of two positive feedback loops, which sense c-di-GMP but at the same time affect the c-di-GMP pool itself (Figure 5A). This suggests that within a certain c-di-GMP

concentration window, PdeL can have a substantial impact on the global c-di-GMP pool and therefore on c-di-GMP-related cellular processes.

To test this, we looked at the effect of PdeL on the formation of biofilms and the escape from preformed biofilms, which both are processes known to be regulated by c-di-GMP (Chua et al., 2014; Newell et al., 2011; Steiner et al., 2013). To this end we chose to test the effect of PdeL on poly-GlcNAc-dependent (Pga) biofilm formation, since it was previously described that this system is post-translationally regulated by c-di-GMP with an activation constant of 62 nM (Steiner et al., 2013). In order to test the effect of PdeL on biofilm entry we took advantage of our P_{lac}-*pdeH* expression system to tune c-di-GMP in strain backgrounds, with initially low c-di-GMP levels. In order to uncouple the translation of the *pga* operon from the upstream BarA-UvrY/CsrA-cascade (Gonzalez Chavez et al., 2010; Palaniyandi et al., 2012; Pernestig et al., 2003; Suzuki et al., 2002; Wang et al., 2005), we expressed the *pga* operon from a weak constitutive promoter. While the wild type strain showed a sharp and steep response to increasing c-di-GMP levels, the *pdeL* mutant prematurely increased biofilm formation at already much lower c-di-GMP levels compared to wild type (Figure 6A). Apparently, one role of PdeL is to buffer c-di-GMP noise and to prevent premature entry into biofilm mode.

Since PdeL is a phosphodiesterase it could in principle also confer an advantage to cells trying to escape from an existing biofilm. We thus designed an experiment in which we compared the ability of a *csrA⁻ ΔpdeH* and a *csrA⁻ ΔpdeH ΔpdeL* to escape from a preformed biofilm upon reduction of c-di-GMP levels through induction of plasmid-borne PdeH. While escape rates remained low over a range of c-di-GMP levels (PdeH induction), a strain harboring *pdeL* displayed significantly higher escape rates even at relatively low PdeH induction (Figure 6B). Strikingly, the PdeH induction at which escape is strongly induced matches the threshold c-di-GMP concentration for *pdeL* expression (> 3 µM) (Figure 5C). Thus, PdeL not only buffers against premature entry into biofilms as c-di-GMP levels increase in response to DGC activity, but it also promotes cellular escape from biofilms as c-di-GMP levels drop in response to PDE activity. These results provide physiological relevance to PdeL as a cellular component facilitating rapid and robust lifestyle switches.

Discussion

Binary switches between alternative cellular programs are key features of natural systems contributing to cellular homeostasis or population fitness in fluctuating environments. The second messenger c-di-GMP directs a series of important cellular processes in bacteria including motility, virulence and biofilm formation. But how are c-di-GMP dependent programs regulated considering that this cellular network might exhibit considerable internal noise and is highly sensitive and complex? Is the internal noise in this network a basis for "all-or-nothing" phenotypes? Are these decisive phenotypes beneficial in nature? And if so how are stochastic fluctuations amplified to drive deterministic and robust lifestyle-decisions? Here we identify the phosphodiesterase PdeL as a central element of c-di-GMP homeostasis in *E. coli*. We demonstrated that PdeL activity and expression respond to c-di-GMP and by coupling enzymatic and transcriptional feedback it provides bistable c-di-GMP regimes and rapid responses at c-di-GMP threshold levels.

Based on our genetic and biochemical data we propose the following working model: PdeL is recruited to the *pdeL* promoter region by the Cra regulator at metabolic conditions that favor gluconeogenesis (Ramseier, 1996). When intracellular c-di-GMP levels are high, PdeL adopts the non-canonical T-state dimer configuration. In this static conformation, the active sites of both protomers are occupied with substrate thereby shifting PdeL into a conformation that is both catalytically and transcriptionally inert. When cellular levels of c-di-GMP drop, the fully loaded and inert T-state is destabilized, thereby shifting the equilibrium to the canonical R-state dimer configuration, which is highly active both as an enzyme and as a transcription factor. This model is supported by the observations that mutations, which generally abolish either substrate binding such as E141A or the stabilization of loop 6 or the dimerization helices in the T-state conformation (E235A, T270A, D295N) lead to derepressed and c-di-GMP-irresponsive *pdeL* transcription.

We conclude that relieving the T-state through reduction of the c-di-GMP regime initiates an equilibrium shift from an inert to a catalytically and transcriptionally highly active PdeL species. This will have to effects: (i) derepression of the catalytic activity of PdeL will further contribute to the decrease of c-di-GMP and (ii) cellular PdeL levels will substantially rise. The latter is of great importance, since apart from the substrate-mediated effect on *pdeL* transcription we observed that *pdeL* transcription and PdeL enzyme activity is a function of PdeL levels itself. Since it is not conceivable, how increasing PdeL levels might positively affect an equilibrium between to dimer species, we suggest that increasing PdeL levels will allow PdeL to bind to the upstream low affinity Cra-independent PdeL-box (CIB) therefore inducing tetramerization of PdeL with a PdeL dimer bound to the Cra-dependent PdeL-box (CDB). We argue that tetramerization will further shift the equilibrium towards the R-state, resulting in full transcriptional activity and thus maximal catalytic activity. This is corroborated by the observation that loss of the CIB impairs maximal promoter response. In addition, tetramerization might aid to displace the general gene silencer H-NS off the intergenic region of *pdeL*. In fact, the intergenic region of *pdeL* displays several regions strongly

resembling the consensus recognition sequence of H-NS, one of which we showed overlaps with the CIB and for which both H-NS and PdeL compete. Thus, occupation of the CIB at increasing PdeL levels likely induces tetramerization of PdeL, eventually aiding a robust ON-state of *pdeL* transcription and catalytic activity.

In this study, we show that placing an enzyme – which at the same time is a transcription factor – in the center of two interconnected positive feedback loops, allows to sense the prevailing c-di-GMP concentration and translate this information into autoregulation. As a c-di-GMP specific phosphodiesterase PdeL will feed back into the global c-di-GMP pool and concomitantly impose robust c-di-GMP regimes. While it is unclear whether the commitment of such a component is to generate stochasticity or to amplify already existing fluctuation, it appears that coupling of a transcription factor with an enzyme is a smart way to fulfill either of the two tasks. This might have implication in both the establishment of environmental biofilm structures as well as survival in the host environment. The need to stably reside in either of the two states becomes evident when microscopically observing *E. coli* macrocolonies. These structures are highly organized displaying vegetative, flagellated cells at the nutrient-rich bottom and curli and cellulose expressing cells in the upper – nutrient limiting – layers (Serra et al., 2013). Here, PdeL could be a key player to maintain low c-di-GMP levels in the lower nutrient rich areas. Moreover, it has been observed that these structures are not homogeneous. In fact, one can frequently find curli-ON and flagellated curli-OFF cells side-by-side even in the upper layers of such macrocolonies (Serra et al., 2013). This might have two implications: (i) According to the cross-sections of the macrocolonies it appears that flagella of cells trapped within these structures serve as a scaffold for secreted curli fibers and cellulose (Serra et al., 2013). (ii) Moreover and in line with our observations, that *pdeL* facilitates cell-dispersal from mature biofilms its bistable nature might be beneficial in order to maintain regions with flagellated cells at the surface of these structures to allow for occasional single-cell dispersal.

We postulate that PdeL is a central module to allow for bet hedging and division of labor in fluctuating environments. Thus, during its voyage through the host, including the shedding into the non-host environment, *E. coli* encounters ever-changing environments to which the phenotypic heterogeneity within a population strongly contributes in terms of survival. Therefore, nature must have selected for modules that drive phenotypic heterogeneity such as PdeL.

Thinking of PdeL as a transcription factor it is hard to reconcile that – with PdeL levels fluctuating between ca. 100 and 500 molecules per cell – PdeL is solely required for c-di-GMP-dependent autoregulation. It is more likely that PdeL engages into two major tasks: (i) autoregulation according to the metabolic- and c-di-GMP-status, which eventually affects the global c-di-GMP pool to facilitate robust lifestyle transitions in a bistable and bimodal manner and (ii) c-di-GMP-dependent regulation of secondary genes involved in either of the two major lifestyles. These two properties could be inextricably linked, since full activation of PdeL activity to affect the global c-di-GMP pool, might

need saturation of all PdeL binding sites on the *E. coli* chromosome. The use of ChIP-Seq and proteomics to unravel and characterize the complete PdeL-regulon will be the aim of future work.

Materials & Methods

Bacterial strains, plasmids and growth conditions

The bacterial strains and plasmids used in this study are listed in Table S1 & S2. *E. coli* K-12 MG1655 from Blattner et al. (Blattner et al., 1997) and its derivatives were grow as indicated in the dedicated methods sections. When needed antibiotics were present at following concentrations: 30 µg/mL chloramphenicol for plasmids and 20 µg/mL chloramphenicol for chromosomal chloramphenicol resistance cassettes, 50 µg/mL kanamycin, 100 µg/mL ampicillin for high copy plasmids and 30 µg/mL for low or single-copy plasmids.

P1 phage lysate preparation and transduction

P1 phage lysate preparation and transduction were carried out as described in (Miller, 1992)

Gene deletions and λ-RED-mediated recombineering

Chromosomal gene deletions and modifications: Gene deletions were essentially carried out either as described by Datsenko et al. (Datsenko and Wanner, 2000) or with the use of a comprehensive mutant library ("Keio collection" (Baba et al., 2006)) and P1 mediated transduction. Chromosomal 3xflag-taging of genes was carried out according to the published method by Uzzau et al. (Uzzau et al., 2001). For unmodified strains AB330 (see strain list Table S1) was used, whereas pKD46 was used for construction of strains already harboring chromosomal modifications. Selection markers were removed by site-specific recombination using pCP20 (Datsenko and Wanner, 2000).

Construction of promoter-lacZ fusions: Construction of chromosomal promoter-*lacZ* fusions were carried out via λ-RED-mediated recombination as described above. AB989 (see strain list Table S1) was used as a recipient strain. The donor PCR fragment harboring the promoter of interest was designed to site-specifically excise P_{rha}-*ccdB* and integrate upstream of the native *lacZ* ORF to generate a merodiploid translational fusion. Successful integration events were selected through growth on rhamnose minimal plates.

Electrophoretic mobility shift assay (EMSA)

5' Cy3-labeled input DNA was generated either via oligonucleotide annealing or PCR. 10 nM of the input DNA and purified proteins were incubated for 10 min at room temperature in buffer consisting of 50 mM Tris-HCl pH 8.0, 50 mM NaCl, 10 mM $MgCl_2$, 10 % glycerol, 1 mM DTT, 0.01 & Triton X-100, 0.1 mg/mL BSA and 25 µg/mL λ-DNA. As indicated in the figures, samples were incubated in the presence or absence of 2 mM $CaCl_2$ and excess c-di-GMP. Samples were run on 8 % polyacrylamide gel. DNA-protein complexes were analyzed using Typhoon FLA 7000 (GE healthcare).

β-galactosidase reporter assay

Strains were grown in TB medium o/n at 37°C. The next day cultures were diluted back 1:500 into fresh medium and grown at 37°C until desired OD600. 500 μL of the culture were mixed with 380 μL Z-buffer (75 mM Na_2HPO_4, 40 mM NaH_2PO_4, 1 mM KCl, 1 mM $MgSO_4$), 100 μL 0.1 % SDS and 20 μL chloroform. Samples were vortexed for 10 sec and left on the bench for 15 min. 200 μL sample were transferred into a clear 96-well plate (Falcon). As substrate 25 μL 4 mg/mL σ-nitrophenyl-b-D-galactopyranoside (σNPG) solution (dissolved in Z-buffer) were added. The initial velocity of the color reaction was determined at a wavelength of 420 nm.

Protein purification

All strepII-tagged proteins were purified using the same method. PdeL$_{EAL}$ variants were purified by a single StrepII-tag affinity purification, whereas for full-length PdeL and other transcription factors a heparin purification step was added.

StrepII purification: All proteins were cloned into a pET28a vector (Novagen) between NcoI and NotI restriction sites. Proteins were overexpressed in BL21 (AI) cells grown at 30°C in 2 L LB medium. For overexpression of mutant protein variants, the corresponding wild type version of the gene was deleted in the overexpression strain. At an OD^{600} of 0.6 the culture was induced with 0.1 % L-arabinose. Cells were harvested 4 h post induction by centrifugation at 5000 rpm for 30 min at 4°C. The cell pellet was resuspended in 7 mL Buffer A (100 mM Tris-HCl pH 8.0, 250 mM NaCl, 5 mM $MgCl_2$, 0.5 mM EDTA, 1 mM DTT) including a tablet of c0mplete mini EDTA-free protease inhibitor (Roche) and a spatula tip of DNaseI (Roche). Cells were lysed by 4 passages of french press and the lysate cleared at 4°C in a table-top centrifuge set at full-speed for 40 min. The cleared supernatant was loaded on 1 mL StrepTactin Superflow Plus resin (QIAGEN). The supernatant was reloaded another two times before washing with a total of 50 mL Buffer A. The column was washed with 10 mL Buffer B (100 mM Tris-HCl pH 8.0, 50 mM NaCl, 5 mM $MgCl_2$, 0.5 mM EDTA, 1 mM DTT). 500 μL aliquots of proteins were eluted with Buffer B supplemented with 2.5 mM d-Desthiobiotin.

Heparin Purification: A 1 mL HiTrap Heparin HP column (GE healthcare) was washed with 10 mL $H^2O_{dest.}$, followed by an equilibration with 10 mL Buffer B. The eluate from the StrepII-tag affinity purification was loaded three times. After loading the column was washed with 10 mL Buffer A followed by a washing step with 10 mL Buffer C (100 mM Tris-HCl pH 8.0, 350 mM NaCl, 5 mM $MgCl_2$, 0.5 mM EDTA, 1 mM DTT). The protein was eluted in 500 μL fractions with a total of 10 mL Buffer D (100 mM Tris-HCl pH 8.0, 2 M NaCl, 5 mM $MgCl_2$, 0.5 mM EDTA, 1 mM DTT). The fractions containing the highest protein concentration were pooled and dialyzed o/n at 4°C against 1.5 L Dialysis Buffer (100 mM Tris-HCl pH 8.0, 250 mM NaCl, 5 mM $MgCl_2$, 0.5 mM EDTA, 1 mM DTT). PdeL$_{EAL}$ variants used for cysteine crosslink assays were dialyzed against CXA Buffer (100 mM Tris-

HCl pH 7.2, 250 mM NaCl, 2 mM EDTA). The final protein concentration was recorded at 280 nm and the content of co-purified nucleotide contaminants determined as a ration of 260/280 nm.

Immunoblotting

Cells were grown in TB medium at 37°C until desired OD600. An equivalent of 1 mL of an OD_{600} of 1.0 was pelleted and resuspended in 100 μL SDS Laemmli buffer. Cells were lysed by boiling the sample at 98°C for 10 min. 8 μL of the total cell extract were loaded onto a 12.5 % SDS-polyacrylamide gel and proteins transferred using a BioRad® wet blot system. Proteins with 3xflag-tag were detected with a 1:10.000 dilution of monoclonal mouse α-Flag monoclonal antibody (Sigma) and a 1:10.000 dilution of polyclonal rabbit α-mouse horseradish-peroxidase (HRP) secondary antibody (DakoCytomation, DK). Proteins were visualized with enhanced chemiluminescence (ECL) detection reagent (Perkin Elmer Life Science) and imaged in a gel imager (GE ImageQuant LAS 4000).

C-di-GMP hydrolysis assays

Phosphate Sensor assay: Phosphate sensor assay was essentially performed as described in (Reinders et al., 2015). Briefly: Conversion of c-di-GMP into pGpG was measured indirectly by a coupled alkaline phosphatase (AP)/phosphate sensor online assay. The terminal phosphate of the pGpG product is cleaved by the coupling enzyme AP (20 U/μl, Roche), and the phosphate concentration is determined from the fluorescence increase through binding of phosphate to the phosphate sensor (0.5 μM; Life Technologies). PdeL and c-di-GMP concentrations were used as shown in the individual experiments. Fluorescence increase was detected by excitation at 430 nm end emission at 468 nm.

FPLC assay: Assay was performed as described in (Sundriyal et al., 2014). Enzymatic activity was assayed offline by FPLC-based steady-state nucleotide quantification following incubation for varying durations. Enzymatic reactions were carried out at 20°C in 100 mM Tris-HCl pH 8.0, 250 mM NaCl, 5 mM $MgCl_2$, 0.5 mM EDTA, 1 mM DTT and 50 M thiamine pyrophosphate as FPLC standard. PdeL and c-di-GMP concentrations were used as described in the result section. The reaction was started by addition of enzyme to a total reaction volume of 600 μl. Samples volumes of 100 μl were withdrawn and the reaction was stopped at different time points by addition of 10 μl of 100 mM and subsequent heating at 98°C for 10 min.

The samples were then analyzed using ion-exchange chromatography (1-mL- Resource-Q column) after addition of 890 μl of 5 mM ammonium bicarbonate ($NH_4 CO_3$) to increase the volume to 1 mL. 500 μL of this was then loaded onto the column. The column was washed thoroughly and the bound nucleotides were eluted with a linear NH_4CO_3 gradient (5 mM to 1 M) over 17 column volumes.

The amount of pGpG product was determined by integration of the corresponding absorption (253 nm) peak after normalization of the data with respect to the internal thiamine pyrophosphate standard.

Cysteine-crosslink assay

10 µM PdeL$_{EAL}$-3xFlag-StrepII variants purified in CXA Buffer (100 mM Tris-HCl pH 7.2, 250 mM NaCl, 2 mM EDTA) were incubated for 10 min at room temperature in presence of 10 mM CaCl$_2$ either in presence or absence of 50 µM c-di-GMP. Proteins were crosslinked for 1 h at room temperature with an 8-fold molar excess (80 µM) of bismaleimidoethane (BMOE) (ThermoFisher Scientific). Crosslink reaction was quenched for 15 min at room temperature by addition of 50 mM DTT. Samples were supplemented with SDS Laemmli buffer and proteins denature by heating at 98°C for 5 min. Samples were loaded on a 12.5 % SDS-polyacrylamide gel and detected by staining with Coomassie Brilliant Blue.

Microscopy

Fluorescence and differential interfenence contrast (DIC) microscopy was performed on a DeltaVision Core (Applied Prescision, USA) microscope equipped with an Olympus 100X/1.30 Oil objective and an EDGE/sCMOS CCD camera. Cells were placed on a PBS pad solidified with 1% agarose. Exposure time for microscopy picture was 0.05 sec for bright field (POL) and 0.3 s for mCherry. For both settings, the ND filter was set to 100% transmission.

C-di-GMP measurements

C-di-GMP measurements were performed according to the published procedure by Spangler at al. (Spangler et al., 2010). In brief: *E. coli* cells were grown in 24 mL TB medium at 37°C until an OD$_{600}$ of 0.5. Cells were pelleted and washed in 300 µL ice-cold H$_2$O$_{dest.}$. After washing the cell pellet was resuspended in 300 µL ice-cold extraction solvent (acetonitrile/methanol/H$_2$O$_{dest.}$, 40/20/20 v/v/v). After pelleting, the supernatant was transferred into a 2 mL safe-lock tube and the extraction procedure repeated twice with 200 µL extraction solvent. Biological triplicates were performed. Measurements were performed in collaboration with the group of Prof. Volkhard Kaever (Institute of Pharmacology, Hannover) via HPLC-MS/MS. Measured values were mathematically converted into cellular c-di-GMP concentration. Constants of *E. coli* cell volume and cfu/mL needed for calculation were experimentally determined.

Attachment assay

Attachment assays were carried out as described by Böhm et al (Boehm et al., 2009). Briefly: 200 µL TB medium provided in a clear 96-well microtiter plate (Falcon) were inoculated 1:40 with an o/n culture grown at 37°C. The plate was incubated statically at 37°C for 24 h unless indicated differently. After recording the OD_{600} of the total biomass, the planktonic phase of the culture was discarded and the wells washed with $H_2O_{dest.}$ from a hose. The remaining attached biomass was stained with 200 µL 0.3 % crystal violet (0.3 % (w/v) in 5 % (v/v) 2-propanol, 5 % (v/v) methanol) for 20 min. The plate was washed with $H_2O_{dest.}$ from a hose and the stained biofilm dissolved in 20 % acetic acid for 20 min. Intensity of crystal violet stain was quantified at 600 nm and normalized to the initially measured total biomass.

Biofilm escape assay
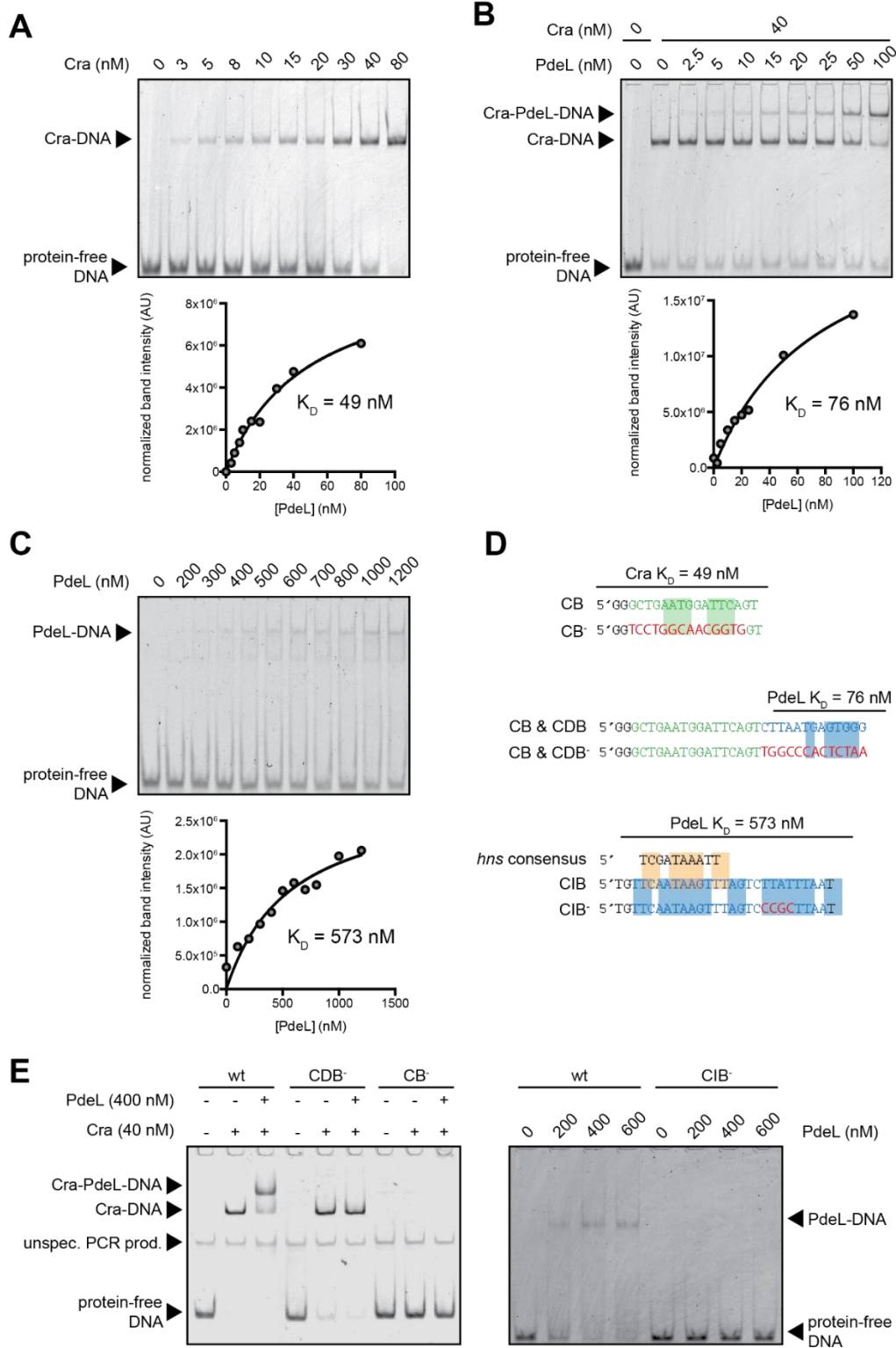
Cells harboring pAR81 (see plasmid list Table S2) were given 7 h time at 30°C to attach to 96-well microtiter plate supplemented with TB medium supplemented with ampicillin. Plate was gently washed with deionized water from a hose and dried for 20 min. Fresh medium supplemented with IPTG to induce plasmid-borne P_{lac}-*pdeH* was added to the wells and incubated for 3 h at 30°C. After incubation, 10 µL of the planktonic phase were isolated to determine cfu/mL by spotting serial dilutions in LA plates supplemented with ampicillin.

Motility assay

A single colony was picked onto a TB swarmer plate (0.3 % agar). Plates were incubated at 37°C for 3-4 h. Swarm halos were recorded with a NIKON Coolpix990 and swarm radius quantified via ImageJ (NIH, USA).

Supplemental Figures

(A) Upper panel: binding of purified Cra-StrepII to *pdeL* intervening region as tested by electrophoretic mobility shift assay (EMSA). Binding is assayed using 5′ Cy3-labeled oligonucleotides spanning the Cra-box (CB) as well as the Cra-dependent PdeL-box (CDB). DNA concentration is kept constant at 10 nM, while Cra protein titration concentration

is shown. Lower panel: Saturation binding fit of quantified band intensities. **(B)** EMSA (upper panel) and binding affinity (lower panel) of purified PdeL-StrepII in presence of co-factor Cra using the same DNA region as indicated in (A). Cra-StrepII concentration was kept constant at 40 nM. In lower panel, the band intensities of the supershift (Cra-PdeL-DNA-complex) were quantified to obtain binding constants. **(C)** Binding affinity of purified PdeL-StrepII to distal Cra-independent PdeL-box (CIB). DNA region containing 10 bp upstream and 33 bp downstream of the CIB was used. **(D)** Recognition sequence of Cra and PdeL to corresponding binding boxes. Upper sequence shows recognition sequence whereas lower sequence highlighted in bold and red shows mutations introduced to abrogate binging Note that mutations abolishing binding of PdeL to the CIB were chose to not affect the putative H-NS consensus sequence. **(E)** Confirmation of abrogated binding of transcription factors by introducing point mutation in the recognition sequences. Left panel: binding of Cra and/or PdeL was tested at 40 nM Cra and 400 nM PdeL concentration. Right panel: binding of PdeL to the CIB and to the mutated CIB (CIB$^-$) was tested at 200 - 600 nM PdeL concentration.
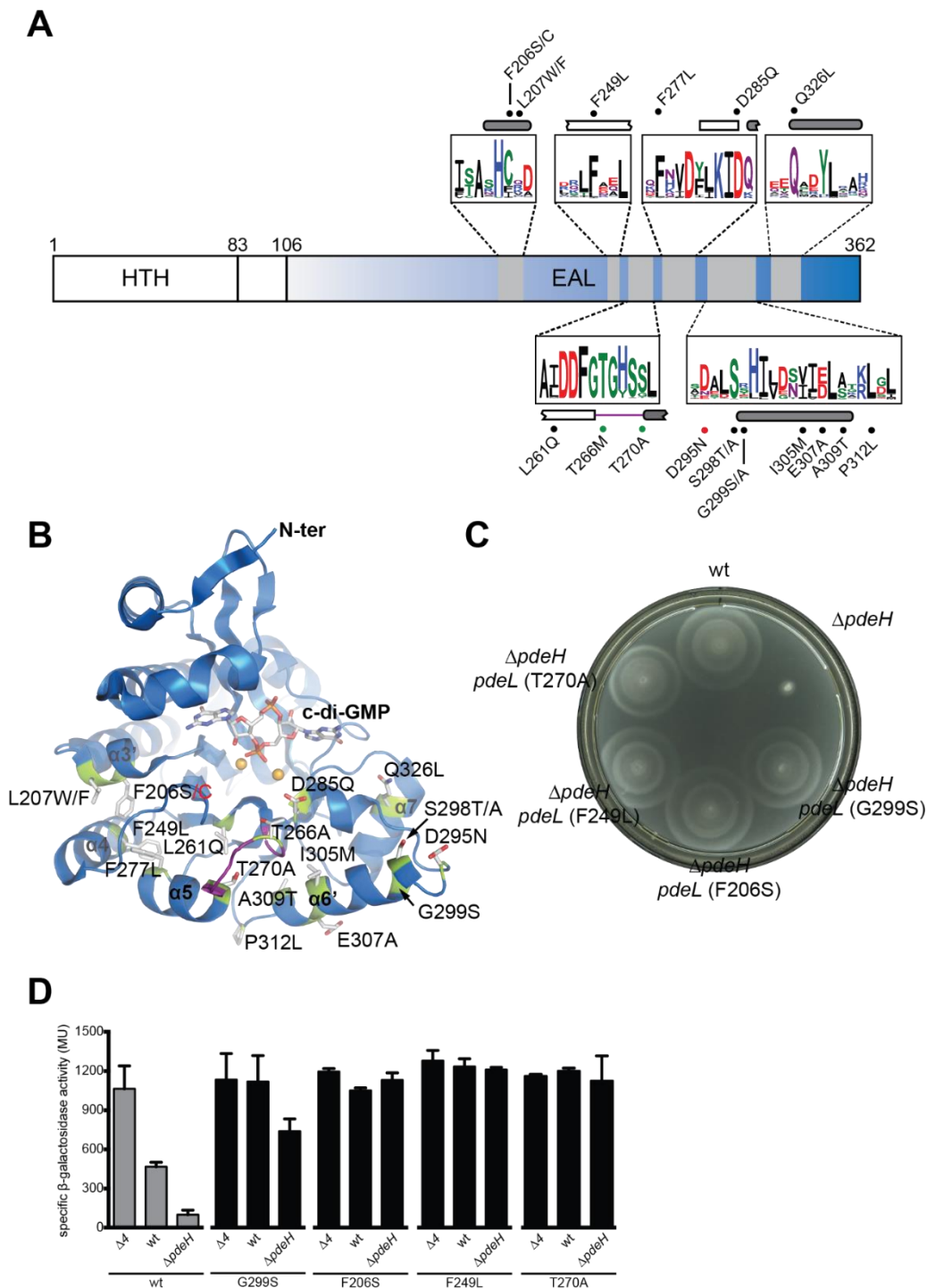
(A) Domain architecture of PdeL protein. Location of isolated motile suppressor alleles are shown as black dots. Red dot indicates aspartic acid responsible for stabilization of repulsive macro-dipole, which is generated by the N-termini of helices $\alpha5_A$ and $\alpha6'_B$ facing each other. Green dots show position of motile suppressor alleles located within highly conserved loop 6. Secondary structural elements in EAL-domain are shown as follows (alpha-helices = rounded grey bars, b-sheets = blank rectangles = line, unstructured regions). Amino acid conservation of neighborhood of motile suppressor mutations is shown as web logo of an alignment of 500 non-redundant EAL-domain proteins. **(B)** Crystal structure of monomer of non-conventional T-state PdeL$_{EAL}$ dimer in presence of Ca^{2+} and c-di-GMP as published in {Sundriyal:2014ez}. Conserved loop 6 is shown in purple. Residues, which resulted in motile suppressor phenotype are shown as sticks. Their position within the crystal structure is highlighted in yellow. **(C)** Swarm plate showing

restoration of FIGURE 10 FIGURE S3: R-STATE-SPECIFIC CYSTEINE-CROSSLINK OF PDEL (Y268C). non-motile phenotype of *ΔpdeH* strain when combined with a selection of motile suppressor allele in PdeL. **(D)** c-di-GMP-dependent *pdeL* transcription of selection of motile suppressor alleles in PdeL. Wild-type PdeL is shown in grey. Note that – with exception of G299S – all tested alleles render the *pdeL* promoter irresponsive to different c-di-GMP regimes.
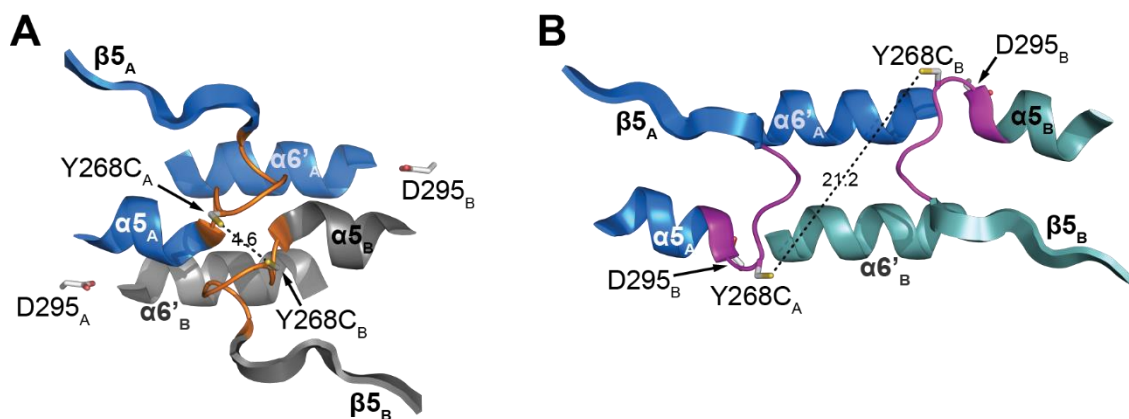
(A) Close-up of loop 6 (orange) and dimerization helices region of R-state dimer configuration of the EAL-domain of PdeL. Individual protomers are colored in marine or grey. Distance between Y268C of two protomers is shown as stippled black lines in Å. **(B)** Loop 6 (magenta) and dimerization helices region of T-state dimer configuration. Protomers here shown in marine and light-teal. Note the almost 5-fold higher distance of the Y268C substitutions compared to (A). Bismaleimidoethane (BMOE) is capable of crosslinking cysteines over a distance of maximal 8 Å.

References

Ackermann, M. (2015). A functional perspective on phenotypic heterogeneity in microorganisms. Nature Publishing Group *13*, 497–508.

Baba, T., Ara, T., Hasegawa, M., Takai, Y., Okumura, Y., Baba, M., Datsenko, K.A., Tomita, M., Wanner, B.L., and Mori, H. (2006). Construction of Escherichia coli K-12 in-frame, single-gene knockout mutants: the Keio collection. Molecular Systems Biology *2*.

Blanpain, C., and Simons, B.D. (2013). Unravelling stem cell dynamics by lineage tracing. Nat Rev Mol Cell Biol *14*, 489–502.

Blattner, F.R., Plunkett, G., Bloch, C.A., Perna, N.T., Burland, V., Riley, M., Collado-Vides, J., Glasner, J.D., Rode, C.K., Mayhew, G.F., et al. (1997). The complete genome sequence of Escherichia coli K-12. Science *277*, 1453–1462.

Boehm, A., Kaiser, M., Li, H., Spangler, C., Kasper, C.A., Ackermann, M., Kaever, V., Sourjik, V., Roth, V., and Jenal, U. (2010). Second Messenger-Mediated Adjustment of Bacterial Swimming Velocity. Cell *141*, 107–116.

Boehm, A., Steiner, S., Zaehringer, F., Casanova, A., Hamburger, F., Ritz, D., Keck, W., Ackermann, M., Schirmer, T., and Jenal, U. (2009). Second messenger signalling governs Escherichia coli biofilm induction upon ribosomal stress. Mol Microbiol *72*, 1500–1516.

Chen, Y., Ho, J.M.L., Shis, D.L., Gupta, C., Long, J., Wagner, D.S., Ott, W., Josić, K., and Bennett, M.R. (2017). Tuning the dynamic range of bacterial promoters regulated by ligand-inducible transcription factors. Nat Commun 1–8.

Chua, S.L., Liu, Y., Yam, J.K.H., Chen, Y., Vejborg, R.M., Tan, B.G.C., Kjelleberg, S., Tolker-Nielsen, T., Givskov, M., and Yang, L. (2014). Dispersed cells represent a distinct stage in the transition from bacterial biofilm to planktonic lifestyles. Nat Commun *5*, 4462.

Datsenko, K.A., and Wanner, B.L. (2000). One-step inactivation of chromosomal genes in Escherichia coli K-12 using PCR products. Proc. Natl. Acad. Sci. U.S.a. *97*, 6640–6645.

Dorman, C.J. (2004). H-NS: a universal regulator for a dynamic genome. Nature Publishing Group *2*, 391–400.

Fang, F.C., and Rimsky, S. (2008). New insights into transcriptional regulation by H-NS. Current Opinion in Microbiology *11*, 113–120.

Ferrell, J.E., Jr (2002). Self-perpetuating states in signal transduction: positive feedback, double-negative feedback and bistability. Current Opinion in Cell Biology *14*, 140–148.

Gonzalez Chavez, R., Alvarez, A.F., Romeo, T., and Georgellis, D. (2010). The Physiological Stimulus for the BarA Sensor Kinase. Journal of Bacteriology *192*, 2009–2012.

Grainger, D.C., Hurd, D., Goldberg, M.D., and Busby, S.J.W. (2006). Association of nucleoid proteins with coding and non-coding segments of the Escherichia coli genome. Nucleic Acids Res. *34*, 4642–4652.

Hengge, R. (2009). Principles of c-di-GMP signalling in bacteria. Nature Publishing Group *7*, 263–273.

Hindley, C., and Philpott, A. (2012). Co-ordination of cell cycle and differentiation in the developing nervous system. Biochem. J. *444*, 375–382.

Holmberg, J., and Perlmann, T. (2012). Maintaining differentiated cellular identity. Nat. Rev. Genet. *13*, 429–439.

Jenal, U., and Malone, J. (2006). Mechanisms of cyclic-di-GMP signaling in bacteria. Annu. Rev. Genet. *40*, 385–407.

Jenal, U., Reinders, A., and Lori, C. (2017). Cyclic di-GMP: second messenger extraordinaire. Nature Publishing Group *15*, 271–284.

Lang, B., Blot, N., Bouffartigues, E., Buckle, M., Geertz, M., Gualerzi, C.O., Mavathur, R., Muskhelishvili, G., Pon, C.L., Rimsky, S., et al. (2007). High-affinity DNA binding sites for H-NS provide a molecular basis for selective silencing within proteobacterial genomes. Nucleic Acids Res. *35*, 6330–6337.

Lopez, D., Vlamakis, H., and Kolter, R. (2009). Generation of multiple cell types in Bacillus subtilis. FEMS Microbiology Reviews *33*, 152–163.

Lori, C., Ozaki, S., Steiner, S., Böhm, R., Abel, S., Dubey, B.N., Schirmer, T., Hiller, S., and Jenal, U. (2015). Cyclic di-GMP acts as a cell cycle oscillator to drive chromosome replication. Nature *523*, 236–239.

Miller, J.H. (1992). A short course in bacterial genetics - a laboratory manual and handbook for escherichia coli and related bacteria (Cold Spring Harbor Laboratory Press).

Mitrophanov, A.Y., and Groisman, E.A. (2008). Positive feedback in cellular control systems. Bioessays *30*, 542–555.

Newell, P.D., Boyd, C.D., Sondermann, H., and O'Toole, G.A. (2011). A c-di-GMP effector system controls cell adhesion by inside-out signaling and surface protein cleavage. PLoS Biol *9*, e1000587.

Palaniyandi, S., Mitra, A., Herren, C.D., Lockatell, C.V., Johnson, D.E., Zhu, X., and Mukhopadhyay, S. (2012). BarA-UvrY two-component system regulates virulence of uropathogenic E. coli CFT073. PLoS ONE *7*, e31348.

Pasque, V., Jullien, J., Miyamoto, K., Halley-Stott, R.P., and Gurdon, J.B. (2011). Epigenetic factors influencing resistance to nuclear reprogramming. Trends Genet. *27*, 516–525.

Patell, S., Gu, M., Davenport, P., Givskov, M., Waite, R.D., and Welch, M. (2010). Comparative microarray analysis reveals that the core biofilm-associated transcriptome of

Pseudomonas aeruginosa comprises relatively few genes. Environ Microbiol Rep 2, 440–448.

Pernestig, A.-K., Georgellis, D., Romeo, T., Suzuki, K., Tomenius, H., Normark, S., and Melefors, Ö. (2003). The Escherichia coli BarA-UvrY two-component system is needed for efficient switching between glycolytic and gluconeogenic carbon sources. Journal of Bacteriology 185, 843–853.

Pratt, L.A., and Kolter, R. (1999). Genetic analyses of bacterial biofilm formation. Current Opinion in Microbiology 2, 598–603.

Ramseier, T.M. (1996). Cra and the control of carbon flux via metabolic pathways. Research in Microbiologoy 147, 489–493.

Rao, F., Qi, Y., Chong, H.S., Kotaka, M., Li, B., Li, J., Lescar, J., Tang, K., and Liang, Z.-X. (2009). The functional role of a conserved loop in EAL domain-based cyclic di-GMP-specific phosphodiesterase. Journal of Bacteriology 191, 4722–4731.

Reinders, A., Hee, C.-S., Ozaki, S., Mazur, A., Boehm, A., Schirmer, T., and Jenal, U. (2015). Expression and Genetic Activation of Cyclic Di-GMP-Specific Phosphodiesterases in Escherichia coli. Journal of Bacteriology 198, 448–462.

Ross, P., Weinhouse, H., Aloni, Y., Michaeli, D., Weinberger-Ohana, P., Mayer, R., Braun, S., de Vroom, E., van der Marel, G.A., van Boom, J.H., et al. (1987). Regulation of cellulose synthesis in Acetobacter xylinum by cyclic diguanylic acid. Nature 325, 279–281.

Serra, D.O., Richter, A.M., and Hengge, R. (2013). Cellulose as an architectural element in spatially structured Escherichia coli biofilms. Journal of Bacteriology 195, 5540–5554.

Sette, M., Spurio, R., Trotta, E., Brandizi, C., Brandi, A., Pon, C.L., Barbato, G., Boelens, R., and Gualerzi, C.O. (2009). Sequence-specific recognition of DNA by the C-terminal domain of nucleoid-associated protein H-NS. Journal of Biological Chemistry 284, 30453–30462.

Shimada, T., Fujita, N., Maeda, M., and Ishihama, A. (2005). Systematic search for the Cra-binding promoters using genomic SELEX system. Genes Cells 10, 907–918.

Shimada, T., Yamamoto, K., and Ishihama, A. (2011). Novel members of the Cra regulon involved in carbon metabolism in Escherichia coli. Journal of Bacteriology 193, 649–659.

Southey-Pillig, C.J., Davies, D.G., and Sauer, K. (2005). Characterization of temporal protein production in Pseudomonas aeruginosa biofilms. Journal of Bacteriology 187, 8114–8126.

Spangler, C., Böhm, A., Jenal, U., Seifert, R., and Kaever, V. (2010). A liquid chromatography-coupled tandem mass spectrometry method for quantitation of cyclic di-guanosine monophosphate. Journal of Microbiological Methods 81, 226–231.

Steiner, S., Lori, C., Boehm, A., and Jenal, U. (2013). Allosteric activation of exopolysaccharide synthesis through cyclic di-GMP-stimulated protein-protein interaction. Embo J 32, 354–368.

Sundriyal, A., Massa, C., Samoray, D., Zehender, F., Sharpe, T., Jenal, U., and Schirmer, T. (2014). Inherent regulation of EAL domain-catalyzed hydrolysis of second messenger cyclic di-GMP. Journal of Biological Chemistry 289, 6978–6990.

Suzuki, K., Wang, X., Weilbacher, T., Pernestig, A.-K., Melefors, Ö., Georgellis, D., Babitzke, P., and Romeo, T. (2002). Regulatory circuitry of the CsrA/CsrB and BarA/UvrY systems of Escherichia coli. Journal of Bacteriology 184, 5130–5140.

Tchigvintsev, A., Xu, X., Singer, A., Chang, C., Brown, G., Proudfoot, M., Cui, H., Flick, R., Anderson, W.F., Joachimiak, A., et al. (2010). Structural Insight into the Mechanism of c-di-GMP Hydrolysis by EAL Domain Phosphodiesterases. Journal of Molecular Biology 402, 524–538.

Tischler, A.D., and Camilli, A. (2004). Cyclic diguanylate (c-di-GMP) regulates Vibrio cholerae biofilm formation. Mol Microbiol 53, 857–869.

Uzzau, S., Figueroa-Bossi, N., Rubino, S., and Bossi, L. (2001). Epitope tagging of chromosomal genes in Salmonella. Proc. Natl. Acad. Sci. U.S.a. 98, 15264–15269.

Veening, J.-W., Smits, W.K., and Kuipers, O.P. (2008). Bistability, epigenetics, and bet-hedging in bacteria. Annu. Rev. Microbiol. 62, 193–210.

Waite, R.D., Papakonstantinopoulou, A., Littler, E., and Curtis, M.A. (2005). Transcriptome analysis of Pseudomonas aeruginosa growth: comparison of gene expression in planktonic cultures and developing and mature biofilms. Journal of Bacteriology 187, 6571–6576.

Wang, X., Dubey, A.K., Suzuki, K., Baker, C.S., Babitzke, P., and Romeo, T. (2005). CsrA post-transcriptionally represses pgaABCD, responsible for synthesis of a biofilm polysaccharide adhesin of Escherichia coli. Mol Microbiol 56, 1648–1663.

CHAPTER 6- DISCUSSION

The results reported in Chapter 2 and Chapter 3 show how pili can mediate surfaced attachment in two distinct organisms. In *C. crescentus* tad-like pili are the only organelle necessary for initial surface attachment. Tad-like pili were originally reported to be incapable of retraction since this type of pili lacks a defined retraction ATPase (Skerker, J.M., and Shapiro, L., 2000; Tomich, M. et al., 2007). However, recent results show that some bacteria have retractable pili despite lacking the retraction ATPase. In *V. cholerae* it was shown that type 4b TCP pili can retract (Ng, D. et al., 2016), with a minor pilin capable of interrupting the assembly process and initiate pilus retraction (see section 1.1.3). Another recent study found that tad-like pili in *C. crescentus* are capable of retraction (Ellison, C.K. et al., 2017), which is confirmed by our results (see Chapter 2). The mechanism that allows retraction in *C. crescentus* is still unclear. We show that in *C. crescentus* retraction of pili mediates standing up, a phenotype that helps to establish long term attachment. It is possible that when multiple pili are pulling in different directions they re-orient the cell body into an upright position. This brings the pole close to the surface and may position the cell optimally for holdfast secretion. Pili also aid the tactile sensor, the flagellar motor, to more efficiently initiate surface contact signalling (Hug, I. et al., 2017). By pulling, pili may deform the membrane and induce conformational changes in the flagellar motor which might alter the proton flux current. This change in proton flux could in turn initiate a surface contact response.

In the past, studies have often explored the response of attachment after few tens of minutes, even hours, for example measuring attachment efficiency for multicellular communities. However, current data from our lab show that surface attachment and responses at the single cell level are much faster. Our results strongly suggest that some pili are extended and ready to grab a surface in planktonic cells. In *C. crescentus* a series of events (attachment, standing up, signalling and secretion of holdfast) is coordinated to establish a long term attachment in a few tens of seconds or less. In *P. aeruginosa* as well, single cell events leading to surface attachment initiate a fast response that results in localization of FimW within about 20 seconds, dependent on a rapid increase in c-di-GMP (see Chapter 3). Twitching starts within minutes of surface adhesion (Shen, Y. et al., 2012). Taken together, these results may suggest that planktonic cells are prepared to attach to surfaces and are ready to quickly switch their lifestyle at the first opportunity, in particular for species like *C. crescentus*, an aquatic organism that benefits from a fixed localization close to a nutrient source. Surface attachment could be the preferred lifestyle for many bacteria, given that biofilms can provide important advantages including nutrient availability and protection (see Introduction, section 1.1.5). However, cells need a "safeguard" to prevent commitment to long term attachment in unfavorable locations. Cells may not determine where they land, but they can decide if they want to stay. *C. crescentus* can limit holdfast secretion in unfavorable conditions despite being in temporary surface contact mediated by pili (Fiebig, A. et al., 2014). Attachment of pili is reversible, therefore if favorable

conditions are not met, adjustments for long term attachment are not taken. *P. aeruginosa* retains an active flagellum when it is on the surface and can use it to detach from a surface (Conrad, J.C. et al., 2011). *V. cholerae* uses pili to select the surface with highest affinity, and only then promotes long term attachment (see section 1.1.5 and 1.1.8) (Utada, A.S. et al., 2014).

In *P. aeruginosa* both the flagellum and pili can adhere to surface (Conrad, J.C. et al., 2011), although pili-mediated surface attachment is more efficient. Pili mediate horizontal twitching and can bring a cell upright, as in *C. crescentus*, but the *P. aeruginosa* pili also mediate walking motility (see Introduction, section 1.1.6), which allows them to explore the surrounding microenvironment (Conrad, J.C. et al., 2011; Jin, F. et al., 2011; Oliveira, N.M. et al., 2016).

The point mentioned above may rise the question of what makes some species capable of twitching and the others not. Both *C. crescentus* and *P. aeruginosa* express on average of 2-4 pili per cell when in contact with a surface, therefore the number of pili expressed is unlikely to be the factor that determines twitching ability. It is possible that twitching depends on the ability to coordinate the activities of individual pili machineries. In the Introduction (section 1.1.8) we saw that *M. xanthus* is able to twitch by localizing the assembly ATPases at the leading pole and increasing their affinity towards the pili machineries (Bulyha, I. et al., 2009). Most pili at this pole will be extended and an occasional binding of PilT, the disassembly ATPase, initiates a retraction event that pulls the cell forward. We can speculate that increasing the affinity of PilT for the pili machineries would increase the chances of multiple pili pulling at the same time. This in turn would rise the chances of multiple pili pulling from the same pole but in different directions, which would bring a cell body in upright position. In *P. aeruginosa* FimX promotes horizontal twitching by limiting retraction events at the leading pole (Jain, R. et al., 2017). Instead, FimW may increase the retraction events at the leading pole, promoting standing up and walking. It is also very important that cells retain at least one pilus attached to the surface at any time to prevent being removed from the surface by flow. Indeed, bacteria like *P. aeruginosa* can efficiently use pili to twitch in flow conditions for long periods of time (Shen, Y. et al., 2012). Instead, *C. crescentus* is not capable of twitching, despite having retractable pili. Holdfast secretion in wild type strains would quickly fix a cell onto the surface and bring an early end to walking. However, holdfast deficient strains remain incapable of walking and can only stand upright. It is possible that in *C. crescentus* elongation and retraction rates are synchronized such that all pili retract at the same time. This makes it more likely that at the end of a retraction event no pili remain attached on the surface. This would explain why cells without holdfast have a very short residence time on surface. Interestingly, our results show a mutant expressing a less cohesive holdfast, the strain *ΔhfsK*, is able to walk over small distances because at any time there is a weak anchor, the weak holdfast, keeping cells at the surface even when all pili are fully retracted.

In *C. crescentus* surface sensing activates the diguanylate cyclase DgcB to increase levels of c-di-GMP inside cells, which in turn activates HfsJ to initiate holdfast secretion, all within seconds after surface contact. (Hug, I. et al., 2017). As we reviewed in the introduction, c-di-GMP is involved in controlling

pili activity in *V. cholerae*, *M. xanthus* and *P. aeruginosa* (Jain, R. et al., 2017; Jones, C.J. et al., 2015; Mignot, T. et al., 2005). Our studies expand the current knowledge on c-di-GMP mediated regulation of pili in *P. aeruginosa*, and we demonstrated that the localization of FimW right after landing is c-di-GMP dependent (see Chapter 3). We show also that c-di-GMP can control pili activity in *C. crescentus*. In Chapter 2 we show evidence that c-di-GMP promotes retraction of pili and that increasing concentrations of c-di-GMP may lead to full retraction of pili. However, the identity and mechanism of the c-di-GMP effector that controls pili activity is still unclear and will be a topic of future research.

The studies included in this thesis and the methods explained in the appendixes can serve as an example of important current trends in methods and approaches used in microbiology research. First, an increasing number of studies are based on single cell experiments. Traditional microbiology methods, primarily based on biochemistry and genetics, test phenotypes of multicellular communities, using plate grown colonies or liquid cultures as samples. However, there are numerous cases where single cell observations can more easily clarify the function of a gene. For example, in Chapter 2 and 3 traditional attachment assays, using only the attached cell mass after hours of growth as a readout, would be insufficient to find subtle differences between mutants, providing little information in how different proteins contribute to attachment. It is also possible for some mutants to display no differences when testing them as multicellular communities, but they could still display peculiar phenotypes at the single cell level.

Second, biology has historically been primarily a descriptive science, however, over time quantification has become more relevant and widely used, providing advantages in terms of objectivity and reproducibility. Single cell quantification has become especially relevant in microbiology, for example to follow single cell growth (Kaiser, M. et al., 2016; Moffitt, J.R. et al., 2012), swimming (Elizabeth Hulme, S. et al., 2008; Mannik, J. et al., 2009) and chemotaxis (Nesper, J. et al., 2017; Oliveira, N.M. et al., 2016; Wessel, A.K. et al., 2013). Numerical data offers the possibility to find correlations between measurable attributes in order to detect phenotypically different sub-populations. The amount of data collected in single cell measurements can be considerable, especially if coupled with high throughput experiments. Therefore, automation of analysis is an important focus for many studies in order to increase the speed of analysis, precision and objectivity. For example, using automated computational analysis it was possible to score and find statistically relevant differences in distribution of FimW among several strains (see Chapter 3). The recent development in the mother machine devices (Kaiser, M. et al., 2016, 2018) provide an example of a device where hundreds of single cells are confined inside microchannels and their growth and changes in fluorescent signals can be observed for hundreds of generations.

Thirdly, microfluidic devices are becoming an increasingly used tool in microbiology, and biology in general. Microfluidics allows to manipulate small volumes while precisely controlling chemical and physical microenvironments and recording an experiment microscopically (Wessel, A.K. et al., 2013). Microfluidic devices provide an ideal tool for performing high throughput experiments and

parallelization, while microscopically observing cells; for this reason they are sometime called "lab-on-a-chip". Our studies (see Chapter 2, 3 and 4) are examples of how microfluidics can be used to force a particular bacterial event or phenotype, thus increasing the chances of recording a specific behaviour. For example, a simple flow channel can exploit the shape of *C. crescentus* cells and encourage cell attachment after division (see Chapter 2 and Hug, I. et al., 2017; Persat, A. et al., 2014), rather than waiting for bacteria to fall into the field of view.

Concluding Remarks

In the present thesis we show that T4P are important organelles of prokaryotes. We show how their role as "sticky ropes" can, directly or indirectly, lead to diverse phenotypes. Pili promote surface attachment, interbacterial aggregation and biofilm formation, all crucial behaviours for acquiring nutrient sources and protection from the surrounding environment. Different T4P can promote retraction to perform walking and positioning on a surface, pivotal for successful colonization and virulence of of some pathogens. We show how-di-GMP can regulate the activity of pili in different organisms, but the mechanisms and effectors are not fully understood and in fact investigating this is currently a subject of active research. The T4P possess similarities shared with T2SS and the archaellum, which points to a common ancestral origin for those organelles. T4P may represent one evolutionary branch of a hypothetical ancestral machinery that was capable of assembling helical filaments. "Sticky ropes" provide such important features for prokaryotes that a diverse family of specialized pili organelles has evolved, including T4P, CU pili, SA pili and T5P.

APPENDIX 1 - MICROFABRICATION

Microfabricating a Mother Machine

The mother machine is a device that allows for trapping single bacteria in microchannels (Kaiser, M. et al., 2016, 2018). These microchannels are 10-30 μm long, but only about 1 μm by 1 μm in height and width, constraining the bacteria to grow in a single line (see Supplemental Figure 1.1). One end of the microchannel is closed, while the other is connected to a 50 μm wide channel. As cells grow, the bottom cell in the microchannel will remain trapped, while the other cells, slowly push one another due to elongation and reach the opening of the microchannel. Flow of fresh media in the channel wash away cells emerging from microchannels, preventing clogging. The microchannels themselves are free of flow. However, the dimensions are small enough that diffusion is fast enough to supply nutrients in equal measure to all cells. The main use of this device is to track the same physical cell over time, namely the one at the bottom of microchannels, and follow how it undergo tens of duplication events. This device can be used to track a fluorescent reporter, to see how some proteins fluctuate at every generation, or how quick a cell reacts upon changes in the media. Moreover, given that hundreds of microchannels can be placed in a single device (see Supplemental Figure 1.1), this allows for high-throughput experiments.
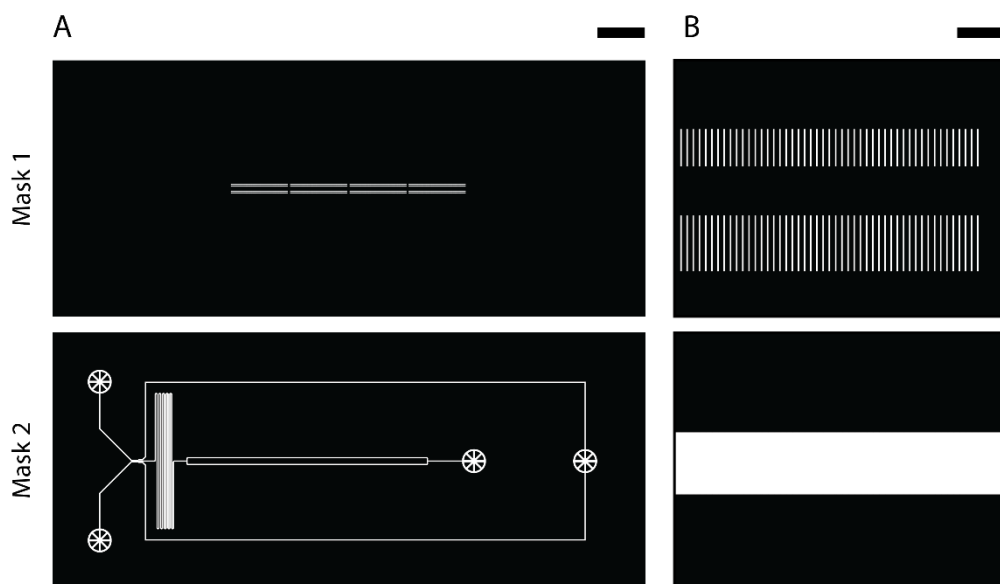
SUPPLEMENTAL FIGURE 1.1 - MASKS FOR MOTHER MACHINE DEVICE

(A) The first layer mask (upper figure) and the second layer mask (lower). The first layer mask shows only rows of microchannels that will flank the main channel in which the media will flow. Note that in this mother machine design the two inlets (left side in lower A picture) create a switch-cross that allows for choosing between two media (see M. Kaiser et al. (2018) for more details). **(B)** Details of the microchannels (upper) and the main channel (lower). [scale bar in A is 2 mm; scale bar in B is 40 μm]

In the following appendix, it will be shown how to create a "mother machine" microfluidic device. We will first introduce the procedure of photolithography, which is necessary to manufacture any microfluidic device. Then we will show how via replica molding it is possible to create multiple copies of the device using a polymer called PDMS. Lastly we will show some preliminary results and an example of how the analysis is conducted
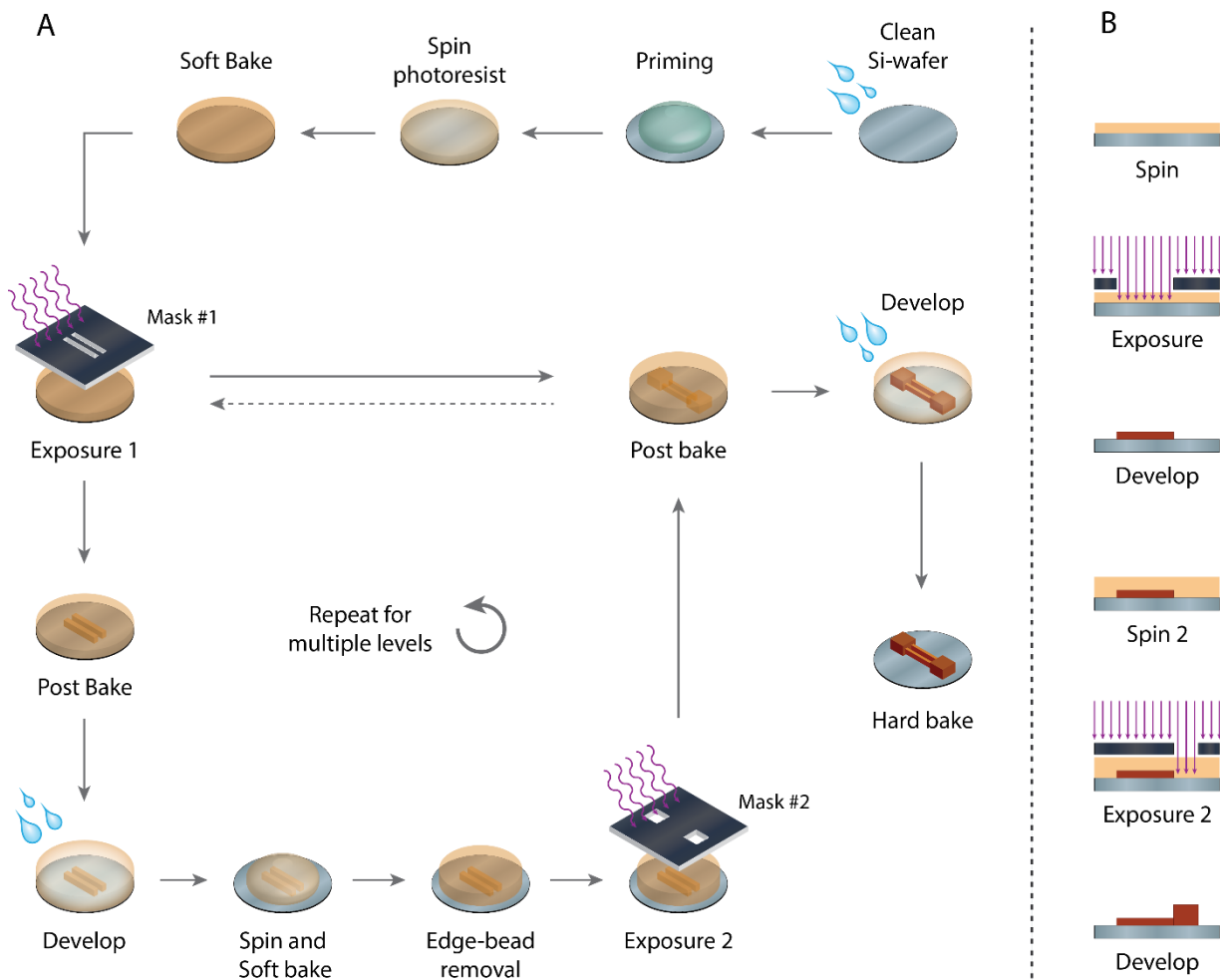
Photolithography

Photolithography is a process used for microfabrication and is a core process core for creating microelectronics (see Supplemental Figure 1.2). Using a photomask with some design drawn on it, it is possible to use light to transfer the design on a surface covered with a light sensitive film, called photoresist. Areas exposed to UV light will undergo polymerization during a heat treatment, while unexposed area will not, allowing for washing away the latter. The features left will be in relief on the surface and are bound to the surface. The height of the features determined during spinning speed and type of photoresist used. Repeating this steps with different masks and different thickness of the photoresist, allows for the creation of complex pattern of features with different heights.
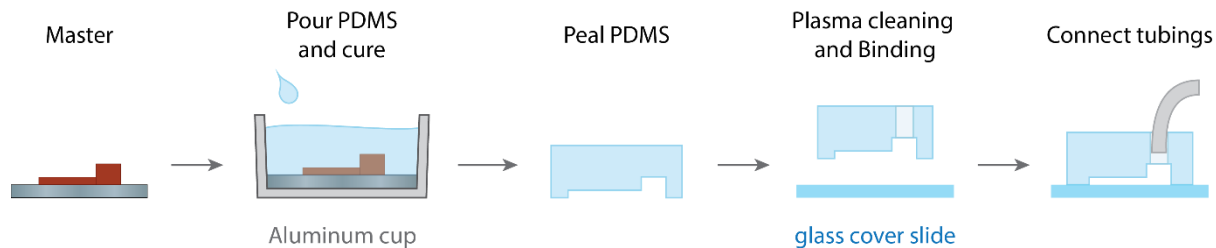
MATERIALS

The three main materials used during photolithography are the following.

- MASK: The first step in microfabrication is to create a photomask (or simply mask). The microfluidic device is drawn in 2D, as looking from above. All the channels, inlets for connecting tubing, outlets, and any other features, are drawn using a CAD program. Once the design is drawn, features that will have the same height are collect together to form different layers of the design. Each layer will be a mask. An example is shown in Supplemental Figure 1.1. The mask for the microchannels of a mother machine is shown in Supplemental Figure 1.1A, while the mask for the main channel and connections are shown in Supplemental Figure 1.1B. Only using both masks in different steps, it is possible to create the desired design (XC). Note that masks have a polarity, according to the photoresist used. Using a negative photoresist, the mask has to be transparent only where the features of our design are present (see Supplemental Figure 1.1).

- WAFER: The surface used to create devices is silicon, in the form of thin discs of 5 to 10 cm in diameters, called wafers. No covalent bond is created between the wafer and the finished photoresist features, but, extensive Van der Waals forces keep them together. The smooth surface of the wafer allow to create the molecular contact with SU8 features and achieve a semi-permanent binding. Moreover, this allows to create very smooth surfaces on the PDMS, which help binding on glass slides (see Replica Molding protocol).

- PHOTORESIST: it can be spin-coated on a surface to cover it with a layer of a specific thickness. The SU-8 (MicroChem Corp.) is a family of photoresist widely used and belong to the group of negative photoresists. Exposing negative photoresist to UV light activate it, which, after a heat treatment, polymerize and create solid features bound to the surface.

A

B

Clean Si-wafer → Priming → Spin photoresist → Soft Bake

Soft Bake → Exposure 1 (Mask #1)

Exposure 1 → Post Bake → Develop → Spin and Soft bake → Edge-bead removal → Exposure 2 (Mask #2)

Repeat for multiple levels

Exposure 2 → Post bake → Develop → Hard bake

Spin → Exposure → Develop → Spin 2 → Exposure 2 → Develop

SUPPLEMENTAL FIGURE 1.2 - STEPS IN PHOTOLITHOGRAPHY

(A) All major steps of fabrication in photolithography. The schematic shows the possibility to do one or multiple exposures and to create one or multi-layer devices. **(B)** Cross-sectional view of the major steps of photolithography to highlight how relief features are created on the Si-wafer.

Master → Pour PDMS and cure (Aluminum cup) → Peal PDMS → Plasma cleaning and Binding (glass cover slide) → Connect tubings

SUPPLEMENTAL FIGURE 1.3 – STEPS IN REPLICA MOLDING

The schematic highlights the major steps of replica molding. The features on the wafer act as a negative stamp and will be cast in the PDMS polymer after curing.

PROTOCOL

The following protocol can be used to create a mother machine device. However, regardless of the SU-8 photoresist being used, the steps of the protocol do not changes. Differences are found in the parameters used involved within each step that are related to the thickness of the layer desired (temperatures, durations, spinning speed …) and each photoresist is provided with a data sheet clarifying the different parameters to change. For clarity, those parameters are highlighted in red in the following protocol. The following protocol can be considered the archetype protocol to be used for creating any desired microfluidic device. For a single layer device the first layer part will be sufficient, plus the "hard bake" step described in the second layer last step. For a multilayer design, as the following, the design always starts form the smallest layer and proceeds to higher and higher features. This hierarchy guaranties that previously created thicker layers do not create a gap between mask and wafer, which would prevent alignment and optimal resolution. For the purpose of microfluidics, the photolithographic steps necessary to create a device are few and the end result is a negative of the PDMS device, called master.

FIRST LAYER: the desired height is 0.7 μm, using SU-8 2000.5. This is the layer that will create the microchannels were single cells will be trapped.

- CLEAN WAFER: wash with acetone, isopropanol, deionized water and then blow-dry the surface

- DEHYDRATE: place the wafer on hot plate for 5 min at ~150°C

- PRIMING: pre-wet the wafer with MCC primer 80/20 (MicroChem Corp.) in order increase adhesion of the photoresist in the next step. Place wafer in the spin-coater and pour MCC primer 80/20 to cover the entire wafer and wait 10 sec. Spin at 5000 rpm for 20-30 sec. Bakes on hot plate at 110°C for1-3 min

- SPINNING 1: pour and cover the entire surface of the wafer with the chosen photoresist, in this case, SU8 2000.5. Then spin according to the following program: (1) 10 sec at 5000 rpm (ramp 3), and (2) 30 sec at 1000 rpm (ramp 5). Remove the wafer and place on a flat surface. Wait 10 min to allow reflow to smooth the surface.

  Troubleshooting: Place the wafer in the precise center of the spin-coater in order to achieve an even spinning and the desired thickness over the entire surface of the wafer. Some photoresists have enough surface tension to wet the other side of the wafer. Clean it with an acetone wet "kleenex". This will prevent to glue the wafer on surfaces in the following steps. Moreover, until the soft bake is completed, the photoresist can still flow. Therefore, avoid tilting the wafer

- SOFT BAKE 1: place the wafer on the hot plate at 65°C for 1 min and then increase to 95°C for 1 min. Allow the wafer to cool down before exposure.

  Troubleshooting: for thin layers the photoresist is relatively liquid and malleable. Quick temperature change from 65°C to 95°C will damage it. On the other hand, thicker photoresist layers require gradual ramping of the temperature, otherwise the layer will warp during the thermal shock, deforming and creating an unevenly thick surface. Indicatively, use the following ramps: for 10 μm, 30°C/min; for 20 μm, 20°C/min; for 50 μm, 5°C/min;

- MASK LAYER 1: choose the mask with the designed microchannels and place it in the mask aligner.

- EXPOSURE 1: switch on the mask aligner in advance and let it warm for 20 min before measuring the lamp intensity. Then place the wafer in the vacuum chalk and load it below the mask. Use the microscope software to modify and perform the exposure parameters. For 0.5 μm use a dose of 62 mJ/cm². After finishing proceed immediately with post bake.

  Troubleshooting: Use i-line filter, CH1 in our mask aligner, for better resolution. Measure the lamp intensity according to the filter used. Moreover, it is recommended to use "hard contact" mode to decrease the distance between the wafer and the mask, which increases the resolution of small features.

- POST BAKE 1: place the wafer on the hot plate at 65°C for 30 min and then to 95°C for 1 min. Allow the wafer to cool down before proceeding.

  Troubleshooting: the principles about thermal shock and ramping, described above in soft bake 1, are also valid for the post bake step.

- DEVELOPMENT: to strip all unexposed photoresist from the surface, develop with SU-8 developer. Rinse for about 1 min, then wash/spray with fresh developer for 10 sec, followed by deionized water. Use pressurized air to dry.

  Troubleshooting: a white film appears if some photoresist is not removed. Keep developing: slightly longer development time will not remove the exposed features. Moreover, agitate the wafer in the solution, this will especially help to remove photoresist between high aspect ratio features.

SECOND LAYER: at a height of 35 μm, using SU-8 3025. This layer will form the main channels, with inlets and outlets, and will be connected to the microchannels.

- SPINNING 2: pour and cover the entire surface of the wafer with the photoresist for the next layer, in this case, SU8 3025. Spin according to the following program: (1) 10 sec at 5000 rpm (ramp 3), and (2) 30 sec at 2100 rpm (ramp 5).

- SOFT BAKE 2A: place the wafer on the hot plate at 65°C for 1 min and then increase to 95°C for 8-10 min. Use a ramp to reach the end temperature of about 15°C/min. Allow the wafer to cool down before the next step.

- BEAD-EDGE REMOVAL: place the wafer back on the vacuum chalk in the spinner. Remove the edge bead via a small stream of developer aimed the edge of the wafer, while the wafer is spinning at 800-900 rpm. Remove until the clean surface of the wafer appears.

  Troubleshooting: the bead edge is always a bit higher than the rest of the layer. It is necessary to bring the mask and the wafer close enough to perform correct alignment. Usually stripping about 0.5 cm from the edge is enough, but it can vary according to wafer size, type of photoresist and the extent of the design. Modern spinners can do this step automatically. Our spinner cannot, therefore, this step has to be carefully done manually.

- SOFT BAKE 2B: we made an incomplete soft bake (2a) to solidify the photoresist and prevent reflow during spinning in the bead-edge removal step. Now we finalize the soft bake: place at 65°C for 1 min and then to 95°C for about 5 min. Use a ramp of about 15°C/min to reach the end temperature.

Troubleshooting: The removal of the edge bead with developer will wet the border. Therefore, it might be necessary to extend a bit the total amount of time for soft bake. If soft bake is incomplete, the photoresist remain wet and will stick on the mask preventing alignment.

- MASK SWAP: change the mask to the second complementary design, the main channel with inlets and outlets.

- EXPOSURE 2: load the mask in the mask aligner. Then place the wafer in the vacuum chalk and load it below the mask. Perform the alignment step before exposure, following the software instruction steps. Use the microscope software to modify the exposure parameters for the new layer. For 35 μm use a dose of 200 mJ/cm². After finishing proceed immediately with post bake.

Troubleshooting: it is good practice to place the wafer in the same orientation and position as in the first exposure, so that finding the feature and aligning with the mask is easier.

- POST BAKE 2: place the wafer on the hot plate at 65°C for 30 min and then increase to 95°C for 5 min. Use a ramp to reach the end temperature, of about 15°C/min. Then, allow the wafer to cool down.

- DEVELOPMENT: strip all unexposed photoresist from the surface using SU-8 developer. Rinse for about 8 min, then wash/spray with fresh developer for 20 sec, followed by deionized water. Use pressurized air to dry.

- HARD BAKE: harden all the features and complete polymerization. Place the wafer on hot plate and cure for 20-30 min at 150°C, ramping by 15°C/min. This step is optional, but recommended to increase the lifetime of features on a wafer.

Replica Molding

The master is a negative of the set of channels and chambers we need to create a microfluidic device (see Supplemental Figure 1.3). However, replica molding is a method allows to use an elastomer (like PDMS) to cast the shape of the features present on a master and in turn create a positive image it. Placing the PDMS and a cover slide in an oxygen plasma activate the surfaces. Placing the two together will allow covalent bonds to seal the microchannels and chambers, creating a finished and usable device.

MATERIALS

- PDMS (polydimethylsiloxane) is a Si-based polymer. It is a cheap biocompatible polymer and transparent, permeable to gasses like oxygen, vapour, carbon dioxide (Berthier et al 2012 - Lab on a Chip). Due to this properties, it is an ideal polymer for prototyping and creating microdevices. Sylgard 184 (Dow Corning) is the one of most commonly used and available. It consists of two solutions, the elastomer and the curing agent. Sold as a two separate components, they are normally to be mixed in a 1:10 ratio of curing agent to elastomer. Heat treatment will then quicker the reaction.

PROTOCOL

- WASH: if dust and smear are present on the surface of the master, wash it with acetone, water, and blow-dry the surface. The master is then placed in a small cup of a slightly larger diameter or the cup can be "built" using aluminium foil.

  Troubleshooting: cover the master at all time when the features are exposed in order to avoid dust to deposit on it. Otherwise it will become part of the PDMS device. Dust can alter the light path under the microscope, and sometime it possesses autofluorescence.

- REPLICA MOLDING: Mix the two components of PDMS in a 1:10 ratio of curing agent to PDMS. Mix vigorously for 2-4 min and then use a vacuum chamber to remove all air bubbles from the prepolymer. Once finished, pour the mixed prepolymer on the master inside the cup. Optimal thickness is around 0.5 cm.

  Troubleshooting: few small bubbles are not an issue, they will disappear during thr curing step. If the PDMS is too thin, it will be hard to place tubings. On the other hand, if the PDMS is too thick, it is harder to create holes and can limit light transmission at the microscope.

- CURE: place the master in the oven at 80°C for at least 4 hours.

- PEAL: using a scalpel cut a circle around the design, and then gently peal off the PDMS. Use a biopsy puncher to create holes though the PDMS at the corresponding inlets and outlets.

  Troubleshooting: the silicon wafer is very fragile, do not push down with the scalpel while cutting, or the pressure may crack the master. If possible cut a wide circle to avoid touching any feature with the scalpel.

- AGING: (optional) place the PDMS device on a hot plate at 150° for 30 min. Place the device with the features side up.

Troubleshooting: after curing many small PDMS molecules are left unbound in the cross-linked polymer. If the device is used, they can diffuse into the medium where they may interact with cells with negative effect on their viability. The aging step can prevent that by finalizing polymerization/cross-linking. Moreover, after plasma cleaning the PDMS surface will remain hydrophilic for longer time if it was aged (Bodas, D., and Khan-Malek, C., 2007; Eddington, D.T. et al., 2006).

- WASH: clean the PDMS block and a cover slide with acetone and water, then blow-dry. This should remove any dust particles which could prevent a true molecular contact between the two surfaces and correct sealing.

- PLASMA CLEANING: Place the casted PDMS and a cover slide in the plasma cleaner (Harrick, PDC-32G). Using a pump bring the air pressure in the chamber to 2 mbar. Then activate the plasma cleaner for 30 s.

- BINDING: immediately after recovering the PDMS and glass slide, place them on top of each other. The oxygen in the plasma enriches both PDMS and glass slide with OH groups. Those can then recombine to form a covalent bond (Si-O-Si) between the glass and the PDMS. Binding start immediately as the two surfaces come into molecular contact with one another. This change can be observed as it happen by close inspection, ensuring the successful binding. Sometime some pressure is necessary to start the process or to remove some air bubbles.

Loading the device and growing cells

A desired culture can be spun down to increase cell density and then injected into the device from the outlet. Most of the trapping occurs at the start, when through capillary action the injected media will fill every microchannel bringing cells inside in the process. Appling pressure and deliberate injecting small air bubbles can help in pushing more cells inside microchannels. An occasional air bubble do not harm cells since surface tension will prevent air filling of microchannels once they are wet. This also makes the system relatively resistant to small perturbations and occasional air bubbles that may be introduced during manual media exchange. Washing is recommended after cell loading, to remove cells from channels and outlets, where they may form biofilms.

Once set, the supply of media can be started and cells can be reliably recorded for several days in a row. Biofilm formation is the main obstacle that can hamper an experiment. Clogging is not the only problem. A big biofilm will release plenty of waste that will alter the growing conditions of any downstream bacteria. A strong flow should also be used to (1) ensure supply of media to all cells and (2) to wash away cells emerging from the microchannels, which are usually the precursor for forming biofilms. For *E. coli* a flow of 1 ml/h is generally used. However, this is not always sufficient and a high flow rate means the reservoir of media will deplete faster. Therefore, the media can be supplemented with 0.5 mg/ml of BSA and 0.05% Tween-80, which in combination with the flow will limit biofilm formation without compromising cell viability.

Preliminary Results:

[The experiments and the main part of the analysis are the contributions of Benjamin Sellner, the microfabrication of the mother machine and part of the analysis where conducted by Matteo Sangermani]

After hard baking raised features are present on the silicon wafer, forming the positive mold of the final design of the device (see Supplemental Figure 1.4). In our mother machine an inlet supplying the media branches in 4 channels and on each side of the channels lie rows of microchannels (see Supplemental Figure 1.4A). Microchannels were designed in blocks with different lengths, ranging from 25 to 50 μm, allowing for testing different bacteria and growth conditions. Microchannels have to be very thin to force cells to grow in a single line. In our lab we were able to build remarkably small microchannels, with a width of only 0.4 μm. (see Supplemental Figure 1.4B) . In Supplemental Figure 1.4C is shown the wafer after finishing the first layer (height: 0.7 μm), while in Supplemental Figure 1.4D is shown the wafer after completing the second layer (height: 15 μm).

In our lab the use of mother machine devices for studying *E. coli* is well established (see Supplemental Figure 1.5). During the loading process cells are trapped inside the microchannels (see Supplemental Figure 1.5A). As cells grow, the original clone that seeded the microchannel will be pushed toward the bottom of the microchannel (see Supplemental Figure 1.5B). Individual cells can be differentiated by phase contrast microscopy due to a small separation at each pole creating a thin clear area. As cell occupy all the space in the microchannel, the cells nearer to the opening are pushed out into the main channel, where the strong flow will wash them away into the waste outlet (see Supplemental Figure 1.5C).
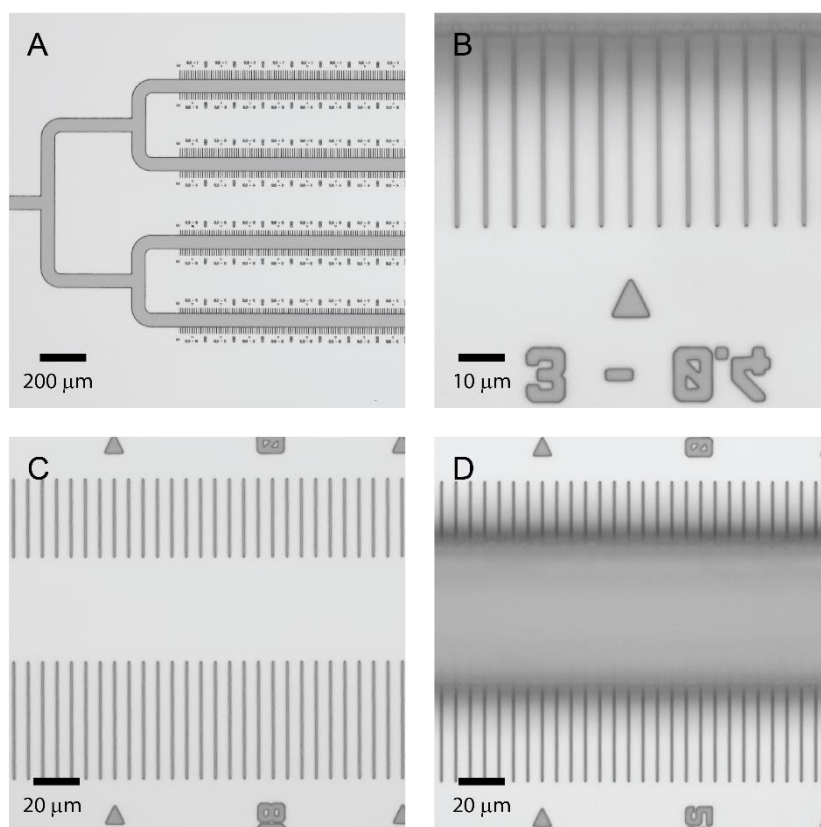
SUPPLEMENTAL FIGURE 1.4 - THE MOTHER MACHINE MASTER

(**A**) The overview of the whole first part of the device, showing the single inlet branching into 4 channels and the rows of microchannels at their sides. (**B**) An enlarged view of microchannels with a width of 0.4 μm and a distance of about 5.5 μm between them. (**C, D**) The master after completing the first layer (C) and the finished master with both layers completed (D). The height in this device was about 0.7 μm for the first layer (microchannels) and 15 μm for the rest of the device (channels and inlets).
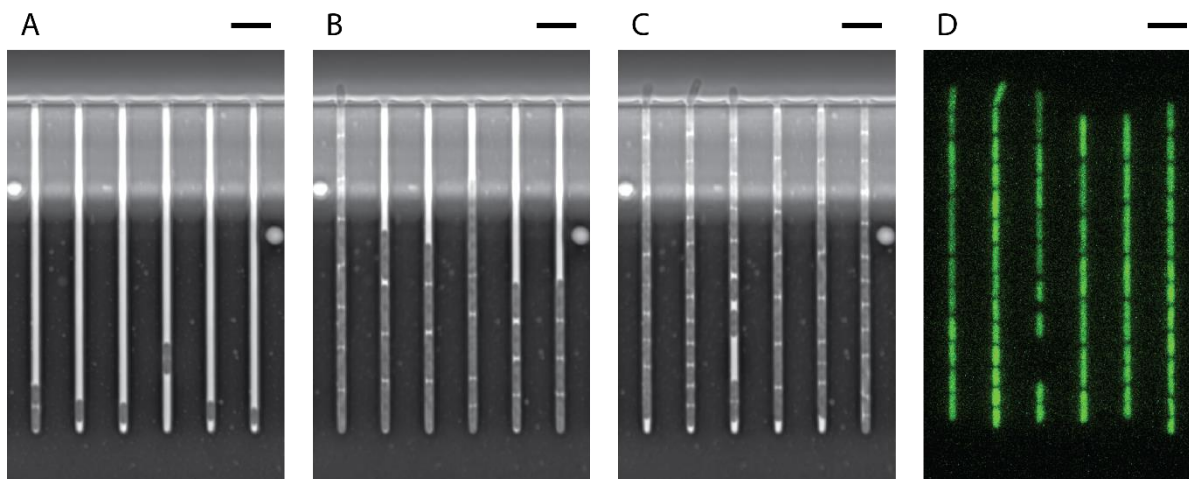
Representative time points of a movie recording the growth of *E. coli* inside a mother machine device. **(A)** Detailed view of a microfluidic device. Each channel is seeded with a single bacteria, near the bottom of each microchannel. **(B, C)** As bacteria grow in the channel, they push one another, trapping the bottom cell at one side and pushing cells out into the main channel on the other side. This can be observed in a couple of microchannels. Septation of cells is clearly visible and can be used to determine individual cells. **(D)** Fluorescence of a mCherry reporter inside the cells taken at same time point as C. Frame A, B and C are each separated in time by about 2 hour. [scale bars represent 5 μm]

In this mother machine experiment the used strain of *E. coli* possesses a *pdeL* gene (see Reinders A. et al., 2015) linked with a mCherry, in order to report the protein level inside the cell (see Supplemental Figure 1.5D). Moreover, the PdeH protein is under the regulation of a lac-promoter (see A. Reinders et al. (2015) and draft A. Reinders et al. (2018) for more details). In such way, the expression levels of PdeL can be observed in relation to the levels of PdeH. This system is currently used to investigate the phenotypic variations within a population and the speed at which single cells can react.

The next step is the analysis of the acquired time-lapses movies. Automated cell identification and analysis of time correlations are difficult tasks. Fortunately, the application MoMA (Mother Machine Analyser) was recently created to analyse high-throughput data acquired by mother machines devices. A detailed description of the program and its use is reported in the papers of M Kaiser et al. (2016) and M. Kaiser et al. (2018). Briefly, MoMA can process the acquired phase-contrast time-lapses images and specifically analyse a single microchannel at a time. The core of the program involves an algorithm that takes each frame and search for septation features separating individual cells within the microchannel. Each cell is then compared with the previous and next frame to keep track of each and create a "cell-line", describing the same physical cell over the course of the movie. All cells, except the one at the bottom, will eventually be pushed out of the microchannel. Therefore, their timeline will be limited. However, the bottom cell is trapped and the cell-line it creates last as long as the experiment itself.

Using the MoMA output file, Benjamin Sellner created a program to analyse the average fluorescent signal inside cells and how it evolves for each cell-line. The results from 10 representative cell-lines are plotted with ad hoc Matlab program created in our lab (see Supplemental Figure 1.6). With no induction of PdeH, the mCherry signal in the first two hours of the experiment is very low. Upon increasing the concentration of IPTG (Isopropyl β-D-1-thiogalactopyranoside) to 65 μM, cells quickly react and the mCHerry signal increases. Not all cells react to the same extent: some cell-lines, like 1 and 5, have a much stronger signal than others. Lowering the concentration of IPTG to 2 μM requires a longer time for the signal to disappear, usually a few generations. A second increase of IPTG to 65 μM, also resulted in a delayed response, although the response was much stronger than the first for all cell-lines.
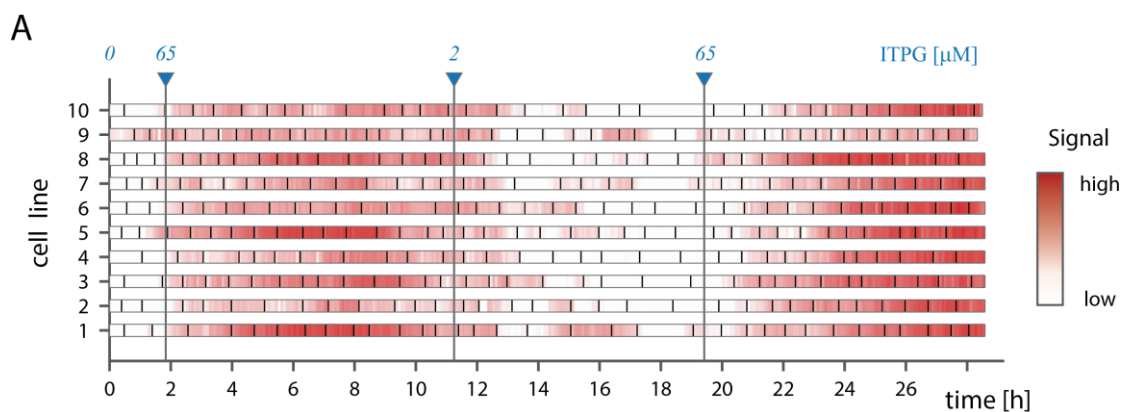
SUPPLEMENTAL FIGURE 1.6 - ANALYSING VIA MOMA

The image shows 10 representative cell-lines during the course of an experiment. Each line reports the expression levels of *pdeL* by analysing the signal of linked mCherry. The result is shown in a red-white color scale. The strain used had a lac-promoter regulating the expression of PdeH. The blue triangle at the top outlines the time points when the IPTG concentration in the media was changed to the value indicated. In each cell-line, the small horizontal lines signal a division event. The generation time during the experiment was on average (48 ± 7) min.

OUTLOOK:

The mother machine system has been successfully established in our lab as a reliable tool and we have already some preliminary analysis available. The significance of the results shown above is still being evaluated. But the provided example shows the potential use of the device in following single cells for an extended period. Cells can be challenged with different media and conditions to observe different responses: variations in growth rate and division time, reporter for a promoter, measure relative levels of proteins etc… Another possible application is the testing of persistence in bacteria, by challenging cells with different antibiotics. For example the survival rate of cells and persistence could be directly observed using this setup.

We were also able to create much smaller mother machines with width of 0.4 µm for the microchannels. This width might be the perfect size to trap smaller bacteria like *C. crescentus* cells. However, one issue remains to be addressed. Preliminary observations showed that the curvature of *C. crescentus* pack the cells tightly inside microchannel. This makes the cell identification extremely difficult if not impossible. However, a strain of *C. crescentus* without the curvature do exist (*ΔcreS*) and using this strain could provide an easy solution to overcome this problem.

APPENDIX 2 - THE THIN CHAMBERS DEVICE

The protocol for manufacturing masters described in the Appendix 1 can be adapted to any design. In this appendix we will show the thin chambers device, a design well establish in our lab (Deshpande, S., and Pfohl, T., 2012, 2015; Göllner, M. et al., 2016). In this device a main channel is flanked by 100 x 100 µm wide and 0.5 to 2 µm high chambers (see Supplemental Figure 2.1A). This chambers are connected to the main channel via a short 2-4 µm wide microchannel. This design is ideal to achieve two goals. First, to confine the bacterial cells in an enclosed space, but without the strong constrains imposed by the mother machine. In fact, cells can still swim and thanks to a quasi-2D constrain cells can be easily tracked (Hug, I. et al., 2017; Nesper, J. et al., 2017). Secondly, the chemical environment that cells are experiencing can be precisely controlled and changed. The main channel supplies a constant flow of media. The small connections, which join chambers to the main channel guaranty that the latter are free of flow. However, nutrient exchange occurs thanks to diffusion and the limited size. Computer simulations show that inside the chambers 100 x 100 µm wide, chemical equilibrium with the main channel is reached in 2-5 minutes after changing conditions. These chambers were best employed when starting with small populations of 1-5 cells to simplify the tracking of swimmers. However, cells could multiply up to a few hundreds before diffusion could not cope with cell's needs.
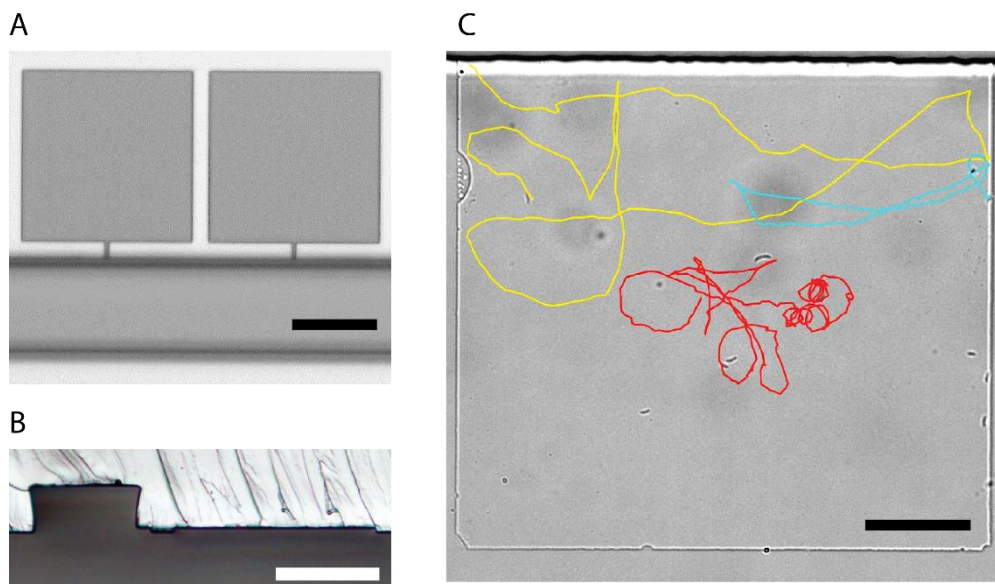
SUPPLEMENTAL FIGURE 2. 1 - THE THIN CHAMBER DEVICE

(A) The thin chamber master shows the design of the device used in our lab. The connection between the thin chambers and main channel is only 10 µm long and about 2 µm wide. **(B)** Cross section of a PDMS device show the main channel, about 20 µm in height. Next to the channel is located a thin chamber, 100 µm wide and only 1 µm in height. **(C)** In this PDMS device several cells where trapped inside. Three swimmers were present and their trajectories were recorded and tracked. [Scale bars in A and B are 50 µm; scale bar in C is 20 µm]

PROTOCOL

The soft lithography and replica molding protocols are very similar to the ones described in the protocol of Appendix 1. There are two important points to consider during replica molding:

- The ageing step is necessary. Chambers are free of flow and the only way to place cells inside is when a liquid is first introduced in an empty device. When a liquid flows in an empty device for the first time, capillary action allows for filling every cavity. Cells present in a medium will be carried along. Aging will make the device to retain a hydrophilic surface for longer times (2-3 hours) allowing for filling chambers by capillarity. The cell density at the moment of loading has to be finely tuned to ensure colonization with a desired number of cells per chamber.

- After plasma cleaning do not press over the PDMS device. The chambers have a low aspect ratio (height-to-width ratio), with less than 2 µm in height. PDMS is flexible and pressure may collapse the roof of the chambers, which will them covalently bind to the glass, compromising the device.

SOME EXAMPLES:

Loading chambers with a small number of cells allow for recording and tracking swimmers. High frame rate movies can be analysed to track individual cells. An example is shown in Supplemental Figure 2.1B, where three swimmers of *C. crescentus* without pili where tracked for a few minutes. The swimmer describing the blue track was quickly stuck to the side of the chambers, perhaps due to the holdfast being secreted. The yellow track have a higher directional persistence compared to the red track, which instead display a repetition of circular trajectories. This can be explained as hydrodynamic trapping that can occur to cells swimming close to a surface (Berke, A.P. et al., 2008).

The thin chambers have extensively been used in two recent papers published from our lab. In I. Hug et al. (2017) cells were placed into thin chambers to observe the onset of holdfast secretion for each individual predivisional and swarmer cell. The advantage was that cells are near a surface and can attach to it, but are not constantly pressed against it, which could alter the cells program, as is the case in traditional agar patch setup. In another study (Nesper, J. et al., 2017), thin chambers where used to track single swimming cells. From these experiments, it was possible to highlight the differences in speed, tumbles and flicks between different strains in order to dissect the role of different CheY-like effector proteins (Cle) in regulating the rotation of the flagellum in *C. crescentus*. The advantage of the thin chambers is that cells are restricted in a quasi-2D environment, which keep cells on a single focal plane, allowing for easier recording by a microscope and requiring a less computationally demanding setup compared to tracking the movement for 3D swimming.
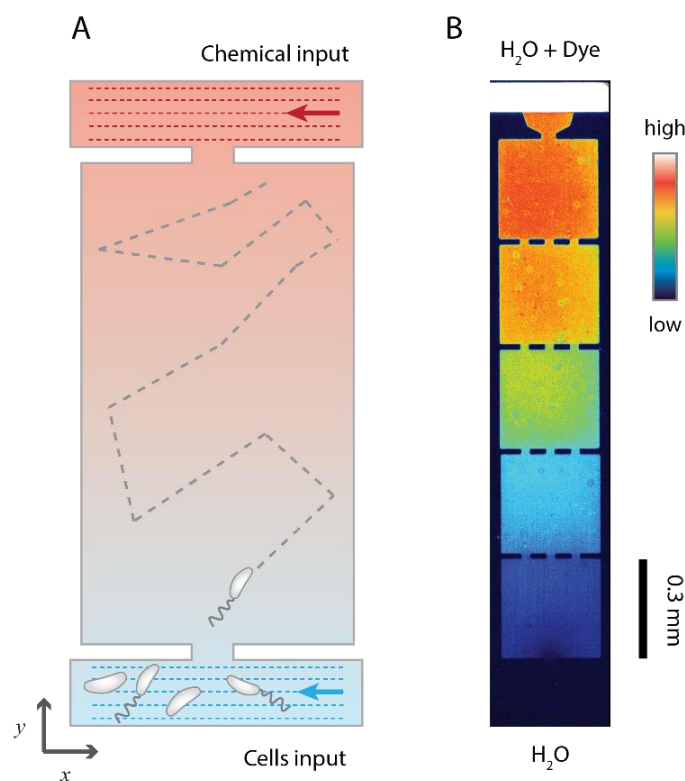
(A) The schematic represent the conceptual idea of a chemotaxis chamber and how the chemical gradient is created. The chamber remains a free flow environment as long as the flow rates in the two channels are equal. **(B)** The chemotaxis chamber was tested with a fluorescent dye, flowing in the upper channel. The dye can diffuse down to the lower channel and create a gradient in the chamber. The gradient could be maintained unchanged for about 1 hour. The device is remarkably big to provide a gradient and decrease the incidence of swimmer hitting side walls

OUTLOOK:

An interesting potential application of thin chambers is in the context of chemotaxis. The setup described in the last example (Nesper, J. et al., 2017), creates an environment inside the chambers that is chemically homogenous. The medium can be exchanged, but a stable gradient cannot be created. Since cells are not subjected to a chemical gradient, differences between strains in chemotaxis cannot be tested. Therefore, we propose the use of a modified thin chamber device to use wide chambers to create a chemical gradient where bacteria can be challenged (Strelnikova, N. et al., 2016).

We created a prototype chemotaxis chamber and preliminary tests demonstrated that the device can create a stable chemical gradient. The chamber is sandwiched between and connected to two channels (see Supplemental Figure 2.2A). If the flow in the two channels is exactly the same, the chamber will remain a flow free environment. The chemoattractant (or repellant) carried by one channel will diffuse and create a gradient across the entire length of the chamber. A preliminary test with this device is shown in Supplemental Figure 2.2B. A stable gradient of a fluorescent dye, whose diffusion coefficient approximate that of glucose, was maintained for more than 1 hour. However,

small perturbation on setup and microscope can create cross flow and disrupt the gradient, invalidating running experiment.

The next important step to test is introducing cells in the chamber. Flowing cells from the opposite channel, as a low-density culture, could be used to introduce cells in the chamber. The connection between chamber and channel offers an opportunity to select swimmer cells. Swimmers carried by the flow can still move laterally within the channel. Therefore, swimmers carried near the opening have the chance to enter the chamber. Cell density, shape and size of the opening can determine the chance of a swimmer to enter the chamber. A similar method is an established approach used to select swimmer from non-swimmer in sperm cell (Swain, J.E. et al., 2013).

The successful establishment of this device will offer the chance to record the phenotype of different strains in a chemical gradient. There are several possible approaches analysis. One example is measuring the rate of tumbles and flicks as function of the concentration of the attractant. Another could be to assess chemotaxis by measuring the time cells use to reach the other end the chamber. Last, to avoid single cell tracking, it is possible to assess cell density at various locations of the chamber and how it changes over time. Dividing the chambers in blocks (see Supplemental Figure 2.2B) can simplify scoring by this approach.

APPENDIX 3 – AVC: AUTOMATED VALVE CONTROLLER

The microdevices described above are straightforward to use and control is limited to the flow rate applied. The drawback is that the flow influences the entire device at the same time: it is not possible to close a section or change the media in only a portion of device without affecting all the other parts. However, it is possible to create valves inside microfluidic devices. Valves allow for closing a channel, diverting the flow, isolating an area, selecting the media or cells to move in a different compartment etc… In this appendix, we will explain how to create PDMS based valves inside a microfluidic device and how to use them.

Microfluidics valves were first conceptualized in the lab of S. Quake (Melin, J., and Quake, S.R., 2007; Thorsen, T. et al., 2002; Unger, M.A., 2000). The idea is to physically close a channel by collapsing a section of it. To accomplish this, it is necessary to create PDMS devices made of two layers (see Supplemental Figure 3.1). The first very thin layer (flow layer) is bound to the glass slide, containing the design to run the experiment. The second layer (control layer) is covalently bound on top of the flow layer and contains a design with close-ended channels. Those channels end at specific positions on top of flow channels in the first layer. Therefore, when pressure is applied in a close-end channel it will expand in the cavity below, since PDMS is elastic. With enough pressure the roof of the flow channel will collapse on the glass and seal the flow channel (see Supplemental Figure 3.2A). The sealing is reversible and last only as long as pressure in the control channel is applied.

This is the setup for a push-down valve. Note that it is possible to create the opposite a push-up valve, where the control layer is the first and the flow layer is the second. The push-up setup presents advantages. For microbiology applications experiments are recorded at the microscope using 100x
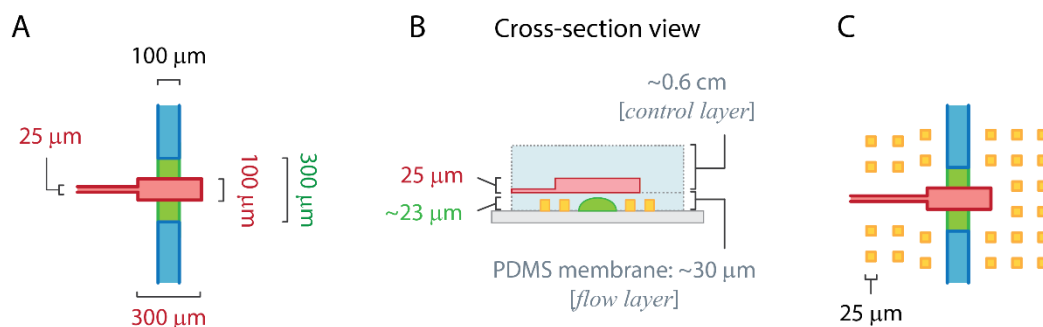
SUPPLEMENTAL FIGURE 3. 1 – DESIGN AND DIMENSIONS OF A STANDARD PDMS VALVE

(A) Top view of a standard valve with dimensions. Blue and green features are in the flow layer. Green parts has dome-shaped cross-section, while blue has rectangular cross-section. In red are depicted the control layer, ending on top of the dome-shaped sections of the flow layer. **(B)** Cross section of a valve as it appears in a PDMS device. **(A)** Top view of a finished valve**.** Yellow square features in B and C are in the flow layer and they serve no function in the finished device, but on the master their presence help in spinning PDMS evenly around the valve area.

magnification. Placing the flow layer even further from the glass could make it impossible to observe cells inside such devices.

A rectangular cross-sectional channel is hard to collapse and even high pressures could leave small openings near the walls. One major difference in the design is to create the section of the flow layer that act as valves with a dome shaped cross-section (see Supplemental Figure 3.1A). Perfect sealing is then possible. Most of the flow layer will be created as described in protocol of Appendix 1 for the mother machines, using SU-8 photoresist, and having rectangular cross section. Dome-shaped sections will be placed only at positions where valves will be located.

HOW TO DESIGN A DEVICE WITH VALVES

The best approach is to draw on CAD how the device will look once on PDMS. This ensures that the different layers and features will align as desired. Only at the very end the different layers, namely valve, flow and control, are separated to create masks. Use different "layers" in the CAD program to facilitate this last step and speed eventual corrections. The size of a typical valve used in our experiment is shown in Supplemental Figure 3.1. If necessary it is possible to scale it to some extent. In Supplemental Figure 3.1B and C, there are yellow features displayed that are part of the flow layer. They are unconnected empty cavities in the PDMS. However, in the master they are pillars. When spinning PDMS those features help to attain an even thickness for the PDMS in the area around the valve. In the result section, we will show an example of a device drawn by CAD (see Supplemental Figure 3.4) The Stanford Microfluidic Foundry from the lab of S: Quake (https://web.stanford.edu/group/foundry/index.html) provide extensive details on criteria for designing valves.

MATERIAL

- WAFER: two wafers are necessary since the flow layer and control layer are created as two independent devices. Only after replica molding the PDMS devices are bound together to create a single device (see below)

- MASK: A minimum of three masks are necessary for any device with valves. (1) The first mask is to create the dome-shaped sections of the flow layer (Note: this is a positive mask, with inverted polarity compared to the one shown in Supplemental Figure 1.1). (2) The second mask contains the majority of the design for the first layer. Together the first and second mask create the flow layer. (3) The third mask is the one containing the design of the control layer.

- PHOTORESIST: The control layer and most of the flow layer are fabricated using SU8 photoresist. However, we will use a positive photoresist, AZ50XT, to create dome-shaped channels. After photolithography the AZ50XT has a features with rectangular cross sections. However, the positive photoresist has a low melting temperature, which upon melting will reflow to create dome-shaped features.

Photolithography

The control layer is a single layer device and can be fabricated as shown in protocol of Appendix 1. The flow layer is a two steps protocol. In the following protocol, we will show how to create the dome-shaped sections.
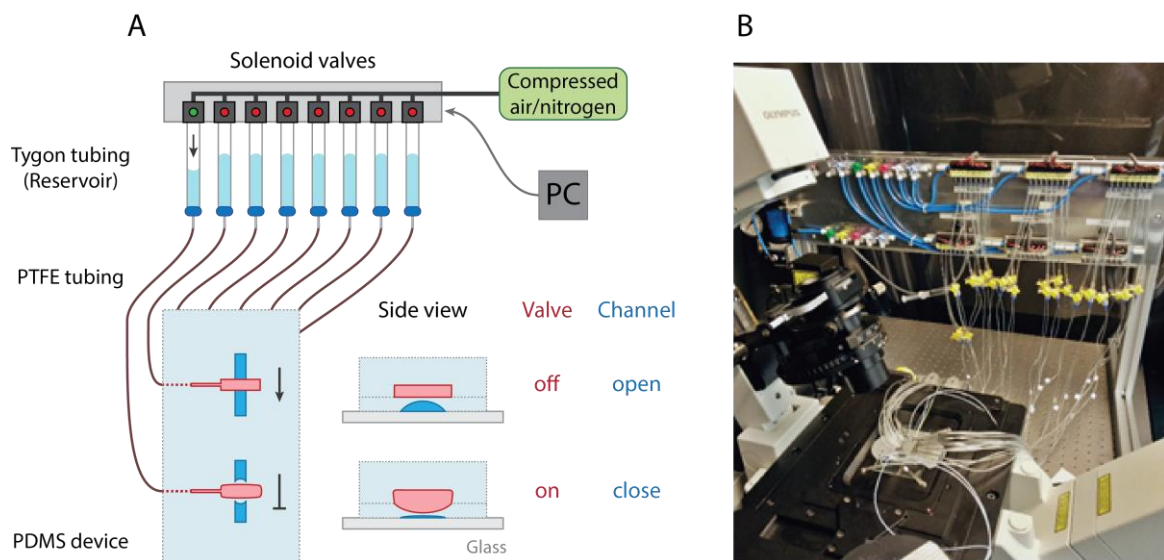
(A) The figure conceptualize how the AVC and the valves work in an assembled setup. The PC controls which pressure goes through the solenoid valves: atmospheric air pressure or the source of compressed air. Doing the latter, the water reservoir in the tygon tubing will be pressed down. Pressure travels through the PTFE tubing and to the terminal end of the control channel in the PDMS device. The increased pressure will dilate the channel and in turn expand into the underlying liquid filled flow channel. With sufficient pressure the roof of the flow channel will collapse, closing the flow channel. **(B)** The setup for an experiment assemble and ready to use. The PDMS device is sitting on the microscope stage and connected with all the tubings. The AVC is in the background.

FIRST STEP – FLOW LAYER: on a blank wafer, we first create the valve sections using AZ50XT and having a height of about 23 µm.

- CLEAN WAFER: wash with acetone, isopropanol, deionized water and then blow-dry the surface

- DEHYDRATE: place the wafer on a hot plate for 5 min at ~150°C

- PRIMING: pre-wet the wafer with HMDS (Bis(trimethylsilyl)amine) primer for adhesion promotion of the photoresist in the next step. Place wafer in the spinner. Cover the entire wafer with HMDS and wait 30 sec. Spin dry at max speed for 30 sec. Bakes on hot plate at 150°C for1-3 min

  Troubleshooting: take precautions while handling HMDS, because it can create sever damage if expose to skin, eyes and if inhaled. The normal protocol that obtains best result is gas deposition of HMDS on the wafer while it sits on the hot plate.

- SPINNING: pour and cover all the surface of the wafer with AZ50XT. Spin according to the following program: (1) 10 sec at 5000 rpm (ramp 5), (2) 30 sec at 2700 rpm (ramp 5) and (3) 1 sec at 4500 rpm (ramp 1). Remove the wafer and place on flat surface. Wait 10 min to allow reflow to smooth the surface.

  Troubleshooting: the troubleshooting described for the protocol in Appendix 1, are valid here as well.

- SOFT BAKE: place the wafer on the plate at 65°C for 1 min and ramp up at a rate of 4°C/min to 112°C and stay for 3 min. Allow the wafer to cool down slowly by switching off the hot plate and letting it cool. Wait for 1-2 h to allow slow rehydration of the photoresist.

  Troubleshooting: to avoid warping of the photoresist layer during temperature changes, it is important to ramp slowly and cool slowly as well.

- MASK LAYER: choose the first mask for the valve sections and place it in the mask aligner.

- EXPOSURE: make a multistep exposure (it is an option in the parameters of the mask aligner). Make 4 cycles of exposure, each of 20 sec and with a rest step of 30 sec between each cycle. Proceed immediately with the development.

  Troubleshooting: use I-line filter, CH1 in our mask aligner, for a better resolution. Since this is a long exposure, a multistep exposure ensures that the layer does not warm too much, which by expanding could deform the shape of the features in the process.

- POST BAKE: there is no post bake step.

  Troubleshooting: the AZ50XT photoresist polymerizes and binds to the wafer at the end of soft bake step. UV light has the opposite effect than in negative photoresists: it breaks the photoresist in the exposed areas. Therefore, no post bake is necessary and during the development all exposed area will be washed away, leaving only the unexposed area to stand.

- DEVELOPMENT: to strip exposed photoresist from the surface, develop the wafer with a 1:3 dilution of developer AZ400K and deionized water. Rinse for about 5 min, then wash/spray with fresh developer for 1 min, finishing with deionized water. Use pressurized air to dry.

  Troubleshooting: development has to be done immediately after exposure.

- REFLOW: this is a long overnight step. Program the hot plate to run as follow: (1) start at 65°C and ramp up at a rate of 15°C/h to 200°C. Remain at this temperature for 13 h. Then cool down to room temperature at a rate of 15°C/h.

FINISHING THE FLOW LAYER

The wafer is now ready to continue fabricating the rest of the design using SU-8, with the protocol described in Appendix 1. It is possible to create one layer or multiple layers, as desired. However, there is a height limit. There should not be any feature higher than the valves. As we will see in replica molding, the flow layer is spun to create a membrane-like roof for the valves. If the device is too thick, the valve will be too rigid and are cannot close. Any feature higher than the valves will not be reproduces by the membrane PDMS.

The valve sections are usually sparsely located and will not influence the remaining steps. The priming step can be skipper, since it necessary only once for a wafer. The major difference is the hard bake temperature. It should be conducted at a lower temperature, but for longer times, e.g. at 120°C for 60-90 min. Higher temperature may softer the AZ50XT and allow it to reflow. Depending on the design, the AZ50XT may reflow in unexpected ways when in contact to the SU-8, compromising their dome-shaped cross section.

Replica molding

The replica molding of a PDMS device with valves requires some additional steps. The flow layer has to be deposited in as a thin "membrane", which is achieved by spinning PDMS in the clean room. The control master instead is created in a way similar to the one described before.

- PREPOLYMER: prepare the PDMS mix beforehand. Mix the two components of PDMS in a 1:10 ratio between curing agent and PDMS, respectively. Mix vigorously for 2-4 min, then use a vacuum chamber to remove all air bubbles from the prepolymer.
- WASH: if necessary, wash wafers with acetone, water and blow-dry the surface.

FLOW LAYER PDMS	CONTROL LAYER PDMS
The flow layer is place in the spin-coater. • REPLICA MOLDING: pour the prepolymer to cover the whole wafer. Spread it and remove bubbles as much as possible • SPIN: according to the following program: (1) 10 sec at 5000 rpm (ramp 5), (2) 60 sec at 2700 rpm (ramp 5), for valves height of 23 μm. Rest on level surface for 5-10 min. **Troubleshooting:** the PDMS is very liquid and will easily reflow. Be very careful not to tilt the wafer. • CURE 1: place the master on the hot-plate at 80°C for at least 40 min. **Troubleshooting:** the purpose of the limited time is to prevent complete polymerization. Instead, we want to covalently bind the two PDMS devices as soon as possible and allow to finalize polymerization and remove unexposed photoresist.	The control master is placed in a small cup of slightly large diameter • REPLICA MOLDING: pour the prepolymer on the master inside the cup. Optimal thickness is around 0.5 cm. **Troubleshooting:** the same one explained in the protocol of Appendix 1. • CURE 1: place the master in the oven at 80°C for at least 40 min. • PEAL: using a scalpel cut a circle around the design. Cut with as big a margin as possible. Then gently peal off the PDMS. **Troubleshooting:** the PDMS will be solid, though still soft. Handle more carefully than usual.

Note: Do not touch any of the PDMS surfaces that need to be bound and keep them covered at all time to prevent dust to deposit. The PDMS devices cannot be washed before the plasma cleaning step.

- PLASMA CLEANING 1: the membrane cannot easily be pealed. Instead proceed inside plasma cleaner with the pealed PDMS control layer. Using a pump bring the air pressure in the chamber to 2 mbar. Then activate the plasma cleaner for 30 sec.

- BINDING 1: immediately after recovering the two PDMS parts align the design of the control layer with the flow layer. Once satisfied press down to initiate covalent binding. Use a stereomicroscope to aid in this step.

  Troubleshooting: place extreme care in the alignment. The plasma cleaned surfaces should not be touched, even with gloves: this will forfeit the ability of surfaces to create covalent binding. In case of wrong alignment, it is possible to immediately detach the control layer and try the procedure again. But this will compromise the ability of parts of the surface to create a covalent bond. The best result is achieved at the first try. It is necessary to create a strong sealing to ensure that the device can withstand the pressure necessary to close the valves without rupturing the two layers.

- CURE 2: complete curing process by placing the device in the oven at 80°C for at least 4 h.

- PEAL: using a scalpel cut a circle that encompass the designs of both layers, and then gently peal off the PDMS. Use a biopsy puncher to create holes though the PDMS at the corresponding inlets and outlets.

  Troubleshooting: if the control layer PDMS has a wide margin, it will ensure that every feature in the flow layer will also have a thick PDMS on top. This is necessary to create a solid device that can be treated as usual and holes can be punched easily. A membrane-thin PDMS device is otherwise very difficult to handle.

From now on the two layers become one device, if binding was done properly. The device can be handled as any other device for binding it to a glass slide, following the last steps of the protocol described in Appendix 1 for the mother machine:

- WASH

- AGING (optional)

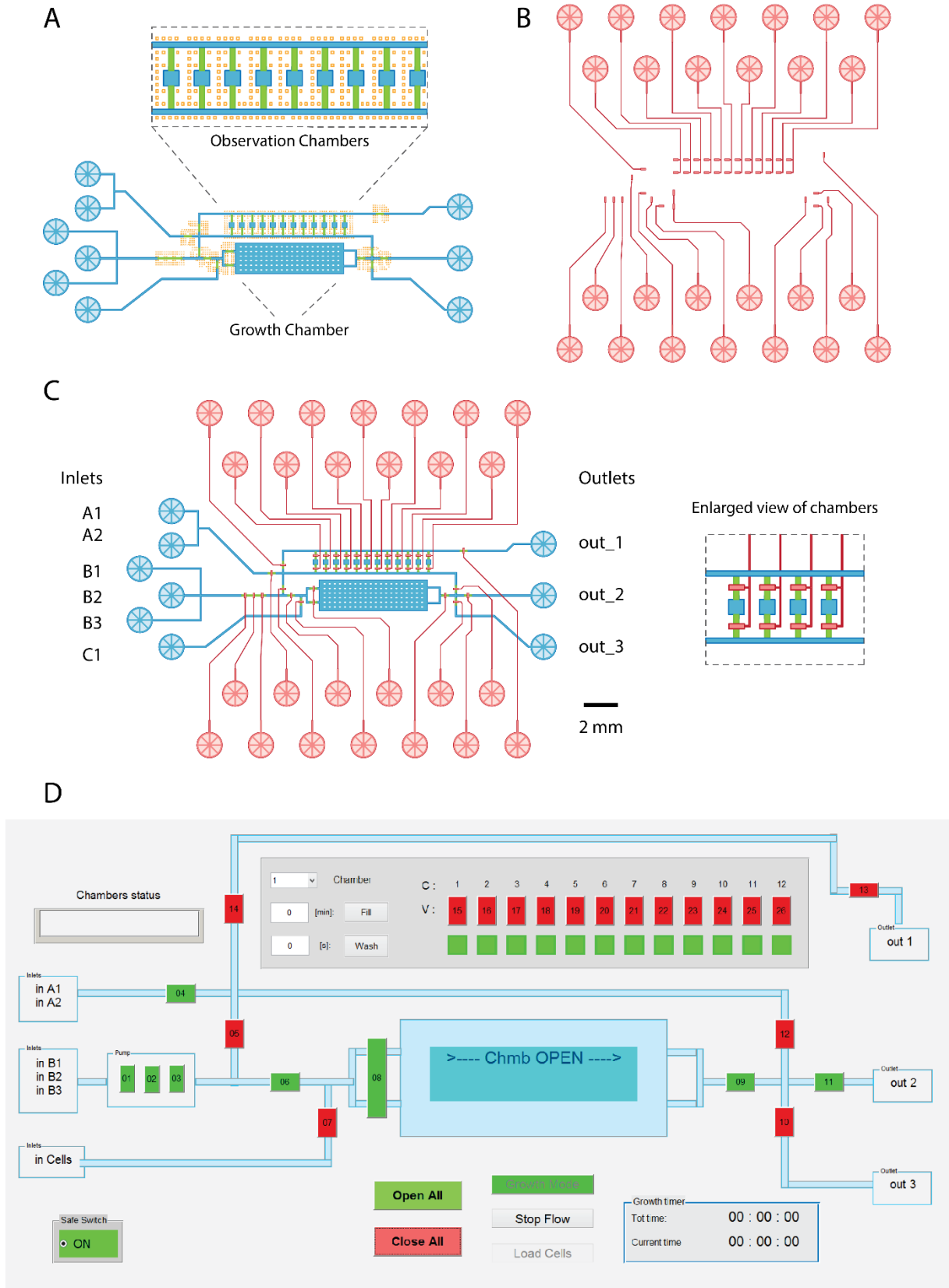- WASH

- PLASMA CLEANING 2

- BINDING 2

The AVC

The valves could be controlled manually, but this would not exploit the full potential of this technology. Therefore, we built an automated valve controller (AVC), also called valve control system. The AVC is connected to all valves and to a computer that can control it. The AVC is programmable, allowing far greater flexibility in how experiments can be conducted. Complexity of the device and experiments can be increased, the action at multiple sites of the device can be coordinated to achieve higher throughput and almost all actions of experiment can be automated. To see how a new AVC can be assembled and how a device is connected to it, consult the protocol paper of R.A. Kellogg et al. (2014), which cover those issues in extensive details. Another source for how to assemble the AVC, especially for the details concerning the electronic box and how to control it via a computer is the following: https://sites.google.com/site/rafaelsmicrofluidicspage/valve-controllers.

HOW THE AVC WORK

In the AVC a set of solenoid valves are connected together and to an electronic controller board, which is plugged to a computer during experiments. Each single solenoid valve has two inputs and one output. Only one of the input can be connected to the output at any time. One input is connected to atmospheric pressure. The other input is connected to a supply of compressed air (or nitrogen). From each output is hanging a small stretch of tygon tubing that will be partly filled with water and act as both, a reservoir and a piston (see below). At the other end of the reservoir a syringe needle is placed which in turn is connected to standard PTFE tubing that are plugged in the microdevice inlet (see Supplemental Figure 3.1B). The pressure necessary to close valves range can vary, depending on the thickness of the PDMS membrane, but generally around 3-4 atmospheres are sufficient.

When no electrical signal is given, each solenoid valve has the input at atmospheric pressure in communication with the output. The column of water in the reservoir is at rest and no significant pressure is applied to the control channel (see Supplemental Figure 3.3A). However, when the signal is given, the input at high pressure is connected to the output, pushing down the water in the reservoirs. The water is incompressible and pressure is transmitted to the terminal end of the control channel, which will dilate and collapse the roof of the underlying flow channel (see Supplemental Figure 3.3B). The action of valves is fast: complete closure or opening of the flow channel occur in about 100 ms.

A — Observation Chambers / Growth Chamber

B

C — Inlets / Outlets

Inlets:
A1
A2
B1
B2
B3
C1

Outlets:
out_1
out_2
out_3

Enlarged view of chambers

2 mm

D

Chambers status

Chamber
0 [min]: Fill
0 [s]: Wash

C : 1 2 3 4 5 6 7 8 9 10 11 12
V : 15 16 17 18 19 20 21 22 23 24 25 26

13

Outlet out 1

Inlets
in A1
in A2

04

05

12

Inlets
in B1
in B2
in B3

Pump
01 02 03

06

08

>---- Chmb OPEN ---->

09

11

Outlet out 2

07

10

Inlets
in Cells

Outlet out 3

Open All

Growth Mode

Stop Flow

Load Cells

Close All

Safe Switch
● ON

Growth timer
Tot time: 00 : 00 : 00
Current time: 00 : 00 : 00

SUPPLEMENTAL FIGURE 3.3 – SYNCHRONY DEVICE: THE LAYOUT

(A) The flow layer is shown in blue and green. The green areas are the domed shaped sections that will function as valves. An enlarged view of the chambers is shown. Inside the big chamber, the white features are pillars, which will prevent that

the ceiling collapses. The yellow features are square pillars, outside the flow channels. They are needed during spin coating to create the flow layer, to ensure homogenous and precise thickness of the PDMS layer around the valves. **(B)** In the control layer of the device each inlet is a closed ended channel. **(C)** The flow and control layer are aligned to show the design of the assembled device. The closed ended channels of the control layer end exactly on top of the valve areas. Each valve controls the open state of a part of a channel. One valve controls the open state of a chamber at both ends (enlarged view on the side). [For clarity, the pillars present (yellow features in A) are not displayed in the combined image C. Scale bars for A, B and C is 2 mm]

(D) Example of a Graphic User Interface to control the AVC. Numbered rectangles are individual valves controlling the state of a valve. In the program there are button to open or close all the valves at once, useful when setting the device and checking the status before and experiment. Button that call special functions defined by the user are, for example, "Fill" and "Wash" in the "Chamber" area. For example, "Fill" will redirect the flow from the growth chamber (in cyan), where bacteria are growing, into one smaller observation chamber. The latter will be opened a brief time and closed right after, trapping some of bacteria brought with the flow.

PROGRAMMING THE AVC

To control the AVC is necessary to create a program. This can be done with Matlab or Labview. In the following web-site it is possible to find libraries of functions and instruction of how to create a program to control the AVC (https://sites.google.com/site/rafaelsmicrofluidicspage/valve-controllers). In this section, we will limit to give a few remarks and suggestions of how to program the AVC. The links indicated above provide libraries with the most basic functions to govern an AVC. The programming of an AVC is primarily the creation of a graphical user interface (GUI) that allows the control of the AVC and shows the state of each valve during an experiment.

The functions used the most are the one governing the opening state of a solenoid valve. These functions allow for the communication with the electronic box of the AVC and sending a signal to a specific solenoid valve. For each valve a specific button can be created that allow us to directly control it. It is possible to create one program that will simply control all valves independently of how they are located on the device. However, such a program limits the ability to coordinates different actions in the device, which is a desirable advantage in this type of devices.

To achieve this each different device requires its own program. The basic button governing the opening and closing of individual valves do not change. However, special buttons can be created, which call functions that coordinate and automate the activity of valves in different locations of the device. For example, to open or close sections of the device, execute repeated, continuously or time specific actions, wash and move specific cells in a new compartment, change media etc.... Moreover, the device can be built to have several designs in parallel, allowing for running multiple experiments at the same time. Valves and an AVC allow for a high degree of freedom and flexibility in the type of devices created, which can be demonstrated by the extensive literature in the field (Melin, J., and Quake, S.R., 2007).

Preliminary Results:

C. crescentus is an important organism for studying the bacteria cell cycle control, primarily due to the possibility of separating new born cells via a process called synchrony. However, due the method used to separate newborn cells it is hard to observe cells right after division. Our lab tried to overcome this issue creating a "synchrony device" that could allow to separate cells on a chip while running the experiment and observe their behaviour right after separation.

The schematic of the device is shown in Supplemental Figure 3.4. The main concept is to create a wide growth chamber in the flow layer, almost 1 cm long, where cells of *C. crescentus* can attach and form a dense biofilm (see Supplemental Figure 3.4A). In a separate section of the device, there are 12 observation chambers. This section can be isolated via valves to ensure that is not contaminated by cells until required. The control layer has 26 closed end channels (see Supplemental Figure 3.4B). Valves are placed at every intersections and every single channel. In "growth mode", the flow from the inlets passes through the growth chamber feeding the cells and washing any present unattached cell. However, the flow can be diverted to go through a specific observation chamber for a brief amount of time. When the observation chamber is closed, a small number of newborn cells flowing in the media can be trapped inside. The device has the potential to trap newborn cells in a separate area right after their separation from the mother cells and observe their swimming behaviour in a different environment.

100 μm ▬
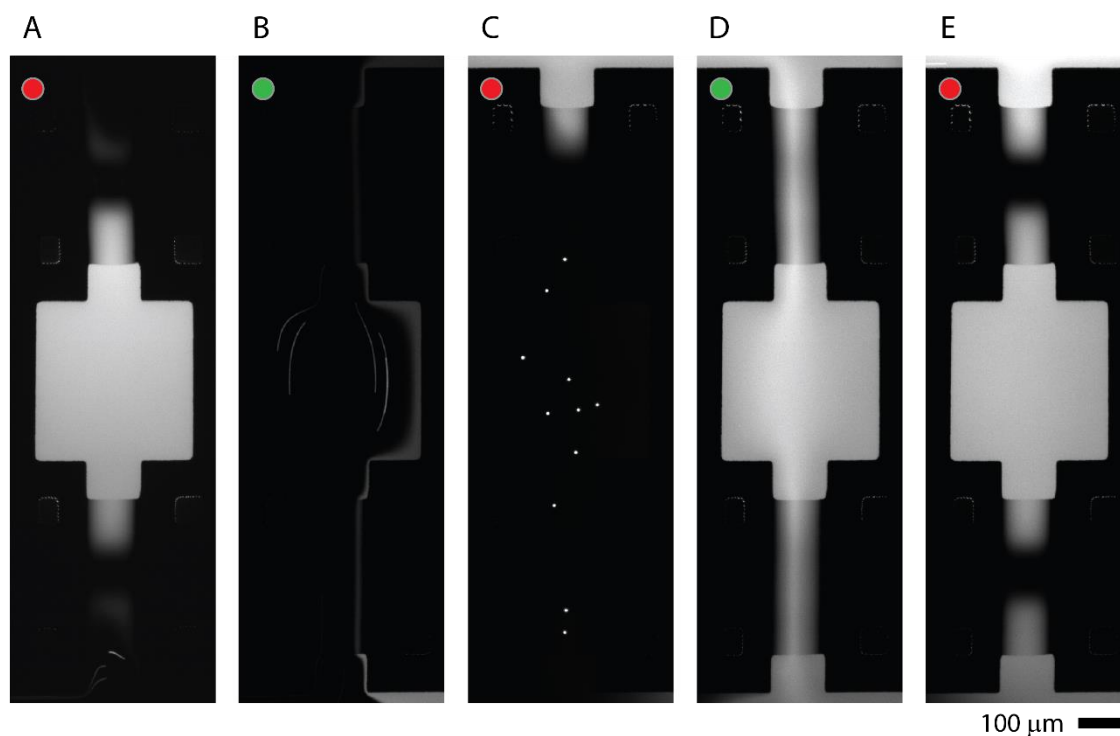
SUPPLEMENTAL FIGURE 3.4 – MEDIA EXCHANGE IN A CHAMBER.

(A) The chamber is closed and loaded with media containing a fluorescent dye. In the upper channel, media is flowing containing fluorescent beads of 3 μm in diameter. **(B)** As the valves are opened the media and beads can flow into the chamber. Beads appear as streaks as they flow. **(C)** The valves are closed, trapping some beads inside the chamber. **(D)** The valves are reopened, washing the chamber with media containing fluorescent dye. **(E)** The valves are closed and the chamber is now free of beads and filled with new media. The process of opening, washing and closing (i.e. from A to C) takes about 1 second. [the circle in the upper right of each image indicate the state of the valves: red is close, green is open]

The testing of the device can be observed in Supplemental Figure 3.5. In this example, the chamber was initially loaded with media containing a fluorescent dye. The chamber's valves are closed and in the upper channels outside media with fluorescent beads is flowing (see Supplemental Figure 3.5A). When the chamber is opened, the flow from the upper channel can be diverted to pass through the chamber. The chamber is washed completely and the beads flow through it (see Supplemental Figure 3.5B). Closing the valves of the chamber will trap beads inside. Now the chamber is again a flow-free and isolated environment where activity and behaviour of the trapped objects could be observed. These observation chambers are wide enough (300 x 300 μm) that nutrient limitation is not an issue, if few cells at a time are trapped inside. Once the observation and experiment is finished, the chamber can be washed again to use it for a new experiment. This is shown in Supplemental Figure 3.5D and E with a fluorescent dye washing the chamber and removing any bead present.

APPENDIX 4 - WHISIT: WHERE IS IT?

PURPOSE

WHISIT is a Matlab-based program and work side-by-side with either of two programs: MicrobeTracker (http://microbetracker.org/, Sliusarenko, O. et al., 2011) or Oufti (http://oufti.org/index.html, Paintdakhi, A. et al., 2016). Both programs are Matlab-based and the core algorithm is to take stacks of bright field images and identify the bacteria present in each single picture. The programs will identify the cell perimeter and create an output file where a set of coordinates and other parameters define each cell in each picture. That is where WHISIT can be used. WHISIT analyse the fluorescence signal inside cells using the "detection" output file generate by either MicrobeTracker or Oufti, in order to quantify how the signal is distributed within cells.

There are several programs for the analysis of foci and count numbers of spots in bacterial cells. However, few addresses how signal is distributed inside cells using a high-throughput and quantitative approach. For this reason the program WHISIT was created in order to address biological questions in studies conducted in our lab (see Chapter 2 and 3). The program defines the
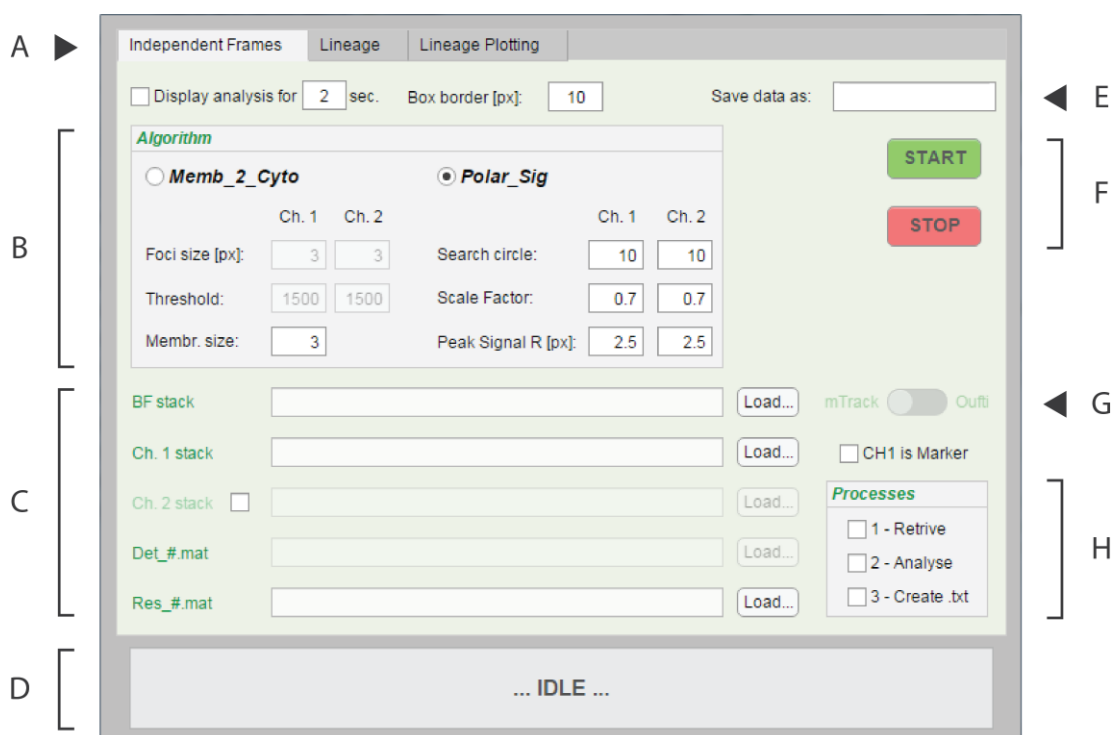
SUPPLEMENTAL FIGURE 4.1 – "INDEPENDENT FRAMES" FUNCTION TAB AFTER START-UP

The first tab "Independent Frames" as it appears after starting the program WHISIT. The different parts of the graphic user interface are: (**A**) the tabs for the different processes, (**B**) the panel for the algorithms and parameters of analysis, (**C**) section for loading input files and image stacks, (**D**) panel to display status of operations, (**E**) rename output files, (**F**) start and stop buttons, (**G**) choose origin of the detection file (MicrobeTracker or Oufti), (**H**) processes to perform with the data.

interior of cells into different areas: membrane, cytosolic and polar compartments. Then these subdivisions are used to perform a more detailed analysis of the fluorescence signals inside a cell rather than simply giving the average intensity value, as it is done by most software. Lastly, WHISIT can plot the fluorescence signal of related cells tracked in time lapse as a lineage tree, allowing for quantifying intergenerational changes. In the following appendix, we will explain how the program works and how to use it. WHISIT was created to be easy to use and no knowledge of programming is required. Results are created in a user friendly format accessible via Excel or any other similar spread-sheet program. In the last section, we will illustrate an outlook for the program and future improvements.

OVERVIEW

After loading the program displays a graphic user interface (GUI), as shown in Supplemental Figure 4.1. The program is composed of three GUI tabs, selectable in the upper part of the window (A in Supplemental Figure 4.1). "Independent frames" allow for the analysis of a stack of images where each frame is unrelated to the others. This is the best approach, when the experiments are a collection of snapshots and each cell in every frame will be considered an independent entry in results. The "lineage" tab performi the analysis of time lapse images. This function track the changes in individual cells over time, tracking them across multiple frames. This approach allow for following the changes occurring across generations, storing the information of divisions and relationships in order to create lineage trees. The result generated in the latter data approach can be used in the third tab "Plot Lineage", to create plots that display changes in fluorescence over generations as a lineage tree. WHISIT can analyse up to two fluorescent channels at a time for a given experiment.

0 – MicrobeTracker or Oufti?

Oufti is the upgraded version of MicrobeTracker and therefore its use is recommended. Oufti has a superior cell identification algorithm, greater flexibility in the parameters chosen for analysis and is less prone to detection errors. A stack of bright field images is given as input and an "Independent frames" analysis should be performed. This approach will consider each frame unrelated from the other and identify any cell within it. A file is generated at the conclusion of the analysis, in the Matlab format ".mat". The file can have any means, therefore, for simplicity we refer to it as <Detection.mat> in the following Appendix. WHISIT can use the result generated by either of MicrobeTracker or Oufti: select from which program the <Detection.mat> was generated at point G in Supplemental Figure 4.1.

The area of fluorescent signal for a cell can be slightly bigger than the area occupiedy in the bright field image. Using stringent or wrong parameters for cell detection could result in cells having a perimeter cut off part of the fluorescent signal. Experiment with parameters in the detection of MicrobeTracker/Oufti to find the correct detection parameters that allow to include the fluorescent

signal correctly. Each microscope and setting can change the acquisition and quality of bright field images, requiring adjustment during detection. Moreover, a good alignment of the fluorescent and bright field images is necessary. WHISIT does not account and cannot correct for possible shifts.

The path to the folders containing the stack of images, for bright field and one to two fluorescent channels, can be loaded in the GUI at area C of Supplemental Figure 4.1. In this area is also loaded the <Detection.mat> and the <ExpN_1_DB.mat> file created after the first step of the analysis process (see below).

TROUBLESHOOTING: NAMING FOLDERS AND IMAGES

The images recorded from an experiment has to be transformed into a stack, which is a folder containing every single frame/images as an individual file, preferably in the ".tif" format. The folder can be named as desired. However, it is important that images being named with the following format: **Prefix_###**. The prefix can be any desired name, length, and can include underscore "_" symbols. Between the last underscore and the file format (i.e. ".tiff"), it must be placed the frame number (###). The frame number for all images in a stack must have the same number of digits (i.e. Frm_0001,…, Frm _0023, Frm _0456). Frame numbers start at one and have to be continuous.

Bright field and fluorescence images taken at the same stage position and/or time point must have the same frame number. This ensures that WHISIT can correlate the cells detected in the bright field, with the correct fluorescence images. Moreover, this name formatting ensure that images are recognized across all programs in the proper order (MicrobeTracker, Oufti and WHISIT). If this is not done, each program could analyse frames in unexpected order, creating mismatches between detection and fluorescence, and in turn generating wrong results.

N.B.: Each microscope can generate images in proprietary formats and as hyperstack. ImageJ and Fiji can easily change naming of files and create stacks. Open the files and then save as "Image Sequence".
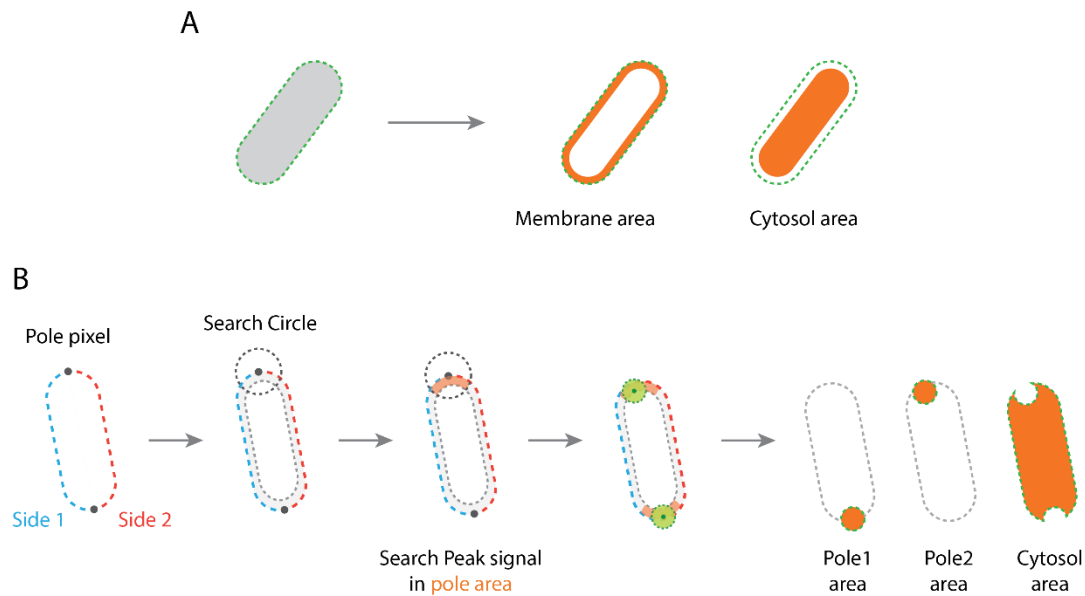
SUPPLEMENTAL FIGURE 4.2 – HOW ALGORITHMS DEFINE AREAS

A schematic representation of the main steps that the program used to create masks for the different cell compartments. In **(A)** is shown the algorithm Memb_2_Cyto, while in **(B)** is shown the algorithm Polar_Sig.

1 - Independent Frames Analysis - How to use it

In the **Algorithm** panel, several parameters can be chosen. At first it is to choose which algorithm to use to analyse the images: Memb_to_Cyto or Polar_Sign (see Supplemental Figure 4.2). According to the one chosen, several additional parameters are available.

ALGORITHMS AND PARAMETERS

The algorithm **Memb_2_Cyto** divides the interior of cells in two compartments for analysis (see Supplemental Figure 4.2A). The "membrane area" extend inward from the perimeter of a cell, with a specific thickness (**Membrane size**). The remaining area is defined as "cytosol area". This algorithm also identifies clusters of signals that are used to make a cross-section of cells and saves the signal profile at this specific positions. Two editable parameters allow for choosing the criteria for selection of the clusters of signal.

NB: We named these signal clustering "**foci**" for simplicity, but we do not use the word "foci" in the classical definition, as round spot of signals. Here with "foci" we are considering a clusters of signal above a specific signal threshold level. Since the shape is not important, so they can have any shape.

- FOCI SIZE: this value determines the minimal area (in pixels) that foci must have to be evaluated. Below such a value they are discarded as noise.

- THRESHOLD: this is the threshold for the pixels value. Above such a value the pixels are examined for patterns and clusters and, if they are above the foci size, they are evaluated.

  N.B.: if this value is too high, no foci will be detected and the relative output file will be empty.

- MEMBRANE SIZE: this value defines the distance (in pixel) by which the membrane area extend from the perimeter of the cell, the latter defined by the detection of MicrobeTracker/Oufti. A value of 0 mean that the membrane correspond to the perimeter itself.

  N.B.: although the membrane is physically at most few tens of nanometers, the emission of fluorescent signals is often about 400-700 nm. This should be considered to cover the membrane area correctly. Recommended values are around one to three.

The algorithm **Polar_Sig** divides the interior of cells in three compartments for analysis (see Supplemental Figure 4.2B). A search area is created as the intersection between a circle whose center is at the pole and the "membrane area". Within this area (orange in Supplemental Figure 4.2B) the program search for the brightest pixel. Using this pixel as center, a circle is drawn proportionally to the search circle. This will define the pole areas. The cytosol area is the remaining area once the pole areas are subtracted. Three additional parameters are related to this algorithm and define criteria to create polar areas.

- SEARCH CIRCLE: create a circle whose center is located at the polar pixel. The radius (in pixels) is defined by the user.

- PEAK SIGNAL: threshold to consider for selecting the brightest pixel within the area defined by the "membrane area" and the "Search circle" (see Supplemental Figure 4.2B).

- SCALE FACTOR: this defines the radius of the circle created with the brightest pixel at its center. The radius is proportional to the "Search circle". The value range is from 0 to 1.

There are two more options available in WHISIT (above B in Supplemental Figure 4.1):

- DISPLAY ANALYSIS: shows a series of plots to check the results produced by the analysis. The result for each single cell is displayed, with several passages and the final "Masks" defining the different areas of the cell. These steps aid to give a visual feedback on the ongoing analysis and to choose the right parameters.

  N.B: from the computational point of view, this can be the most time consuming step. It can be skipped if right parameters are known and tested, speeding up the analysis.

- BOX BORDER: when analysing fluorescence images, a cropped image of each cell is create and stored in the results. The data created is therefore not only a database of numbers, but also contains all the images related to each cell. This value determines the extra border to add to a cropped image of single cells. It does not change analysis results, but should be at least >10 pixels.

  N.B.: if a cell is located close to the border of a frame, there can be error in analysis. It is recommended to exclude cells during cell detection in MicrobeTracker or Oufti, which are closer than the box border distance.

PROCESSES OF ANALYSIS

Analysis proceed in three separate steps that have to be run in order:

- RETRIEVE CELLS: retrieves the cells detected from the analysis file <Detection.mat> generated from MicrobeTracker or Oufti. Data is reorganized in a new format and named <ExpN_1_DB.mat>. This file is necessary for the next step (Analysis) and is not anymore compatible for using with MicrobeTracker or Oufti.

- ANALYSE: initiates analysis of the fluorescent signal using the algorithm and parameters selected. <ExpN_1_DB.mat> file and stack of images (bright field, channel 1 and channel 2) are provided as inputs (selected in section C of Supplemental Figure 4.1). <ExpN_1_DB.mat> remain unchanged and a new output file <ExpN_2_DB.mat> is created.

- CREATE.TXT: generates Excel file(s) that report the main results (see section Output File Format for details).

  N.B.: Saving the output files can take some time, during which WHISIT may appear frozen. This depends on the number of cells and frames analysed.
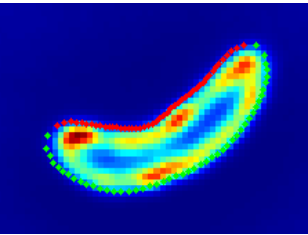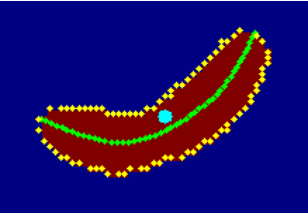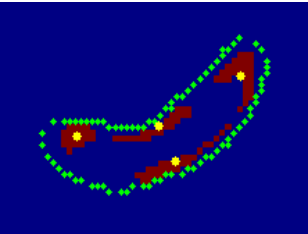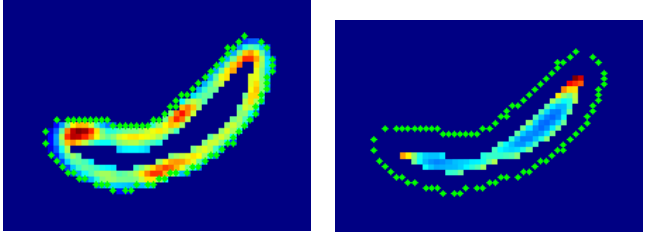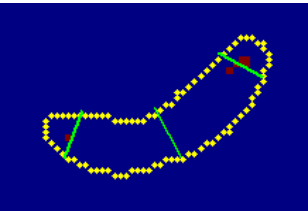

To summarize, the output file created are the following:

- <ExpN_1_DB.mat>: the intermediate file after "Retrive cells" process. Since it is not changed during analysis, it can be reused to generate a new analysis using different parameters.

- <ExpN_2_DB.mat>: it has all the content of <ExpN_1_DB.mat> plus all the results created during analysis of the fluorescent images. Can be accessed using Matlab to perform further analyses if wished.

- <ExpN_txt>: this is a report file that can be opened with Excel and easily performs statistics and draws chats of the results. For more details on the data structure see the Output File Format section. The algorithm Memb_2_Cyto generates two of such files, while the algorithm Polar_Sign generate only one file.
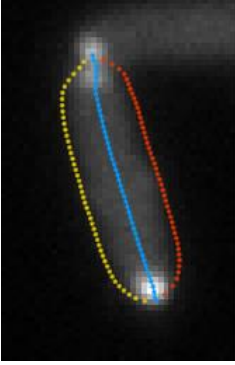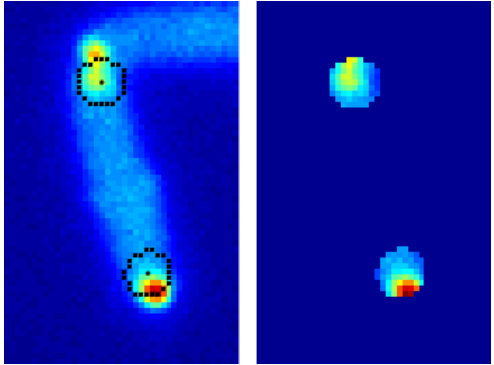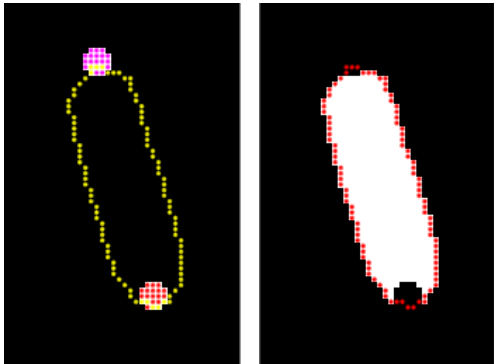
ExpN can be any name assigned in the field E of Supplemental Figure 4.1.

The **STOP** button can be used at any point during second step "Analyse". If it is pressed it will interrupt the analysis. However, data analysed will be lost. If you push START, it starts all over from the first cell. Data is saved only at the end of the step analysis.

THE ALGORITHM MEMB_2_CYTO – HOW DOES IT WORKS

Description	Step
The cell outline identified in the bright field image is used as a mask to isolate the fluorescence signal of the specific cell. A cropped image of the cell of interest is generated and used for all subsequent calculations.	
The perimeter of a cell is converted in a set of pixel coordinates (yellow points). The cell longitudinal axis of a cell and the area are some of parameters calculated.	
The next step involves identification of signal clusters (foci) using *Signal threshold* and *Foci size* as criteria. For each of those clusters a mask is generated and stored. Later each mask can be used to calculate the average signal intensity, areas, etc…	
The algorithm then identifies the membrane (right picture) and cytosol area (left picture). The program generate masks that define the two areas. Those mask are then used to calculate the fluorescent signal in each specific compartment The **Membrane size** is the main parameter that defines the extent of those areas.	
For each foci a profile line is created. This line runs through the center of the foci and is orthogonal to the cell axis. The profile line is an array of pixel values for the fluorescent signal where the line passed. This create signal profile at those position that can be plotted.	

THE ALGORITHM POLAR_SIG - HOW DOES IT WORKS

Description	Step
The cell outline identified during detection is superimposed to the fluorescence channel. The cell coordinates are divided in two side (yellow and red points). The blue line is the cell axis	
At the extremities of each pole a circle is drawn (in black, right picture). This is then used to isolate each pole and in each area the algorithm search the pixel with the highest intensity value (left picture).	
From the highest intensity value a smaller circular area is drawn and will define the mask for each pole. The picture on the left shows the two polar mask (magenta and rec) together, and in yellow the cell outline is represented. In the picture on the left is shown the mask for the cytosol, minus the poles.	

FORMAT OF OUTPUT FILES FOR MEMB_2_CYTO ANALYSIS

There are 2 *.txt* files generated with tab-separated columns. WHISIT can analyse two fluorescent channels at a time. Therefore, data is organized in CH1, the results for the fluorescent channel 1, and CH2, the results for the fluorescent channel 2.

CELL.TXT

Data is collected from the cell point of view, meaning **each row is the result for the analysis of an individual cell**, with all related information.

	Column value	Description
1	Frame	Frame at which cell appears
2	Cell Num	Cell ID number, as assigned at detection by MicroTracker or Oufti
3	Cell Length	Axial length of the cell [pixel]
4	Area Cyto	Area of the cytosol area [pixel^2]
5	Area Membr	Area of the membrane area [pixel^2]
6	Area Cell	Area of the whole cell [pixel^2]
7		
8	CH1_Number Foci	Sum of all the pixel values in the fluorescent CH1 inside the cytosol
9	CH1 Foci_A IN Membr_A	Fraction of area of all "foci" that reside in the membrane area
10	CH1 Foci_A IN Cyto_A	Fraction of area of all "foci" that reside in the cytosol area
11	CH1 Membr_A IN Foci_A	Fraction of membrane area occupied by "foci"
12	CH1 Cyto_A IS Foci_A	Fraction of cytosol area occupied by "foci"
13	CH1 Avg Foci eccentricity	Average eccentricity of "foci". How round is an ellipse: value of 0 is a perfect circle, value of 1 an infinitely stretched ellipse.
14	CH1 Avg Foci Area	Average area of the all "foci" present in the cell [pixel^2]
15	CH1_Avg Foci distance	Average distance between the foci center and cell center of mass [pixel]
16	CH1_Avg Int Membr	Average intensity value of the signal in the membrane area

17	CH1_Avg Int Cyto	Average intensity value of the signal in the cytosol area
18	CH1_Avg Int Cell	Average intensity value of the signal in the cell area
19	CH1 Avg_BkGr_noise	Average background pixel value outside cells, calculated for the frame in which the cell resides
20	CH1_Min_px_value_Frame	Minimum pixel value in the CH1 frame where the cell is
21	CH1_Max_px_value_Frame	Maximum pixel value in the CH1 frame where the cell is
22		
23	CH2_Number Foci	
24	CH2 Foci_A IN Membr_A	
25	CH2 Foci_A IN Cyto_A	
26	CH2 Membr_A IS Foci_A	
27	CH2 Cyto_A IS Foci_A	
28	CH2 Avg Foci eccentricity	
29	CH2 Avg Foci Area	
30	CH2_Avg Foci distance	Exacetelly the same as described above, but the values are relate to the fluorescent channel_2. If only one channel was analysed, this columns will be empty.
31		
32	CH2_Avg Int Membr	
33	CH2_Avg Int Cyto	
34	CH2_Avg Int Cell	
35	CH2 Avg_BkGr_noise	
36	CH2_Min_px_value_Frame	
37	CH2_Max_px_value_Frame	

FOCI.TXT

Data is collected from the foci point of view: **meaning each row is the result for the analysis of single "foci" (cluster of signal).** Many cells can have multiple foci and each will be treated independently. Since two channels can be analysed, the program generate two Foci.txt files, one for each channel.

	Column value	Description
1	Foci area	Area of the focus
2	Abs Foci_A in Membr_A	Fraction of area of a specific focus that resides in the membrane area
3	Abs Foci_A in Cyto_A	Fraction of area of the specific focus that resides in the cytosolic area (column 2 + 3 must give a result of 100%)
4	Avg Int signal	Average intensity of the signal in the focus
5	Eccentricity	Average eccentricity of the focus
6	Distance from cell Center	Average distance of the focus from the cell center
7	Length cell it belongs	Length of the cell the foci belongs to
8	Avg_BkGr_noise	Average pixel value in the background area for the frame in which the cell belongs to
9	Min_px_value_Frame	Lowest pixel value in the whole frame in which the cell belongs to
10		
11	From 11 onward	Signal profile perpendicular to the cell axis and crossing the focus center. Each profile is normalized to be of length 25 (which is also the highest length/width possible), with additional zeros left-right in order to center the array. Since the center is where the cell axis passes, this allows comparison between different signal profiles

FORMAT OF OUTPUT FILE FOR POLAR_SIG ANALYSIS

WHISIT can analyse two fluorescent channels at a time. Therefore, data is organized in CH1, the results for the fluorescent channel 1, and CH2, the results for the fluorescent channel 2.

CELL.TXT

Data is collected from the cell point of view: **each row is a cell entry** with all related information about a specific cell

	Column value	Description
1	Frame_Num	Frame at which cell appears
2	Cell Num	Cell ID number, as assigned at detection by MicroTracker or Oufti
3	Cell_Length	Axial length of the cell [pixel]
4	Cell_Area	Area of the whole cell [pixel²]
5	CH1_Cyto_AvgSig	Average intensity value of the signal in the cytosol
6	CH1_Cyto_Area	Area of the cytosol [pixel²]
7	CH1_Cyto_Sig_sum	Sum of all the pixel values in the fluorescent CH1 inside the cytosol
8	CH1_P1_AvgSig	Average signal CH1 at the pole_1
9	CH1_P1_Area	Area of the intensity value of the signal CH1 at pole_1 [pixel²]
10	CH1_P1_Sig_sum	Sum of all the pixel values in the fluorescent CH1 inside the pole_1
11	CH1_P1-Cyto_ratio	Ratio of the average values between pole_1 and cytosol for CH1
12	CH1_P2_AvgSig	Average signal CH1 at the pole_2
13	CH1_P2_Area	Area of the intensity value of the signal CH1 at pole_2 [pixel²]
14	CH1_P2_Sig_sum	Sum of all the pixel values in the fluorescent CH1 inside the pole_2
15	CH1_P2-Cyto_ratio	Ratio of the average values between pole_2 and cytosol for CH1
16		

| 17	CH1_Avg_BkGr_noise	Average background pixel value outside cells, calculated for the frame in which the cell resides
18	CH1_Min_px_value	Minimum pixel value in the CH1 frame where the cell is
19	CH1_Max_px_value	Maximum pixel value in the CH1 frame where the cell is
20		
21	CH2_Cyto_AvgSig	
22	CH2_Cyto_Area	
23	CH2_Cyto_Sig_sum	
24	CH2_P1_AvgSig	
25	CH2_P1_Area	
26	CH2_P1_Sig_sum	
27	CH2_P1-Cyto_ratio	Exacetelly the same as described above, but the values are relate to the fluorescent channel_2. If only one channel was analysed, this columns will be empty.
28	CH2_P2_AvgSig	
29	CH2_P2_Area	
30	CH2_P2_Sig_sum	
31	CH2_P2-Cyto_ratio	
32		
33	CH2_Avg_BkGr_noise	
34	CH2_Min_px_value	
35	CH2_Max_px_value	

2 - Lineage and Lineage Plot

The "Lineage" function tab is very similar to "Independent Frames" (see Supplemental Figure 4.3). Algorithm, parameters and options for the most part are the same. There are two differences: the function work in a single step and that it requires as input an additional file containing the tracking of cells.

The additional information to provide for the "Lineage" function is tracking of cells in the time lapse. This file is a list of tracks, where each track is a set of *xy*-coordinates of the position of a given cell in all the frames it appears in a time lapse. This file is created manually by the user, i.e. using the mTrack plugin of ImageJ. Lastly, the "Lineage" function works in a single step. Provided the inputs parameters, the list of tracks and <Detection.mat> the program can start analysis and at its end provides a single result file. This file is a list of "cell lineages", where the results of the analysis on fluorescence as well as organizing cells and their relationships are stored.
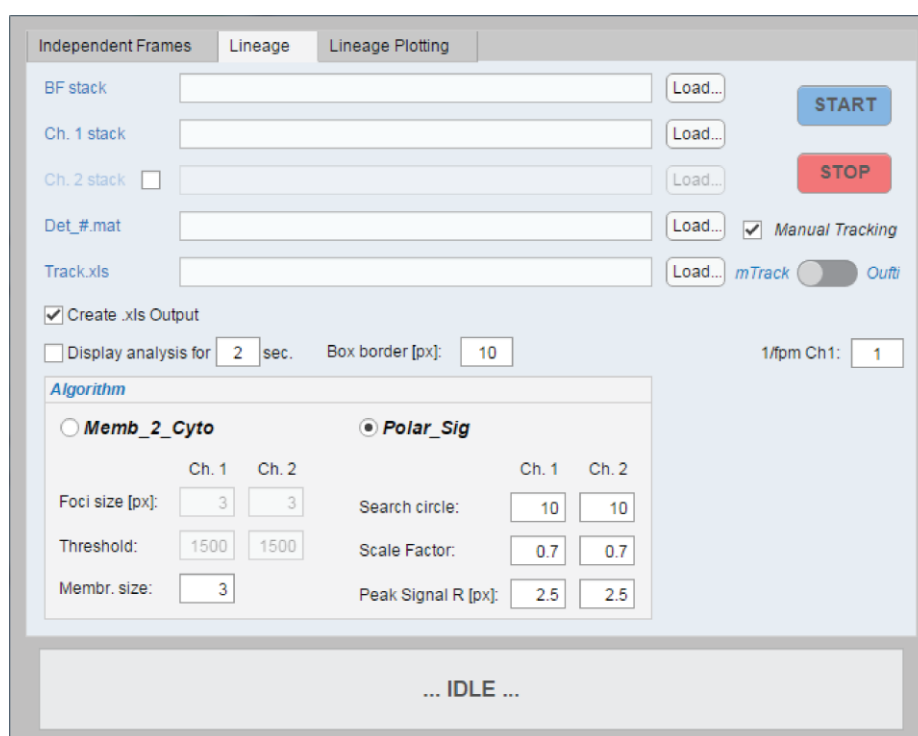
SUPPLEMENTAL FIGURE 4.3 – LINEAGE FUNCTION TAB
The tab GUI for the "Lineage" tab. It is very similar to the tab of "Independent Frames". Read above for the description of most parameters and options.
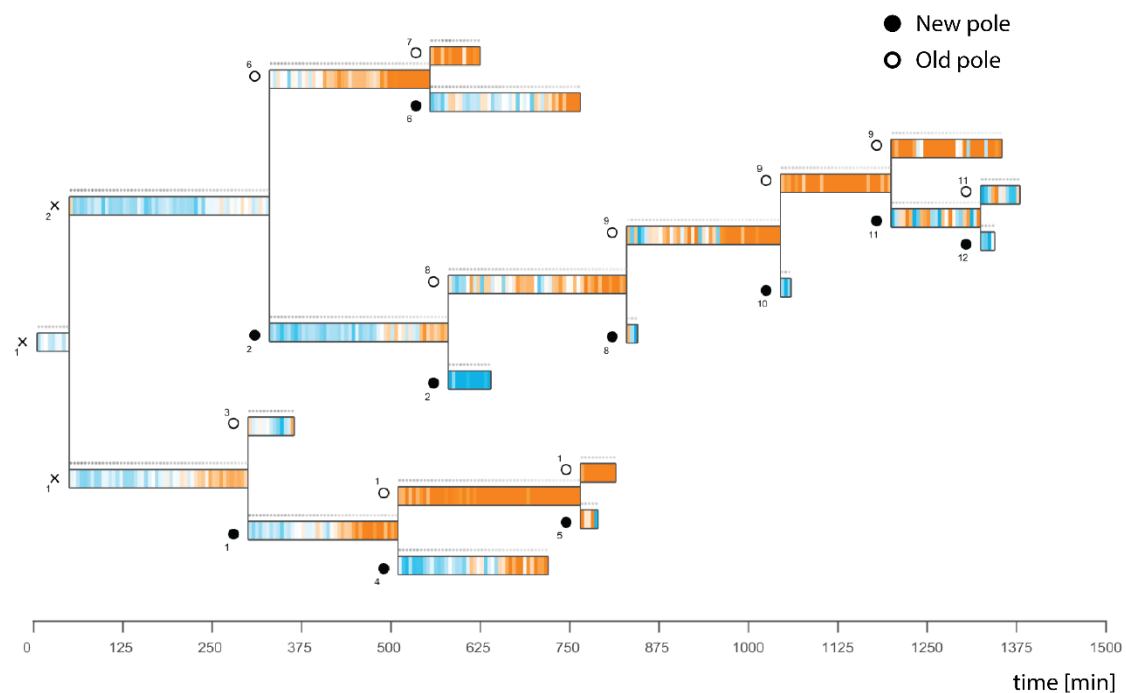
SUPPLEMENTAL FIGURE 4. 4 – PLOT CREATED WITH FUNCTION "LINEAGE TREE"

The plot show the lineage tree starting from a single *P. aeruginosa* cell and tracking all of its descendants. The time lapse was over 24 hours and followed the fluorescent signal of FimW, which can be distributed at the pole or diffused in the cytosol. The colour coded branches of the tree display the ratio of fluorescence between cytosol (blue) and pole (orange). At a division point each daughter is marked with a black dot if the daughter was originated from the old pole, and with a white dot if it originated from the new pole. For the first 2 generations there is no knowledge about poles origin and cells are marked with an X. It is possible to appreciate a consistency in this tree. At each generation, as cells approach division the fluorescence is localized more into the poles than in the cytosol. Interestingly, the fluorescence is not inherited uniformly: daughter cells generated from the old pole get most of the signal, which remain polarly distributed. The cells at the new pole have a signal diffused in the cytosol and tend to swim away of the field of view. In fact most of those cells are tracked for few frames after division.

Outlook:

The Lineage Plot offers many different ways to plot the results, but cell segmentation is missing. This would allow for dividing cells longitudinally in segments of equal size. Fluorescence distributions over the cell longitudinal axis could be more precisely represented, allowing for example to follow some fluorescent foci moving over time from one pole to the other.

Most of the improvements to WHISIT are focused in the "Lineage" function. At present the function relays on manual tracking of cells in order to aid in generating "cell lineages". While manual tracking can appear as a disadvantage, it allows to track cells in a greater variety recording conditions. First, most of the time lapses in microbiology are recoded at frame rate of few minutes. With this rate, displacement of bacteria between any two frames can be considerable (non-motile cells still push one another due to elongation). MicrobeTracker and Oufti have automated tracking functions, but they easily introduce significant errors if the frame rate is not high enough. Secondly, our lab is interested in cells with pili, resulting in bacteria moving even more between any two frames, making automated tracking impossible. At low density cultures, tracking of twitching cells in a time lapse is

easily accomplished by human mind, while impossible or prone to errors if done by computers. Moreover, automated tracking is a considerably long process and any object in the image, i.e. microfluidic features, will "confuse" the program. Therefore, despite being more work-intense, manual tracking present several advantages and ensure tracking in almost any condition.

At present state the "Lineage" function is working, but there are several aspects that can be improved. The manual tracking is done using an external program. The user must create the list manually (i.e. using Excel) and follow some rules on its layout: for example, grouping tracks that share a common ancestor together. This made it easier to create a working function, but there are many instances in which the user can introduce errors without noticing. Therefore, one improvement is to create a tracking function in WHISIT. This will avoid the need of using an additional program and tracking lists will be automatically stored in WHISIT as they are generated. A tracking function could also make corrections easier. At present, any error has to be tracked back and correct using the external program in which it was generated, lengthening the whole process. Further improvement is also to include the tracking data in the results, allowing to see the changes in fluorescence as function of the cell movement.

BIBLIOGRAPHY

Chapter 2, 3, 4 and 5 include their own Bibliographies. The following Bibliography gathered the references for Chapter 1, 6 and Appendixes.

Achtman, M. et al. (1999). Yersinia pestis, the cause of plague, is a recently emerged clone of Yersinia pseudotuberculosis. Proc. Natl. Acad. Sci. *96*, 14043–14048.

Alm, R.A. et al. (1996). Identification of a novel gene, *pilZ*, essential for type 4 fimbrial biogenesis in *Pseudomonas aeruginosa*. J. Bacteriol. *178*, 46–53.

Armbruster, C.E., and Mobley, H.L.T. (2012). Merging mythology and morphology: The multifaceted lifestyle of Proteus mirabilis. Nat. Rev. Microbiol. *10*, 743–754.

Attridge, S.R. et al. (1996). Relative significance of mannose-sensitive hemagglutinin and toxin- coregulated pili in colonization of infant mice by Vibrio cholerae El Tor. Infect. Immun. *64*, 3369–3373.

Backert, S., and Meyer, T.F. (2006). Type IV secretion systems and their effectors in bacterial pathogenesis. Curr. Opin. Microbiol. *9*, 207–217.

Belas, R. (2014). Biofilms, flagella, and mechanosensing of surfaces by bacteria. Trends Microbiol. *22*, 517–527.

Berke, A.P. et al. (2008). Hydrodynamic attraction of swimming microorganisms by surfaces. Phys. Rev. Lett. *101*, 1–4.

Berleman, J.E. et al. (2006). Rippling is a predatory behavior in Myxococcus xanthus. J. Bacteriol. *188*, 5888–5895.

Berry, J.-L., and Pelicic, V. (2015). Exceptionally widespread nanomachines composed of type IV pilins: the prokaryotic Swiss Army knives. FEMS Microbiol. Rev. *39*, 134–154.

Biais, N. et al. (2010). Force-dependent polymorphism in type IV pili reveals hidden epitopes. Proc. Natl. Acad. Sci. *107*, 11358–11363.

Bieber, D. et al. (1998). Type IV pili, transient bacterial aggregates, and virulence of enteropathogenic Escherichia coli. Science *280*, 2114–2118.

Bieber, D. et al. (2010). Virulence of Enteropathogenic Escherichia coli Type IV Pili , Transient Bacterial Aggregates , and Virulence of Enteropathogenic Escherichia coli. Science (80-.). *2114*.

Bodas, D., and Khan-Malek, C. (2007). Hydrophilization and hydrophobic recovery of PDMS by oxygen plasma and chemical treatment-An SEM investigation. Sensors Actuators, B Chem. *123*, 368–373.

Brinton, C.C. (1959). Non-Flagellar Appendages of Bacteria. Nature *183*, 782–786.

Bulyha, I. et al. (2009). Regulation of the type IV pili molecular machine by dynamic localization of two motor proteins. Mol. Microbiol. *74*, 691–706.

Bundock, P. et al. (1995). Trans-kingdom T-DNA transfer from Agrobacterium tumefaciens to Saccharomyces cerevisiae. Embo J *14*, 3206–3214.

Burrows, L.L. (2012). Pseudomonas aeruginosa Twitching Motility: Type IV Pili in Action. Annu. Rev. Microbiol. *66*, 493–520.

Busch, A. et al. (2015). Molecular mechanism of bacterial type 1 and P pili assembly. Philos. Trans. R. Soc. A Math. Phys. Eng. Sci. *373*, 20130153–20130153.

Campos, M. et al. (2013). The type II secretion system - a dynamic fiber assembly nanomachine. Res. Microbiol. *164*, 545–555.

Carbonnelle, E. et al. (2004). Type IV pilus biogenesis in Neisseria meningitidis: PilW is involved in a step occurring after pilus assembly, essential for fibre stability and function. Mol. Microbiol. *55*, 54–64.

Cehovin, A. et al. (2013). Specific DNA recognition mediated by a type IV pilin. Proc. Natl. Acad. Sci. *110*, 3065–3070.

Chandran Darbari, V., and Waksman, G. (2015). Structural Biology of Bacterial Type IV Secretion Systems. Annu. Rev. Biochem. *84*, 603–629.

Chang, Y.W. et al. (2017). Architecture of the Vibrio cholerae toxin-coregulated pilus machine revealed by electron cryotomography. Nat. Microbiol. *2*.

Chang, Y.W.Y.-W. et al. (2016). Architecture of the type IVa pilus machine. Science (80-.). *351*, aad2001-aad2001.

Chen, I., and Dubnau, D. (2004). DNA uptake during bacterial transformation. Nat. Rev. Microbiol. *2*, 241–249.

Chiavelli, D.A. et al. (2001). The Mannose-Sensitive Hemagglutinin of Vibrio cholerae Promotes Adherence to Zooplankton. Appl. Environ. Microbiol. *67*, 3220–3225.

Choudhury, D. et al. (1999). X-ray structure of the FimC-FimH chaperone-adhesin complex from uropathogenic Escherichia coli. Science *285*, 1061–1066.

Christen, M. et al. (2016). Quantitative Selection Analysis of Bacteriophage φcbK Susceptibility in Caulobacter crescentus. J. Mol. Biol. *428*, 419–430.

Cleary, J. et al. (2004). Enteropathogenic Escherichia coli (EPEC) adhesion to intestinal epithelial cells: Role of bundle-forming pili (BFP), EspA filaments and intimin. Microbiology *150*, 527–538.

Colwell, R.R. et al. (2003). Reduction of cholera in Bangladeshi villages by simple filtration. Proc. Natl. Acad. Sci. *100*, 1051–1055.

Comolli, J.C. et al. (1999a). Pili binding to asialo-GM1 on epithelial cells can mediate cytotoxicity or bacterial internalization by Pseudomonas aeruginosa. Infect. Immun. *67*, 3207–3214.

Comolli, J.C. et al. (1999b). *Pseudomonas aeruginosa* gene products PilT and PilU are required for cytotoxicity *in vitro* and virulence in a mouse model of acute pneumonia. Infect. Immun. *67*, 3625–3630.

Conner, J.G. et al. (2017). The ins and outs of cyclic di-GMP signaling in Vibrio cholerae. Curr. Opin. Microbiol. *36*, 20–29.

Conrad, J.C. et al. (2011). Flagella and pili-mediated near-surface single-cell motility mechanisms in P. aeruginosa. Biophys. J. *100*, 1608–1616.

Costa, T.R.D. et al. (2015). Secretion systems in Gram-negative bacteria: structural and mechanistic insights. Nat. Rev. Microbiol. *13*, 343–359.

Costa, T.R.D. et al. (2016). Structure of the Bacterial Sex F Pilus Reveals an Assembly of a Stoichiometric Protein-Phospholipid Complex. Cell *166*, 1436–1444.e10.

Craig, L., and Li, J. (2008). Type IV pili: paradoxes in form and function. Curr. Opin. Struct. Biol. *18*, 267–277.

Craig, L. et al. (2003). Type IV pilin structure and assembly: X-ray and EM analyses of Vibrio cholerae toxin-coregulated pilus and Pseudomonas aeruginosa PAK pilin. Mol. Cell *11*, 1139–1150.

Craig, L. et al. (2004). Type IV pilus structure and bacterial pathogenicity. Nat. Rev. Microbiol. *2*, 363–378.

Craig, L. et al. (2006). Type IV Pilus Structure by Cryo-Electron Microscopy and Crystallography: Implications for Pilus Assembly and Functions. Mol. Cell *23*, 651–662.

Criss, A.K. et al. (2005). The frequency and rate of pilin antigenic variation in *Neisseria gonorrhoeae*. Mol. Microbiol. *58*, 510–519.

Daum, B. et al. (2017). Structure and in situ organisation of the pyrococcus furiosus archaellum machinery. Elife *6*, 1–21.

Deshpande, S., and Pfohl, T. (2012). Hierarchical self-assembly of actin in micro-confinements using microfluidics. Biomicrofluidics *6*, 1–13.

Deshpande, S., and Pfohl, T. (2015). Real-time dynamics of emerging actin networks in cell-mimicking compartments. PLoS One *10*, 1–19.

Du, Y. et al. (2002). Role of fraction 1 antigen of Yersinia pestis in inhibition of phagocytosis. Infect. Immun. *70*, 1453–1460.

Dunger, G. et al. (2014). *Xanthomonas citri* subsp. *citri* Type IV Pilus Is Required for Twitching Motility, Biofilm Development, and Adherence. Mol. Plant-Microbe Interact. *27*, 1132–1147.

Durand, É. et al. (2003). Type II Protein Secretion in Pseudomonas aeruginosa : the Pseudopilus Is a Multifibrillar and Adhesive Structure Type II Protein Secretion in Pseudomonas aeruginosa : the Pseudopilus Is a Multifibrillar and Adhesive Structure. J. Bacteriol. *185*, 2749–2758.

Eddington, D.T. et al. (2006). Thermal aging and reduced hydrophobic recovery of polydimethylsiloxane. Sensors Actuators, B Chem. *114*, 170–172.

Elizabeth Hulme, S. et al. (2008). Using ratchets and sorters to fractionate motile cells of Escherichia coli by length. Lab Chip *8*, 1888.

Ellison, C.K. et al. (2017). Obstruction of pilus retraction stimulates bacterial surface sensing. Science (80-.). *358*, 535–538.

Evans, K.J. et al. (2007). Predation by Bdellovibrio bacteriovorus HD100 requires type IV pili. J. Bacteriol. *189*, 4850–4859.

Faruque, S.M. et al. (2006). Transmissibility of cholera: In vivo-formed biofilms and their relationship to infectivity and persistence in the environment. Proc. Natl. Acad. Sci. *103*, 6350–6355.

Felek, S. et al. (2011). Contributions of chaperone/usher systems to cell binding, biofilm formation and Yersinia pestis virulence. Microbiology *157*, 805–818.

Fiebig, A. et al. (2014). A Cell Cycle and Nutritional Checkpoint Controlling Bacterial Surface Adhesion. PLoS Genet. *10*.

Flemming, H.-C. (2011). The perfect slime. Colloids Surfaces B Biointerfaces *86*, 251–259.

Fröls, S. et al. (2008). UV-inducible cellular aggregation of the hyperthermophilic archaeon Sulfolobus solfataricus is mediated by pili formation. Mol. Microbiol. *70*, 938–952.

Fronzes, R. et al. (2009). The structural biology of type IV secretion systems. Nat. Rev. Microbiol. *7*, 703–714.

Galván, E.M. et al. (2007). The Psa fimbriae of Yersinia pestis interact with phosphatidylcholine on alveolar epithelial cells and pulmonary surfactant. Infect. Immun. *75*, 1272–1279.

Geibel, S. et al. (2013). Structural and energetic basis of folded-protein transport by the FimD usher. Nature *496*, 243–246.

Ghosh, A., and Albers, S.-V. (2011). Assembly and function of the archaeal flagellum. Biochem. Soc. Trans. *39*, 64–69.

Giltner, C.L. et al. (2012). Type IV Pilin Proteins: Versatile Molecular Modules. Microbiol. Mol. Biol. Rev. *76*, 740–772.

Gold, V.A.M. et al. (2015). Structure of a type IV pilus machinery in the open and closed state. Elife *4*, 1–12.

Göllner, M. et al. (2016). A self-filling microfluidic device for noninvasive and time-resolved single red blood cell experiments. Biomicrofluidics *10*, 1–11.

Guerrero-Ferreira, R.C. et al. (2011). Alternative mechanism for bacteriophage adsorption to the motile bacterium Caulobacter crescentus. Proc. Natl. Acad. Sci. *108*, 9963–9968.

Guzzo, C.R. et al. (2009). PILZ Protein Structure and Interactions with PILB and the FIMX EAL Domain: Implications for Control of Type IV Pilus Biogenesis. J. Mol. Biol. *393*, 848–866.

Hall-Stoodley, L. et al. (2004). Bacterial biofilms: from the Natural environment to infectious diseases. Nat. Rev. Microbiol. *2*, 95–108.

Hamilton, H.L., and Dillard, J.P. (2006). Natural transformation of Neisseria gonorrhoeae: from DNA donation to homologous recombination. Mol. Microbiol. *59*, 376–385.

Heinemann, J.A., and Sprague, G.F. (1989). Bacterial conjugative plasmids mobilize DNA transfer between bacteria and yeast. Nature *340*, 205–209.

Hélaine, S. et al. (2005). PilX, a pilus-associated protein essential for bacterial aggregation, is a key to pilus-facilitated attachment of Neisseria meningitidis to human cells. Mol. Microbiol. *55*, 65–77.

Hélaine, S. et al. (2007). 3D structure/function analysis of PilX reveals how minor pilins can modulate the virulence properties of type IV pili. Proc. Natl. Acad. Sci. *104*, 15888–15893.

Hendrickx, A.P.A. et al. (2011a). Architects at the bacterial surface-sortases and the assembly of pili with isopeptide bonds. Nat. Rev. Microbiol. *9*, 166–176.

Hendrickx, A.P.A. et al. (2011b). Architects at the bacterial surface — sortases and the assembly of pili with isopeptide bonds. Nat. Rev. Microbiol. *9*, 166–176.

Hepp, C., and Maier, B. (2016). Kinetics of DNA uptake during transformation provide evidence for a translocation ratchet mechanism. Proc. Natl. Acad. Sci. *113*, 12467–12472.

Hilleringmann, M. et al. (2009). Molecular architecture of Streptococcus pneumoniae TIGR4 pili. EMBO J. *28*, 3921–3930.

Holz, C. et al. (2010). Multiple pilus motors cooperate for persistent bacterial movement in two dimensions. Phys. Rev. Lett. *104*, 1–4.

Hospenthal, M.K. et al. (2016). Structure of a Chaperone-Usher Pilus Reveals the Molecular Basis of Rod Uncoiling. Cell *164*, 269–278.

Hospenthal, M.K. et al. (2017a). A comprehensive guide to pilus biogenesis in Gram-negative bacteria. Nat. Rev. Microbiol. *15*, 365–379.

Hospenthal, M.K. et al. (2017b). The Cryoelectron Microscopy Structure of the Type 1 Chaperone-Usher Pilus Rod. Structure *25*, 1829–1838.e4.

Hug, I. et al. (2017). Second messenger–mediated tactile response by a bacterial rotary motor. Science (80-.). *358*, 531–534.

Imam, S. et al. (2011). Identification of Surprisingly Diverse Type IV Pili, across a Broad Range of Gram-Positive Bacteria. PLoS One *6*, e28919.

Islam, S.T., and Mignot, T. (2015). The mysterious nature of bacterial surface (gliding) motility: A focal adhesion-based mechanism in Myxococcus xanthus. Semin. Cell Dev. Biol. *46*, 143–154.

Izoré, T. et al. (2010). Structural Basis of Host Cell Recognition by the Pilus Adhesin from Streptococcus pneumoniae. Structure *18*, 106–115.

Jain, R. et al. (2017). Interaction of the cyclic-di-GMP binding protein FimX and the Type 4 pilus assembly ATPase promotes pilus assembly. PLoS Pathog. *13*, 1–23.

Jarrell, K.F., and McBride, M.J. (2008). The surprisingly diverse ways that prokaryotes move. Nat. Rev. Microbiol. *6*, 466–476.

Jin, F. et al. (2011). Bacteria use type-IV pili to slingshot on surfaces. Proc. Natl. Acad. Sci. *108*, 12617–12622.

Jones, C.J. et al. (2015). C-di-GMP Regulates Motile to Sessile Transition by Modulating MshA Pili Biogenesis and Near-Surface Motility Behavior in Vibrio cholerae. PLoS Pathog. *11*, 1–27.

Kachlany, S.C. et al. (2000). Nonspecific Adherence by Actinobacillus actinomycetemcomitans Requires Genes Widespread in Bacteria and Archaea. J. Bacteriol. *182*, 6169–6176.

Kachlany, S.C. et al. (2001a). Genes for tight adherence of Actinobacillus actinomycetemcomitans: from plaque to plague to pond scum. Trends Microbiol. *9*, 429–437.

Kachlany, S.C. et al. (2001b). flp-1, the first representative of a new pilin gene subfamily, is required for non-specific adherence of Actinobacillus actinomycetemcomitans. Mol. Microbiol. *40*, 542–554.

Kaiser, M. et al. (2016). Tracking single-cell gene regulation in dynamically controlled environments using an integrated microfluidic and computational setup . bioRxiv 1–30.

Kaiser, M. et al. (2018). Monitoring single-cell gene regulation under dynamically controllable conditions with integrated microfluidics and software. Nat. Commun. *9*, 212.

Kang, H.J. et al. (2009). The Corynebacterium diphtheriae shaft pilin SpaA is built of tandem Ig-like modules with stabilizing isopeptide and disulfide bonds. Proc. Natl. Acad. Sci. *106*, 16967–16971.

Karuppiah, V., and Derrick, J.P. (2014). Type IV pili--a numbers game. EMBO J. *33*, 1732–1734.

Kazmierczak, B.I. et al. (2006). Analysis of FimX, a phosphodiesterase that governs twitching motility in Pseudomonas aeruginosa. Mol. Microbiol. *60*, 1026–1043.

Kellogg, R.A. et al. (2014). High-throughput microfluidic single-cell analysis pipeline for studies of signaling dynamics. Nat. Protoc. *9*, 1713–1726.

Kinosita, Y. et al. (2016). Direct observation of rotation and steps of the archaellum in the swimming halophilic archaeon Halobacterium salinarum. Nat. Microbiol. *1*, 1–9.

Kirn, T.J. et al. (2000). Delineation of pilin domains required for bacterial association into microcolonies and

intestinal colonization by Vibrio cholerae. Mol. Microbiol. *35*, 896–910.

Klausen, M. et al. (2003a). Biofilm formation by Pseudomonas aeruginosa wild type, flagella and type IV pili mutants. Mol. Microbiol. *48*, 1511–1524.

Klausen, M. et al. (2003b). Involvement of bacterial migration in the development of complex multicellular structures in Pseudomonas aeruginosa biofilms. Mol. Microbiol. *50*, 61–68.

Kloppsteck, P. et al. (2016). Structure of the fimbrial protein Mfa4 from Porphyromonas gingivalis in its precursor form: implications for a donor-strand complementation mechanism. Sci. Rep. *6*, 22945.

Kolappan, S. et al. (2016). Structure of the neisseria meningitidis type IV pilus. Nat. Commun. *7*, 1–12.

Korotkov, K. V. et al. (2012). The type II secretion system: Biogenesis, molecular architecture and mechanism. Nat. Rev. Microbiol. *10*, 336–351.

Lewis, K. (2007). Persister cells, dormancy and infectious disease. Nat. Rev. Microbiol. *5*, 48–56.

Li, G. et al. (2012). Surface contact stimulates the just-in-time deployment of bacterial adhesins. Mol. Microbiol. *83*, 41–51.

Li, Y. et al. (2003). Extracellular polysaccharides mediate pilus retraction during social motility of Myxococcus xanthus. Proc. Natl. Acad. Sci. *100*, 5443–5448.

Linke, C. et al. (2010). Crystal structure of the minor pilin FctB reveals determinants of group A streptococcal pilus anchoring. J. Biol. Chem. *285*, 20381–20389.

Liu, B. et al. (2014). Helical motion of the cell body enhances Caulobacter crescentus motility. Proc. Natl. Acad. Sci. *111*, 11252–11256.

Liu, X. et al. (2010). Identification and characterization of a phosphodiesterase that inversely regulates motility and biofilm formation in Vibrio cholerae. J. Bacteriol. *192*, 4541–4552.

Low, H.H. et al. (2014). Structure of a type IV secretion system. Nature *508*, 550–553.

Lu, S. et al. (2015). Nanoscale Pulling of Type IV Pili Reveals Their Flexibility and Adhesion to Surfaces over Extended Lengths of the Pili. Biophys. J. *108*, 2865–2875.

Luo, Y. et al. (2015). A hierarchical cascade of second messengers regulates Pseudomonas aeruginosa Surface Behaviors. MBio *6*, 1–11.

Maier, B., and Wong, G.C.L. (2015). How Bacteria Use Type IV Pili Machinery on Surfaces. Trends Microbiol. *23*, 775–788.

Maier, B. et al. (2002). Single pilus motor forces exceed 100 pN. Proc. Natl. Acad. Sci. *99*, 16012–16017.

Maier, B. et al. (2004). A force-dependent switch reverses type IV pilus retraction. Proc. Natl. Acad. Sci. U. S. A. *101*, 10961–10966.

Makarova, K.S. et al. (2016). Diversity and evolution of type IV pili systems in Archaea. Front. Microbiol. *7*, 1–16.

Malvankar, N.S., and Lovley, D.R. (2012). Microbial nanowires: A new paradigm for biological electron transfer and bioelectronics. ChemSusChem *5*, 1039–1046.

Malvankar, N.S. et al. (2011). Tunable metallic-like conductivity in microbial nanowire networks. Nat. Nanotechnol. *6*, 573–579.

Mannik, J. et al. (2009). Bacterial growth and motility in sub-micron constrictions. Proc. Natl. Acad. Sci. *106*, 14861–14866.

Marathe, R. et al. (2014). Bacterial twitching motility is coordinated by a two-dimensional tug-of-war with directional memory. Nat. Commun. *5*.

Mazmanian, S.K. et al. (1999). *Staphylococcus aureus* sortase, an enzyme that anchors surface proteins to the cell wall. Science (80-.). *285*, 760–763.

McBride, M.J. (2001). Bacterial gliding motility: multiple mechanisms for cell movement over surfaces. Annu. Rev. Microbiol. *55*, 49–75.

McCallum, M. et al. (2016). PilN Binding Modulates the Structure and Binding Partners of the Pseudomonas aeruginosa Type IVa Pilus Protein PilM. J. Biol. Chem. *291*, 11003–11015.

McCallum, M. et al. (2017). The molecular mechanism of the type IVa pilus motors. Nat. Commun. *8*, 1–10.

McCarter, L. et al. (1988). Flagellar dynamometer controls swarmer cell differentiation of V. parahaemolyticus. Cell *54*, 345–351.

McLaughlin, L.S. et al. (2012). Structural insights into the Type II secretion nanomachine. Curr. Opin. Struct. Biol. *22*, 208–216.

Melin, J., and Quake, S.R. (2007). Microfluidic Large-Scale Integration: The Evolution of Design Rules for Biological Automation. Annu. Rev. Biophys. Biomol. Struct. *36*, 213–231.

Mercier, R., and Mignot, T. (2016). Regulations governing the multicellular lifestyle of Myxococcus xanthus. Curr. Opin. Microbiol. *34*, 104–110.

Merz, A.J. et al. (2000). Pilus retraction powers bacterial twitching motility. Nature *407*, 98–102.

Mignolet, J. et al. (2018). More than a Tad: spatiotemporal control of Caulobacter pili This review comes from a themed issue on Cell regulation. Curr. Opin. Microbiol. *42*, 79–86.

Mignot, T. et al. (2005). Regulated pole-to-pole oscillations of a bacterial gliding motility protein. Science (80-.). *310*, 855–857.

Misic, A.M. et al. (2010). P. aeruginosa PilT Structures with and without Nucleotide Reveal a Dynamic Type IV Pilus Retraction Motor. J. Mol. Biol. *400*, 1011–1021.

Moffitt, J.R. et al. (2012). The single-cell chemostat: an agarose-based, microfluidic device for high-throughput, single-cell studies of bacteria and bacterial communities. Lab Chip *12*, 1487.

Negus, D. et al. (2017). Predator Versus Pathogen: How Does Predatory Bdellovibrio bacteriovorus Interface with the Challenges of Killing Gram-Negative Pathogens in a Host Setting? Annu. Rev. Microbiol. *71*, 441–457.

Nesper, J. et al. (2017). Cyclic di-GMP differentially tunes a bacterial flagellar motor through a novel class of CheY-like regulators. Elife *6*, e28842.

Ng, D. et al. (2016). The Vibrio cholerae Minor Pilin TcpB Initiates Assembly and Retraction of the Toxin-Coregulated Pilus.

Ni, L. et al. (2016). Bacteria differently deploy type-IV pili on surfaces to adapt to nutrient availability. Npj Biofilms Microbiomes *2*, 15029.

Nivaskumar, M. et al. (2014). Distinct docking and stabilization steps of the pseudopilus conformational transition path suggest rotational assembly of type IV pilus-like fibers. Structure *22*, 685–696.

Nudleman, E., and Kaiser, D. (2004). Pulling Together with Type IV Pili. J. Mol. Microbiol. Biotechnol. *7*, 52–62.

O'Toole, G.A. et al. (2016). Sensational biofilms: surface sensing in bacteria. Curr. Opin. Microbiol. *30*, 139–146.

Oliveira, N.M. et al. (2016). Single-cell twitching chemotaxis in developing biofilms. Proc. Natl. Acad. Sci. *113*, 6532–6537.

Paintdakhi, A. et al. (2016). Oufti: An integrated software package for high-accuracy, high-throughput quantitative microscopy analysis. Mol. Microbiol. *99*, 767–777.

Park, H.S.M. et al. (2001). Structural alterations in a type IV pilus subunit protein result in concurrent defects in multicellular behaviour and adherence to host tissue. Mol. Microbiol. *42*, 293–307.

Peabody, C.R. (2003). Type II protein secretion and its relationship to bacterial type IV pili and archaeal flagella. Microbiology *149*, 3051–3072.

Pelicic, V. (2008). Type IV pili: e pluribus unum? Mol. Microbiol. *68*, 827–837.

Persat, A. et al. (2014). The curved shape of Caulobacter crescentus enhances surface colonization in flow. Nat. Commun. *5*, 3824.

Persat, A. et al. (2015). Type IV pili mechanochemically regulate virulence factors in *Pseudomonas aeruginosa*. Proc. Natl. Acad. Sci. *112*, 7563–7568.

Phan, G. et al. (2011). Crystal structure of the FimD usher bound to its cognate FimC-FimH substrate. Nature *474*, 49–53.

Planet, P.J. et al. (2003). The Widespread Colonization Island of Actinobacillus actinomycetemcomitans. Nat. Genet. *34*, 193–198.

Pohlschroder, M. et al. (2011). Archaeal type IV pilus-like structures-evolutionarily conserved prokaryotic surface organelles. Curr. Opin. Microbiol. *14*, 357–363.

Poweleit, N. et al. (2016). CryoEM structure of the Methanospirillum hungatei archaellum reveals structural features distinct from the bacterial fl agellum and type IV pilus. Nat. Microbiol. *2*, 1–11.

Pratt, J.T. et al. (2007). PilZ domain proteins bind cyclic diguanylate and regulate diverse processes in Vibrio cholerae. J. Biol. Chem. *282*, 12860–12870.

Rakotoarivonina, H. et al. (2002). Adhesion to cellulose of the Gram-positive bacterium Ruminococcus albus involves type IV pili. Microbiology *148*, 1871–1880.

Ramboarina, S. et al. (2005). Structure of the bundle-forming pilus from enteropathogenic Escherichia coli. J. Biol. Chem. *280*, 40252–40260.

Reguera, G. et al. (2005). Extracellular electron transfer via microbial nanowires. Nature *435*, 1098–1101.

Reinders, A. et al. (2015). Expression and Genetic Activation of Cyclic Di-GMP-Specific Phosphodiesterases in Escherichia coli. J. Bacteriol. *198*, 448–462.

Ribbe, J. et al. (2017). Role of Cyclic Di-GMP and Exopolysaccharide in Type IV Pilus Dynamics. J. Bacteriol. *199*, 1–10.

Roux, N. et al. (2012). Neglected but amazingly diverse type IVb pili. Res. Microbiol. *163*, 659–673.

Rusconi, R., and Stocker, R. (2015). Microbes in flow. Curr. Opin. Microbiol. *25*, 1–8.

Saiman, L., and Prince, A. (1993). Pseudomonas aeruginosa pili bind to asialoGM1 which is increased on the surface of cystic fibrosis epithelial cells. J. Clin. Invest. *92*, 1875–1880.

Sampaleanu, L.M. et al. (2009). Periplasmic domains of Pseudomonas aeruginosa PilN and PilO form a stable heterodimeric complex. J. Mol. Biol. *394*, 143–159.

Satyshur, K.A. et al. (2007). Crystal structures of the pilus retraction motor PilT suggest large domain movements and subunit cooperation drive motility. Structure *15*, 363–376.

Sauer, M.M. et al. (2016). Catch-bond mechanism of the bacterial adhesin FimH. Nat. Commun. *7*.

Schaik, E.J. Van et al. (2005). DNA Binding : a Novel Function of Pseudomonas aeruginosa Type IV Pili DNA Binding : a Novel Function of *Pseudomonas aeruginosa* Type IV Pili. J. Bacteriol. *187*, 1455–1464.

Schilling, J. et al. (2010). Transcriptional activation of the tad type IVb pilus operon by PypB in Yersinia enterocolitica. J. Bacteriol. *192*, 3809–3821.

Seitz, P., and Blokesch, M. (2013). DNA-uptake machinery of naturally competent Vibrio cholerae. Proc. Natl. Acad. Sci. *110*, 17987–17992.

Shen, Y. et al. (2012). Flow directs surface-attached bacteria to twitch upstream. Biophys. J. *103*, 146–151.

Shi, W., and Zusman, D.R. (1993). The two motility systems of Myxococcus xanthus show different selective advantages on various surfaces. Proc. Natl. Acad. Sci. U. S. A. *90*, 3378–3382.

Shi, W. et al. (1993). Chemotaxis plays a role in the social behaviour of Myxococcus xanthus. Mol Microbiol *9*, 601–

611.

Skerker, J.M., and Berg, H.C. (2001). Direct observation of extension and retraction of type IV pili. Proc. Natl. Acad. Sci. *98*, 6901–6904.

Skerker, J.M., and Shapiro, L. (2000). Identification and cell cycle control of a novel pilus system in Caulobacter crescentus. EMBO J. *19*, 3223–3234.

Sliusarenko, O. et al. (2011). High-throughput, subpixel precision analysis of bacterial morphogenesis and intracellular spatio-temporal dynamics. Mol. Microbiol. *80*, 612–627.

Soucy, S.M. et al. (2015). Horizontal gene transfer: Building the web of life. Nat. Rev. Genet. *16*, 472–482.

Srivastava, D. et al. (2013). Cyclic di-GMP inhibits Vibrio cholerae motility by repressing induction of transcription and inducing extracellular polysaccharide production. Mol. Microbiol. *90*, 1262–1276.

Strelnikova, N. et al. (2016). Formation of Actin Networks in Microfluidic Concentration Gradients. Front. Mater. *3*, 1–9.

Sun, H. et al. (2000). Type IV pilus of Myxococcus Xanthus is a motility apparatus controlled by the frz chemosensory system. Curr. Biol. *10*, 1143–1146.

Swain, J.E. et al. (2013). Thinking big by thinking small: application of microfluidic technology to improve ART. Lab Chip *13*, 1213.

Takhar, H.K. et al. (2013). The platform protein is essential for type IV pilus biogenesis. J. Biol. Chem. *288*, 9721–9728.

Tamayo, R. et al. (2010). Growth in a biofilm induces a hyperinfectious phenotype in Vibrio cholerae. Infect. Immun. *78*, 3560–3569.

Taylor, R.G., and Welch, R.D. (2008). Chemotaxis as an emergent property of a swarm. J. Bacteriol. *190*, 6811–6816.

Teschler, J.K. et al. (2015). Living in the matrix: Assembly and control of Vibrio cholerae biofilms. Nat. Rev. Microbiol. *13*, 255–268.

Thomas, W.E. et al. (2002). Bacterial adhesion to target cells enhanced by shear force. Cell *109*, 913–923.

Thomson, N.R. et al. (2006). The Complete Genome Sequence and Comparative Genome Analysis of the High Pathogenicity Yersinia enterocolitica Strain 8081. PLoS Genet. *2*, e206.

Thorsen, T. et al. (2002). Microfluidic Large-Scale Integration. Science (80-.). *298*, 580–584.

Tobe, T., and Sasakawa, C. (2002). Species-specific cell adhesion of enteropathogenic Escherichia coli is mediated by type IV bundle-forming pili. Cell. Microbiol. *4*, 29–42.

Tomich, M. et al. (2007). The tad locus: postcards from the widespread colonization island. Nat. Rev. Microbiol. *5*, 363–375.

Ton-That, H., and Schneewind, O. (2003). Assembly of pili on the surface of Corynebacterium diphtheriae. Mol. Microbiol. *50*, 1429–1438.

Ton-That, H., and Schneewind, O. (2004). Assembly of pili in Gram-positive bacteria. Trends Microbiol. *12*, 228–234.

Touhami, A. et al. (2006). Nanoscale Characterization and Determination of Adhesion Forces of Pseudomonas aeruginosa Pili by Using Atomic Force Microscopy. J. Bacteriol. *188*, 370–377.

Trieu-Cuot, P. et al. (1985). In vivo transfer of genetic information between gram-positive and gram-negative bacteria. EMBO J. *4*, 3583–3587.

Tsang, P.H. et al. (2006). Adhesion of single bacterial cells in the micronewton range. Proc. Natl. Acad. Sci. *103*, 5764–5768.

Unger, M.A. (2000). Monolithic Microfabricated Valves and Pumps by Multilayer Soft Lithography. Science (80-.). *288*, 113–116.

Utada, A.S. et al. (2014). Vibrio cholerae use pili and flagella synergistically to effect motility switching and conditional surface attachment. Nat. Commun. *5*, 1–8.

Varga, J.J. et al. (2006). Type IV pili-dependent gliding motility in the Gram-positive pathogen Clostridium perfringens and other Clostridia. Mol. Microbiol. *62*, 680–694.

Vignon, G. et al. (2003). Type IV-like pili formed by the type II secreton: specificity, composition, bundling, polar localization, and surface presentation of peptides. J. Bacteriol. *185*, 3416–3428.

Wang, F. et al. (2017). Cryoelectron Microscopy Reconstructions of the Pseudomonas aeruginosa and Neisseria gonorrhoeae Type IV Pili at Sub-nanometer Resolution. Structure *25*, 1423–1435.e4.

Wessel, A.K. et al. (2013). Going local: technologies for exploring bacterial microenvironments. Nat. Rev. Microbiol. *11*, 337–348.

Wurpel, D.J. et al. (2013). Chaperone-Usher Fimbriae of Escherichia coli. PLoS One *8*.

Xiao, K. et al. (2016). Low Energy Atomic Models Suggesting a Pilus Structure that could Account for Electrical Conductivity of Geobacter sulfurreducens Pili. Sci. Rep. *6*, 1–9.

Xu, Q. et al. (2016). A Distinct Type of Pilus from the Human Microbiome. Cell *165*, 690–703.

Zahavi, E.E. et al. (2011). Bundle-forming pilus retraction enhances enteropathogenic Escherichia coli infectivity. Mol. Biol. Cell *22*, 2436–2447.

Zavyalov, V. et al. (2010). Adhesive organelles of Gram-negative pathogens assembled with the classical chaperone/usher machinery: Structure and function from a clinical standpoint. FEMS Microbiol. Rev. *34*, 317–378.

Zhang, Y. et al. (2012). From individual cell motility to collective behaviors: Insights from a prokaryote, Myxococcus xanthus. FEMS Microbiol. Rev. *36*, 149–164.

Zusman, D.R. et al. (2007). Chemosensory pathways, motility and development in Myxococcus xanthus. Nat. Rev. Microbiol. *5*, 862–872.